Università dell'Insubria
Dipartimento di Matematica e Fisica

Doctor of Philosophy Dissertation

Advanced Manufacturing Techniques for X-ray and VHE Gamma-ray Astronomical Mirrors

by

Dervis Vernani

Supervisors: Dott. Giovanni Pareschi
Dott. Gianpiero Tagliaferri

XXIII ciclo di Dottorato di Ricerca - Astronomia ed Astrofisica
Como, 2011

Index

Introduction

In the history of the X-ray Astronomy the employment of focusing telescopes has been possible so far only in the soft x-ray energy band (0.1-10 keV), whereas in the hard x-ray energy band (10-100 keV), due to some limitation in the mirror technology (shallow reflection angles leading to very small effective areas), only collimated or coded-mask detectors could have been used (BeppoSAX, INTEGRAL, SWIFT). The best sensitivity in the hard x-ray band has been obtained up to now by the collimated detector PDS flown aboard BeppoSAX satellite (sensitivity of ~ 1 mCrab with an integration time of 10^5 seconds). For this reason, both in Astrophysical and Cosmological filed, a number of important questions are still waiting for spectroscopic and photometric observations in the hard x-ray band with high definition and high sensitivity focusing techniques. The technology needed to efficiently focalizing the hard x-ray is in an advanced phase of development and several research groups are working on this topic worldwide. One of these groups, already well-known for the development of XMM-Newton and JET-X/Swift optics, is the Italian group at the Brera Astronomical Observatory (INAF-OAB) located in Milano. INAF-OAB group works on a solution based on the use of interferential multilayer coating with nanometric depth-graded reticular spacing, to be applied on top of the single reflective layer soft x-ray mirrors replicated by electroforming. The concept of multilayer is to create a synthetic reticular structure (like in the natural crystals) by depositing an alternate layer sequence of a low density material, acting as spacer, and an high density material, acting as reflector. The constant spacing multilayers give high reflectivity of the hard x-rays, but in a limited-bandwidth centered on the Bragg peak. In the astronomical applications a reflectivity over a broad energy band is obtained by using variable spacing multilayer structures consisting of bilayers having modulated thicknesses.

The main goal of this thesis is to contribute in the development of the technologies for the future x-ray telescopes and specifically for the New Hard X-ray Mission and eROSITA

(Spectrum-RG) missions. Other important next future x-ray missions, currently under advanced study and worth to be mentioned, are NuSTAR (USA) and ASTRO-H (Japan).

The New Hard X-ray Mission (NHXM) is being developed in Italy as an evolution of the original HEXIT-SAT project and is now the hard x-ray project of reference for the Italian high energy community. NHXM is meant to provide a real breakthrough on a number of hot astrophysical issues, by exploiting the most advanced technology in broad-band (0.2 – 80 keV) high angular resolution (<20 arcsec HEW) grazing incidence mirrors and spectroscopic detectors, together with the use of a high efficiency imaging polarimeter. Such issues can be summarized in two main headings:

- making the census of the population of black holes in the Universe and probing the physics of accretion in the most diverse conditions;
- investigating the particle acceleration mechanisms at work in different contexts, and the effects of radiative transfer in highly magnetized plasmas and strong gravitational fields.

These topics were identified as top priority in the study commissioned by the Italian Space Agency (ASI) in 2004 to the Italian scientific community with contracts involving Thales-Alenia Space Italy (TAS-I, Turin), the Media Lario Technologies (MLT, Lecco) company and the INAF institution. NHXM benefits from the phase A study of the canceled French-Italian-German SIMBOL-X mission (2007-2008) and has been recently subjected to a scientific phase B study financed by ASI. Media Lario Technologies company (www.media-lario.com) received a contract from ASI in 2009 for a Technology Development Program (ASI-TDP) aiming at improving the technology readiness level with also in-house adoption of hardware for the metrology/manufacturing of the multilayer x-ray optics.

Spectrum-RG is a Russian - German x-ray astrophysical observatory scheduled for lunch in 2013. German Space Agency (DLR) is responsible for the development of the key mission instrument - the x-ray grazing incident mirror telescope eROSITA. The second experiment is ART-XC - an x-ray mirror telescope with a harder response than eROSITA, which is being developed by Russia (IKI, Moscow and VNIIEF, Sarov). The name eROSITA stands for extended Roentgen Survey with an Imaging Telescope Array. The general design of the eROSITA x-ray telescope is derived from that of ABRIXAS: a bundle of 7 mirror modules with short focal lengths make up a compact telescope which is ideal for survey observations. Similar designs had been proposed for the missions DUO and ROSITA but were not realized. Compared to those, however, the effective area in the soft x-ray band has now much increased

by adding 27 additional outer mirror shells to the original 27 ones of each mirror module. The requirement on the on-axis resolution has also been confined, namely to 15 arc seconds HEW. For these reasons the prefix "extended" to the original name "ROSITA" had been added. The scientific motivation for this extension is founded in the ambitious goal to detect about 100000 clusters of galaxies which trace the large scale structure of the Universe in space and time.

The main scientific goals are:

- to detect the hot intergalactic medium of 50-100 thousand galaxy clusters and groups and hot gas in filaments between clusters to map out the large scale structure in the Universe for the study of cosmic structure evolution;
- to detect systematically all obscured accreting Black Holes in nearby galaxies and many (up to 3 Million) new, distant active galactic nuclei;
- to study in detail the physics of galactic x-ray source populations, like pre-main sequence stars, supernova remnants and x-ray binaries.

Max-Planck-Institute für extraterrestrische Physik (MPE) is the scientific institute responsible for the eROSITA Payload. Media Lario Technologies (MLT) is the industrial enabler for the manufacturing of the Optical Payload for eROSITA - including the flight quality mandrels, and it is currently in the C/D Phase of the project.

The research activity described in this thesis has been carried out at Media Lario Technologies company and at the Brera Astronomical Observatory under the tutoring of INAF-OAB researchers Dott. Giovanni Pareschi and Dott. Gianpiero Tagliaferri. **The research activity of the author of this thesis** is focused on the development of an advance polishing technique for the **mandrels** to be used as masters in the mirrors **replication by electroforming**. The goal is to implement a process where the mandrels can be manufactured with a high accuracy (< 6 arcsec HEW) and low roughness (< 0.2 nm rms) within a consistent short time. In the contest of the eROSITA and NHXM (projects currently running in MLT) the author participated as technical/scientific responsible, investigating innovative mandrels manufacturing technologies (e.g. Single Point Diamond Turning, shape corrective polishing) representing an evolution of the standard approach used so far. In this frame the author has also contributed to the adoption of a customized deterministic polishing machine and a customized 3D metrology device for the mandrel geometrical characterization.

An additional research activity, performed by the author at Media Lario Technologies company and at the Brera Astronomical Observatory, is focused on the development of

lightweight **glass mirrors** manufactured via **cold-slumping technique** for Imaging Atmospheric Cherenkov Telescopes (IACT). Very High Energy (VHE) gamma rays, with photon energies in the TeV range, can be detected by ground based experiments. In fact, such high energy photons interact high in the upper atmosphere and generate an air shower of secondary particles. These particles emit the so-called Cherenkov light, a faint blue light. The mirror elements here developed have a sandwich-like structure where the reflecting and backing facets are composed by glass sheets with an interposed honeycomb aluminum core. This effort found application at the world's largest IACT, the 17m **MAGIC II telescope** (currently operating in Roque de los Muchachos - La Palma, Canary Islands), where 112 mirrors (~ 1 squared meter each), manufactured with the newly developed cold-slumping technique here described, are installed.

1 Principle of Gracing Incidence X-ray Astronomy Telescopes

In 1895, Röntgen announced his discovery of x-rays (Roentgen, 1895), and in 1912, Von Laue devised an experiment to prove that x-rays undergo diffraction through a crystal. The experiment, performed physically in the same year by Friedrich and Knipping (Laue, 1912), verified in the smallest details the theoretical predictions of Laue, providing at the same time, the experimental proof of the wave nature of x-rays and the crystals lattice structure. A year later, W. H. and W. L. Bragg, starting from the same idea of Laue, realized a much more sophisticated device showing that wavelength trains diffracted by the crystal lattice planes are adding in phase only when the following relation is satisfied (Bragg & Bragg, 1918):

$$n\lambda = 2d\sin\theta$$

where θ is the angle of incidence, d is the spacing of the crystal lattice planes and n is an integer called "order of reflection". To our knowledge, the first x-ray image was obtained from Enrico Fermi, as part of its dissertation work at the University of Pisa (Fermi, 1922), using the iron K emission lines and a suitably shaped device composed of Mica mineral crystals. The technique of reflection was in this case a diffraction from the crystalline planes of Mica (see Figure 1-1). In 1923 Compton demonstrated the possibility to reflect x-rays by using a very smooth surface and a very small incidence angles ($\leq$ 1deg), thus giving rise to the term "grazing incidence reflection" (Compton, 1923). Since there was the presence of total reflection, the x-ray interaction with the matter began to be described by a refractive index having numerical values less than one. The discovery of the Compton gave rise to a new research in the field of x-ray imaging, although the application more attractive at that time was for microscopy with a much higher resolution than optical.

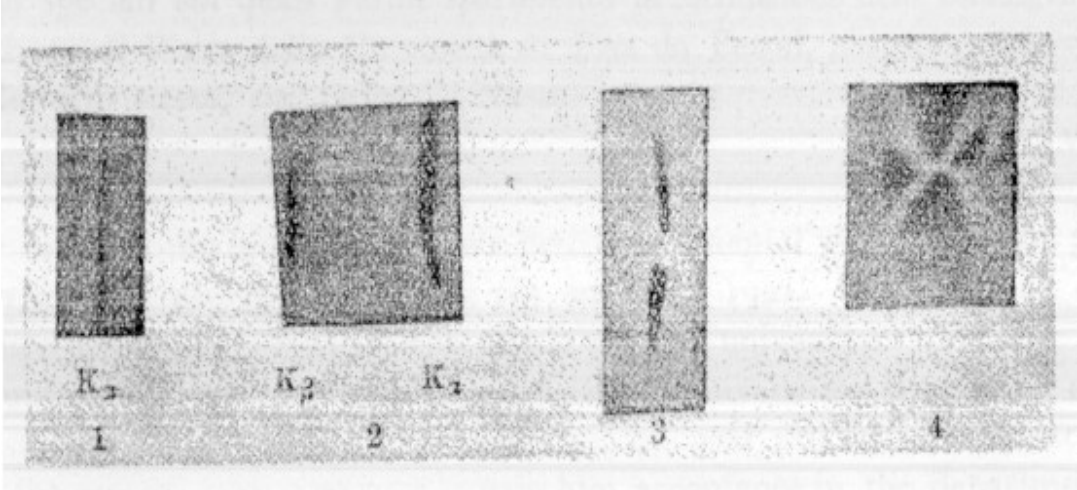

Figure 1-1. First images on photographic plate obtained by x-ray reflection at Bragg, during an experiment performed by Enrico Fermi in 1922 (Fermi, 1922).

In 1929, Jentzsch presented a work related to the construction of optical imaging, which demonstrated the impossibility to obtain good images using a single reflection from spherical mirror, due to the extreme astigmatism resulting in grazing incidence condition (Jentzsch, 1929). Within the same work Jentzsch proposed the use of a single mirror with two different radii of curvature; despite the idea to realize optical imaging with good capacity had been routed in this work, it was only in 1948 that Kirkpatrick and Baez were able to get the first two-dimensional x-ray image (Kirkpatrick & Baez, 1948). The focusing system of Kirkpatrick-Baez is based on two separate mirrors, one for vertical focus and one for the horizontal focus, and it is still used in x-ray microscopy applications because of its great usefulness in the case of asymmetric sources (such as synchrotron radiation). Ehrenberg, in 1949, after several experiments, focused its attention on the presence of out of focus x-rays not due to aberration effects and attributed it correctly to physical imperfections on the surface of the mirrors (Ehrenberg, 1949a). The idea of Ehrenberg was to describe imperfections of a surface through Fourier series: at a given spatial frequency the x-rays are diffracted into two images, with distance from the focus inversely proportional to the spatial frequency and with intensity proportional to the square of the amplitude of the wave. Ehrenberg showed that, to obtain decent images, the surfaces of mirrors should be made much more smooth (Ehrenberg, 1949b). In the early 1950s, there was facing two major problems for the implementation of appropriate systems to x-ray imaging:

1. a mirrors configuration that could improve the deficiencies of Kirkpatrick-Baez systems(limited opening, low resolution and geometrical aberration) was missing;
2. a technology enabling the realization of revolution geometry mirrors with the precision and smoothness required should had to be developed. It was also required a metrology able to control the process and make it repeatable.

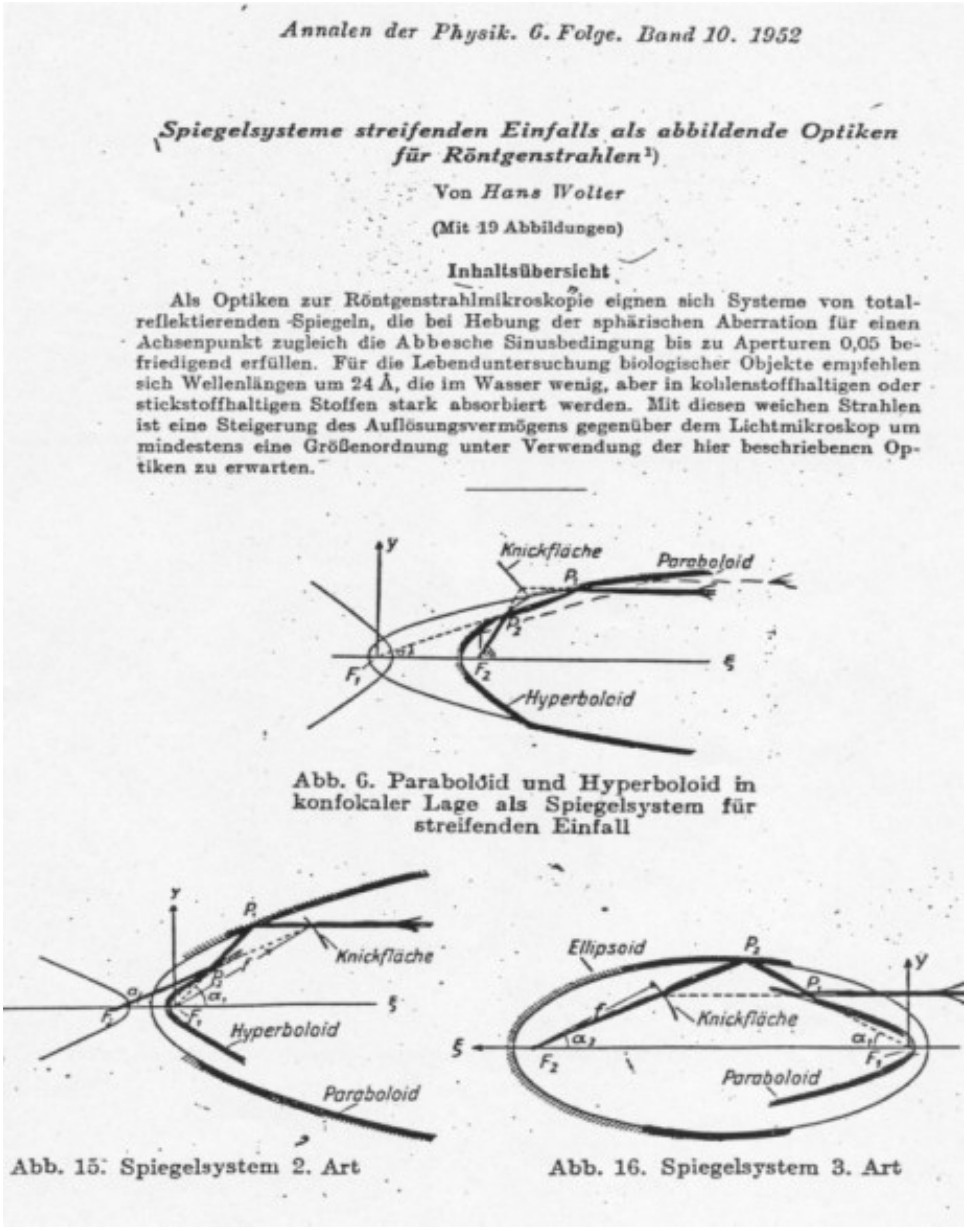

Annalen der Physik. 6. Folge. Band 10. 1952

Spiegelsysteme streifenden Einfalls als abbildende Optiken für Röntgenstrahlen[1])

Von *Hans Wolter*

(Mit 19 Abbildungen)

Inhaltsübersicht

Als Optiken zur Röntgenstrahlmikroskopie eignen sich Systeme von totalreflektierenden Spiegeln, die bei Hebung der sphärischen Aberration für einen Achsenpunkt zugleich die Abbesche Sinusbedingung bis zu Aperturen 0,05 befriedigend erfüllen. Für die Lebenduntersuchung biologischer Objekte empfehlen sich Wellenlängen um 24 Å, die im Wasser wenig, aber in kohlenstoffhaltigen oder stickstoffhaltigen Stoffen stark absorbiert werden. Mit diesen weichen Strahlen ist eine Steigerung des Auflösungsvermögens gegenüber dem Lichtmikroskop um mindestens eine Größenordnung unter Verwendung der hier beschriebenen Optiken zu erwarten.

Abb. 6. Paraboloid und Hyperboloid in konfokaler Lage als Spiegelsystem für streifenden Einfall

Abb. 15. Spiegelsystem 2. Art

Abb. 16. Spiegelsystem 3. Art

Figure 1-2. Image of the work of Wolter of 1952 in which the solution for the x-ray reflection in grazing incidence is shown (Wolter, 1952a).

The first problem was solved by Wolter in 1952 (Wolter, 1952a), which analyzed aspheric mirrors with concentric revolution figures (paraboloids, hyperboloids and ellipsoids) and showed that, in order to get a real image on an extended field of view, x-rays had to undergo two reflections in a paraboloid/hyperboloid (Wolter I and Wolter II) or paraboloid/ellipsoid (Wolter III) mirrors, mounted in coaxial and confocal condition (see Figure 1-2). The technological difficulties in achieving so highly aspheric mirrors was immediately clear to Wolter and therefore the impossibility, in the immediate future, to apply the discovery in scientific instruments.

The second problem was solved in the context of x-ray astronomy research with the realization of the first focusing telescopes for sky observation.

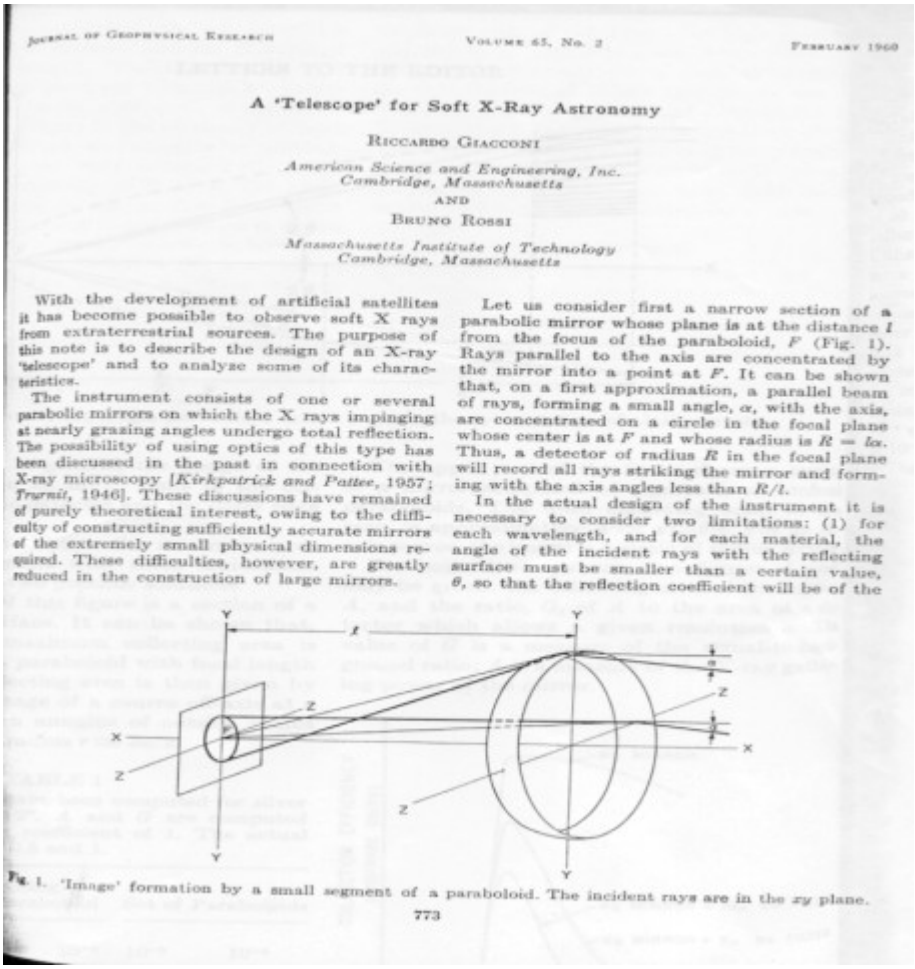

JOURNAL OF GEOPHYSICAL RESEARCH VOLUME 65, NO. 2 FEBRUARY 1960

A 'Telescope' for Soft X-Ray Astronomy

RICCARDO GIACCONI
American Science and Engineering, Inc.
Cambridge, Massachusetts
AND
BRUNO ROSSI
Massachusetts Institute of Technology
Cambridge, Massachusetts

With the development of artificial satellites it has become possible to observe soft X rays from extraterrestrial sources. The purpose of this note is to describe the design of an X-ray 'telescope' and to analyze some of its characteristics.

The instrument consists of one or several parabolic mirrors on which the X rays impinging at nearly grazing angles undergo total reflection. The possibility of using optics of this type has been discussed in the past in connection with X-ray microscopy [*Kirkpatrick and Pattee*, 1957; *Fruemit*, 1946]. These discussions have remained of purely theoretical interest, owing to the difficulty of constructing sufficiently accurate mirrors of the extremely small physical dimensions required. These difficulties, however, are greatly reduced in the construction of large mirrors.

Let us consider first a narrow section of a parabolic mirror whose plane is at the distance l from the focus of the paraboloid, F (Fig. 1). Rays parallel to the axis are concentrated by the mirror into a point at F. It can be shown that, on a first approximation, a parallel beam of rays, forming a small angle, α, with the axis, are concentrated on a circle in the focal plane whose center is at F and whose radius is $R = l\alpha$. Thus, a detector of radius R in the focal plane will record all rays striking the mirror and forming with the axis angles less than R/l.

In the actual design of the instrument it is necessary to consider two limitations: (1) for each wavelength, and for each material, the angle of the incident rays with the reflecting surface must be smaller than a certain value, θ, so that the reflection coefficient will be of the

Fig. 1. 'Image' formation by a small segment of a paraboloid. The incident rays are in the xy plane.

773

Figure 1-3. 1960 article front page from Giacconi and Rossi on telescopes for soft x-ray astronomy

Dating back to 1948, the discovery made by Burnight (Newell, 1953) by exposing photographic plates in the upper atmosphere by a V2 rocket, revealed x-ray emission by the Sun and gave rise to the era of x-ray astronomy research. In 1960, Rossi and Giacconi (Giacconi & Rossi, 1960) suggested that x-ray astronomy could have gained great benefit from using focusing optic, leading them to an improvement of collection area, angular resolution and signal to noise ratio. This was the first time that the possibility of using grazing incidence optics as a constructive method of telescopes was considered. Giacconi, Rossi and collaborators (Giacconi, 1979), already in 1962, had revealed the first non-solar celestial x-ray source (SCO-X), using a rocket-borne Geiger counter. The first flight of a Wolter I telescope type occurred aboard a rocket in October 1963, and in this circumstance it succeeded in capturing the first image of the Sun with a grazing incidence telescope, with a resolution better than 1 arc minute.

The first x-ray focusing telescope, orbiting the Earth aboard a satellite, was launched in November 1978 and remained operational for two and a half years. It was carried by the second of three American satellites High Energy Astronomy Observatory (HEAO-2) and was renamed Einstein after launch. Einstein telescope, thanks to a signal to noise ratio unmatched compared to that of collimated detectors used hitherto, represented a huge step forward for scientific research, revealing x-ray radiation from almost all classes of astronomical objects known, from nearby stars to quasars at cosmological distances (Van Speybroeck, 1979). Einstein telescope, as well as the European miniature version EXOSAT (de Korte, 1981), was used in pointing mode on preselected targets, covering only a small fraction of the sky.

The collection of an x-ray telescope is proportional to the focal length and to the square of the incidence angle of the impinging radiation. The solution adopted to increase the collecting area is to nest more mirrors in a confocal configuration (Figure 1-4).

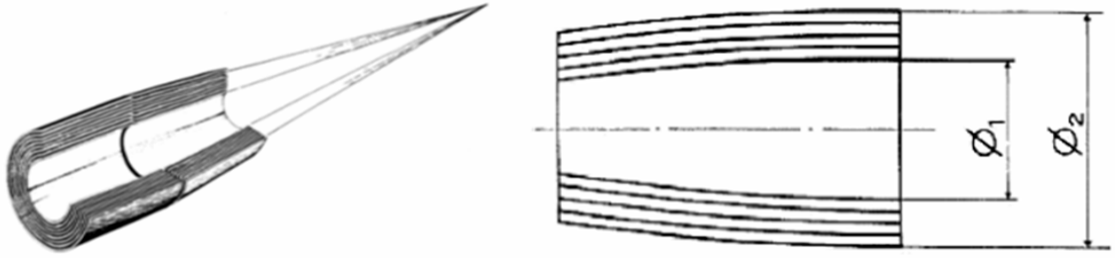

Figure 1-4. Example of a grazing incidence telescope with a series of confocal nested Wolter I type mirrors

The first complete x-ray survey of the sky with focusing optics was made in 1990 by ROSAT satellite (Aschenbach, 1985) with a sensitivity of 1000 times greater than UHURU (the previous and first survey mission with direct view instruments). In the first six months of the mission, ROSAT catalogued more than 150,000 items then move on to the stage pointing where deeply observed a wide range of objects with a resolution of 3 arcsec. A detailed morphology of supernova remnants and clusters of galaxies and the detection of diffuse x-ray emission by molecular clouds appeared among several scientific discoveries.

The Japanese-American satellite ASCA (Serlemitsos, 1995), launched in February 1993, was the first x-ray astronomy satellite to make use of a CCD detector, combining a good imaging capabilities with an extended spectral resolution, and a large effective area. ASCA allowed to study in detail the broad lines of Iron (Tanaka, 2001) of the AGNs, proving the presence of a strong gravity near the nucleus.

A recent mission of x-ray astronomy that had a great echo was SAX, renamed BeppoSAX in honour of Prof. Giuseppe Occhialini, born from an Italian scientific program with the participation of the Dutch Agency for Aerospace programmes (NIVR). Launched from Cape Canaveral in 1996, BeppoSAX ended its mission in 2002, after obtaining a series of successes. With its devices, for the first time has covered more than three decades of energy – from 0.1 to 300 keV – with a relatively large effective area, good resolution and a discrete sensitivity. For the soft x-ray, the first focusing telescope realized with the technique of Nickel replication by electroforming was used. This technique has been developed for the mission, as a result of a research project conducted entirely by the Italian scientific community. Thanks to the wide range in energy and the focusing optics in the range 0.1–10 keV (Citterio, 1988), BeppoSAX has been able to determine the position of Gamma Ray bursts with an accuracy of 1 arc minutes, to follow and monitor for the first time this type of astronomical event in the x-ray band.

An evolution of the replica technique by electroforming had been adopted to manufactured the optics of XMM-Newton mission. Launched by ESA with ARIANE 504 carrier in December 1999, XMM-Newton is equipped with an unprecedented effective area and an optical monitor, the first to fly aboard an x-ray space observatory. The replication technique allowed to nest in the same module 58 mirrors with an angular resolution of 15 arc seconds. With the replication technique, in fact, it is possible to trade-off the optical performance w.r.t. the thickness of the mirror shells. The lower the thickness the higher the number of mirror that can be nested; the lower the thickness the lower the optical performance of the optic. With the huge collecting area and long exposures, XMM-Newton is still allowing observations with great sensitivity.

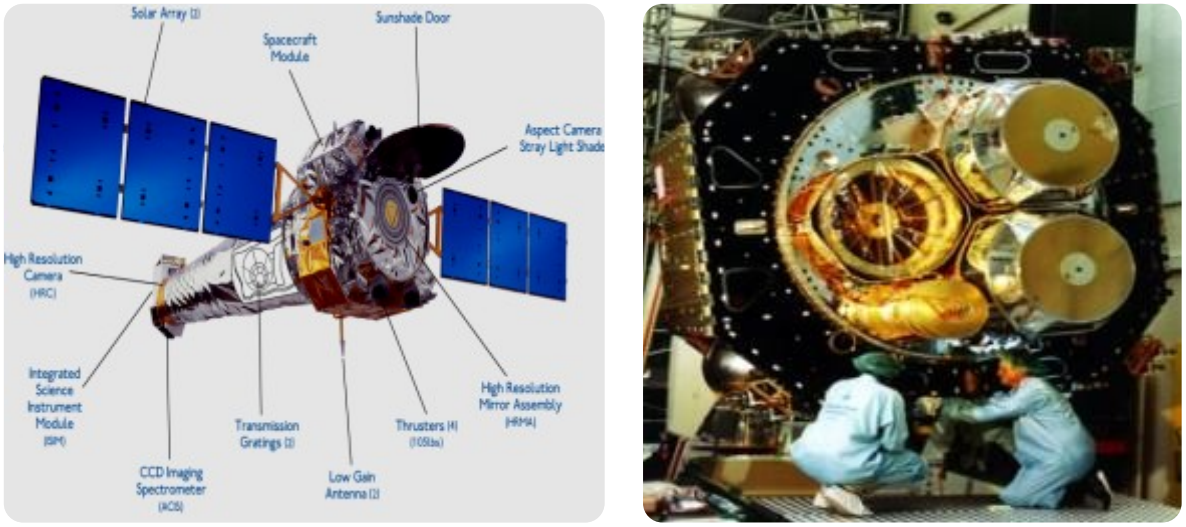

Figure 1-5. 3D images of the Chandra X-ray observatory satellite (left) and the XMM-Newton satellite (right).

Another space observatory currently under operation is Chandra (Weisskopf, 2000) by NASA, put into orbit by the Space Shuttle Columbia in July 1999 (see Figure 1-5). The optics of the telescope of Chandra have been realized with the direct polishing technique, achieving angular resolution of 0.5 arc seconds. The combination of a high angular resolution, a discrete collecting area (obtained thanks to a very long focal length) and the sensitivity to higher energies of soft x-ray spectrum makes possible the study of extremely weak sources, also strongly absorbed in crowded fields.

Above 10 keV the reflectivity of single layer coatings collapses suddenly, unless you assume very long focal lengths and/or very small angles of incidence. For energies above the idea is to take advantage of constructive interference phenomena through the use of multilayer coatings.

1.1 Basic of x-ray optical physics

1.1.1 Optical constants in x-ray

The problem of x-ray reflection comes from the values of the optical constants of materials at such energies. In fact, the propagation of x-rays in matter is described by a complex refractive

index with real part less than the unit:

$$\tilde{n} = 1 - \delta - i\beta = 1 - \frac{r_0 \lambda^2}{2\pi} N_{AT} \left(f_1 - i f_2 \right) \tag{1.1}$$

where the optical constants δ and β are known respectively as the refractive index and absorption index. These quantities are both real and, typically, the refractive index δ takes on values between $10^{-2} \div 10^{-5}$, while absorption index β takes on values ranging between $10^{-2} \div 10^{-6}$. The small value of δ indicates that the real part of the refractive index is near to the unit, and so the angles of refraction are very small. Physically this means that the frequency of x-rays is much greater than the frequency of oscillation of the bound electrons in the matter and therefore the medium can be considered to be immersed in a gas of electrons with a plasma frequency lower than the frequency of the radiation (Spiller, 1994). In addition to that, the radiation is extinct exponentially, primarily for photoelectric effect, when it crosses a material. In x-ray astronomy conventional refractive lenses cannot be used to focus the radiation, due to the small angles of refraction and (mostly) to the absorption of a typical thickness values of lenses. Even the conventional normal incidence optics cannot be used at wavelengths of x-rays, due to the small reflectivity.

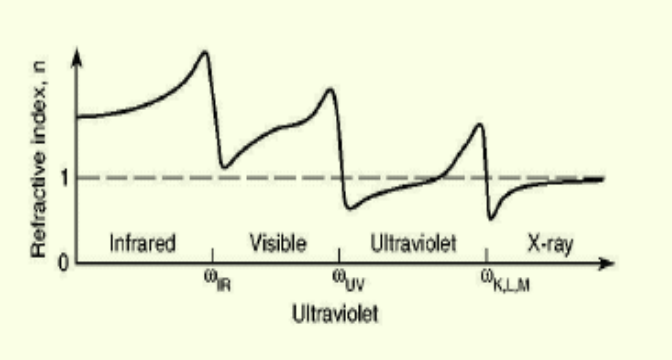

Figure 1-6. Trends of the real part of the refractive index as a function of frequency: x-ray refractive index is at values less than 1 (Attwood, 1999).

Figure 1-6 shows the trend of the refractive index to vary with the frequency of radiation: in x-rays, with the exception of the area near the absorption edge where it has a rapid decline (phenomenon of anomalous dispersion), the refractive index tends to increase with the frequency but remains less than the unit.

From the second equality of equation (1.1) you can express the optical constants as function of the density of atomic scattering factors of a material:

$$\delta = \frac{r_0 \lambda^2}{2\pi} \frac{\rho}{AW} f_1 \tag{1.2}$$

$$\beta = \frac{r_0 \lambda^2}{2\pi} \frac{\rho}{AW} f_2 \tag{1.3}$$

where r_0 is the classical electron radius, ρ/AW represents the number of atoms/cm^3, and $f = f_1 - if_2$ is the complex atomic scattering factor.. The optical constants depend on the density of materials, via the atomic scattering factors, and are often difficult to determine.

1.1.2 Fresnel equations and Total Reflection phenomena

If a plane wave propagating in a medium with optical constants δ_1 e β_1 arrives in the $\boldsymbol{k}_i$ direction with an angle θ_0 on a perfectly smooth surface of a material with optical constants δ_2 ($> \delta_1$) e β_2, in general, it will give rise to both a transmitted and a reflected wave.

In Figure 1-7 the case concerning a perpendicularly polarized wave is represented.

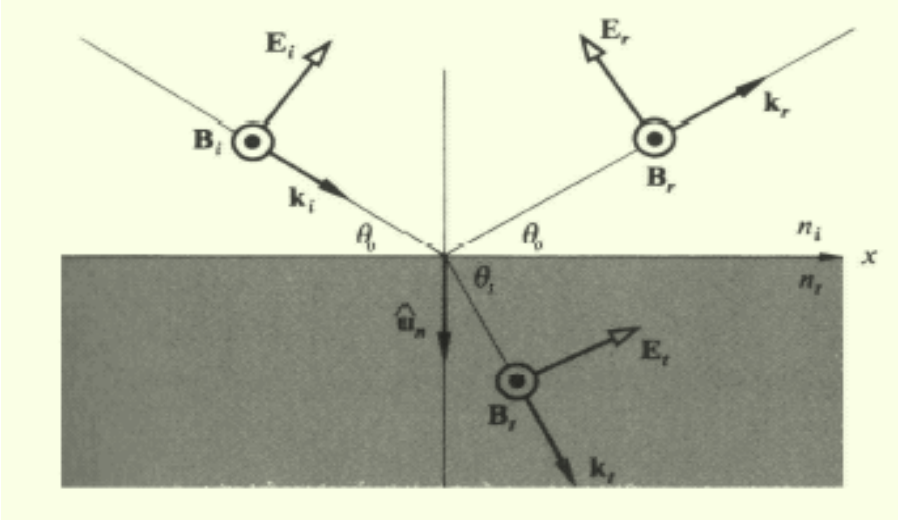

Figure 1-7. Radiation incidence on the surface of separation of two medium in the case of perpendicular polarization (type s polarisation).

Invoking the continuity of the magnetic field and electric field vectors before and after the impact and using Snell's law, the Fresnel equations can be derived (Michette & Buckley, 1993):

$$r_s = \frac{\sin\theta_0 - \left[\tilde{n}^2 - \cos^2\theta_0\right]^{1/2}}{\sin\theta_0 + \left[\tilde{n}^2 - \cos^2\theta_0\right]^{1/2}} \tag{1.4}$$

$$t_s = \frac{2\sin\theta_0}{\sin\theta_0 + \left[\tilde{n}^2 - \cos^2\theta_0\right]^{1/2}} \tag{1.5}$$

these equations are valid in the case of perpendicular polarisation with vacuum as first medium ($\delta_1=\beta_1=0$ e $\beta_2\neq0$), and describe the reflection amplitude *r* and transmission amplitude *t*. The intensity of reflection (commonly called reflectivity) is then given by the squared module of the reflection amplitude *r*:

$$R = |r|^2$$

From Fresnel equations, being the real part of the refractive index less than the unit, the angles of incidence that have non-zero reflectivity are very small. Snell's law, in the grazing incidence geometry, can be expressed as follows:

$$\frac{\cos\theta_0}{\cos\theta_t} = \frac{1-\delta_2}{1-\delta_1} \tag{1.6}$$

and so, in the case of a medium vehicle with $\delta_1 \approx 0$ (air or vacuum) the critical angle θ_c below which reflection takes place is given by:

$$\cos\theta_c = 1-\delta_2 \tag{1.7}$$

The reflectivity curves at the energy of 5 keV versus the angle of incidence for a dense material, such as Nickel, and for a less dense material, such as Silicon, are represented in Figure 1-8. A gradual decrease of the reflectivity with the increasing of the incidence angle can be clearly noted, followed by a faster decrease proportional to $sin^{-4}\theta_0$.

It is defined "Total Reflection" the reflection that takes place before the point of flexion determined by critical angle θ_c of the radiation, although in reality it is not entirely reflected due to absorption.

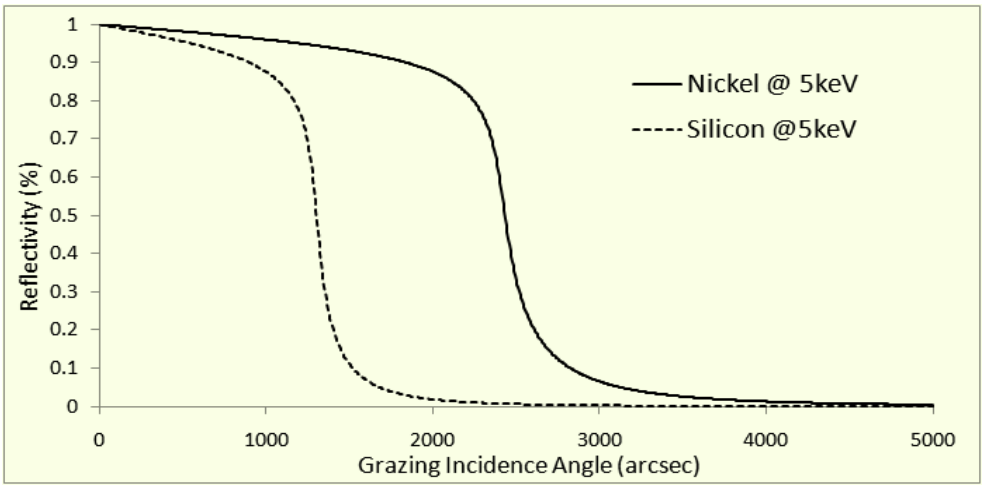

Figure 1-8. Reflection intensity at different energy and material density. It can be seen how the critical angle is inversely proportional to the energy and somehow proportional to the electron density of the material.

For the critical angle of materials the following relation of proportionality is valid:

$$\theta_c \propto \sqrt{\rho}/E \tag{1.8}$$

The dependence of the critical angle from energy fixes a maximum energy at which it is still possible to exploit the phenomenon of total reflection. Even for the denser materials this energy stands around 10 keV at shallow angles in the order of 0.2 deg.

Although the equations above listed relate to reflection by flat surfaces, they can be applied to curved surfaces as long as the radius of curvature is much greater than the wavelength. In the case of x-rays this condition is basically always verified.

The approach here followed does not consider the atomic nature of the reflective surface, and therefore the effects of atomic scattering factors. These effects can be modelled by considering the surface as a series of atomic layers (Smirnov, 1977):

$$r_s = \frac{\sin\theta_0 - \left[\sin^2\theta_0 - 2(\delta + i\beta)\right]^{1/2}}{\sin\theta_0 + \left[\sin^2\theta_0 - 2(\delta + i\beta)\right]^{1/2}} \tag{1.9}$$

This is essentially the same expression derived with the non-atomic approach, in which the terms δ e β can be ignored.

1.1.3 Reflection from real surfaces

In the previous paragraphs the effects of the surface roughness has not been taken into account. The surface roughness, leading to a variation of the angle of incidence on the surface, reduces the mirror reflectivity and significantly affect the performance of an x-ray telescope in terms of effective area and angular resolution. There are different ways in which the surface roughness of a surface can be treated, leading to very similar results. The approach commonly used is the one originally developed by Debye in the 1913 to analyze the effects of thermal vibrations of a crystal lattice on the x-ray scattering (Debye, 1913). This approach is valid for the crystalline surfaces, but the resulting formulas can be used to model the roughness of any surface. For an unperturbed lattice, the reflectivity *R* is given by the square of the summatory of amplitudes reflected from each point of the lattice:

$$R \propto \sum_n \exp\left(\frac{2\pi i}{\lambda}\vec{r}_n \cdot \vec{K}\right)\sum_m \exp\left(-\frac{2\pi i}{\lambda}\vec{r}_m \cdot \vec{K}\right) \tag{1.10}$$

where $\boldsymbol{r_n}$ is the position of the nth point and $\boldsymbol{K}$ is the scattering vector:

$$\vec{K} = \vec{k}_i - \vec{k}_r \qquad \left|\vec{K}\right| = 2\sin\vartheta_0 \tag{1.11}$$

If the lattice points moving of a $\boldsymbol{u_n}$ distance, the resulting the reflectivity is:

$$R_d = \sum_n \sum_m \exp\left(\frac{2\pi i}{\lambda}(\vec{r}_n - \vec{r}_m)\cdot\vec{K}\right)\exp\left(\frac{2\pi i}{\lambda}(\vec{u}_n - \vec{u}_m)\cdot\vec{K}\right) \tag{1.12}$$

If the average displacement of the surface roughness is σ, then the average value $(\boldsymbol{u_n - u_m})\cdot\boldsymbol{K}$ can be equaled to σ^2. Now we can define the p_{nm} quantity in this way:

$$p_{nm} = \frac{2\pi}{\lambda}(\vec{u}_n - \vec{u}_m)\cdot\vec{K} = \frac{2\pi\sin\theta_0}{\lambda}(\vec{u}_{nK} - \vec{u}_{mK}) \tag{1.13}$$

where u_{nK} is the component of $\boldsymbol{u_n}$ along the $\boldsymbol{K}$ direction, and then the second exponential equation (1.12) may develop as:

$$e^{ip_{nm}} = 1 + ip_{nm} - \frac{p_{nm}^2}{2!} + \cdots = 1 - \frac{\langle p_{nm}^2\rangle}{2!} + \frac{\langle p_{nm}^4\rangle}{4!} - \cdots \tag{1.14}$$

and for small displacement w.r.t. the wavelength, only the first two terms remain:

$$e^{ip_{nm}} \approx e^{-\langle p_{nm}^2 \rangle/2} \tag{1.15}$$

The average value of $(u_{nK} - u_{mK})^2$ is given by:

$$\left\langle (u_{nK} - u_{mK})^2 \right\rangle = \left\langle u_{nK}^2 \right\rangle + \left\langle u_{mK}^2 \right\rangle - 2\left\langle u_{nK} u_{mK} \right\rangle \tag{1.16}$$

If the surface roughness is distributed randomly we will have that:

$$\left\langle u_{nK}^2 \right\rangle = \left\langle u_{mK}^2 \right\rangle = \sigma^2 \quad , \quad \left\langle u_{nK} u_{mK} \right\rangle = 0$$

$$\frac{\left\langle p_{nm}^2 \right\rangle}{2} = \left(\frac{4\pi \sin\theta_0}{\lambda} \right)^2 \frac{\left\langle (u_{nK} - u_{mK})^2 \right\rangle}{2} = \left(\frac{4\pi \sin\theta_0}{\lambda} \right)^2 \sigma^2 \tag{1.17}$$

The average reflectivity from a real surface compared to the theoretical perfectly smooth surface is given by:

$$\left\langle R_d \right\rangle = R \cdot \exp\left[\left(\frac{4\pi\sigma \sin\theta_0}{\lambda} \right)^2 \right] \tag{1.18}$$

The reflectivity, as calculated using the Fresnel equations, is reduced by an exponential factor when you consider a real surfaces. The quantity σ is called the Debye-Waller roughness.

1.2 Gracing incidence optical systems

The considerations made in the first paragraph of this chapter show that, to effectively focus the x-ray radiation, neither normal incidence reflective mirrors nor refractive lenses can be used. On the contrary, it is necessary to use grazing incidence optics with peculiar geometrical shape that plays a crucial role in the formation of images.

Now we will discuss the geometric properties of grazing incidence mirrors, and in particular how to avoid the aberrations that characterize them.

1.2.1 Aberrations from spherical surfaces

Astigmatism, spherical aberration and coma aberration, occur consistently in grazing incidence reflection by spherical surfaces.

1.2.1.1 Astigmatism

Astigmatism is an image formation error that occurs when the focal length of the rays reflected along the meridian is greater than the ones reflected along the sagittal plane. It can be shown that for a spherical mirror of radius r and small angles of incidence θ, there is the following relationship for the meridians focal length f_M (Michette & Buckley, 1993):

$$f_M = \frac{r\theta}{2} \tag{1.19}$$

this expression for focal length, is a consequence of the apparent decrease of the mirror radius in the meridian direction, due to perspective effects. In the perpendicular direction, on the other hand, there is not a perspective representation and the corresponding sagittal focal length f_S is given by:

$$f_S = \frac{r}{2\theta} \tag{1.20}$$

Each direction acts as a cylindrical mirror and, in the case of a point object, two different images are formed, which will coincide only if $f_S = f_M$. This is what happens in normal incidence, whereas in grazing incidence the images are very astigmatic ($f_S / f_M = 1/\sin^2\theta$).

1.2.1.2 Spherical aberration and Coma

Spherical aberration occurs because the angle of incidence varies along the surface of the mirror. With reference to Figure 1-9, the distance of the image from the point of incidence varies with the angle a, and it is linked to the spherical aberration S according to the following relation:

$$S = \Delta v \sin\gamma \approx \Delta v \gamma \tag{1.21}$$

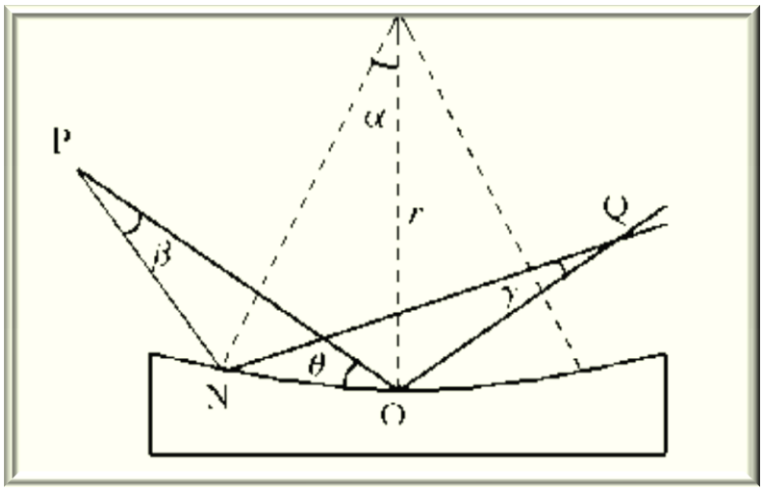

Figure 1-9. Outline of image formation on a spherical mirror in grazing incidence geometry.

Through geometrical considerations, one can show that the angle of convergence γ and the variation of distance Δv are proportional to α. The magnification M is given by the ratio between the distance of the object and image relative to the point of incidence. It follows that the spherical aberration is proportional to α^2, and that the deviation is always from the same part of the image relative to $\alpha = 0$.

Coma aberration is a consequence of the change in magnification $M = \beta/\gamma$ between the centre and the exterior of a mirror. An optic system not affected by coma aberration must have satisfied the Abbe sine condition, for which all paths relative to the geometric rays reflected from the system shall give rise to the same magnification M.

1.2.1.3 Abbe sine condition

With reference to Figure 1-10, a collimated beam incident on a focusing system, the Abbe's rule is satisfied only if:

$$\Gamma = \frac{h}{sen\alpha} = \cos t \tag{1.22}$$

where Γ is the focus-optic distance, h is the distance from the optical axis of the beam and α is the angle seen by the focus. This rule states that the angular separation surface on which the paraxial rays and the prolongation of the reflected rays intersect, should be a sphere centered on the focus. This condition, easily verifiable in the case of paraxial rays, is necessary and sufficient

to avoid the scattering of extraxial rays. More precisely, this rule sates that for objects with a diameter smaller than the object's distance, the diameter of the image relative to the beam is proportional to the square of the distance from the optical axis.

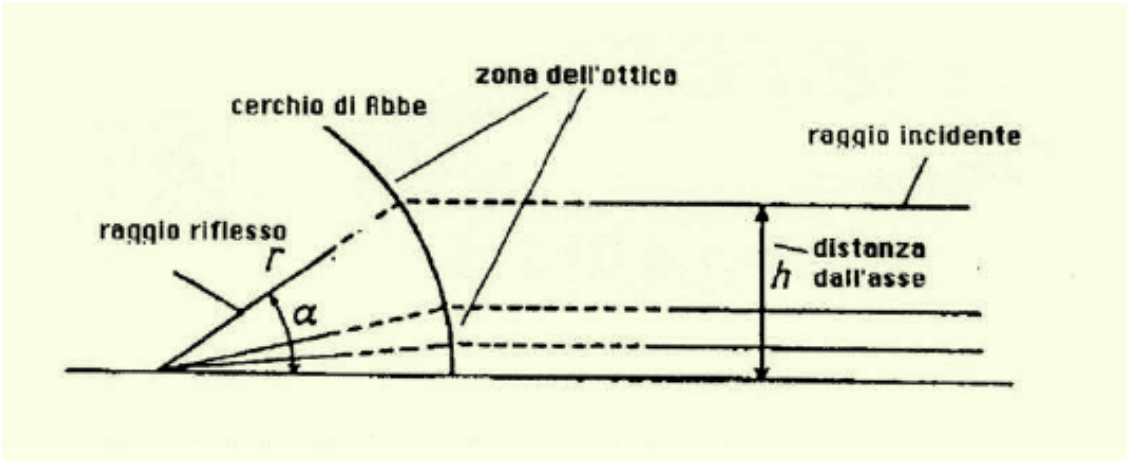

Figure 1-10. Abbe sine rule for the image of an object at infinity.

1.2.2 Aberration reduction: aspherical mirror

From the discussions just made on aberrations, we can conclude that in x-ray is not possible to use a spherical mirror. Even denser materials like Platinum have critical angles of a few degrees, so astigmatism may not be reduced to acceptable levels; spherical aberration and coma may be reduced only through the use of limited openings, which entails a loss in the area of collection and angular resolution. To reduce aberrations at acceptable levels compound systems and aspherical mirrors must be used.

To obtain an aspheric mirror with equal meridian and sagittal focal lengths, the surface must have a toroidal shape with two curvature radii r_M and r_S such that:

$$r_S = r_M \sin^2 \theta \tag{1.23}$$

this condition removes astigmatism for a single reflection in grazing incidence. With a single reflection also the spherical aberration can be eliminated by the use of a parabolic mirror (who however suffers from obliquity), but the coma aberration can be eliminated only partially.

1.2.3 Double reflection optical systems

Aberrations can be reduced significantly, and in some cases completely eliminated, by using an optical systems composed by two consecutive grazing incidence mirrors. These systems are mainly of two types:

- one developed by Kirkpatrick and Baez in 1948 (Kirkpatrick & Baez, 1948);
- one invented by Wolter in 1952 (Wolter, 1952a).

1.2.3.1 Kirkpatrick-Baez system

Kirkpatrick-Baez system makes use of two (or more) mirrors whose plans meridians are perpendicular. The simplest configuration (Figure 1-11) consists of two cylindrical mirrors with equal radii of curvature. This system produces extended images of extended real objects, but the two mirrors are not coextensive and the distance of the object for the sagittal reflection of the second mirror is larger than for the meridian reflection in the first mirror. It follows that the magnification is different in the two directions and this effect is called animorfotismo. Most devices are designed to work around this problem, e.g. using a reflective surface in the same plane of the first or rotating properly the detector. It is also possible to draw a system in which both mirrors are the same distance from the object, but such a solution is difficult to achieve in practice. To reduce significantly the coma aberration the Abbe sine condition must be satisfied and to the purpose four reflections are required, two for each direction. The Kirkpatrick-Baez is used in applications for x-ray microscopy because of its great usefulness in the case of asymmetric sources due to the possibility to change the magnification in the two directions. It was used at the dawn of x-ray astronomy aboard some rocket-borne missions but has never been used in space missions, although proposed as a solution in some cases (Gorenstein, 1988).

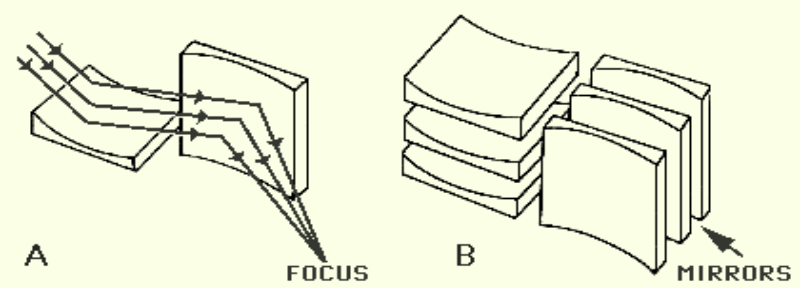

Figure 1-11. Kirkpatrick-Baez optical system in a combination of two elements (A) and a combination of several elements in parallel to increase the total collector area (B).

1.2.3.2 Wolter systems

In order to eliminate spherical aberration and astigmatism also a single mirror can be used, but the coma aberration with it is persistent. A solution to this problem was proposed by Hans Wolter in 1952, which showed that the Abbe sine condition could be satisfied in good approximation using two mirrors in succession, the first parabolic inbound and outbound hyperbolic (Wolter, 1952a). There are also other two configurations, called Wolter II and III, based always on combination of conics that restrict the coma aberration, but at the same openness they require longer focal lengths (see Figure 1-12). The Wolter I configuration allows a reduction of about a factor of 2 of the focal length compared to a single reflection optical dish, and having to work in space, this is a very important property. The three Wolter geometries are able to offer excellent performance for sources close to the axis, the principal surface has the shape of a paraboloid of revolution around the optical axis that, in the paraxial region, approximates well a sphere. For extraxial rays the coma aberration grows linearly with distance from the optical axis, but in this case other types of aberration in quadratic dependence, such as the curvature of field, are dominant. The field of view with the correct image is therefore limited to a few tens of arcmins.

For applications in x-ray astronomy, the Wolter I optical system the geometry shows several advantages compared to the others Wolter geometries and to the Kirkpatrick-Baez, and in fact, it has been widely used in this field:

1. Grazing incidence mirrors have a very small collection area, and the Wolter I geometry allows to increase it by joining together multiple mirrors coaxial and confocal mirrors
2. Unlike Kirkpatrick-Baez, the Wolter I mirrors can be made from a single piece, reducing the problems of alignment, ensuring greater structural stability and consequently improving the angular resolution.
3. The Wolter I geometry can be approximate by two trunks of cone, achievable more easily and more cheaply. This solution generate a worsening of the angular resolution and the greater the focal length/diameter ratio the better the approximation works.

Wolter, in 1952, proposed a different kind of geometry (called Wolter-Schwarzschild) that, by means of small deviations from the conic curves, meet perfectly the Abbe sine condition eliminating every order coma (Wolter, 1952b). This system has major manufacturing difficulties due to the abrupt change in slope between the two surfaces. Einstein is the only space x-ray astronomy mission which has made use of Wolter-Schwarzschild mirrors.

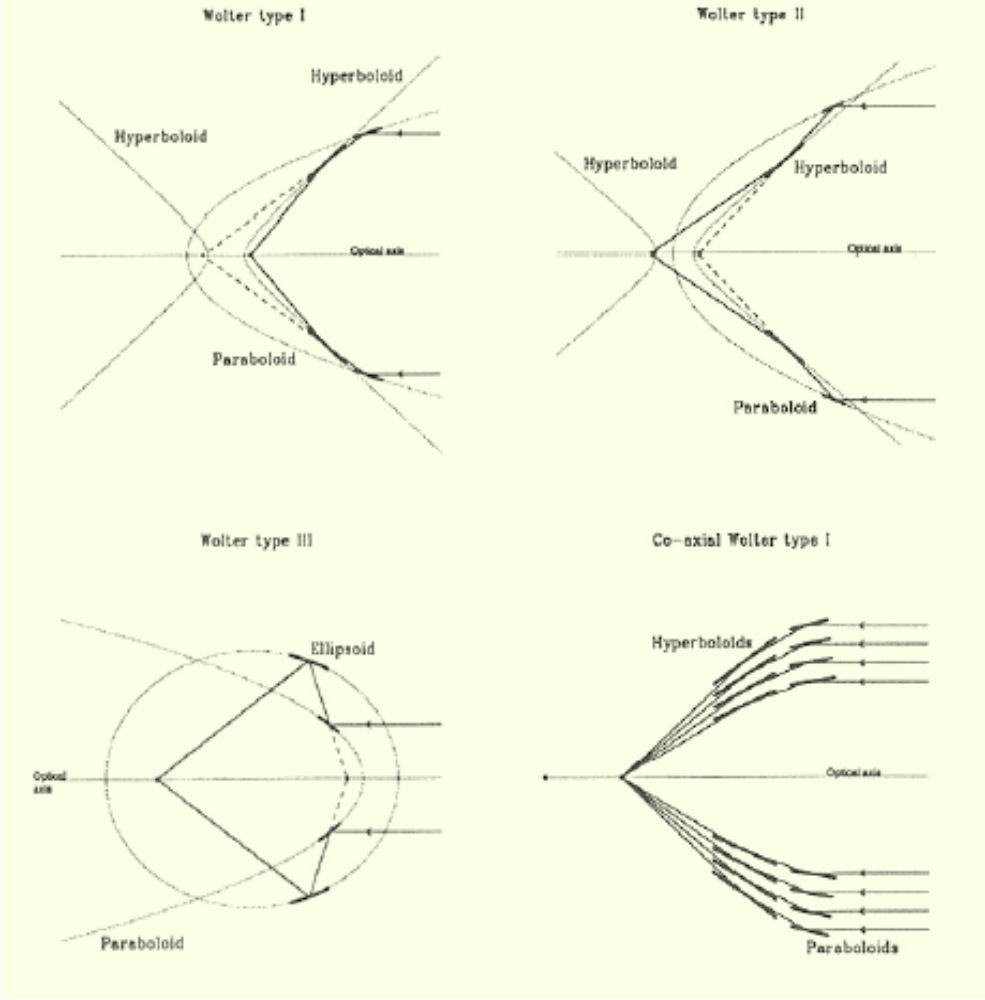

Figure 1-12. Operation scheme of double reflection Wolter type I, II and III optical systems.

1.2.4 Geometrical collecting area

With reference to Figure 1-13, the angle of incidence in the focus is four times the angle of incidence θ on the primary mirror, and the angle of incidence on the secondary mirror is equal to the angle of incidence θ on the primary mirror. The relation between the radius and focal length can be derived:

$$r = F \tan 4\theta \cong 4F\theta \tag{1.24}$$

where F is the focal length measured from the junction of the mirrors (intersection plane) and the approximation is valid in the case of very small angles of incidence.

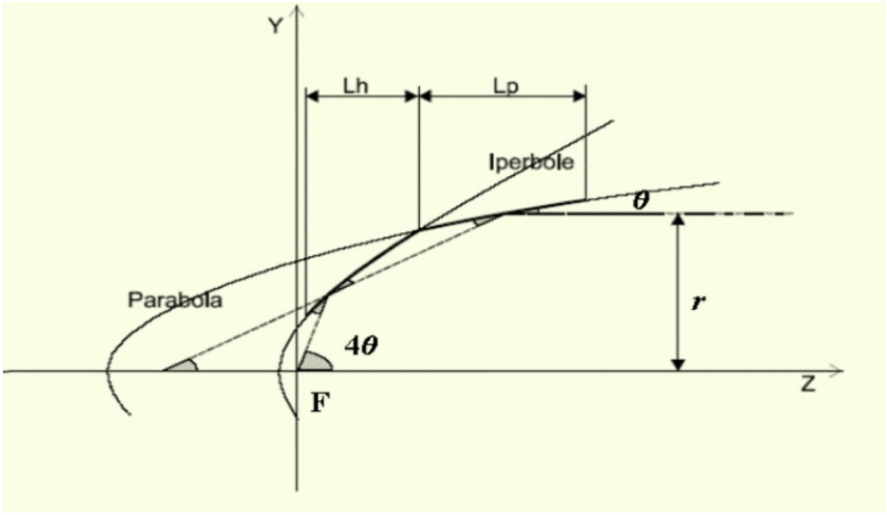

Figure 1-13. Geometrical parameters in a grazing incidence optics of Wolter type I. The angle of incidence on the focus is four times the angle of incidence on the primary mirror. The focal length is measured from the junction of mirrors and r is the radius at the junction.

A photon to be focused should be reflected by the primary mirror. The collection area is then the projection of the mirror on the plane perpendicular to the optical axis:

$$A_{Coll} = 2\pi r \Delta r = 2\pi r L \tan\theta \cong 8\pi F L \theta^2 \tag{1.25}$$

where L is the length of the primary mirror, although typically the two mirrors have the same length, and r is the radius at the junction of the mirrors. In the case of confocal mirrors the angles of incidence grows with the radius. For this reason, the reflection of the most energetic rays takes place in the innermost mirrors, which have a low collecting area, while the outermost mirrors offer an higher collecting area for low energies rays.

1.3 Multilayer coatings and their application in x-ray Astronomy

A multilayer is a synthetic lattice formed by a succession of layers of different materials, deposited on a substrate which acts as a mechanical support. For each interface the incident radiation is partly transmitted, absorbed and reflected, in accordance with the Fresnel formulas (see section 1.1.2). The reflectivity of a multilayer can be calculated according to a cinematic theory, in which the reflections of individual layers are treated independently and then added

vectorially (neglecting the effects of refraction and extinction), or rather according to a dynamic theory, which takes into account all the interactions of radiation with different layers using a recursive calculating procedure (Spiller, 1994) (Underwood & Barbee, 1981).

1.3.1 Multilayer as modulated synthetic grating

Above 10keV a high hard x-ray reflectance can be obtained using a reflective material structured in successive layers equally spaced grid, so that the reflections of the surfaces of individual layers compounded in phase (Figure 1-14). For a specific energy, the increase in reflectivity due to constructive interference takes place only for certain angles of incidence. This is what happens in nature with the crystals, in which the constant spaced atomic planes, give a high reflectivity even at high energies when the condition of Bragg is satisfied:

$$m\lambda = 2d\sin\theta_m \tag{1.26}$$

where m is an integer describing the order of diffraction and d is the spacing between atomic planes. Suitably shaped crystals are commonly used in x-ray spectroscopy and synchrotron sources for wavelengths lower than 2 nm. The possibility of using synthetic structures was seen already in the 1930s, in an attempt to get devices with greater precision and versatility of those available in nature, but the practical difficulties in recreating the distance between atomic planes of crystals, have been overcome only in the 1960s (Dinklage & Frerichs, 1963).

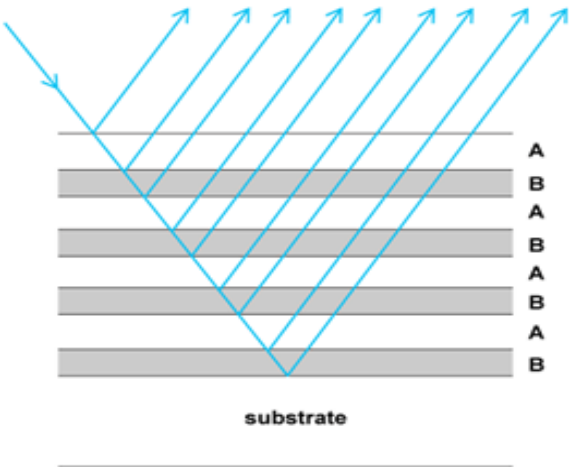

Figure 1-14. Multilayer based on constructive interference from partial reflected waves, similar to the Bragg reflection from the crystals.

1.3.2 Bragg reflection in multilayer

At the interface between two media 1 and 2, with complex refractive indices $\tilde{n}_1 = 1 - \delta_1 - i\beta_1$ and $\tilde{n}_2 = 1 - \delta_2 - i\beta_2$, the amplitude of reflection can be calculated using the equation (1.2):

$$r_s = \frac{\tilde{n}_2^2\left(\tilde{n}_1^2 - \cos^2\theta_1\right)^{1/2} - \tilde{n}_1^2\left(\tilde{n}_2^2 - \cos^2\theta_2\right)^{1/2}}{\tilde{n}_2^2\left(\tilde{n}_1^2 - \cos^2\theta_1\right)^{1/2} + \tilde{n}_1^2\left(\tilde{n}_2^2 - \cos^2\theta_2\right)^{1/2}} \tag{1.27}$$

where θ_1 and θ_2 are the angles of incidence in the two media, related to the angle of incidence θ_0 by the Snell's law. The reflectivity interfaces between layers increase whit the difference in the refractive indexes of the two materials, as can be deduced from the following formula for the reflectivity at the j-th interface:

$$r_j = \frac{\left(\delta_j - \delta_{j+1}\right)}{2\sin^2\theta_j} \tag{1.28}$$

valid for angles greater than the critical angle and energy typical of the x-rays radiations. The ideal solution would be to keep the reflective material layers separated by the vacuum, but in reality a multilayer mirror is composed of alternating layers of an high density material (reflective layer) and a low density material (spacer). A constant spaced multilayer is usually described as a succession of bilayers and by two parameters: the total thickness $d = d_1 + d_2$ and the relative thickness Γ given by the ratio between the higher density material thickness and total thickness.

Bragg's equation valid for the crystals, requires a change in the case of multilayer due to the presence of refraction and absorption:

$$m\lambda = 2d\sin\theta_m\sqrt{1 - \frac{2\bar{\delta}}{\sin\ \theta_m}} \tag{1.29}$$

where $\bar{\delta} = \delta_1\Gamma + \delta_2(1-\Gamma)$ is the average value of the refractive indexes of the two components of the multilayer. The angles at which the peak reflectivity takes place are larger than those given by the pure Bragg condition.

The total reflected wave from a multilayer can be divided into the components reflected by the heavy-light interface and the light-heavy interface. The phase difference $\Delta\Phi$ in the waves

reflected by two interfaces of the same type gives the greatest constructive interference when the following relation is verified:

$$\Delta\Phi_j + \Delta\Phi_{j+1} = m\pi \tag{1.30}$$

The phase shift between two interfaces gives rise to the maximum interferential coupling when it is equal to $\pi/2$ (and so the factor Γ is equal to 0.5). This solution is optimal in situations where there is no absorption, as in the reflection of neutrons, while in the reflection of x-rays it is convenient to use a lower value for Γ.

1.3.3 Hard x-ray depth graded multilayers

The possibility offered by the multilayer to efficiently reflect hard x-rays can be used to improve the performance of the focusing telescopes for x-ray astronomy. The constant spacing multilayers give high reflectivity of x-rays, but in a limited-bandwidth centered on the Bragg peak. In astronomical applications a reflectivity over a broad energy band is preferable, and this can be obtained by using variable spacing multilayer structures consisting of bilayers having modulated thicknesses. The effect of a variable spacing in the 10-100 keV region is shown in Figure 1-15, in which you can see how the reflectivity is much more distributed along the energy range compared to the cases of constant spacing and single layer.

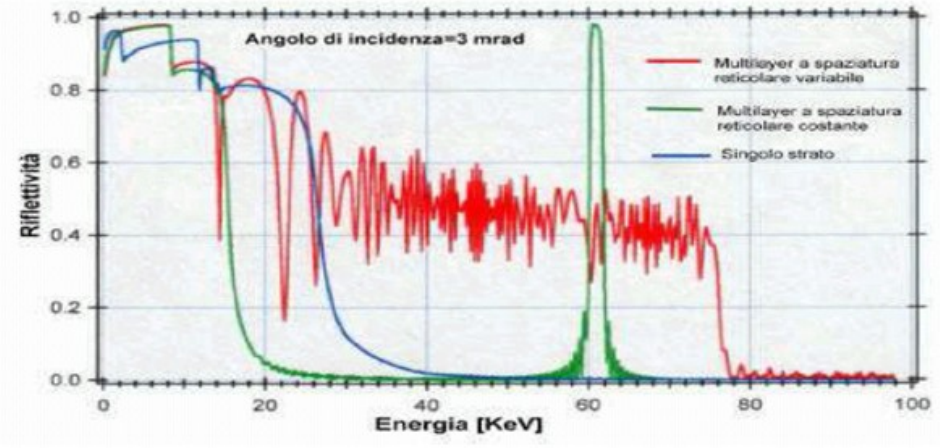

Figure 1-15. Reflectivity as a function of energy of the radiation corresponding to the typical single-layer structures (blue line), multilayer with constant spacing (green line) and multilayer with variable spacing (red line). The use of variable spacing allows to extend the reflectivity to a much wider energy band.

Because of absorption the lower energy photons can penetrate only the more superficial layers, whereas the higher energy photons can penetrate more in deep. For this reason it is convenient to put the thicker bilayers outside and decreasing the thickness with the depth.

For designing a depth-graded multilayer for a specific application, one has to determine the proper thickness law, the total number of bilayers and the materials, in order to achieve the most suitable reflectivity curve. The simplest assumption about the sequence of layers is that it is linear, and being the number of bilayers N needed to reflect a wavelength λ proportional to λ^2, for given values of N and Γ, the number of the thinner layers must be greater than the thicker layers. The formula commonly used to define the thickness sequence is the power law proposed by Joensen (Joenson, 1995):

$$d_i = \frac{a}{(b+i)^c} \tag{1.31}$$

in which the parameters a, b and c are existing within the limits $a,c > 0$ and $b > -1$. The parameter a is usually defined by the maximum wavelength to be reflected, and from the Bragg's law expressed in the equation (1.26) a rough estimate can be done:

$$a \approx \lambda_{MAX} / 2sen\theta \tag{1.32}$$

Parameters b and c are obtained from the maximization of a chosen figure of merit (FOM), which for example can be represented by the integrated effective area in the largest possible bandwidth. The number of bilayers in the depth-graded multilayered (N > 100) is much greater than that of the constant spacing multilayer.

1.4 Properties of x-ray telescopes

X-ray telescopes with improved sensitivity, effective area and angular resolution over a wide field of view in comparison to the already existing space observatories is one of the future objectives in astrophysics:

- The minimum flux detectable by an x-ray telescopes (i.e. **sensitivity**) is limited by the signal-to-noise ratio in the detector, often higher than the sources x-ray emittance.
- The **angular resolution** of a telescope determines its capability to avoid "confusion"

between the individual sources present within the same field of view. As it will be shown in this paragraph, the angular resolution is also important to limit the signal-to-noise ratio, thus affecting the sensitivity of a telescope.

- The **effective area** is of fundamental importance, since it determines the statistic robustness of the signal and the minimum achievable sensitivity.
- The **field of view** (FOV) is the angular extent of the observable sky at any given moment.

1.4.1 Sensitivity

Both for direct view telescopes and focusing telescopes, the real flux of a source is measured by subtracting the sky background from the total number of counts registered by the detector. A disadvantage of the direct view telescopes is that one is forced to measure the background in an area of the sky more distant from the source w.r.t. a focusing telescope. In the direct view telescopes, simply collimated or encoded with masks, the signal is revealed on a very large area (because of an angular resolution of several arcmin) and the poissonian statistics fluctuation of the background noise photons is very high, thus limiting the sensitivity in the flux. In the focusing telescopes the photons are concentrated on a small portion of the detector reducing advantageously the poissonian statistical fluctuation.

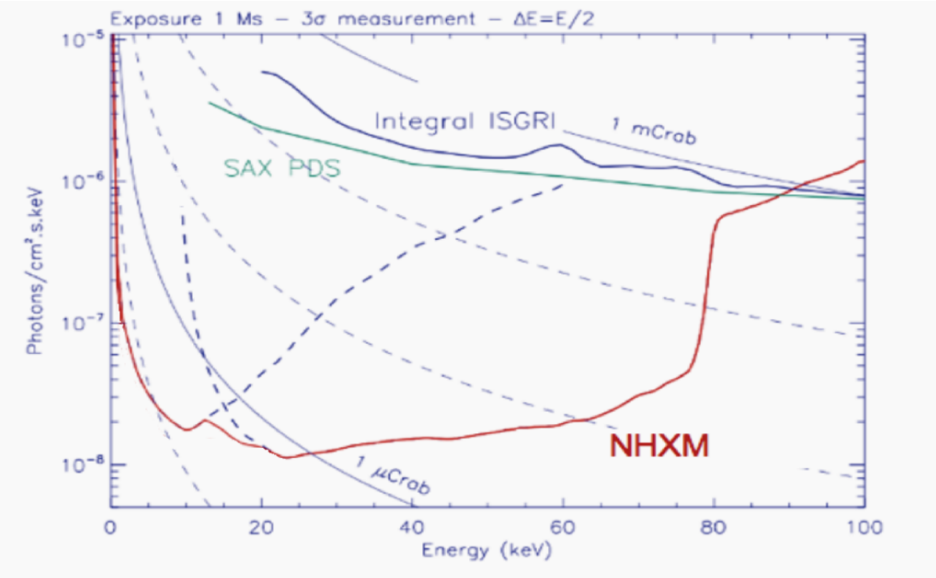

Figure 1-16. Comparison of sensitivity (3σ confidence) of space missions in hard x-ray.

Figure 1-16 shows a comparison of the sensitivity of current and past space missions with the one to be provided by the next future hard x-ray mission NHXM. The time of integration considered is 1 Ms and the energy band of integration is 50% of the energy. There is no doubt that the best sensitivity so far achieved in the hard x-ray band (10-100 keV) is the one of PDS direct view collimated instrument of BeppoSAX. With the use of a focusing x-ray telescope, it will be possible to distinguish hard x-ray sources with flux in the order of microCrab[1].

Direct view telescopes, simply collimated, having an opening area A_d and a detection efficiency ε for an energy band ΔE are characterized by a signal-to-noise ratio given by the following expression:

$$S = \frac{\varepsilon F A_d T_{\text{int}} \Delta E}{\sqrt{2 B A_d T_{\text{int}} \Delta E}} \tag{1.33}$$

where F is the flux of a source, T_{int} is the time of observation, and B is the background flux recorded by the detector. S represents the confidence interval, or in other words the number of sigma as a level of confidence for the measurement. Then the minimum detectable flux F_{in} will be given by:

$$F_{\text{min}} = \frac{S}{\varepsilon} \sqrt{\frac{2B}{A_d T_{\text{int}} \Delta E}} \tag{1.34}$$

From this relation it is possible to see that, given a direct view telescope with an opening area A_d, to improve the sensitivity of a an order of magnitude one should increase the area by a factor of 100.

A focusing telescope, instead, is characterized by the portion of the area where the photons are

[1] For the Crab Nebulae it is assumed the following spectrum: $F(E) = 10 \times E^{-2.05}$ ph cm^{-2} s^{-1} keV^{-1}

focused A_d, and by the effective area A_{eff} that depends on the reflection efficiency of telescope (Ricker & Vallerga, 1983):

$$S = \frac{n\varepsilon\eta F A_{eff} T_{\text{int}} \Delta E}{\sqrt{nBA_d T_{\text{int}} \Delta E}} \tag{1.34}$$

where η is the fraction of photons that are effectively focused in the area A_d and n is the number of mirror modules in the telescope. The minimum detectable flux is therefore given by:

$$F_{\text{min}} = \frac{S}{\varepsilon\eta A_{eff}} \sqrt{\frac{BA_d}{nT_{\text{int}} \Delta E}} \tag{1.35}$$

1.4.2 Angular resolution

By improving the angular resolution of the x-ray telescopes, we are able to better spatially resolve the photons distribution and so the details of the x-ray sources (see Crab Nebula in Figure 1-17). The two-dimensional distribution is described by a function called Point Spread Function (PSF) and also by the Modulation Transfer Function (MTF), which is the Fourier transform of the PSF. Another useful quantity is the Encircled Energy (EE), which describes the fraction of photons focused as a function of radial distance from the optical axis.

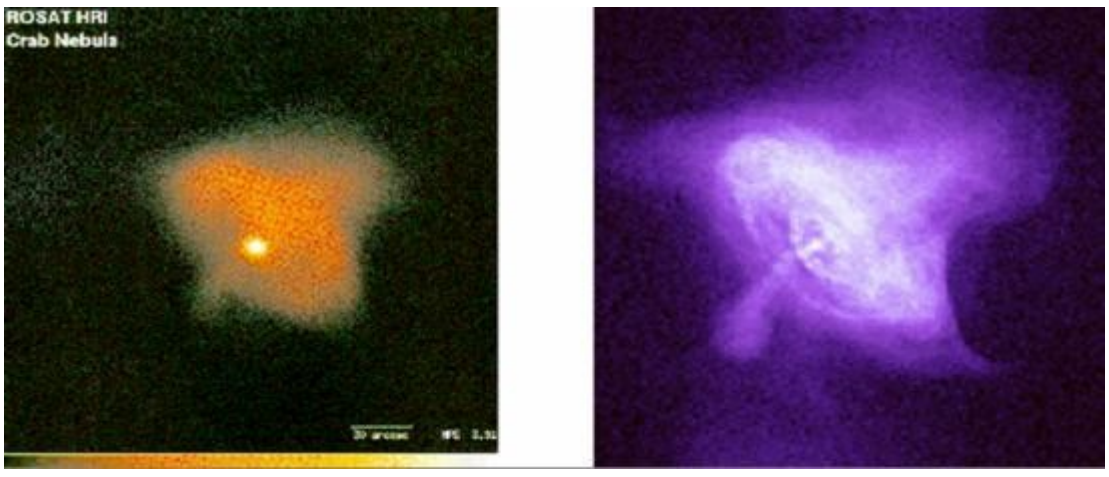

Figure 1-17. Comparison of the Crab Nebula image in the soft x-ray as seen by ROSAT (HEW ~ 3") and Chandra (HEW ~ 0.5"). The increase in angular resolution allowed to distinguish the details of this and other sources.

The PSF of an x-ray source does not have a Gaussian pattern and it is rather characterized by pronounced wings. For this reason it is more significant to use a parameter called Half Energy Width (HEW), or Half Power Diameter (HPD), rather than the more common Full Width Half Maximum (FWHM) used for other wavelengths. The HEW is the angular diameter at which the 50% of the Encircles Energy is confined.

To determine the number of discrete sources detectable by a mission with given values of angular resolution and sensitivity, it is required a priori prediction on the Log (N) – Log (S) distribution (the Log (N) – Log (S) relation defines the distribution of the number of sources (N) as a function of flux density (S), the lower the flux limit the higher the number of sources existing). Once the density of sources expected at a certain flux limit is calculated, one has to defined a criteria to determine the confusion limit between the sources, estimating the probability of having two sources within the size of the HEW.

1.4.3 Effective area

The effective area of a mirror is defined as the product between the geometric collecting area (see paragraph 1.2.4) and the reflection efficiency. With reference to the x-rays properties in grazing incidence, a large effective area cannot be achieved through a single mirror, but it is necessary to use multiple confocal nested mirrors and possibly more replication of the same mirror module.

The effective area depends on the energy of the radiation and is given by the formula:

$$A_{eff} = A_{Coll} R_{\theta}^{2}(E) \cong 8\pi F L R_{\theta}^{2}(E)\theta^{2} \tag{1.36}$$

where $R_{\theta}(E)$ is the reflectivity of the single mirror, squared for double reflection. A mirror that has an angle θ w.r.t. the optical axis will be in total reflection until the relation $\theta < \theta_{crit}(E)$ is satisfied. For x-ray focusing telescopes with typical incidence angles in the order of a few thousandths of radiant, the maximum energy at which the material has reflectance, and thus a sufficient effective area, can be fixed at 10 keV. To extend the capability of reflectance at energy greater than 10 keV one can use grazing incidence optics coated with multilayer coating, or telescopes with very long focal length and very low incidence angles.

2 Manufacturing Technologies of X-ray Mirrors for Astronomy

The technology of x-ray mirrors had, in recent years, substantial progress in extending the performance of the telescopes. In this chapter the classical manufacturing techniques so far adopted in the realization of single-layer focusing telescopes, and new technological solutions for next generation telescopes are described. Particular emphasis is given to the solution of the reduced thickness mirror shell replication by e-forming, showing the **pivotal contribution of the mandrels to the final performance of the telescope (§ 2.4.1)**.

2.1 Choosing the right materials

In the manufacturing of grazing incidence mirrors the first important choice is about a suitable material forming the mechanical support (substrate), in terms of its thermo-mechanical properties and the its aptitude to be superpolished. The substrate has to be figured to the required shape and superpolished to the required roughness, before being used as the mirror or as the master for mirror replication. The reflecting material can be composed by the substrate itself or, most commonly, by an additional coating (single-layer or multilayer).

2.1.1 Criteria for the mirror substrates

Different criteria may be considered for choosing the best suitable material to form the mirror substrate. An ideal material should have a low CTE (Coefficient of Thermal Expansion), an high thermal conductivity and a low tendency to deform in heat spikes.

For what concerns the thermal properties, low CTE materials are preferred because are less sensitive to variations in temperatures in the space environment. However, this problem can be solved by controlling the mirror temperature in the space environment via an active thermal control system. In this case the material must possess a good thermal conductivity to avoid non homogeneities in temperature along the mirror. A good agreement between the CTE parameters of the mirrors and the material forming the mechanical structure is another important condition to be respected.

For what concerns the mechanical properties, the mechanical instability of a mirror is caused by external or internal tensions, and therefore it is important to use a manufacturing technique that produces the lowest possible internal tension. A suitable material has a high diametric and specific stiffness defined by the density ρ and the and Young Module E. The material also needs to have mechanical properties that make it workable in order to obtain very smooth surfaces. In addition, lower density materials allow you to better respect the limits of weight, often very small, imposed by the space missions. Table 2-1 and Table 2-2 lists the mechanical and thermal properties of materials often used for grazing incidence optics in x-ray astronomy.

Table 2-1. Thermal properties at room temperature for some materials that have been already used or can be used as substrates for grazing incidence for x-rays optics (Michette & Buckley, 1993) (Citterio, 2000a) (Citterio, 2001).

Material	**Thermal Expansion** α **(K^{-1})**	**Thermal Conductivity** **k ($W\ m^{-1}K^{-1}$)**	**Specific Heat** **C ($Jkg^{-1}K^{-1}$)**	**Peak Distortion** $\alpha\rho C/k$
Aluminium	2.5×10^{-5}	237	899	2.5×10^{-1}
Nickel	1.4×10^{-5}	90	444	6.1×10^{-1}
CVD SiC	2.4×10^{-6}	250	700	0.2×10^{-1}
Silicon	2.6×10^{-6}	148	710	0.3×10^{-1}
Zerodur	1.5×10^{-7}	6	820	0.5×10^{-1}

Table 2-2. Mechanical properties for some materials that can be used as substrates of grazing incidence optics for x-rays optics (Michette & Buckley, 1993) (Citterio, 2000a) (Citterio, 2001).

Material	**Density** ρ **(kg m^{-3})**	**Young Module** E **(GPa)**	**Specific Stiffness** E/ρ	**Diametric Stiffness** E/ρ^3
Aluminium	2700	76	2.81×10^{-2}	3.8
Nickel	8900	180	2.05×10^{-2}	0.3
CVD SiC	3210	460	1.45×10^{-1}	14
Silicon	2330	90	2.86×10^{-2}	7.1
Zerodur	2550	90	3.53×10^{7}	5.4

2.1.2 Criteria for the reflecting layers

Up to now the reflective surfaces of the grazing incidence telescopes were composed of a single layer deposited on the substrate, apart from the early pioneering experiments on rocket which uses just the bare substrate material. In this case the choice is quite straightforward, since the transition from the Total Reflection condition to a condition of close-to-zero reflectivity occurs more gradually for denser materials. On the other hand the denser materials (heavy metals) absorb more for the photoelectric effect. So the choice is limited among the heavy metals with a low absorption coefficient, chemically stable with the material of the substrate.

Gold is the most used reflective material for the focusing telescopes so far built, with the exception of Einstein (HEAO-2), in which the reflective surface was in Nickel, Suzaku (ASTRO-EII), where some mirrors have been coated with Platinum, and Chandra (AXAF), in which the Iridium has been used.

Table 2-3. Materials of the optics for the major x-ray astronomy missions.

Mission	***Einstein***	***ROSAT***	***ASCA***	***Beppo SAX***	***Chandra***	***XMM-Newton***	***Suzaku***
Year	1978	1990	1993	1996	1999	1999	2005
Substrate	Glass	Zerodur	Aluminium	Nickel	Zerodur	Nickel	Aluminium
Reflective Layer	Nickel	Gold	Gold	Gold	Iridium	Gold	Gold / Platinum

The criteria for the selection of suitable materials to the realization of reflective multilayer film can be summarized in the following three points (Spiller, 1981):

- spacer material must have a low photoelectric absorption coefficient at the wavelength of interest and so it must have a low atomic number *Z*;
- the second material must have a high reflectivity, so the material must have medium to high *Z* and the as low as possible photoelectric absorption coefficient;
- the interfaces of the materials shall be made sufficiently smooth, without inter-diffusion and chemically stable.

The multilayer films for astronomical applications shall consist of a high number of bilayers (> 200). As a matter of fact, with the existing coating deposition techniques, the quality of the layer interfaces becomes worse with the increasing of the number of the layers. Also the roughness of the layers increases and propagates, starting from the substrate, with the number of deposited layers.

To reduce as much as possible the number of bilayers, the materials composing the multilayer shall have the highest possible density contrast and be less absorbent. To minimize the effects of stress, the multilayer materials must have coefficients of thermal expansion as similar as possible. To reduce plastic deformation the Young Modules of the materials shall be sufficiently high.

Table 2-4. Comparison of the thermo-mechanical properties of some materials used in multilayer coatings for hard x-ray astronomy.

Material	**Density** ρ **(g cm^{-3})**	**CTE at 25°** $(10^6 \times K^{-1})$	**Young Module E (GPa)**	**Couples**
C	1.8 – 2.6	7.1	6.5 – 9	Ni/C; Pt/C
Si	2.33	2.6	47 – 131	Mo/Si; W/Si
Ni	8.90	14.0	180	Ni/C
Pt	21.45	8.8	168	Pt/C
W	19.30	4.5	411	W/Si
Mo	10.20	4.8	329	Mo/Si

As spacer element Carbon minimizes the extinction of photons by photoelectric effect and generates stable interfaces with many heavy metals. However, for wavelengths just below its K_α line (~0.3 *keV*) is too absorbent and Silicon is preferable.

Molybdenum is poorly absorbent is usable with Silicon only until its lower energies K_α line (~17 *keV*). Nickel is fine for hard x-ray reflection, except for the low density that obliges to use many bilayers.

Tungsten/Silicon couple offers a good combination of optical properties for hard x-ray and it is relatively easy to be deposited. Tungsten has anyway the *K* absorption edge at the energy of 69.5 keV, thus limiting the maximum observable energy of the spectrum.

Platinum/Carbon couple, is the one that offers the highest hard x-ray reflectivity with the fewest number of bilayers, thanks to the very high density contrast. These two elements have also very similar coefficient of thermal expansion (see Table 2-4). Platinum/Carbon couple has an excellent chemical stability and can be deposited with stable interfaces. The *K* absorption edge of Platinum is at 78.4 keV.

2.2 Multilayer deposition via Magnetron Sputtering technique

The ability to deposit the reflective surface with the precision required, plays a crucial role in the realization of a grazing incidence optics for hard x-ray astronomy. So far the focusing telescopes for x-ray astronomy were used with relatively thick layer coatings (~ 100 nm), since they are designed to operate solely under total reflection. In order to exploit fully the potential interference of multilayer structures, you must be able to deposit alternating layers of different materials with thickness up to the order of tens of Angstroms, with roughness comparable to the one of the underlying substrate. Multilayer technology therefore implies the need for control of various parameters on a very accurate deposition process.

The process in which fast ions bombard a sample, with its consequent evaporation, is called **sputtering**. Physically, incident atoms collide elastically with the target atoms, without chemical reactions (the used ions are always inert gases). The ions transfer their momentum to target atoms, so they leave the surface. The emission of target material is connected to secondary electron emission, ion reflection at the target surface, ion implantation, emission of photons, structural changes in the target. The properties of the emitted particles depend on the bombarding ions, their kinetic energy, incidence angle, atomic mass, target material and its structure. The maximum energy transfer rate is reached when the atomic mass of the target and the ions is the same.

The **sputtering yield** (the number of emitted atoms per incident ion) varies with the energy of the incident ions. Sputtering starts at energies approximately equal to the heat of sublimation (tens of eV). Above this threshold, the yield increases and reaches a maximum at 10 keV. For higher energies the penetration depth causes ion implantation and less effective momentum to the target atoms. The high energies lead to formation of very dense films with high refractive indices and low environmental shifts, in addition to a good smoothness. Moreover, the evaporation rate is physically related to the ion flux and is very stable: the thickness control is

even obtained by time calibration.

Magnetron sputtering is a technique that was developed to reduce the substrate heating and to improve the deposition rate at moderate voltages. The concept is that the free electrons can be trapped by magnetic fields and controlled. The magnetic fields are weak enough so that the paths of heavy ions and charged sputtered atoms are not significantly affected, but the electrons are confined in vicinity of the target, and do not bombard the substrate. Moreover, the electrons are trapped in a close race-track without touching the solid surfaces, so that they can ionize the gas more efficiently, and a lower pressure (10^{-3} mbar) is necessary to sustain the plasma: a further advantage is the lower number of collisions between the sputtered atoms and the plasma ions, which results in higher energy of sputtered particles.

One of the most effective arrangements is the planar magnetron (see Figure 2-1). It consists of a copper body with a plane front surface to which the target plate is attached. Magnets inserted into the copper body from the back side create a toroidal-shaped magnetic field in front of the target. Many arrangements and designs are possible, provided that the magnetic field (200-500 G) is perpendicular to the electric field along a closed path. In such conditions the drift velocity of electrons is perpendicular to both fields, and so they follow a closed path. The plasma impedance is substantially reduced (the voltage required is about 300-700 V), and current densities of 60 mA/cm^2 can occur at power densities of 40 W/cm^2.

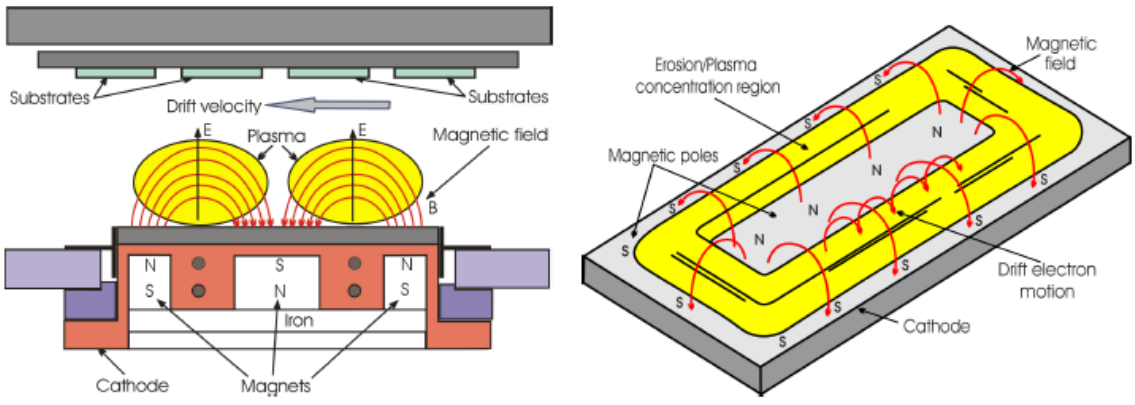

Figure 2-1. A typical arrangement for Magnetron Sputtering deposition method: side and top view.

The distance between target and substrates is usually larger than the extension of the plasma cloud so that the substrates are not directly in contact with the plasma: the extension of the plasma lobes may be controlled varying the magnetic field. The more the extension is close to

substrate, the more the ions condense at high energies. The properties of the film may then be varied tuning the magnetic field.

The erosion of the material is, however, non uniform. Most of the erosion occurs in the high-density plasma regions: directly connected is the low uniformity (5%) of the deposited layer. The bombardment of fast electrons is also non uniform, the substrate is heated at higher temperatures where the magnetic field is weaker.

2.3 Different manufacturing approaches of the past and current missions

The solution adopted to increase the collecting area of the grazing incidence telescopes is to nest more mirrors in a confocal configuration. The number of mirrors that can be nested into a given aperture diameter depends on their thickness, which in turn depends on the technique of manufacturing.

There are 3 techniques that have been used so far for the realization of the grazing incidence telescopes of the major x-ray astronomy missions:

1. the technique of direct machining/polishing processing of the mirrors
2. the technique of segmented thin foils
3. the technique of replication by Nickel electroforming

The technique of thin foils is the technique that allows you to get the smaller thickness and therefore allows to nest the highest number of mirrors, while direct processing technique is in the opposite situation. However, there is in general an inversion of priorities, in the sense that with higher thickness one can get more precise geometric shape and thus better angular resolutions of the mirrors. The replica technique by Nickel electroforming locates in the intermediate position, allowing to manufacture mirror shells with good angular resolution and limited mirror thicknesses.

Table 2-5 summarizes the performance of the main soft x-ray astronomy missions with reference to the manufacturing technique of their focusing telescopes. It can be seen how the values of the angular resolution and the values of the effective area vary consistently with technique used.

Table 2-5. Performance of the major x-ray astronomy missions ordered by the different technique used to manufacture the mirrors of their focusing telescopes.

	Einstein	***ROSAT***	***Chandra***	***BeppoSAX***	***XMM-Newton***	***ASCA***	***Suzaku***
Manufact. Technique	Direct Polishing	Direct Polishing	Direct Polishing	Replica	Replica	Thin Foils	Thin Foils
Geometry	Wolter-Schwarz.	Wolter I	Wolter I	Double cone	Wolter I	Double cone	Double cone
Modules (#)	1	1	1	4	3	4	4
Mirror for Module (#)	4	4	4	30	58	120	175
Thickness (mm)	20	16 - 25	35	0.2 - 0.4	0.47 - 1.1	0.125	0.155
Collecting Area	350 cm^2	1100 cm^2	1100 cm^2	123 cm^2	2000 cm^2	410 cm^2	580 cm^2
Resolution (HEW)	4”	3”	0.5”	60”	15”	200”	100”
Focal Length	3.45 m	2.4 m	10 m	1.8 m	7.5 m	3.5 m	4.75 m
Max Diameter	58 cm	83.5 cm	120 cm	16.2 cm	70 cm	35 cm	40 cm
Incidence Angles	40’ - 70’	65’ - 147’	27’ - 52’	14’ - 37’	17’ - 40’	29’ - 43’	18’ - 36’

2.3.1 Optics produced via direct polishing of the mirrors (ROSAT, Chandra)

This is the technique used to manufacture the firsts x-ray astronomy focusing optics (Einstein, ROSAT). The optics manufactured with this direct processing are characterized by very precise geometric profiles, capable of angular resolutions in the range of the arc seconds.

The mirrors are made of materials with high rigidity and low CTE (Quartz or Zerodur) by directly working the optical substrate. The Wolter profile is generated by means of milling machines, on the two conical surfaces separately, and the surface finishing is achieved by superpolishing. At the end of the manufacturing cycle the substrates are coated with a metallic reflective layer. To support this type of machining, the thickness of the substrate shall be in the range of 20-30 mm, and so it is possible to nest only a few mirrors. In this way, the effective area achievable is pretty limited, unless a very large focal lengths is used (>10m) to increase the diameter of the aperture.

With this technique the best results achieved are on the still operative Chandra Observatory (Weisskopf, 2000). The angular resolution of the Chandra telescope in terms of HEW is 0.5 arc seconds. The use of this type of telescopes is mainly aimed at the observation of extended sources (galaxies, clusters of galaxies, supernova remnants) or cosmological investigations (long observations of low energy cosmic x-ray sources), for which an optimum performance in terms of angular resolution is requests.

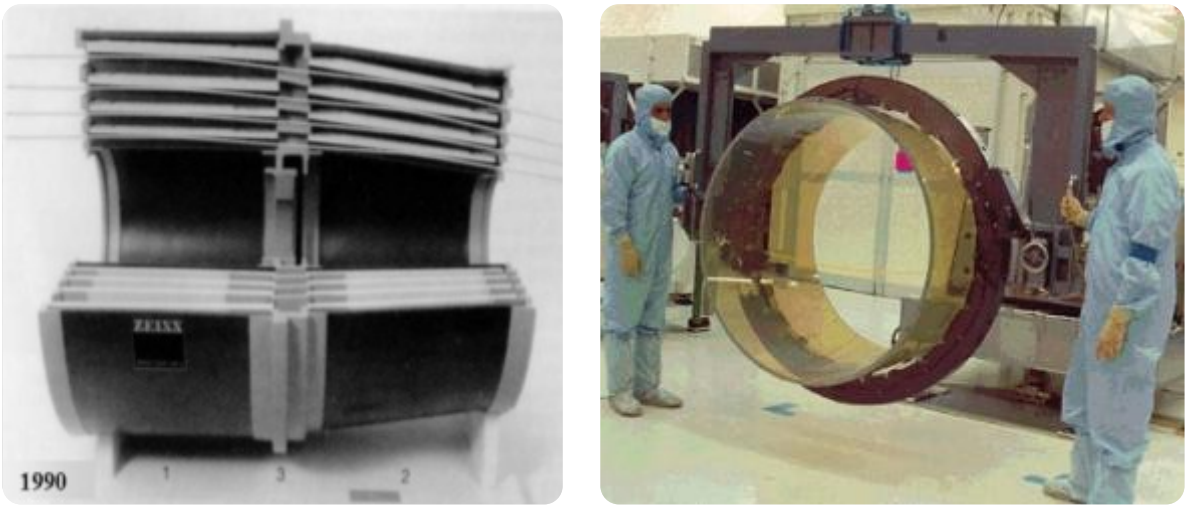

Figure 2-2. (left) section of ROSAT telescope consisting of four confocal mirrors; (right) one of the four Chandra monolithic mirrors during a phase of the integration.

2.3.2 Optics produced via thin foils technique (ASCA, Suzaku)

Examples of x-ray astronomy missions with telescopes manufactured adopting this technique are ASCA SODART (1993 and 1998) and ASTRO-EII (2005). ASTRO-EII, renamed Suzaku after its successful lunch, is a replacement of ASTRO-E which was lost for the failure of launch vehicle on 10 February 2000.

This method relies on the implementation of a number of mirror segments formed by thin sheets of light metal material (i.e. aluminum). The segments are appropriately curved or epoxy-replicated (Kunieda, 2001), coated with a proper reflective material and assembled in cylindrical symmetry to form sectors of the complete optic. With this technique it has been used a double cone approximation of the Wolter geometry, through the use of large radius-to-focal ratio.

Thanks to the reduced thickness (100-400 micron) and light weight mirrors, with this technique it is possible to integrate a large number of mirrors (up to 200). However, the best angular resolution achieved so far was is in the order of some arcmin HEW, due to the difficulty in giving the right profile to the mirrors, to mechanical deformations of the structures and/or imprecise techniques used for the assembling of the sectors.

These telescopes are used primarily in applications of polarimetry, spectroscopy and x-ray timing, for which the effective area is a priority with respect to image quality. Figure 2-3 shows a mirror module of ASTRO-EII and a segment of the ASTRO-E mission formed by 175 aluminum mirrors.

Figure 2-3. (left) image of one of the four mirror module of the Suzaku mission consisting of 175 aluminum mirrors; (right) image of one of the four quadrants of one mirror module of ASTRO-E.

2.3.3 Optics produced via replication by Nickel e-forming (XMM, SWIFT)

The replica technique using galvanic Nickel was developed prior at the IFCTR Institute of Milan, and later at the Brera Astronomical Observatories (INAF-OAB) and Media Lario Technologies company (MLT) for the realization of the focusing x-ray telescope for the Italian satellite BeppoSAX (Citterio, 1988). The MLT company, by using this technique, has been successfully completed the x-ray telescopes of JET-X/Swift (Citterio, 1996) (Burrows, 2000) and XMM-Newton (de Chambure, 1999). The procedure is sketched in Figure 2-4:

- First there is the need to procure a superpolished mandrel with the profile corresponding to the negative of the mirror to be replicated; the mandrels so far used are composed by an aluminium core and a Nickel/Phosphorous overcoating, where is possible to reach lower surface roughness w.r.t. the aluminium.
- The mandrel is cleaned and coated with thin layer of Gold, which will constitute the reflecting surface of the mirror, by means of an e-beam evaporation process in vacuum.
- The gold coated mandrel is immersed in an electrolytic Nickel bath where the electroforming takes place, and here it remains until the Nickel layer, which will constitute the optical mechanical substrate, has reached the desired thickness (typically between 0.4 – 1.5 mm).
- The last step of the process, is to separate the mirror from the mandrels by cooling, exploiting the difference in the CTEs of Nickel and aluminium.

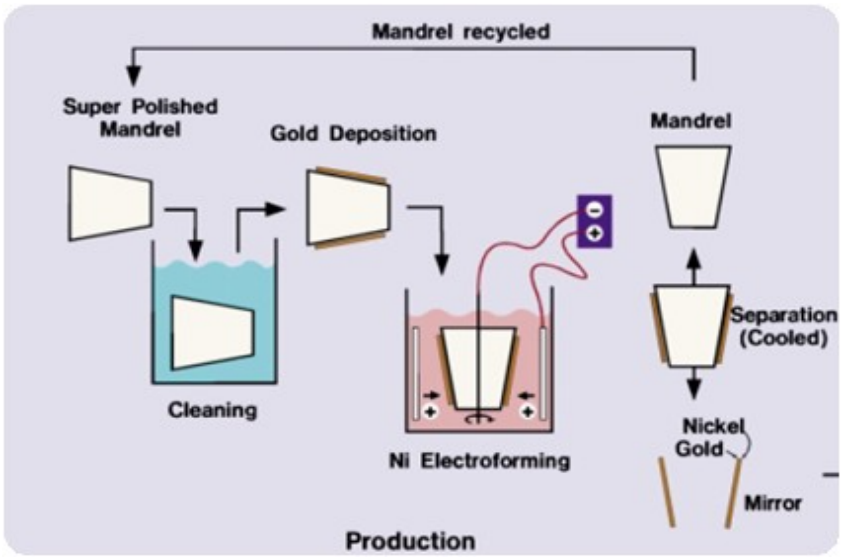

Figure 2-4. Steps of the replica process by e-forming (ESA courtesy).

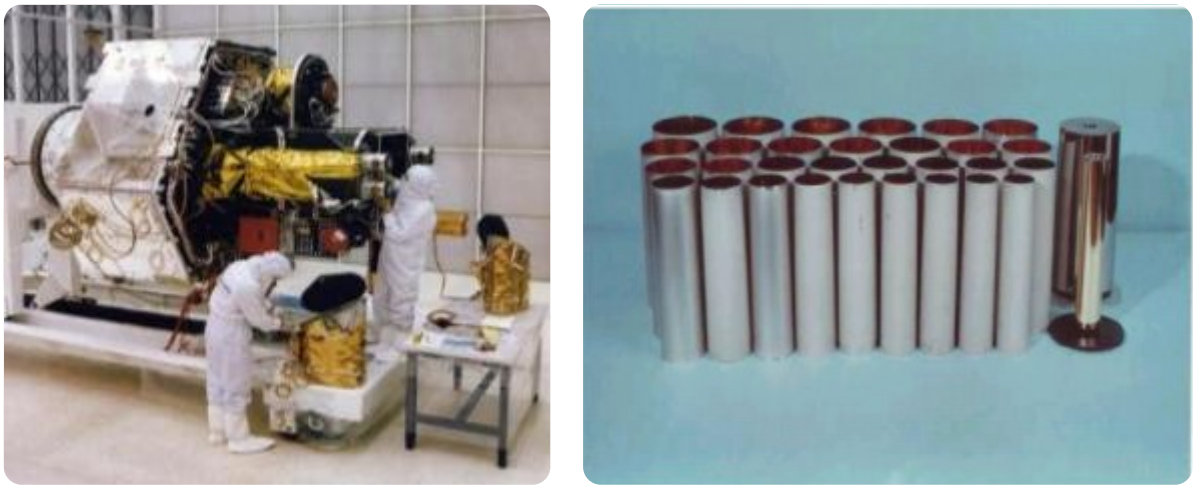

Figure 2-5. (left) the BeppoSAX x-ray telescopes during integration in the satellite; (right) the entire series of mirrors produced for one of the four modules of the BeppoSAX satellite with two of the mandrels used for replication.

This technique allows the creation of cylindrical symmetry mirrors (Wolter or any other complex geometry) in a single monolithic frame, avoiding the problem of alignment between the parabolic and hyperbolic surface. Not having to undergo direct machining, the final thickness of the mirror can be limited, allowing to nest together more mirrors and achieve an high effective area (see Figure 2-6). The cylindrical symmetry gives the structure a remarkable mechanical strength, allowing quite precise surface accuracy and angular resolution of 10-15 arc seconds HEW.

The mandrel can be reused for many replicas to produce more identical mirror modules, saving time and resources. With this technique the surface of the reflective material is the one that are deposited in direct contact with the superpolished mandrel. This surface is usually smoother, and therefore has a greater reflectivity, because the thin film deposition has the tendency to increase the roughness as a function of the deposited thickness.

The mirror thickness is a key parameter for the performance of the telescope Thicker mirror are less sensitive to thermal deformation, gravity load and mechanical vibration, but the drawbacks are an higher weight and a lower filling rate. Thinner mirror allows to contain the overall weight and to nest a greater number of mirrors, but the drawbacks are the limit in the thermo-mechanical properties and in the capability to replicate and maintain the mandrel angular resolution.

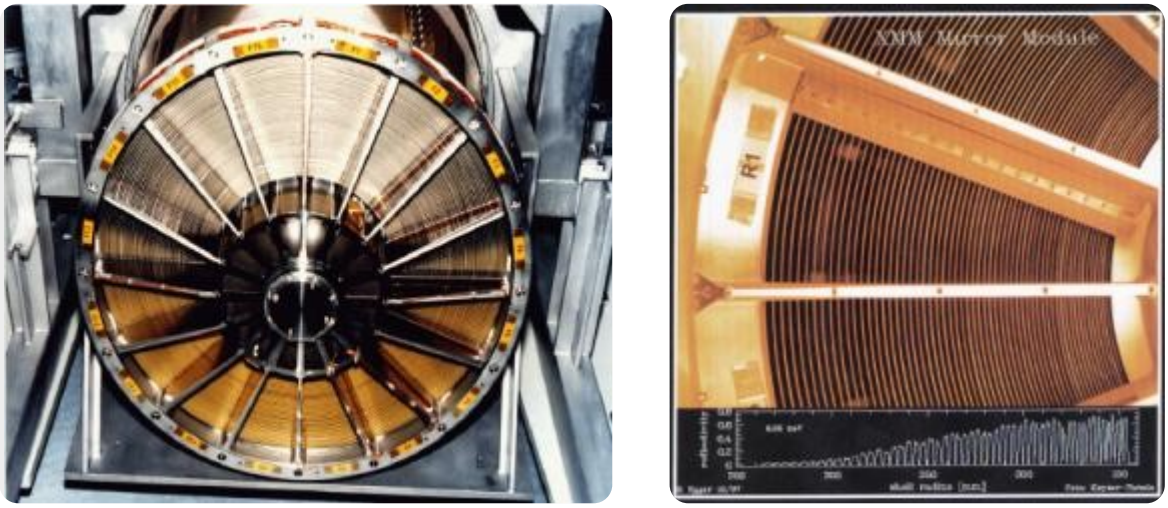

Figure 2-6. (left) one of the three modules of the XMM-Newton satellite, consisting of 58 mirrors replicated by Nickel e-forming technique; (right) enlarged view of the mirror module showing the high filling rate that can be achieved.

2.4 New manufacturing approaches for next future missions

A number of different x-ray optics technologies have been developed to maturity, optimised, and refined for space missions, and significant investments have been made to develop each of those. Despite the fact that these missions were designed and built to achieve a range of goals, requiring different effective areas and angular resolutions, their performances show a clear correlation. The situation of the major next missions is completely different, since they requires a substantial increase in effective area combined with a high angular resolution.

Existing technologies are not consistent with the requirements of next future missions, because it would lead to excessively heavy and expensive optics, and/or not able to produce the requested effective area and angular resolution. For these missions, the scientific community is trying to push forward the existing technologies by developing processes with thinner metallic substrates and/or with very light material.

Particular emphasis is given to the solution of the reduced thickness mirror shell replication by e-forming, foreseen for NHXM and eROSITA telescopes, showing the **importance of the mandrels contribution to the final performance** of the telescope.

2.4.1 Replication by e-forming of mirror shell with reduced thickness (NHXM, eROSITA)

The high density of the Nickel (about 3 times the density of aluminum, glass and silicon) is the main intrinsic limit of the electroforming technology when applied to the requirements of the most ambitious new missions (i.e. ATHENA/IXO). High effective areas are achieved with big apertures and with high number of mirrors and/or modules, leading to a huge total mass if the thickness-to-diameter ratio of the existing mirrors is considered. The angular resolution of the telescopes consisting of mirrors produced with the replication by e-forming is on the order of 10-15 arc seconds HEW, when a thickness-to-diameter ratio of 1.5 (μm/mm) is considered (as per XMM-Newton x-ray mirrors).

The goal of the ongoing developments is to reduce as much as possible the thickness-to-diameter ratio (a order of ~ 2) while maintaining the angular resolution better than 15 arc seconds HEW in order to fulfill the NHXM requirements. It is well known that for a quasi-cylindrical shell, the deformation due to a generic load is indirectly proportional to the cubic power of the thickness. Therefore, a strong reduction of the thickness increases the risks to have plastic deformation during the separation of the shell from the mandrel and possibly during the handling and integration process of the shells. For these reasons, in addition to the pure Nickel, also other alloys, such as Nickel-Cobalt (NiCo) and Nickel-Cobalt-Phosphorous (NiCoP), are being considered. These alloys are characterized by better stiffness and superior yield properties w.r.t. to the pure Nickel.

The above approach is the **baseline for the NHXM mission**, with nanostructured multilayer hard x-ray reflecting coatings sputtered onto the internal surface of the gold coated NiCo thin mirrors. As one can expect, **the final roughness and shape of the multilayer coated mirrors are strongly influenced by the mandrel starting performance**, as they defined a starting level that in general can only be worsen. Some engineering models with Ni and NiCo integrated shells coated with W/Si and Pt/C multilayer films (up to 200 bilayers) have already been developed and tested at the PANTER-MPE x-ray calibration facility under ASI contracts demonstrating the technological feasibility (Pareschi, 2009).

The status-of-the-art of the development of the replication technology for NHXM is described in more details in the Chapter 7.

For eROSITA, being a soft x-ray mission, there is no need for the multilayer coatings and the mirror shells are just gold coated. The **eROSITA 378 x-ray mirrors** shells are currently being

manufactured (at June 2011) via nickel electroforming technique by Media Lario Technologies company (MLT) by using the same thickness-to-diameter ratio of XMM-Newton. Nevertheless, it is a challenge to achieve a comparable angular resolution of XMM because of the different design (5 times shorter focal length and 2 times shorter mirror length – 300mm against the 600mm of XMM). ZEISS company obtained an angular resolution of 22 arc seconds HEW on the fabrication of ABRIXAS telescope, even by using a thickness-to-ratio 1.7 times greater w.r.t. to XMM-Newton (Friedrich, 1998):

- The shorter length of the mirrors gives less margin to the border deformation caused by the Nickel residual internal stress
- The shorter focal length gives a more pronounced deviation of the double cone form the Wolter geometry. In the case of eROSITA the deviation of the parabolic/hyperbolic profiles from the double cone is in the order of 10-20 μm. When applied to the traditional polishing of the mandrels, this characteristic entails a tendency to rapidly degrade the shape accuracy. **For the manufacturing of the new 27 outermost NiP coated mandrels, it has been necessary to develop an advance figuring/polishing technique**, allowing to produce them with an angular resolution consistently < 6 arcsec HEW and a roughness of 0.3 nm rms (between 1 mm and 0.002 mm spatial frequency range) (see also Chapter 6).

The status of the eROSITA telescope production and the x-ray performance are reported in the Chapter 8.

In order to understand **the influence of producing mandrels** with good angular resolution and very low roughness, in the fulfillment of the scientific requirements of the missions, it is convenient to have a look to an example of error budget allocation in the hard x-ray domain (@ 30 keV, see Table 2-6), taking into account all the contributions leading to the final HEW:

- averaged mandrel geometrical shape accuracy
- averaged mirror shell replication accuracy
- averaged mirror shell integration deformation
- scattering of the final roughness resulting from the contribution of the mandrel, the gold coating and multilayer growth
- contribution of the alignment errors between the mirror shells
- thermo/mechanical deformation of the Mirror Module

Any additional error in the mandrel would reflect into a degradation of the final performance.

Table 2-6: Example of a preliminary error budget allocation for an hard x-ray mission. In order to stay within the goal of 20 arc seconds HEW at the energy of 30 keV, the shape of the mandrels shall be in the order of 6-7 arc seconds HEW and the roughness in the order of 0.2nm rms (i.e. with a scattering contribution to the HEW lower than 12 arc seconds).

Error Source	**HEW contribution**
$HEW_{GEOMETRIC\ -\ MIRROR\ SHELL}$	12.8"
($HEW_{GEOMETRIC\ -\ MANDREL}$	(7.0"
$HEW_{GEOMETRIC\ -\ REPLICATION}$	8.5"
$HEW_{GEOMETRIC\ –\ INTEGRATION}$)	6.5")
$HEW_{XRS\ –\ MANDREL,\ REPLICATION,\ MULTILAYER}$ (@30 keV)	12.1"
$HEW_{MIRROR\ SHELL\ ALLIGNMENT}$	1.5"
$HEW_{\ THERMAL\ GRADIANT}$	9.0"
$HEW_{TOTAL\ -\ RSS}$	**20.0"**

2.4.2 Future thin foils mirrors (ASTRO-H, GEMS)

Over the 30 years of development, there has been substantial improvement in foil mirror performance. The angular resolution has improved incrementally with each new generation of mirror. The introduction of epoxy replication removed the energy dependence of the point-spread function. More accurately machined and stiffer housings have reduced misalignments. Better substrates and forming mandrels have reduced figure errors on individual segments. Nevertheless, no foil mirror has attained an angular resolution better than about one arcmin. The intrinsic angular resolution due to the conical approximation is generally small compared with any of the other terms. Addressing errors across a broad front can potentially lead to a considerably better mirror. Still it is unlikely that an aluminum foil mirror will ever achieve

angular resolution substantially better than one arcmin (Petre, 2010).

Aluminum has numerous desirable attributes as a substrate material for foil mirrors: low density, easy to form, moderate cost, good surface properties. Nevertheless it is not ideal; it is flimsy, cannot be formed in three dimensions (i.e., cannot impart the axial curvature of a true Wolter mirror), and most importantly the surface quality of even the best material limits the attainable resolution. Hailey et al. (Hailey, 1997) performed a careful characterization of the surface properties of Aluminum and concluded that the surface properties limit the angular resolution of even a perfectly aligned aluminum foil mirror to 25 arcsec.

Epoxy replication has become the baseline approach for making foil mirrors. Astro-H is the next major Japan/US x-ray observatory, currently under development in Japan for a 2014 launch, that will make use of the advanced thin foils technique trying to achieve 60-90 arcsec HEW. Foil mirrors also are being utilized on the Gravity and Extreme Magnetism Small Explorer (GEMS), a mission devoted to x-ray polarimetry scheduled for a 2014 launch.

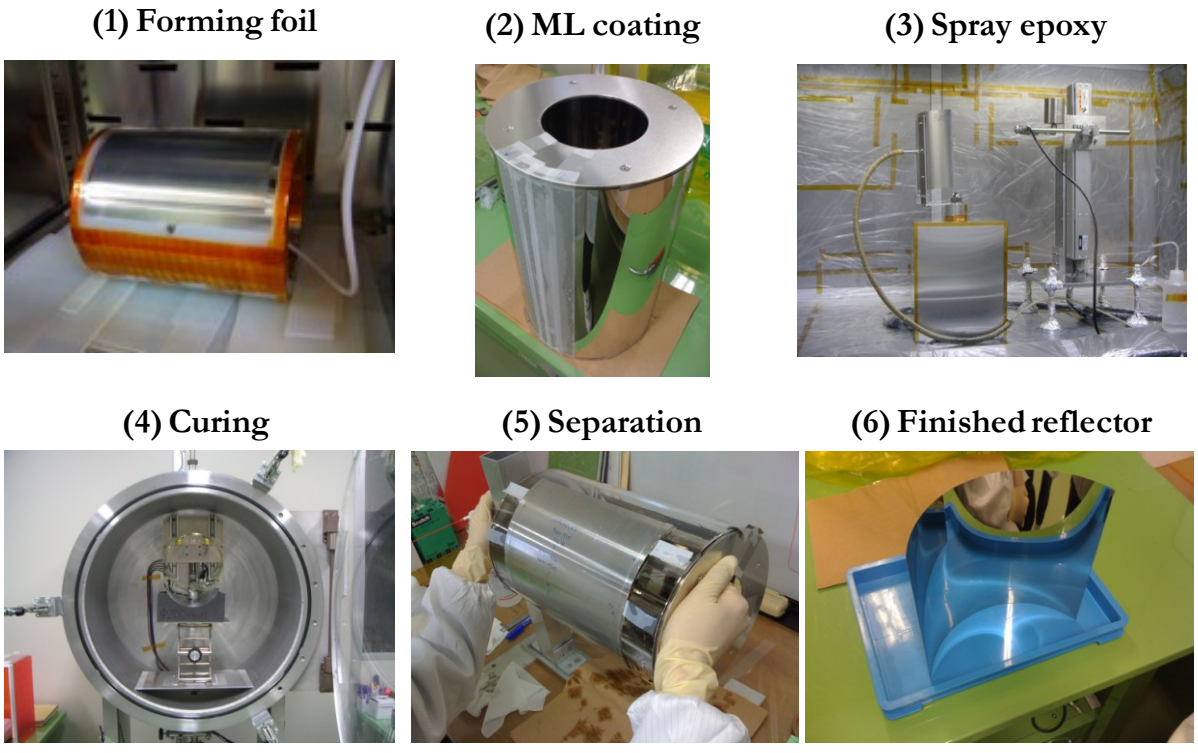

Figure 2-7. ASTRO-H aluminum multilayer coated thin foils process: the coating is deposited on a mandrel and transfer to the pre-formed aluminum back plain by means of epoxy resin replication (Nagoya University credits).

2.4.3 Hot slumping of thin glass sheets (NuSTAR, ATHENA/IXO)

The most promising alternative material, and one that has produced a revolution in thin substrate mirrors, is glass. In searching for an alternative substrate for aluminum for hard x-ray mirror for a balloon instrument, Hailey et al. (Hailey, 1997) showed that the intrinsic surface quality of commercially available borosilicate glass is far superior to that of aluminum.

The density of high-temperature Borofloat® glass is one of the lowest for Silicon-based glasses, and it has a good resistance to abrasion and scratching. The low coefficient of thermal expansion, the good resistance to thermal shock and the ability to be used at different temperatures defines a good thermal stability. Thermal and mechanical characteristics (even at thicknesses of 200–400 μm) adapt to scientific space missions applications where, due to the large size, the temperature of the mirrors cannot be actively controlled.

Hailey developed a thermal slumping approach to form the glass to its approximate shape. The slumping approach introduced by Hailey et al. (Hailey, 1997) entails suspending a flat piece of glass substrate across a concave mandrel, and slowly thermally cycling it so that the glass assumes the form of the mandrel. While the figure of the substrate was not precise (Hailey was using cylindrical mandrels) the excellent microroughness of the surface was preserved. A slow thermal cycle in which the glass is annealed as it cools allows the glass to largely retain its mechanical properties.

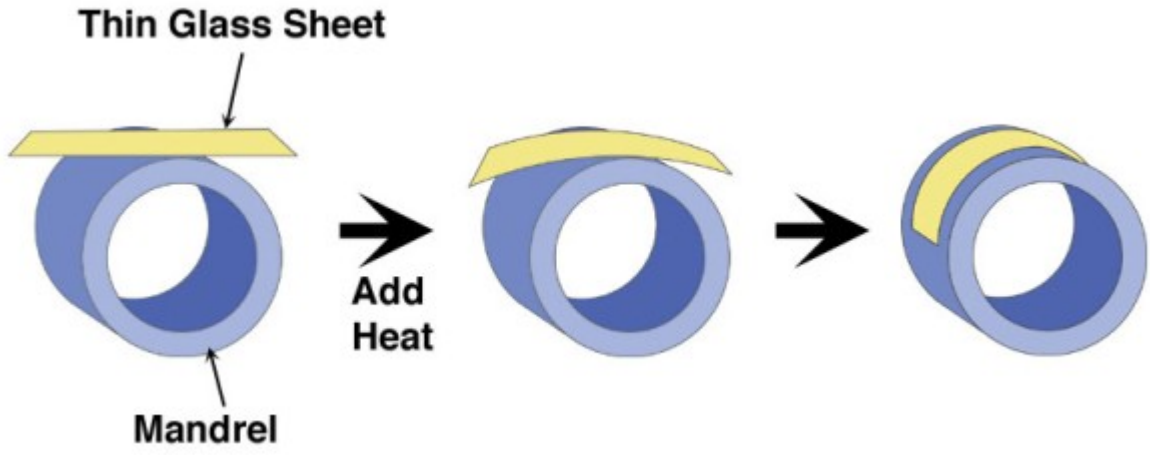

Figure 2-8. The basic idea of the hot slumping process, in this case with a convex mandrel (NASAGlobalAstro credits).

In the most advanced approach, the glass is slumped onto a convex mandrel. The primary reason for using a convex mandrel is because in a concave mold, thickness variations in the substrate, even if they are fractions of a micron, would introduce figure errors even in a substrate that conforms exactly to the mold. Use of a convex mold means that the x-ray reflecting surface comes into contact with the mandrel, with a possible degradation of the mirror surface roughness.

The challenges faced in forming precise mirror segments are (Petre, 2010):

- mandrels with sufficiently high quality figure need to be mass produced;
- distortions introduced into the glass from the slumping must be controlled. The most destructive distortions are those with spatial frequencies in the millimeter to centimeter range, the so-called midfrequency errors;
- any x-ray reflective coating deposited onto the substrate must not distort it via biomorphic stresses.

The coated substrates must next be mounted accurately in a module without distorting the optical figure. Bending moments applied at mounting points propagate across the entire substrate, compromising the figure. What makes the mounting extremely challenging is that the substrates are flimsy, bending under their own weight.

The Nuclear Spectroscopy Telescope Array (NuSTAR), a Small Explorer expected to be launched in 2012, will features a pair of conical slumped glass mirror modules. The angular resolution requirement is 60 arcsec (HPD); the goal is 40 arcsec. The mirror substrates are heat formed into a cylindrical shape using convex mandrels (polished commercial grade fused silica).

Figure 2-9. Enlargement of one NuSTAR mirror module being produced with hot slumping technique.

In 2007, Constellation-X and XEUS missions were merged into the International X-ray Observatory (IXO). For Constellation-X, the baseline implementation utilized slumped glass, with technology development led by GSFC (Zhang, 2008). For XEUS, the baseline mirror was a Silicon Pore Optic. Slumped glass was considered a backup technology for XEUS, with technology development at the Max Planck Institut für Extraterrestrische Physik (MPE) and at the Brera Astronomical Observatory (INAF-OAB) (Ghigo, 2009). All three institutions are participating in the glass technology development for IXO. The angular resolution of the entire observatory is to be 5 arcsec; to achieve this, the mirror angular resolution must be ~3-4 arcsec.

2.4.4 Silicon pores optics (ATHENA)

X-ray optics require superpolished mirror surfaces. Similar requirements are imposed on the surface finish of the latest generation silicon wafers for the electronics industry. These are already commercially mass produced and very substantial investments have been made by the semiconductor industry to achieve the high quality surface finish. The surface roughness corresponds to that required for X-ray optics and the figure errors are within the error budget for a few arc second angular resolution optic. In addition, the surfaces of such double-sided polished wafers are very parallel, with very small thickness variations (Bavdaz, 2010).

The silicon pore optics production can be grouped as follows:

- production of ribbed and wedged silicon plates,
- coating of the plates,
- assembly into stacks of tens of plates,
- assembly of two stacks to form a mirror module.

The production of silicon mirror plates starts with dicing SEMI standard <100> 300mm silicon wafers, which are double sided polished and 0.775mm thick, into square plates. The ribbing process dices grooves into the silicon substrate, thereby creating:

- the pores forming the channels for the x-rays to pass through,
- (the ribs providing the required structural stiffness when bonded in a stack, and
- a thin membrane.

During stacking the plates will be elastically deformed to create approximations of the curved surfaces of a Wolter I optic. To minimise the strain energy, one reduces the membrane thickness to a level sufficient to meet the figure requirements of the final optic.

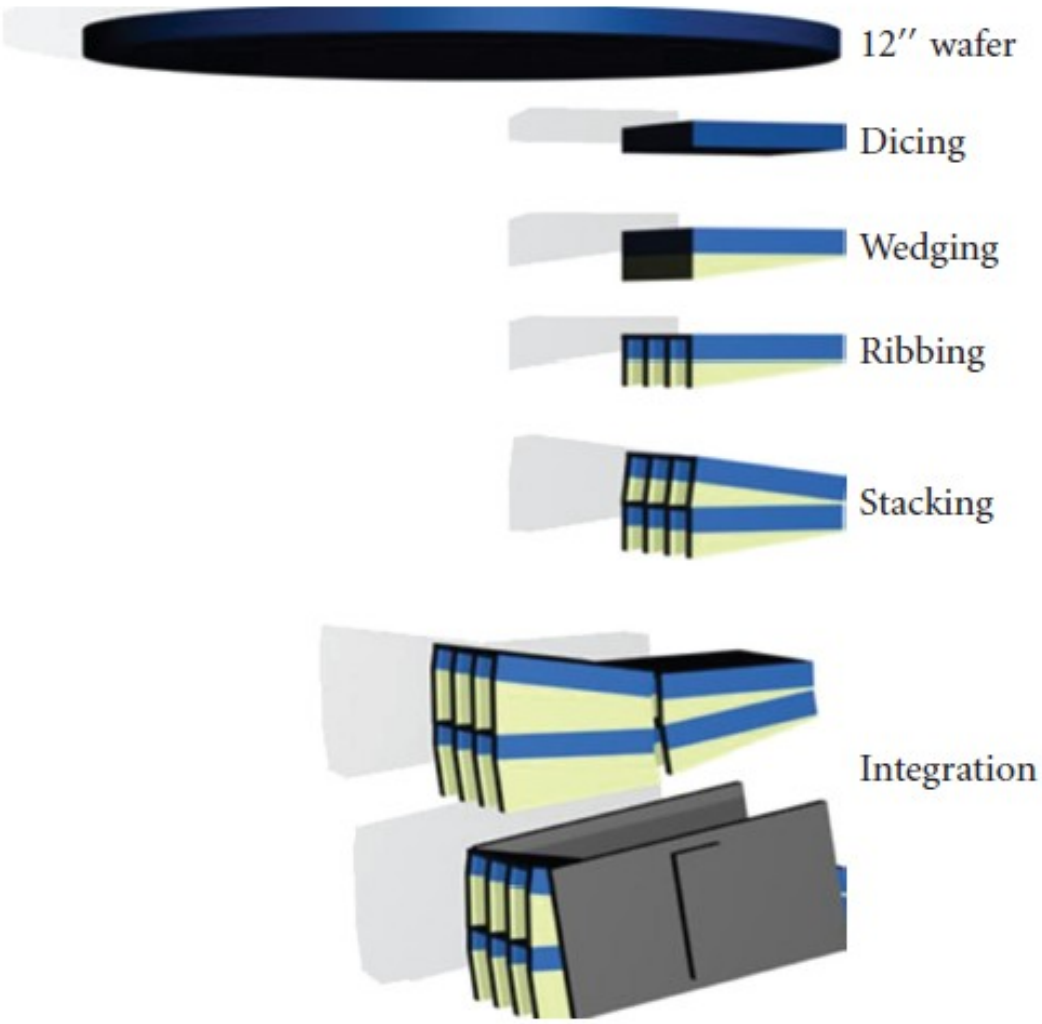

Figure 2-10. The production of SPO modules starts with commercial silicon wafers and utilises, as far as possible, existing methods and processes (Bavdaz, 2010).

The mounting concepts of the x-ray optics technologies used by the missions flown to date share one common aspect. The optical mirror elements, be it closed shells or shell segments, are attached to the support structure on individual points. In most cases, a spider structure is used, to which the optical mirror element is attached at the intersection points. The Silicon Pore Optics relies on a different mounting concept. The x-ray mirror elements are mounted along densely spaced lines, via ribs, which attach to the back of the mirror element. The mirror element becomes much stiffer, and its figure much less distorted by the mounting elements (Bavdaz, 2010).

The pore structure is obtained when mirror elements are stacked, attached to each other front-to-back. Due to their dense packing, the required thickness of these walls is very small and the overall loss in geometric area is, therefore, comparable with that of the classical spider obscuration. In the SPO technology, the mounting ribs are made of the same material as the mirror elements. Actually, the mirror element and the ribs are manufactured from a single piece of silicon crystal. Therefore, the thermal expansion coefficient (CTE) of the mirror elements and ribs is identical.

Silicon Pore Optics, under development in Europe, forms the ESA baseline technology for the International X-ray Observatory (IXO) candidate mission studied jointly by ESA, NASA, and JAXA.

Currently, conical approximations to the Wolter 1 geometry are the baseline for the technology development, since metrology and the associated data analysis is somewhat simplified. In the case of IXO, the conical approximation contributes about 3 arcsec to the HEW budget. Once the angular resolution performance of the SPO modules produced will approach closely the IXO requirements, the technology developments will start to use true Wolter geometries.

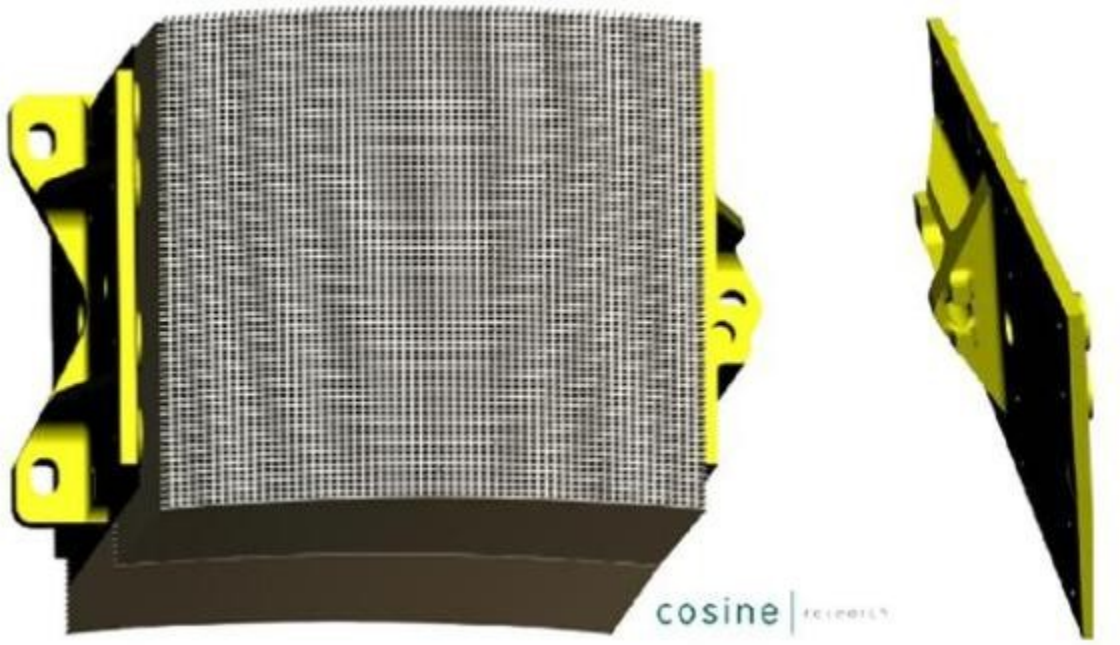

Figure 2-11. A mirror module, consisting of two mirror stacks, coaligned to form a Wolter-I optics, is fixed by two brackets (Cosine Research B.V. credits).

3 Overview of the Soft and Hard next future X-ray Missions

3.1 The NHXM Observatory Science and Payload

The New Hard X-ray Mission (NHXM) is a proposed mission being developed in Italy as an evolution of the original HEXIT-SAT project and it is now the hard x-ray project of reference for the Italian high energy community (Tagliaferri, 2011). The hard-x-ray regime (above 10 keV) remains ripe for exploration at the high sensitivities and fine angular scales afforded by newly-developed hard-x-ray optics. Also ripe for exploration is the field of x-ray polarimetry, a fundamental tool, so far virtually unused, to understand the physics and morphology of x-ray sources, where non-thermal and/or spherical emission is common. NHXM is meant to provide a real breakthrough on a number of hot astrophysical issues, by exploiting the most advanced technology in broad-band (0.2 – 80 keV) high angular resolution (<20 arcsec HEW) grazing incidence mirrors and spectroscopic detectors, together with the use of a high efficiency imaging polarimeter. Such issues can be summarized in two main headings:

- making the census of the population of black holes in the Universe and probing the physics of accretion in the most diverse conditions;
- investigating the particle acceleration mechanisms at work in different contexts, and the effects of radiative transfer in highly magnetized plasmas and strong gravitational fields.

These topics were identified as top priority in the study commissioned by the Italian Space Agency (ASI) in 2004 to the Italian scientific community with contracts involving Thales-Alenia Space Italy (TAS-I, Turin), the Media Lario Technologies (MLT, Lecco) company and the INAF institution. NHXM benefits from the phase A study of the canceled French-Italian-German SIMBOL-X mission (2007-2008) and has been recently subjected to a scientific phase

B study financed by ASI. Media Lario Technologies company (www.media-lario.com) received a contract from ASI in 2009 for a Technology Development Program (ASI-TDP) aiming at improving the technology readiness level with also in-house adoption of hardware for the metrology/manufacturing of the multilayer x-ray optics.

The relevance of the scientific topics has already prompted the approval of three missions, aimed at their investigation. However, because of intrinsic (design) limits, several major goals lie beyond their capability. They are: NuSTAR (USA, due for launch in 2012), with prominent lacking in the soft band (5-80 keV) and angular resolution (about 60" HEW at 30 keV); ASTRO-H (Japan, 2014), with a much worse angular resolution (about 90" at 30 keV) and separated telescopes to cover the soft and hard X-ray energy band; GEMS (USA, 2014), a non-imaging polarimeter mission which must be rotated to average systematic effects (for a constant source).

The NHXM payload subsystems have already been, or are currently being, studied as part of previous national efforts. Therefore, although the payload elements proposed are at the forefront of technology, their readiness permits a launch date of 2020 without compromising performance. The payload includes:

- 4 MM (Mirror Module) with good imaging capability in the band 0.3-80(120) keV;
- 3 MM are coupled with 3 SIC (Spectral-Imaging Camera);
- 1 MM is coupled with the PIC (Polarimetric Imaging Camera);
- 1 WFXRM (Wide Field X-Ray Monitor) sensitive in the 2-50 keV band to find active and transient sources.

The selection of an equatorial LEO (Low Equatorial Orbit) together with a careful design of an active and passive shielding allows us to reach the very low and stable background required for a successful mission. The satellite will also have the capability to repoint, on a 1 hour timescale, to a target detected by WFXRM in an interesting state which satisfies predefined figures of merit. The goals of the mission will be reached in a three-year lifetime, although this can be naturally ex-tended.

The payload subsystems are part of NHXM study contracts either financed by ASI in Italy, or as part of activities in other countries. Therefore a well defined plan is in place allowing to reach a TRL $\geq$ 5 (ESA standard) for all payload subsystems by the end of the assessment phase. The NHXM scientific goals set the technical requirements listed in Table 3-1.

Table 3-1. NHXM scientific requirements

Parameter	Value
Energy band:	0.3 – 80(120 goal) keV
FOV (at 30 keV)	≥ 12 arcmin
On-axis sensitivity	≤ 10^{-14}c.g.s.(~0.5 μCrab), 10-40 keV, 3σ, 1Ms, Γ=1.6 power law spectrum
On-axis effective area:	≥ 300 cm^2 at 0.5 keV
	≥ 1000 cm^2 at 2-8 keV
	≥ 350 (500) cm^2 at 30 keV
	≥ 100 cm^2 at 70 keV
	≥20 cm^2 at 100 keV (goal)
LED background	< 1×10^{-3} cts s^{-1} cm^{-2} keV^{-1}
HED background	< 2×10^{-4} cts s^{-1} cm^{-2} keV^{-1}
Angular resolution (HEW)	≤ 15”(10” goal) E<10 keV ≤ 20”(15” goal) E<30 keV ≤ 40” at E=60 keV (goal)
E/ΔE	40-50 at 6 keV 60 at 60 keV
Polarisation sensitivity	9.7% MDP in 100 ks for 1 mCrab (2-10 keV) & 1.8 mCrab (6-35 keV)
Wide Field X-Ray Monitor Sensitivity	2 mCrab in 50 ks at 5 σ (2-50 keV); triggering on a 0.5 Crab source in 1 s, providing the position in < 1 min, FOV= 2.9 sr partially coded, 0.5 sr fully coded
Absolute pointing reconstruction	3” (radius 90%)
Mission duration	3 years + provision for at least 2 years extension

Virtually every class of astrophysical object, from ultra-compact BHs (Black Holes) and NSs (Neutron Stars), through normal stars, and star formation regions to diffuse hot plasma pervading galaxies and clusters of galaxies has been found to emit x-rays. Even planets and comets are known to be x-ray sources. Thanks to these advances we know the three primary physical processes behind the emission of energetic radiation: **accretion physics, particle acceleration mechanisms, astrophysical shock.** Thermal and non-thermal components can be cleanly separated above 10 keV, but unfortunately more than four orders of magnitude separate the sensitivity in hard x-rays achieved by BeppoSAX, Suzaku, INTEGRAL and Swift from that achieved by x-ray telescopes below 10 keV. In addition, x-rays are usually emitted in highly aspherical geometries so that high degrees of polarization are expected (in contrast to the optical band, dominated by stellar processes). Unfortunately, although x-ray polarimetry was born in the '70s, advancements have so far been marginal.

3.1.1 Black hole census, cosmic evolution and accretion physics

Accretion onto compact objects (stellar or SMBHs, neutron stars, white dwarfs) efficiently converts gravitational energy into radiation. This is the dominant process producing x-rays in the Universe. The cosmic history of accretion is encoded in the CXB (Cosmic X-ray Background), which peaks at ~30 keV (see Figure 3-1) and is mostly produced at z=1-2. We know that the CXB is probably produced at z~1, meaning that most AGN (Active Galactic Nuclei) power is emitted at rest frame energies ~60 keV or above. Below 10 keV the CXB is largely dominated by the active growth of unobscured SMBHs (Super Massive Black Holes). This, however, is a small fraction of the peak where only 1-2% is currently resolved into discrete sources. The origin of this hard emission, the sources responsible for its production, and the complex interplay between the AGN power and their host galaxies remain poorly understood. Resolving ≥70% of the CXB at its peak will uncover elusive AGNs heavily obscured by gas and dust. They can bridge the factor of two gap between the local SMBH density and that inferred at higher redshift. Follow-up studies of these objects will provide invaluable insight into the interplay between the SMBH growth and the evolution of their host galaxies. Polarimetry and broad-band x-ray spectroscopy will provide information on the nature of the AGN primary component and the hard reflection component from circum-nuclear matter. Accretion can occur at very different rates. At very low accretion rates the complex physics involved will be investigated through the broad-band spectroscopy of the SMBH at the

Galactic Centre, taking advantage of its flaring variability. Since this region is extremely crowded, excellent imaging capability is mandatory. A very special source is the Cloud SgrB2, with a typical reflection spectrum: polarimetry will determine if it is illuminated by the SMBH at the centre of our Galaxy, probing its past state of activity.

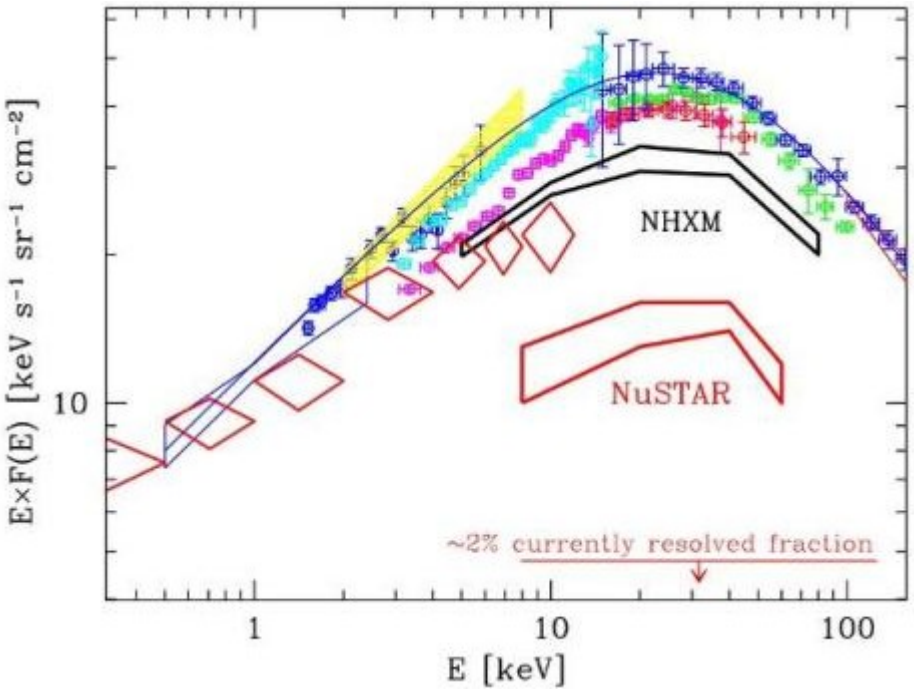

Figure 3-1. CXB spectrum measured by various experiments. Red diamonds: fraction of the CXB resolved into discrete sources by Chandra and XMM-Newton. NHXM will resolve ≥70% of the CXB where it peaks, finding these elusive sources up to z~2. The black region mark the CXB fraction resolved by NHXM in 1Ms (lower envelope) and 2Ms (upper envelope).

3.1.1.1 Black Holes census and cosmological evolution

The SMBH mass density extrapolated from available AGN luminosity functions, falls short by a factor ~2 with respect to the SMBH mass density measured from galaxies in the local Universe. This difference suggests the presence of a large population of hitherto unidentified heavily obscured AGNs - the so-called CT AGNs (objects with an obscuring screen of gas and dust suppressing the nuclear radiation by photoelectric absorption and Compton recoil even in X-rays). Indeed, many AGN synthesis models for the CXB predict a large volume density of CT AGNs; however, a more complex x-ray spectrum for AGN at z>1 can also produce the

observed CXB (Treister, 2009). To break the degeneracy we need direct identification of CT AGNs. In the local Universe a few tens CT AGNs have been discovered by BeppoSAX, INTEGRAL and Swift. At higher redshift the situation is even worse (Comastri, 2011). Candidate CT AGNs can be selected in infrared surveys because their UV and X-ray radiation intercepted by the circum-nuclear gas and dust is reradiated at infrared wavelengths, and indeed many candidate CT AGNs have been discovered by Spitzer up to z~2 (Fiore, 2009), and many more will be discovered by JWST and ALMA telescopes during the next decade at even higher redshift. However, X-ray observations provide by far the best estimate of obscuration by neutral gas, and directly measuring the primary accretion power.

Discovering highly obscured AGNs is important also because they may reveal a key phase in galaxy evolution corresponding with the onset of AGN feedback. AGN activity is thought to be triggered by channeling of matter toward the galaxy nucleus, where it can accrete onto a central SMBH. The same cold gas and dust can intercept the line of sight to the nucleus, and therefore a natural expectation is that the early, black hole growth phase is also highly obscured. Once a SMBH reaches masses $>10^{7-8}$ MSun, the AGN can efficiently heat the galaxy ISM through winds, shocks, and high-energy radiation, inhibiting further accretion and star-formation and making the galaxy colors redder. Unfortunately, our current understanding of the feedback processes is still rather primitive. One of the most promising strategies is to target objects where feedback is in action, i.e. young AGNs still in the process of blowing away their cocoon of dust and gas. Finding these elusive objects up to z=1-2, the golden age of AGN and galaxy activity, is a primary goal for NHXM. This will allow us to measure accurately and for the first time the cosmological evolution of highly obscured AGNs, thus assessing the role of AGN feedback in galaxy transformation and evolution. Herschel, ALMA, JWST will provide ancillary information on the obscured AGN host galaxies (mass, star-formation rate, stellar populations age) and/or map the AGN outflows and its impact on galaxy ISM (Inter Stellar Medium).

While NuSTAR will resolve ~20-30% of the 10-30 keV CXB (thus discovering heavy obscuration in a few tens AGNs in dedicated surveys), most of the NuSTAR CT AGNs will be at z<0.5, far from redshift range at z~1-2 corresponding to the peak of AGN and galaxy activity (Figure 3-1). Furthermore, because of the relatively modest quality of its optics (beam area 10 times wider than that of NHXM) NuSTAR will be strongly limited by confusion, and it will discover few, if any, sources not previously detected below 10 keV by Chandra and XMM. To discover a significant number of new sources we need to resolve a fraction of the CXB at E>10 keV higher than that currently resolved at 5-10 keV (~50%).

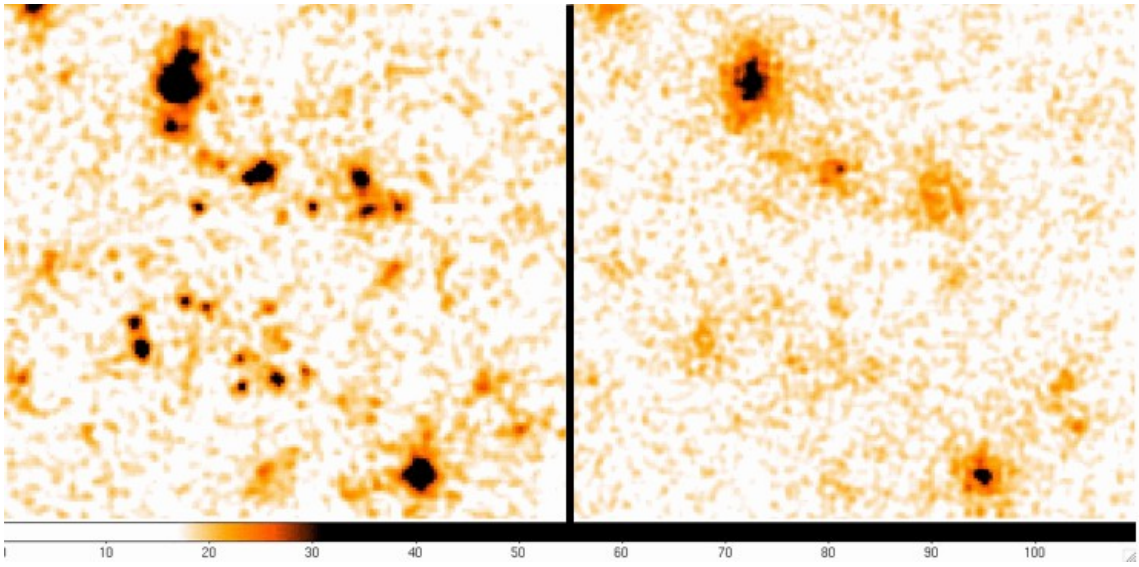

Figure 3-2. 2 Ms NHXM (left) and NuSTAR(right) 10-40 keV simulations of a ~10' region of the CDFS. A PSF with 15" HEW on axis has been assumed for NHXM and 45" HEW for NuSTAR. Two input source catalogs have been used: 1) sources detected by Chandra in the 2-10 keV band (Luo, 2008); 2) the candidate highly obscured AGN selected in the mid-infrared by Fiore et al. (Fiore, 2008).

Figure 3-2 shows a simulation of a 2 Ms NHXM observation of an area of CDFS (Chandra Deep Field-South) in the 10-40 keV band. NHXM can detect about 40 sources in this field down to a flux limit of 3×10^{-15} cgs (8-10 of these sources will be CT AGNs, 3-4 of which at z>1). NuSTAR can detect only 8-10 sources in the same field, with just 1 CT AGN. The NHXM limit corresponds to ~75% of the 10-40 keV CXB, comparable to that resolved in soft X-rays with the first Chandra observations (Mushotzky, 2000) (Giacconi, 2001).

3.1.1.2 Accretion physics: AGN

The broadband emission observed in AGNs depends on the complex interplay between a cold accretion disc and a hot corona of ionized plasma. Reflection and/or transmission from cold and warm matter located far from the nucleus further complicate the picture. Broadband x-ray spectroscopy and simultaneous polarimetry provide the most direct information on the nature of the primary component originating from the hot corona, and the hard reflection component coming from circum-nuclear matter (accretion disk and/or torus), this allows a comprehensive study of the disk/corona system.

It is widely believed that comptonization is the responsible for the AGN primary emission, but the origin and geometry of the putative hot corona are largely unknown. For bright sources NHXM will precisely measure the continuum up to 70-80 keV. This will allow the determination of the high-energy cut-off to within 10% (even if it is at 200 keV), in a 100 ks observation of a bright Seyfert 1 galaxy, and strongly constrain the corona temperature. If the seed photons arise from or near the accretion disc, the radiation field will be aspherical, thus ensuring a (geometry-dependent) large polarization degree (Haardt & Matt, 1993) (Schnittman & Krolik, 2010), well within NHXM capability at least for the brightest sources.

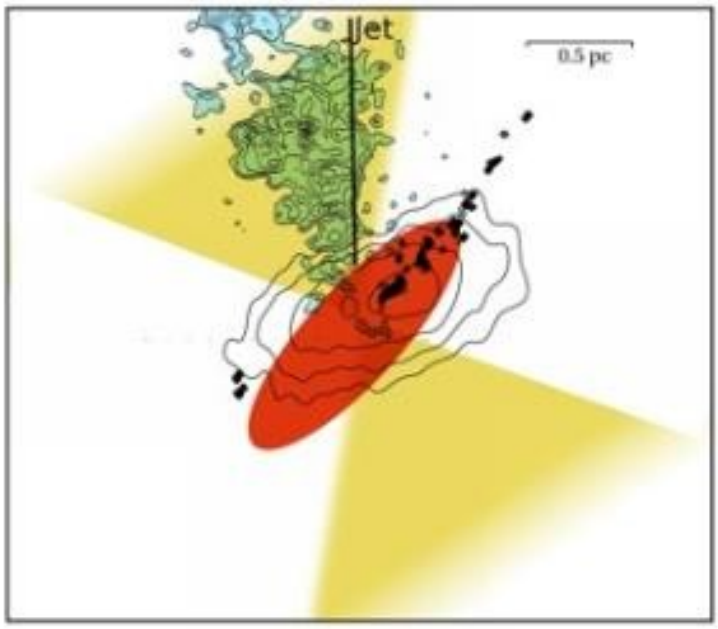

Figure 3-3. Composite picture of the inner region of NGC 1068, from Raban et al. (Raban, 2009). Red: compact dust component; black contours: 5GHz radio emission; yellow: ionization cones; blue: HST [OIII].

The reflection component is highly polarized. This property, when applied to the innermost accretion disk, can be exploited to measure the BH spin. When applied to the torus, it can be used to constrain the torus geometry and to compare its alignment with other spatial components, like the optical ionization cone. Indeed, the conical shape of the latter component is believed to be due to the collimating effect of the torus. Compton-thick AGNs, in which the x-ray emission is dominated by the reflection components, are the best sources for such measurements.

3.1.1.3 Accretion physics: X-Ray Binaries (XRBs)

Accretion physics can be studied in detail over shorter time scales in nearer and therefore brighter systems, namely Galactic XRBs. XRBs are systems in which a compact object accretes matter from a companion. The broadband spectroscopic and polarimetric capabilities of NHXM will shed light on the interplay between the accretion disc, the hot corona and the jet originating close to the compact object, similar to such effects in AGN, but on time scales allowing the monitoring of the modifications of these components. The WFXRM will allow to study in detail the evolution of transient sources and to catch systems in their extreme and rare states.

Many BH and NS binaries are transient, and undergo complex spectral changes on different time scales. In their soft state, the flux is dominated by thermal emission from the accretion disc, and a faint hard emission is often observed. Conversely, hard emission, extending well above 100 keV, dominates in the hard state, with a fainter thermal disk component below 1 keV. The nature of the hard x-ray emission in BH (and weakly magnetized NS) binaries is not clear, but appears to have an origin similar to that observed in AGNs. Most models interpret it as thermal, hybrid or non-thermal Comptonization, depending on the source state. However, according to some models jet contribution can be important and even account for the entire observed radiation. The broadband coverage of NHXM is crucial to characterize the full spectral distribution in all different states. The addition of simultaneous x-ray polarimetry is vital to disentangle the various emission components and to constrain the geometry of the system. For example, Schnittman and Krolik (Schnittman & Krolik, 2010) predict a polarization of several % for the hard-state spectrum with a 90 deg swing from parallel to perpendicular to the disk going from low to high energy. The detailed properties of this transition give information on the geometry of the scattering corona. NuSTAR will provide an incomplete picture, as it does not cover the low-energy part of the spectrum, crucial for a successful spectral decomposition. GEMS cannot resolve variations on the polarization on timescale shorter than tens of minutes, while these sources are highly variable on such timescales. NHXM will have both capabilities simultaneously.

The monitoring of the state transitions (quiescence → hard → soft and back, through different intermediate states) is crucial because it witnesses the evolution and interplay between the disc/corona system and the onset of relativistic jets (Fender, 2004). Only the general evolution is known thanks to INTEGRAL and RXTE (Joinet, 2008) (Motta, 2008). Detailed time-

resolved, broadband spectroscopy and polarimetry are crucial to study the evolution of thermal and non-thermal components. An efficient observing campaign on these objects requires their continuous monitoring, to re-point the narrow field instruments when they are found in the interesting states. The WFXRM onboard NHXM will serve this purpose.

3.1.2 Acceleration mechanism and non-thermal emission

Winds and jets from AGNs propagate for extremely long distances (Mpc scales) and can be responsible for significant energy injection into the interstellar matter in galaxies and intra-cluster gas. However, despite a wealth of observations on this feedback process, the physics behind the formation of jets and their emission mechanisms remain quite poorly understood. Similarly, cosmic rays are believed to be accelerated in shocks, both in supernova remnants and in the intra-cluster medium. However, the details of shock development and cosmic ray production remain a mystery. Sensitive broadband imaging, spectroscopy and polarimetry can provide breakthroughs in all these problems. One particular case is the Crab Nebula, a historical laboratory of high-energy astrophysics. This is the only x-ray source with known "global" polarization, of order 20%, due to synchrotron radiation. Combining imaging polarimetry and broad-band spectral mapping will allow us to map the magnetic field for the first time, providing long-awaited probe of the freshly accelerated electron population.

3.1.2.1 Blazar and microquasar jets

The process of jet formation following accretion from the disk should be revealed in the study of erratic flaring in the light curve of micro-quasars. These ejection phenomena can be directly associated with the status of the system before and after the flare. Broadband spectroscopy and polarimetry of the spikes would confirm the nature of relativistic blobs at the very moment of their injection into the jet. In radio-loud AGNs, timescales are much longer, but broadband spectroscopy and polarimetry can very efficiently separate jet emission, which is most likely due to synchrotron/inverse Compton processes, from accretion disk emission (including its x-ray corona and reflection). Blazars show two emission peaks, associated with synchrotron and IC processes. If due to synchrotron, x-rays must be highly polarized. The combination of x-ray and optical-infrared polarimetry can then assess whether the same electron population gives rise to the emission in both bands, i.e. we can directly probe the jet structure. Time resolved

broadband spectroscopy during flares observed in both optical-infrared and x-rays can also be used to constrain the electron populations and the jet structure. If x-rays are due to IC, the degree of polarization depends on the nature of seed photons, synchrotron photons or disk. In the first case the polarization angle of the synchrotron and IC emission should be the same. Multi-band polarimetry can therefore solve the long-standing issue of the nature of the jet seed photons. The elusive bulk Compton emission of cold jet electrons can be detected through the presence of a small excess of emission around 10 keV, which should be very highly polarized. If detected, this tells us the value of the bulk Lorentz factor and leptonic content of the jet.

Strong (with respect to the optical) and hard x-ray emission, a signature of a beamed jet, can be used to identify blazars and to measure the jet power. In the most powerful blazars the optical emission comes from accretion, and for these we can measure the BH mass and the accretion rate and thus compare jet and accretion powers. Since powerful blazars are the most luminous hard x-ray sources above 20-50 keV, we can find them at large redshift, providing a census in jetted systems, of large BH above z~4. Finding high mass BHs in even a few blazars (aligned) implies the existence of many more BH (in misaligned, thus faint, objects) with the same mass.

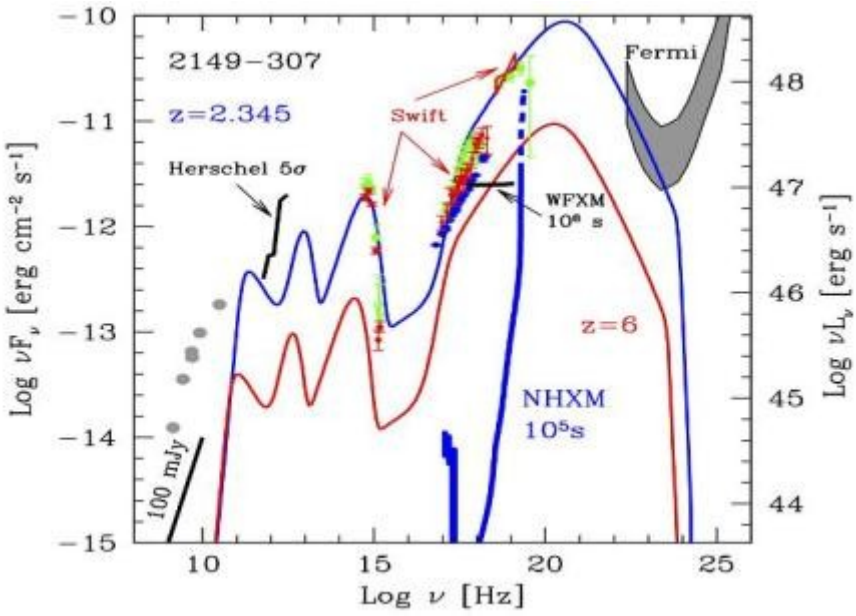

Figure 3-4. SED of 2149-307, a powerful FSRQs detected in the hard x-ray band. In these sources NHXM can observe the rising part of the high-energy bump, where most of the power is released, providing accurate spectral and polarimetric variability information on timescales of few thousand sec. The red curve is the model reproducing the same SED at z=6, still well within the NHXM capability.

The WFXRM can easily detect x-ray flares in low power BL Lacs (among the brightest x-ray extragalactic sources) and in some powerful and more distant flat spectrum radio quasars, providing a trigger for the re-pointing of NHXM for a spectroscopic and polarimetric follow up. It can also serendipitously find new hard x-ray BL Lacs, that are the best candidate TeV emitters. Since Blazar spectra extend over >10 decades, synergies are crucial with radio, infrared, γ-ray and TeV observatories.

3.1.2.2 Acceleration mechanisms in clusters of galaxies

AGN jets and outflows can strongly affect the intra-cluster medium of clusters of galaxies, there releasing energy in the form of accelerated particles and shock waves. Furthermore, shocks with typical Mach numbers 2-4 are produced during the assembly of clusters of galaxies through merging of subunits, when a large quantity of energy is redistributed between the main intra-cluster medium components: hot baryons, relativistic particles and magnetic fields. While the former component is currently rather well known, only limited information is available on the latter components. Diffuse radio emission is observed in many clusters, both at the centre (haloes) or periphery (relicts). It is interpreted as synchrotron emission from relativistic e^- in μG magnetic fields. Recent radio observations suggest that diffusive shock acceleration operates on clusters of galaxies similarly to SNRs (Supernovae Remnants), and are capable to produce energetic cosmic rays (Van Warren, 2010). IC scattering of the CMB on the same relativistic e^- can produce non-thermal x-rays. The study of both shocks and non-thermal components can shed new light on the formation and evolution of clusters of galaxies.

The non-thermal component is outshined by the thermal continuum below ~10 keV, while it can be recovered in the 20-40 keV band. NHXM can detect non-thermal emission down to a flux limit of ~10-12 cgs in this source, a factor of 3-10 lower than possible with NuSTAR and Astro-H. NHXM has significant advantages over previous missions: 1) unlike Chandra and XMM-Newton it is in a low Earth orbit and features active shielding significantly enhancing the ratio of cluster surface brightness emission to instrumental background; 2) the NHXM band-pass extends from below 1 keV to 80 keV, with obvious advantages when attempting to measure high temperatures. NuSTAR will have a similar internal back-ground but a much more limited band pass. Most important, its image quality will not allow the identification and the study of shocks other than in the nearest and largest structures, nor it will allow the exclusion of contaminant sources such as hard AGNs. Both shocks characterization and searches for non-

thermal emission will exploit synergies with radio LOFAR and SKA observations.

3.1.2.3 Acceleration mechanisms in Supernovae Remnants

The process of particle acceleration can be conveniently studied in much more detail in nearer and brighter systems such as SNRs. The synchrotron radiation from relativistic e^- is a diagnostic tool for the mechanism of diffusive acceleration in SNR shocks, believed to be the source of the cosmic rays up 10^{15} eV. Whereas thermal emission is usually confined to soft x-rays, synchrotron (as well as non-thermal bremsstrahlung) emission is best studied at higher energies, using high-quality spatially resolved broadband spectroscopy and polarimetry, all features that make NHXM suitable for this kind of study. Measuring the cut-off frequency provides the maximum energy of electrons (if the magnetic field is known); while the azimuthal variation of this maximum energy along the SNR shock and of the polarization will provide its dependence on the ambient magnetic field orientation. In addition, a comparison of hard x-ray and TeV images can provide information on ion acceleration. Depending on their relative morphologies and fluxes, TeV emission can be dominated by either IC (Inverse Compton) radiation from the same electrons emitting synchrotron x–rays, or by hadronic emission through π+ decay.

So far, only a few young shell-type SNRs have been observed above 10 keV, and only by non-imaging instruments or coded mask detectors. In a few SNRs (G347.3-0.5, Vela Jr, G1.9+0.3) the synchrotron emission dominates the entire x-ray spectrum. In many other sources synchrotron emission coexists with thermal emission. In both cases hard X-ray high angular resolution spectropolarimetry is the most direct way to disentangle the thermal and non-thermal emission.

In brightest remnants like CAS-A, which fit within the FOV of MEP (Medium Energy Polarimeter), we can identify the regions of hard x-ray emission and measure polarizations of the order of a few % on ~10 angular bins. SN 1006 is the archetype non-thermal shell-type SNR. NHXM could detect radiation up to ~30 keV in its brighter x-ray limbs, allowing measurements of both the synchrotron spectral index and the cut-off frequency using x-ray data alone: comparison with the radio spectral index then allows a search for deviations from the power-law spectrum, testing the shock modification level. The unique polarimetric capabilities of NHXM can effectively constrain the average magnetic field direction where particles are accelerated. Radio polarization maps of SN 1006, which already provide information on the field orientation, show peaks up to 30%; in x-rays one may expect to find similar values.

3.1.2.4 Gamma Ray bursts

While the Lorenz factor in Blazar jets can reach a value of several tens, it can reach a value of thousands in Gamma Ray Burst (GRB) jets, making these objects the most powerful accelerators in the Universe. Despite the enormous progress occurred in the last 10 years, the GRB phenomenon is still far from being fully understood. Two issues can be tackled with NHXM:

1. The afterglow emission above 10 keV is almost completely unexplored. The only detection of hard X-ray emission from a GRB (the very bright GRB990123 with the BeppoSAX/PDS) challenged the standard scenario in which the dominant mechanism is synchrotron radiation produced in shocks of a ultra-relativistic fireball with the ISM.
2. Polarization measurements of afterglow emission may probe GRB jets. Theoretical models (Ghisellini & Lazzati, 1999) (Lazzati & Begelman, 2009) predict a change of the polarization angle by 90 degrees in correspondence of the jet break, where the relativistic beaming due to the high speed of the emitting region becomes larger than the actual beam of the jet.

The NHXM WFXRM will detect and localize ~30 GRB/year, 20% of which are expected at z>5. The GRB can be repointed to on <1 hr timescale, allowing both broadband spectroscopy and sensitive polarimetry.

3.1.3 Physics of matter under extreme conditions

Broadband x-ray spectroscopy and polarimetry can efficiently probe the behaviour of matter in extreme gravitational and magnetic fields. General relativistic effects on emission line profiles, on the continuum shape and on the polarization properties of the radiation emitted by the accretion disk can be used to estimate the BH spin, a key parameter in understanding black hole birth and growth. The line and continuum methods already provide precise (in statistical terms) results. These are, however, often in disagreement each other, indicating insufficient control of systematics. This is likely due to poor knowledge of the underlying continuum. This can be overcome only by broadband, high throughput observations. A third, independent method to measure the black hole spin also exists. This exploits the spin-dependent rotation with energy of the polarization angle of the disk emission. Polarimetry extended to the 10-35 keV band will allow the detailed study of the broad cyclotron resonance, in accreting high-

magnetic field x-ray pulsars where high polarizations are expected. Polarization measurements will test models for the transfer of radiation in these extreme conditions, and determine the field geometry.

Dark matter can be probed by looking at galaxies and clusters of galaxies where the annihilation/decay of three of the main candidates (neutralinos – the lightest particles of super-symmetric extension of the standard model for particles, axions and sterile neutrinos) can provide electromagnetic signatures in the X-ray band of NHXM. The two main chains of neutralino annihilation are: the γ-rays produced by the decay of p_0 and secondary $e^{\pm}$ produced by the decay of p^+. The former process produces a continuum spectrum at E>1GeV. The secondary $e^{\pm}$ produced in the latter process can make X-rays through bremsstrahlung, synchrotron and inverse Compton emission. Simulations shows that NHXM sensitivity limits are competitive with those of the Fermi-LAT, for a broader range of magnetic field intensities.

3.1.4 Mirror Module Assembly

The 4 identical NHXM Mirror Modules will be based on nested confocal electroformed Nickel-Cobalt alloy (NiCo) shells with Wolter I profile. The electroforming technology has already been successfully used for the Ni gold-coated x-ray mirrors of BeppoSAX, Jet-X/Swift and XMM-Newton satellites and it is now used for the mirrors of the eROSITA mission. For the NHXM mirrors, a few technological modifications will be applied from development programs over the past several years:

1. NiCo alloy, introduced a few years ago at NASA/MSFC, now can also be deposited in Italy at Media Lario Technologies (MLT), instead of pure Nickel. NiCo is characterized by better stiffness and superior yield properties. This permits a reduction in the thickness of the mirrors (2 times thinner than the XMM-Newton Ni shells);
2. nanostructured multilayer x-ray reflecting coatings, permitting a larger FOV and an operating range from 0.3 keV up to 80 keV and beyond. These will be sputtered on to the internal surface of the gold-coated NiCo mirror thin shells after replication from the mandrels. This process was previously developed at CfA and now also in Italy at MLT, under an ASI contract.

Several engineering models with Ni and NiCo integrated shells coated with W/Si and Pt/C multilayer films (up to 200 bilayers) have already been developed and tested at the PANTER-

MPE x-ray calibration facility demonstrating feasibility with a microroughness of < 0.4nm (Pareschi, 2009).

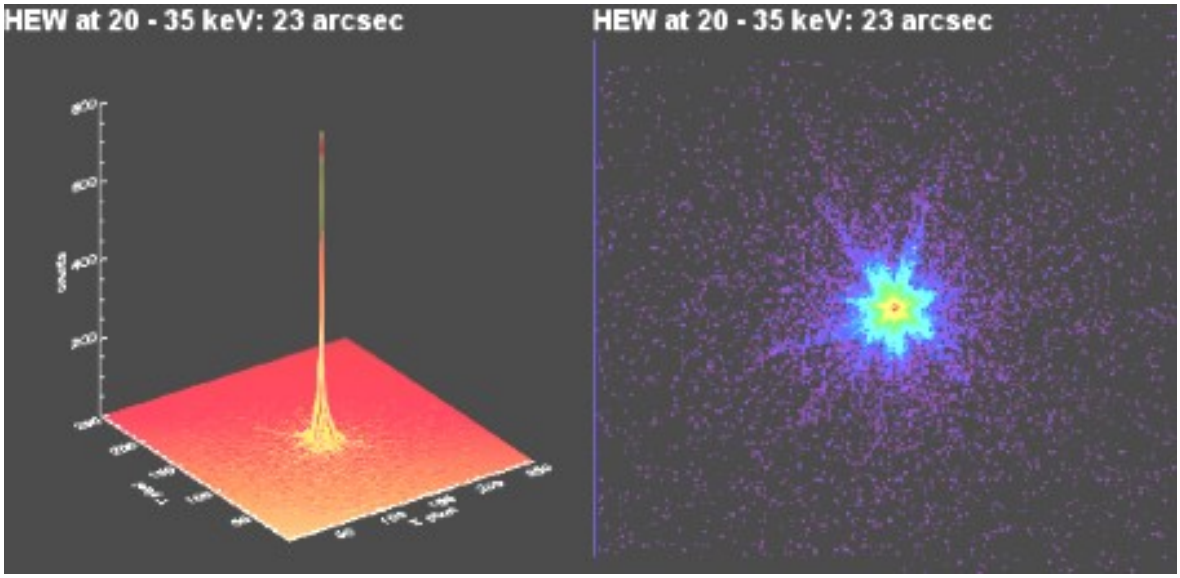

Figure 3-5. Image taken in the range 20-35 keV. The structure of the spider arms can be seen. The HEW is already very near to the requirements.

3.1.4.1 The opto-mechanical design of the Mirror Module

Each MM is equipped with 70 (in the baseline configuration) Wolter-I Mirror Shells (parabola + hyperbola) with a focal length of 10 m and interface diameters in the range ~390 to ~150 mm. This shell configuration can already be fabricated with the current technological set-up at Media Lario Technologies. The general layout of a mirror module envisages a "classical" configuration with an external case with variable thickness (1.5 mm to 4 mm), a height of 600 mm and a diameter ~425 mm. High performance stainless steel (i.e. SAF2507) is used to match the CTE of the NiCo shells. Front, rear and side flanges are envisaged to bolt the case to the spiders and the mounting spacer respectively (Basso, 2010). This configuration has been extensively studied via FEM analysis by the same BCV engineering company that studied the MM of BeppoSAX, Jet-X, XMM-Newton and Swift.

The mirror shells are glued at each end to spoke wheels called "spiders" (as for BeppoSAX and JET-X/Swift), each one equipped with 18 spokes and an additional ring located nearly at spoke mid span.

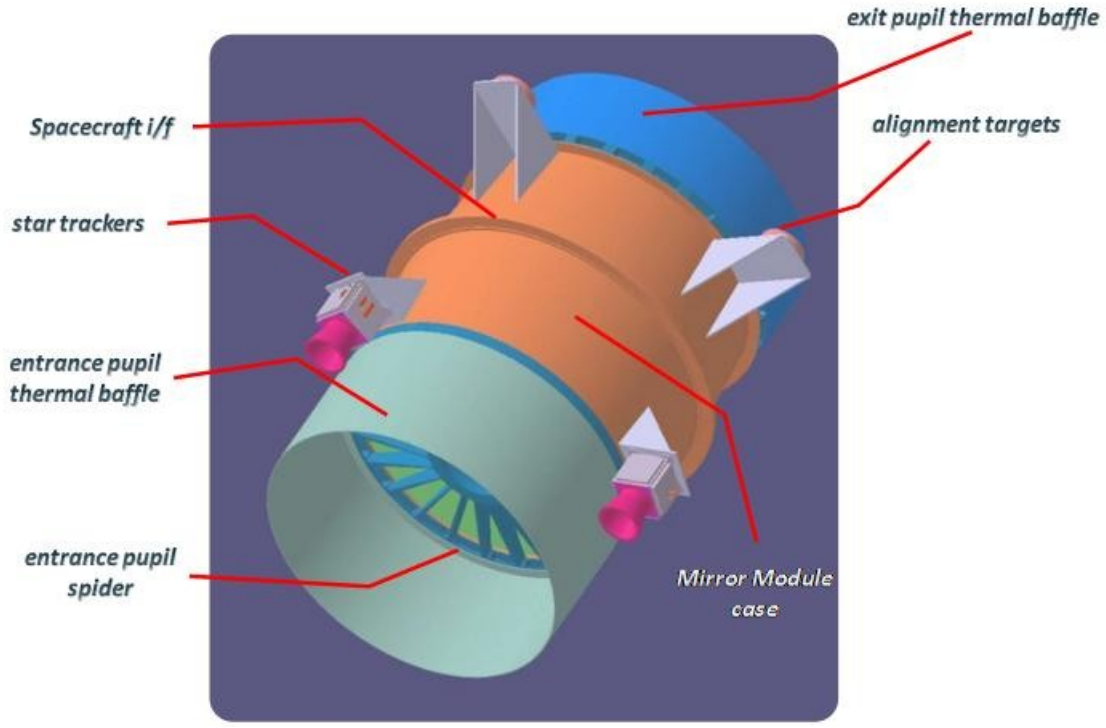

Figure 3-6. MM configuration considered for the FEM thermal and mechanical analysis

3.1.4.2 The auxiliary items

Various auxiliary devices will be installed on the MM: a magnetic diverter to prevent background electrons reaching the detector, a thermal baffle and a thermal blanket to maintain the mirror temperature, and an x-ray precollimator to keep the background low (this is optional and not foreseen in the baseline configuration).

3.1.4.3 The effective area

The effective area for three mirror modules is shown in Figure 3-7 for the baseline and for the goal configuration achieved by filling the internal hole of each MM with an additional 20 mirror shells (to a minimum shell diameter of 110 mm). These shells can be manufactured via direct replication of multilayers (e.g. Pt/C/Ni) from TiN-coated superpolished mandrels (a technology developed at CfA in collaboration with NASA/MSFC and DTU). These shells would add 5 kg to each MM. It should be noted that the baseline presents a very good effective area in the 0.3-10 keV region (>1600 cm2) and > 350 cm2 at 30 keV. The FOV is >12 arcmin

(50% vignetting) up to 50 keV. In the goal configuration the mirror sensitivity is extended up to 120 keV.

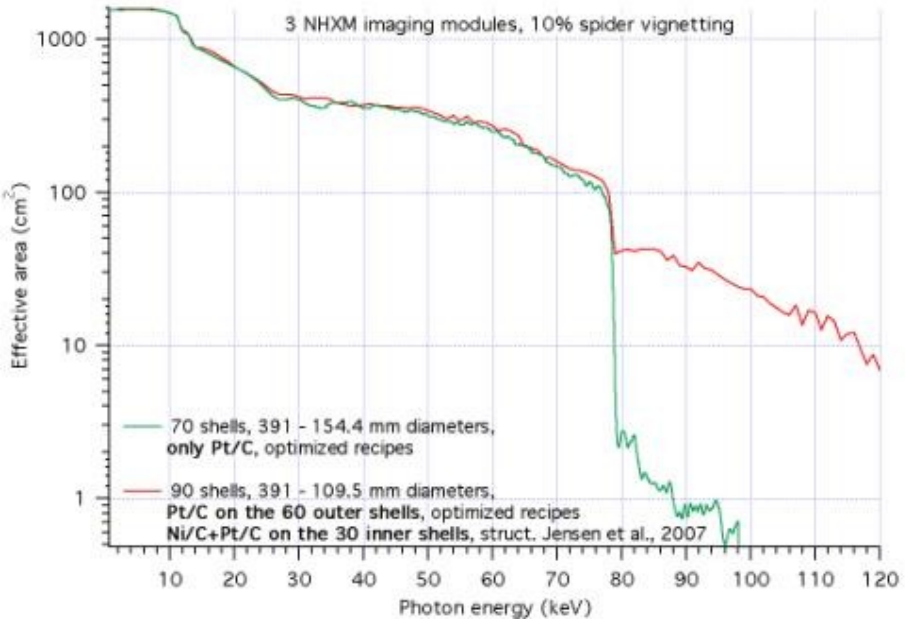

Figure 3-7. Effective Area (3 MM): baseline (green), goal (red)

Table 3-2. Main parameters of one NHXM MM (in parenthesis are the values of the goal configuration)

Geometrical profile	Wolter I
Focal length	10 m
Mirror length	60 cm
Max/min shell diam.	40/15(10) cm
# of spiders	2
# of spokes per spider	18
Spiders & case material	SAF2507 stainless steel
# of shells per module	70 (90)
Wall material	electroformed NiCo
Wall thickness	0.35-0.15 mm
Coating	Pt/C multilayer

The total mass for the 4 MMs will be ~ 530 kg, for the worse case (90 shells with precollimator).

Table 3-3. Dry mass budget for a single MM

ITEM	**Mass [kg]**	**Source**
Spiders	13.43	prototype
Case	14.89	prototype
Mirror shells	73.03 (78)	prototype
X-ray pre-collimator	10.00	XMM
Magnetic diverter	5.00	Swift
Baffle/thermal cover	5.00	Swift
Adapter	4.03	estimate
Bolts & rivets	2.00	estimate
TOTAL	127.38 (132.38)	

3.1.5 Focal Plane Cameras Assembly

X-rays focused by the mirror enter the camera via an extended graded baffle tube, which protrudes 900 mm from the focal plane. The baffle is mechanically supported by a conical structure, mounted on the camera at the instrument platform interface plane. A door aperture sits in front of a filter wheel, which is mounted directly in front of the LED (Low Energy Detector). The door is normally closed for ground testing. The main camera body can be evacuated to facilitate bench testing and to protect delicate filters from acoustic excitation during launch. The door is opened on orbit by venting a bellows via a HOP (High Output Paraffin) actuated valve. A stepper-motor controlled, four-aperture filter wheel is mounted directly in front of the LED and is mechanically supported by the door chamber assembly. The filter wheel will provide an open and a closed position, one position with a medium filter and one with a calibration source.

The LED and HED (High Energy Detector) detectors are hosted inside two very compact detector modules that will also provide an active and passive shielding to minimize the shielding

mass by being in close proximity to the detectors Figure 3-9. The two modules will come together only at the end, allowing for independent development.

The LED detector requires active cooling in order to achieve the -80 (goal is -60) ºC operating temperature and this is achieved by use of a Peltier cooler. Heat from the hot side of the cooler is conducted to the camera coldfinger interface on the rear of the camera via thermal links that are routed around the HED. Based on experience of similar cooling requirements and interface temperatures, a two-stage Peltier cooler is envisaged, with a power requirement of approximately 10 W.

The HED thermal interface will be made at the hot side of the TEC by attaching to the thermal links, or directly to the LED module. For a nominal cold finger temperature of -40 ºC, the HED operation temperature of -20 ºC will be easily achieved. A small amount of heater power (~1 W) may be required to provide temperature stability of the HED. Both the LED and HED are suspended from the main structure by thermally isolating mounts.

3.1.5.1 The Low Energy Detector (LED)

LED shall satisfy the requirements listed in Table 3-4. Based on them and given the requirement to reach TRL ≥ 5 at the final selection, an e2v technologies, back illuminated, NIMO, CCD-230/231 with 30μm pixels (2048×2048 format) has been selected. An aluminum coating can be applied to the device in order to filter out background light.

Table 3-4. LED specifications.

PARAMETER	**VALUE**
Energy Range	0.3-10 keV
Focal Plane Size	40×40 mm^2
Pixel size	100 - 200 μm
Energy resolution	120-150 eV at 6 keV
Background	$< 1\times10^{-3}$ cts s^{-1}cm^{-2} keV^{-1}

This detector is already available as Commercial Off-The-Shelf (COTS) with a depletion layer of 70μm, with an ongoing program to get deeper depletion (80-120μm, with a goal of 150μm). The baseline is a 120μm (goal 150μm) depletion layer device, with the following key

characteristics:

- Back illuminated CCD – with high low- energy QE
- 10 full frames per second acquisition rate
- Frame-transfer, image area 6cm × 6cm
- Non-inverted mode operation (operating temperature ~-80°C)
- Readout noise of 3 electrons (rms)
- A store region to avoid image/spectral degradation during readout
- Multiple output nodes (high speed readout)
- 2-4× on-chip column/row binning
- QE 98% at 6 keV and 59% at 10 keV

The low-energy detector can be thinned to ~150μm to ensure adequate transmission for energies above 10 keV. Windowing mode operation will enable high-speed readout, ~50-100 s^{-1}, avoiding pileup for bright sources (with a pixel size of 100μm we can observe a 100 mCrab source with less than 5% pileup).

Each detector module will comprise; a CCD detector, a TEC-based thermal cooling system (the nominal operating temperature is -80 °C) and a store shield. Two low mass flexis with 37-way micro-D connectors will be incorporated in the detector package to carry the drive and power signals from the CCD to the proximity readout electronics. The CCD connections can be wire bonded directly to the flex. The CCD carrier will be bonded to a TEC (Thermal Electric Cooler) using an adhesive with high thermal conductivity and (the warm side of) the TEC will be bonded to a thermal heat sink plate. A BEE (Back Ends Electronics) based on an AD-converter and FPGA circuit will complete the LED assembly.

During the assessment phase the use of a fully-depleted CCD (150μm) with a column parallel readout mode will be evaluated. Moreover the possibility to use a Macropixel detector based on an active pixel sensors concept will be explored. More specifically DEPFETs (DEpleted P-channel Field Effect Transistor) have been already extensively studied and characterized by the participating German institutions in the context of Simbol-X and IXO.

3.1.5.2 The High Energy Detectors (HED)

The HED will be mounted below the LED and will perform spectral imaging of hard x-ray photons in the 7-120 keV energy band.

Table 3-5. LED specifications.

PARAMETER	VALUE
Energy Range	7-120 keV
Focal Plane Size	40×40 mm^2
Pixel size	200 - 350 μm
QE	>95 %
Energy resolution	1 keV at 60 keV
Absolute timing accuracy	50 μs (10 as a goal)
Background	< 2×10^{-4} cts $s^{-1}cm^{-2\,22}keV^{-1}$
Temp range	-40 to -20 º C

The HED baseline is a 1-2 mm thick pixellated CdTe detector read out by a bump-bonded ASIC chip. The CdTe sensor is a Schottky type diode with Al contacts on the junction side. This type of configuration collects electrons at the pixels, and holes at the uniform ohmic contact on the opposite side. It can be operated at 1-2 kV bias voltage with very low leakage current (<1pA/mm^2) and the required energy resolution, if the temperature is maintained in the -20°C to -40°C range. A first CdTe+ASIC hybrid module has already been realized at the INFN-Pisa laboratories (Bellazzini, 2010). Schottky CdTe crystals with the smallest available pitch (80μm) have been produced, according to our design and requirements (118604 hexagonal pixels over an area of 25×28 mm^2), by ACRORAD. The hybrid module has been obtained by bump bonding the Aluminum pads of the crystal to the pixels of a dedicated large-area ASIC (25×28 mm^2) developed at the Pisa laboratory. The bump-bond processing has been made by AJAT, a Finnish Microelectronics Company, successfully proving the proposed technology (99% good connections). The next step is to develop a new dedicated ASIC bump-bonded to a CdTe crystal with the characteristics required by NHXM.

The baseline ASIC is being developed by INFN-Pisa, with an architecture which descends from the XPOL ASIC. The HED-ASIC will work in auto-triggering mode, transferring the amplitude (energy) information of a limited number of pixels around the triggering channel (dead time <10 μs). The active area will be arranged as a 2×2 matrix of four CdTe-ASIC hybrids, each

20×20mm^2 wide. The 4 hybrids are mounted on a ceramic PCB (Printed Circuit Board) that hosts only passive filters. The flat cables communicate with the FPGA-based BEE that sit outside the cold region. The detector is very compact, robust and light, with only 6 W of power consumption. The copper flange below the PCB permits thermal regulation by passive cooling for the operating temperature below -20 °C.

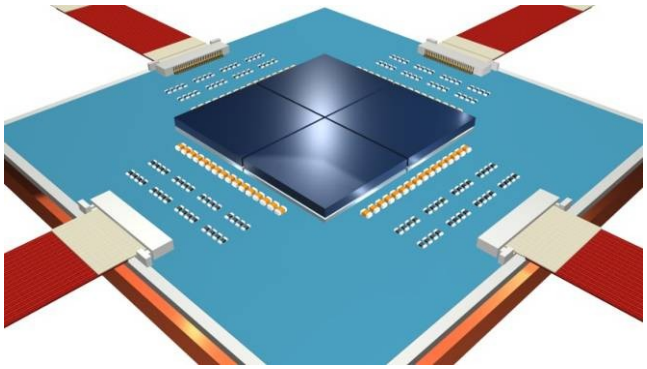

Figure 3-8. HED sensor. The 4 crystals (2×2cm^2 area each) are mounted side by side with very limited separation (~0.2mm). The copper flange below the PCB is the thermo-mechanical interface of the HED.

The mechanical structure of the HED is a square box containing the outer chassis, a thermal insulator supporting the inner electronics and the electronics board supporting the Detector-ASIC-hybrid. The HED will be equipped with a set of floating DC converters, including programmable high voltage for detector biasing.

3.1.5.3 Shielding system

Passive and active shielding surrounds the detection units except for the solid angle corresponding to the optics focused beam. Scintillating fibers with an active layer of inorganic scintillator constitute the anti-coincidence system. The function of the passive shield is to absorb most of the photons and low energetic particles while the role of the active shielding is to reject the pass-through of charged particles and hard-x-/soft-γ-ray photons. For the passive shielding, a graded configuration (used also for the camera baffles) composed of ≤ 3 mm of Tantalum, 2.2 mm of Tin, 0.48 mm of Copper, 0.27 mm of Aluminum (and 0.1 mm of Carbon for those parts directly facing the Low Energy Detector), is coupled with a 2 cm inorganic scintillator (BGO or CsI) and an array of plastic scintillating fibers of 1 mm of diameter

(multilayer ribbons) as shown schematically in Figure 3-10.

The active layer of inorganic scintillator, in anti-coincidence with the HED, detects background hard x-ray photons and provides a better background rejection than the inorganic anticoincidence and pulse height, particularly above 10 keV. The ribbon fibers, made of a polystyrene and read by multianode photomultipliers, represent the anticoincidence for charged particles, characterized by a position sensitive capability with a Minimum Ionizing Particle detectable energy threshold as low as 200 keV. Preliminary simulations show that the background requirements can be meet with our configuration.

Dedicated front-end and readout electronics for both the inorganic scintillator and the scintillating fibers are foreseen. A power consumption of 3 W is required for the fully operational anticoincidence system.

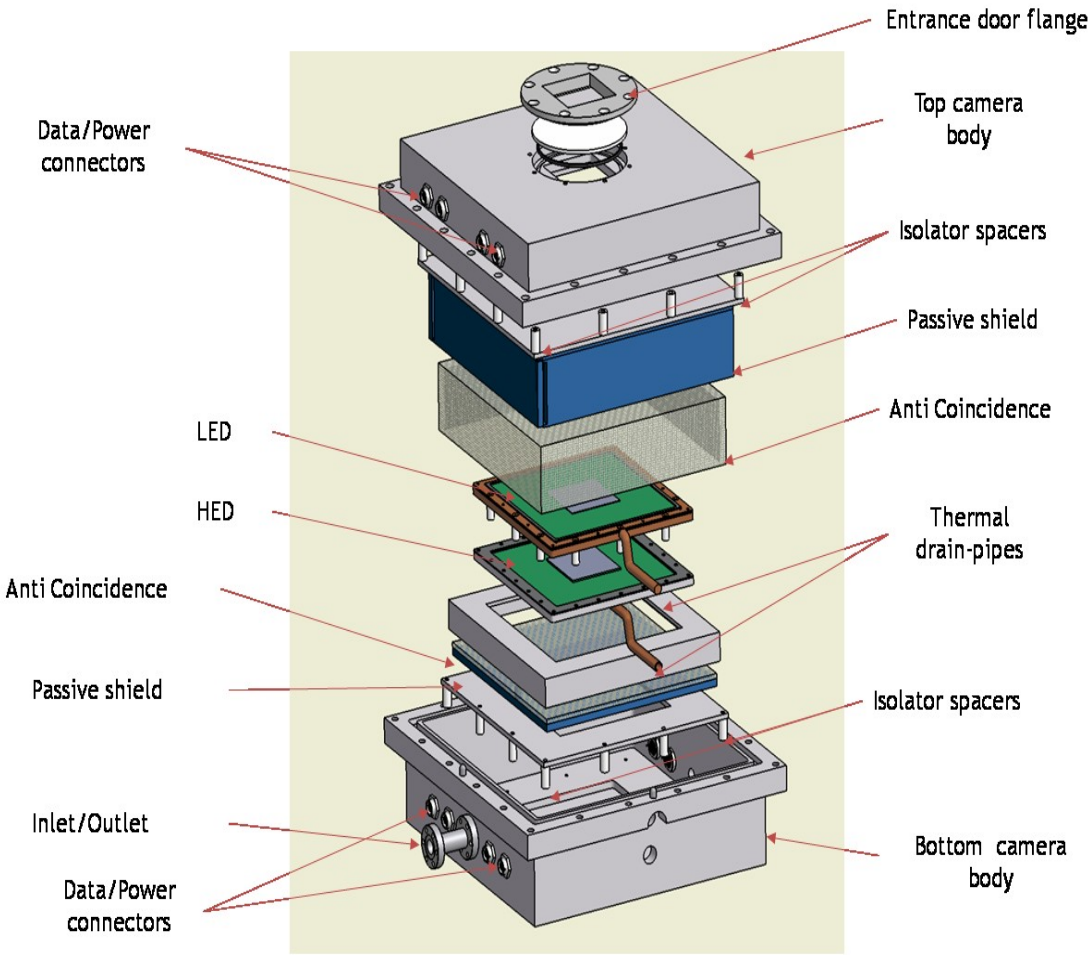

Figure 3-9. LED and HED modules exploded view.

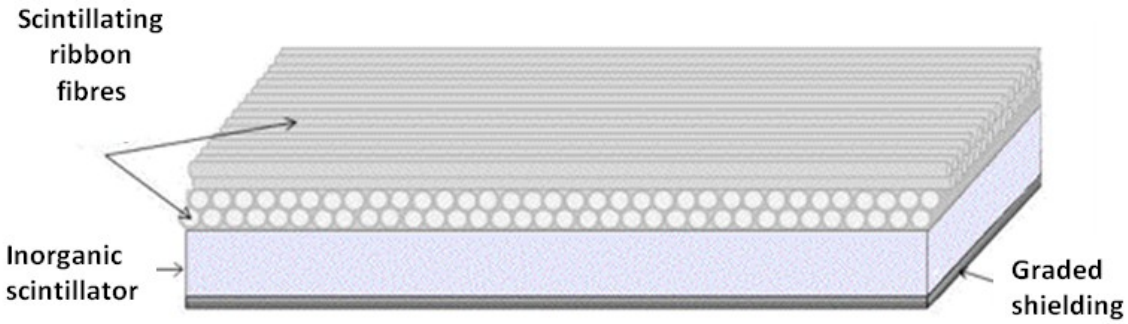

Figure 3-10. Schematic of the passive and active shielding. The graded shielding, the inorganic scintillator and the two orthogonal double-layer ribbon scintillating fibres surrounding the focal plane detectors. The fibres are the items closest to the detectors.

3.1.6 X-ray Polarimeter

The angular distribution of s-photoelectrons produced by polarized x-rays is 100% modulated. The GPD polarimeter (Gas Pixel Detector) (Bellazzini, 2009) images the ionization tracks produced in the gas by the photoelectron, allowing reconstructing of the direction of the first part of the track before it is randomized by scattering (see Figure 3-11). X-rays are converted in a gas cell a few cm. thick. The electrons of the ionization track are drifted toward a GEM (Gas Electron Multiplier), a thin bi-metalized micro-perforated insulator When a suitable bias is applied, the electrons, traversing the holes, are multiplied in a proportional mode by a factor 500-2000. The amplified charge is collected by a dedicated ASIC which is the active anode of the GPD. The top layer of the CMOS ASIC (1.5 cm x 1.5 cm), is hexagonally patterned with 105600 pixels on a 50 μm pitch. Each pixel contains a complete low-noise (50el) amplification chain. The ASIC is auto-triggered and is able to identify a small region around the event, transferring to the output the signals of a limited number of pixels. Simple algorithms, allow for the accurate determination of the basic parameters such as the impact point and the initial emission direction. The photon energy is extracted from the GEM and, simultaneously, from the ASIC with the energy resolution of a good typical proportional counter. The GPD, permits space, energy and time resolved polarization measurements. The intrinsically homogeneous and symmetric response, the simultaneous analysis of all the angles and the negligible background allows for devising a non-rotating polarimeter. Most of these characteristics are not present in photoelectric polarimeters based on the Time Projection Chamber techniques

Two detectors, inside a single camera, can be alternatively located at the focus of one NHXM telescope, by a sliding (or a rotary) device (see Figure 3-11): a low energy polarimeter (LEP) and a medium energy polarimeter (MEP) (Soffita, 2010).

Their characteristics are summarized in Table 3-6.

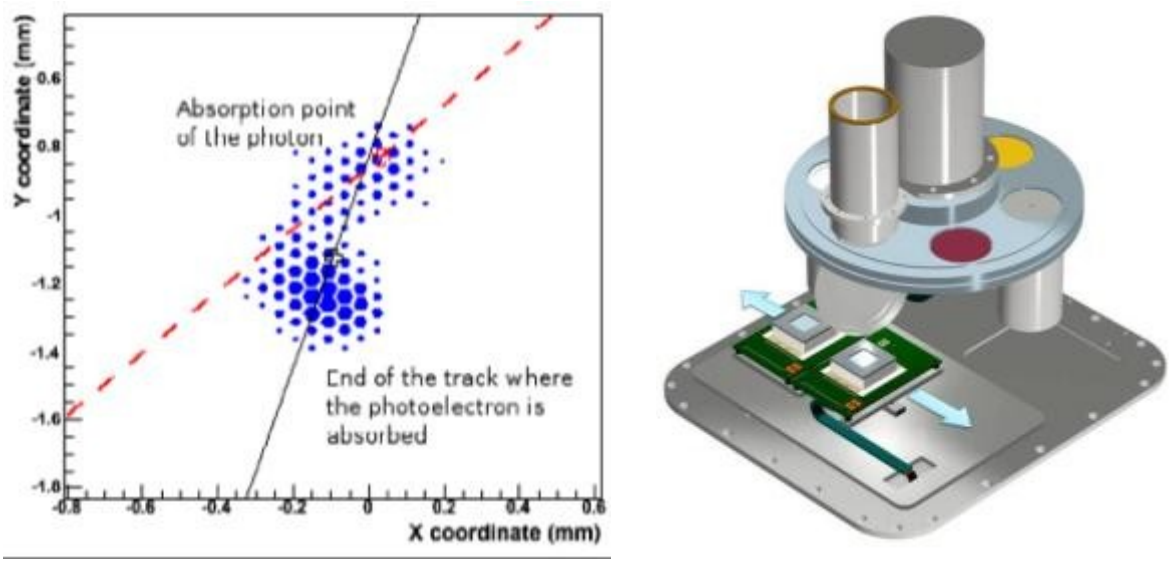

Figure 3-11. (left) An actual track imaged by the LEP GPD currently operating; (right) the focal plane assembly.

3.1.7 Wide-Field X-ray monitor

The WFXRM is based on the two Wide Field Camera Units (WFCU) that are combined to form a single Wide Field Camera (WFC), allowing for a very modular configuration. The baseline assumes two WFCs located inside the central platform cylinder and co-aligned with the NHXM pointing direction. The addition of another four units, which would permit full sky coverage, is under evaluation.

The WFCU is formed by a 20x20 cm silicon drift detector coupled to a 35x35 cm 2D Asymmetric Coded Mask. The WFCU design is based on the heritage of the x-ray monitor in the Italian mission AGILE, successfully operating since 2007 (Feroci, 2010), demonstrating the

feasibility of a large-area, light, compact and low-power x-ray imager with an arcmin resolution and steradian-wide field of view.

Table 3-6. Main characteristics of NHXM polarimeters

Number of pixels	105600
Pixel size	50μm
Sensitive area	1.5 cm x 1.5 cm
FOV	5.2 ' × 5.2 '
Energy resolution	<20 % at 6 keV
Image capability (driven by optics)	LEP 15" MEP 20"
Energy range	LEP 2-10 keV MEP 6-35 keV
Timing	8 μs resolution
Mixture	LEP: He20% + DME80% MEP: Ar60% + DME40%
Thickness & Pressure	LEP: 1 cm 1 bar MEP: 3 cm 3 bar
Background	LEP: 0.1μCrab MEP: 0.4 μCrab
Minimum Detectable Polarization	LEP 9.7%; MEP 13 % @ 1 mCrab in 10^5 s
Temperature range	0-20 ºC

In the current WFCU design, the performance is improved by using 450-μm-thick, large-area and multi-linear Silicon Drift Detectors (SDDs) (Vacchi, 1991), built on the heritage of the ALICE Inner Tracking System, operating since 2008 at the LHC of CERN.

The technology of drifting photoelectrons towards a small-size, low-capacitance collecting

anode, via a linear electric field as in the ALICE design, permits an energy resolution of 250-500 eV FWHM over a large area (50 to 80 cm^2) between 2 and 50 keV (Zampa, 2011). These results were obtained with a spare ALICE detector, instrumented with discrete read-out.

The SDD detector has a one-dimensional read-out: the charge cloud is drifted from the point of absorption to the grounded anodes by a parallel electric field sustained by a high voltage (~1400 V) divider. The 294 μm anode pitch (in the ALICE SDD) provides a spatial resolution between 20 and 60 μm in the direction parallel to the anodes by charge weighting (Campana, 2011). The charge diffusion in the Si during the drift makes the Gaussian distribution of the charge over multiple contiguous anodes a unique encoder of the position of each event along the drift channel. Thus, despite the 1-D electronics read-out, each SDD has an asymmetric 2-D position resolution of ~50μm and ~3mm in each dimension, respectively. The time resolution is limited by a drift time of 5μs.

Based on these detector properties, a WFCU is designed following the SuperAGILE concept, by placing a thin Tungsten asymmetric 2-D coded mask 15 cm away from the detector layer providing an angular resolution of 3 arcmin × 1.5°.

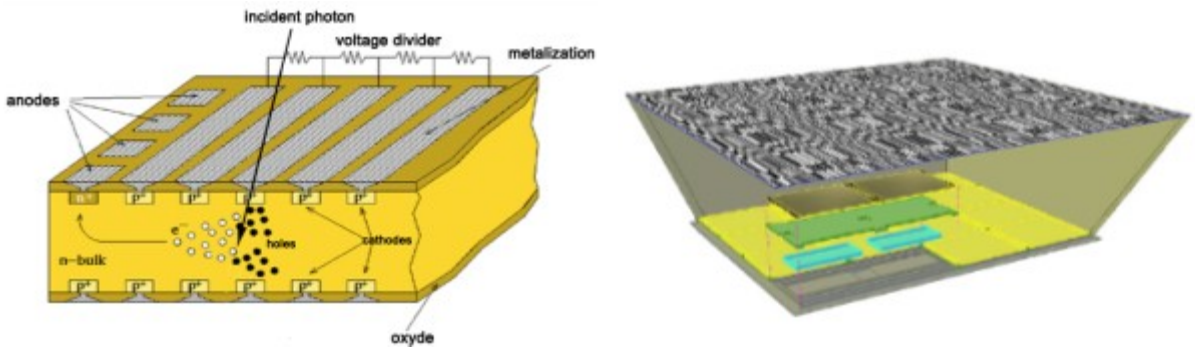

Figure 3-12. (left) working principle of the SDD; (right) the baseline configuration of one WFCU.

A thin passive shield prevents photons of the diffuse x-ray background from entering the field of view, acting as a supporting structure for the coded mask as well,. Assuming a SDD read-out based on the ASIC being developed by the INAF-INFN-University collaboration in Italy (including the on-chip ADC), the analogue power consumption is 3W at room temperature. A WFC is composed of 2 WFCUs, rotated by 90º to each other in order to achieve simultaneous fine angular resolution in both coordinates. However the coarse angular resolution on the second direction offers the great advantage of an independent 2-D angular resolution for each

camera, and a significant reduction of the confusion limit for each unit in crowded fields.

The data processing requires an FPGA-based BEE for filtering, event cluster analysis, pedestal calculation and subtraction, common mode noise subtraction and time tagging. According to the WFXRM main goal, fast burst triggering (GRB in <1 s) and location (PSLA <1 arcmin), the WFC must operate in an autonomous mode with an onboard data processing software, which requires a dedicated DPU. The WFXRM data will be sent to ground in photon-by-photon mode only for the triggered sources for 5 minutes. For the rest of the time it will work in monitoring mode, integrating imaging on board every 5 min.

Table 3-7. Requirements of the WFC

Fully-coded FoV	0.40 sr
Partially-coded FoV	2.90 sr
FoV zero response	120 deg
Angular Resolution	3’
PSLA (5σ)	<1 arcmin
On-axis sensitivity (5σ, 1 s)	0.5 Crab
On-axis sensitivity (5σ, 50 ks)	<3 mCrab
Time Resolution	~10 μs
Detector area	800 cm^2
Energy Range	2-50 keV
Energy Resolution (FWHM)	250-500 eV
Dry mass	26 kg
DPU+BEE dry mass	12 kg
Mechanical volume	35x70x20 cm

3.2 eROSITA Science and Payload

Spectrum-RG is a Russian - German X-ray astrophysical observatory. Germany is responsible for the development of the key mission instrument - the x-ray grazing incident mirror telescope eROSITA. The second experiment is ART-XC - an x-ray mirror telescope with a harder response than eROSITA, which is being developed by Russia (IKI, Moscow and VNIIEF, Sarov). Mission launch is scheduled for 2013.

The name eROSITA stands for extended Roentgen Survey with an Imaging Telescope Array. The general design of the eROSITA x-ray telescope is derived from that of ABRIXAS: a bundle of 7 mirror modules with short focal lengths make up a compact telescope which is ideal for survey observations. Similar designs had been proposed for the missions DUO and ROSITA but were not realized. Compared to those, however, the effective area in the soft x-ray band has now much increased by adding 27 additional outer mirror shells to the original 27 ones of each mirror module (see Figure 3-13). The requirement on the on-axis resolution has also been confined, namely to 15 arc seconds HEW. For these reasons the prefix "extended" to the original name "ROSITA" had been added. The scientific motivation for this extension is founded in the ambitious goal to detect about 100000 clusters of galaxies which trace the large scale structure of the Universe in space and time (Predehl, 2010).

The main scientific goals are:

- to detect the hot intergalactic medium of 50-100 thousand galaxy clusters and groups and hot gas in filaments between clusters to map out the large scale structure in the Universe for the study of cosmic structure evolution,
- to detect systematically all obscured accreting Black Holes in nearby galaxies and many (up to 3 Million) new, distant active galactic nuclei and
- to study in detail the physics of galactic x-ray source populations, like pre-main sequence stars, supernova remnants and x-ray binaries.

The x-ray telescope consists of 7 identical and co-aligned mirror modules, each formed by 54 nested Wolter I mirror shells, currently under manufacturing at MLT company. The assembly of the 7 mirror modules forms a compact hexagonal configuration with 1300 mm diameter and will be attached to the telescope structure which connects to the 7 separate CCD cameras in the

focal planes. The co-alignment of the mirror module enables eROSITA to perform also pointed observations. In the following the main parameter of the eROSITA mission are reported:

- **Energy Band**: 0.5 - 10 keV
- **On-axis Angular Resolution**: < 15" (HEW) @ 1.49 keV; <20" (HEW) @ 8.04 keV
- **Field of View**: 61' (circular)
- **Angular Resolution over the FoV**: < 26" (HEW)
- **On-axis Effective Area per module @ 1keV**: 364 cm^2 (335 cm^2 with QE and filter)
- **Number of mirror modules**: 7
- **Focal Length**: 1600 mm
- **Mirror Length**: 300 mm
- **Diameter of each Mirror Module**: 358 mm
- **Energy Resolution**: 138 eV at 6 keV (FWHM)
- **Exposure Time per CCD-Frame**: 50 msec
- **Orbit**: L2
- **Mission Lifetime**: > 7 years

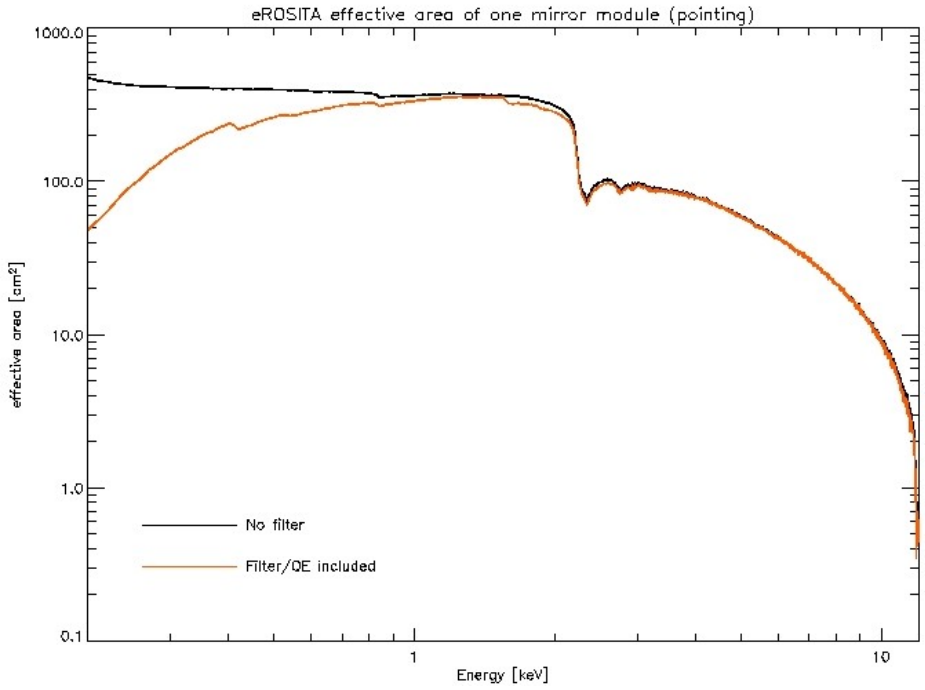

Figure 3-13. On-Axis effective area of one eROSITA mirror module with filter and CCD quantum efficiency included (red curve) and without filter (black curve).

Figure 3-14. eROSITA Demonstrator Model tested in 2008.

A demonstrator model (DM), completed in 2008, did not meet the eROSITA requirements but could serve as a qualification model. After investigations of many details of the processes of mandrel manufacturing, electroforming, release, and integration, the optical performance could be significantly improved. In 2009, a test module consisting of 5 mirror shells has demonstrated good x-ray performance. The angular resolution of single mirror shells and the alignment of the shells have fulfilled the scientific requirements: the angular resolution at 1.49 keV (Al-K line) is of the order of 15" and at 8.04 keV (Cu-K line) well below 20". The eROSITA project is now in the C/D phase and the flight models (FM) are being produced (see Chapter 8).

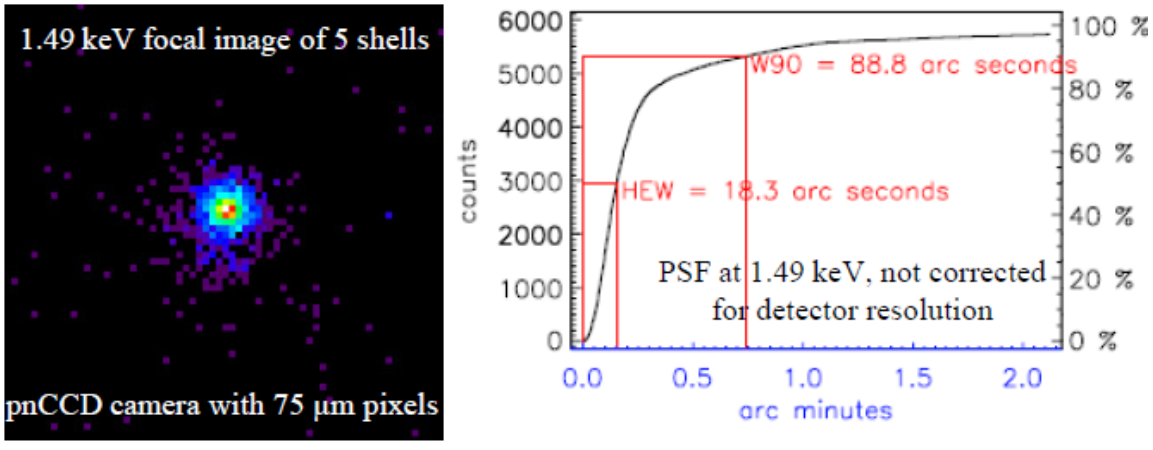

Figure 3-15. Five shells test module: HEW @ 1.49 keV 18.3"/14.8" (subtracting detector resolution); HEW @ 8.04 keV 17.6"/13.9" (subtracting detector resolution).

3.2.1 Dark Energy

The nature of the mysterious Dark Energy that is driving the Universe apart is one of the most exciting questions facing astronomy and physics today. It may be the vacuum energy providing the Cosmological Constant in Einstein's theory of General Relativity, or it may be a time-varying energy field. The solution could require a fundamental revolution in physics.

The discovery of Dark Energy has come from three complementary techniques: observations of distant supernovae, the microwave background, and clusters of galaxies. Together these leave no doubt that only 4% of the Universe is made up of baryons, and the majority is Dark Energy (73%) and Dark Matter (23%), which govern the structure and evolution of the Universe on the largest scales. Clusters of Galaxies are the largest collapsed objects in the Universe. Their formation and evolution is dominated by gravity, i.e. Dark Matter, while their large scale distribution and number density depends on the geometry of the Universe, i.e. Dark Energy.

In addition to the constraints on the structure and mass content of the Universe, x-ray observations of clusters provide information on the rate of expansion of the Universe, the fraction of mass in visible matter and the amplitude of primordial fluctuations. The amount and nature of DE (Dark Energy) can be tightly constrained by measuring the spatial correlation features and evolution of a sample of about 50000 galaxy clusters over the redshift range $0<z<1.5$. Such an x-ray survey will discover all collapsed structures with mass above $3.5\times10^{14}h^{-1}$Msun at redshifts $z<2$. Above this mass threshold the tight correlations between x-ray observables and mass allow direct interpretation of the data.

DE affects both the abundance and the spatial distribution of galaxy clusters. Measurements of the number density $d^2N/dMdz$ and the three–dimensional power spectrum P(k) of clusters are complementary (have different parameter degeneracies) to other DE probes, such as Type Ia SNe or CMB (Cosmic Microwave Background) anisotropies, and precisely constrain cosmological parameters. In particular, a survey of 50000 clusters of galaxies will allow to measure the «baryonic wiggles» imprinted on the power spectrum of primordial fluctuations, which gives an independent measurement rod for precision cosmology.

3.2.2 Obscured Accretion

Most of the light created after the «dark ages» in the Universe comes from active centers of

galaxies, emitted either by vigorous star formation processes or by prodigious supermassive black holes residing in the centre of almost every galaxy, swallowing stars and gas. It was only realized in recent years, that most of this energy output must be obscured in the galaxies behind thick veils of gas and dust. Only in ranges of the electromagnetic spectrum, where the light can penetrate these cocoons, i.e. at hard x-rays and in the infrared, can these phenomena be studied. Deep surveys in the hard x-ray range with Chandra and XMM-Newton, in the mid-infrared with Herschel and in the sub-mm with the SCUBA and MAMBO bolometers, together with population synthesis models, have shown that both the cosmic star forming rate and the black hole feeding rate were about two orders of magnitude higher in the early universe than today. The decline of this activity occurred at a surprisingly recent stage in cosmic history and is as yet not understood.

In particular, deep x-ray surveys have shown, that lower-luminosity AGN (Seyfert galaxies) show a maximum in space density much later in cosmic time, compared to the powerful quasars. Also, there are indications that the fraction of obscured sources increases strongly with decreasing x-ray luminosity. The x-ray background has almost completely been resolved below 2 keV, but only about 50% have been resolved above 5 keV, even in the deepest Chandra and XMM-Newton surveys. Many hidden, but still very active black holes should therefore be lurking in rather nearby galaxies, waiting to be detected by a hard x-ray survey. A survey in the hard x-ray band was defined as one of the future priorities in the last «Decadal Survey» of the American National Academy of Sciences. This was also the goal of the ABRIXAS mission which failed in 1999 due to a design error in the spacecraft power system. An imaging hard x-ray survey is still of high scientific interest and not yet planned by any other project than eROSITA.

3.2.3 Survey

A 4-years all-sky survey are envisaged for eROSITA including:

- A long exposure survey to discover obscured black holes and galactic sources;
- two deep fields of ~ 100 deg^2 around ecliptic poles;

The survey phase is then followed by a pointing phase of three years.

3.2.4 Mirror Module Assembly

Although there are many possible configurations, only Wolter-I optics (paraboloid + hyperboloid) have got real importance in x-ray astronomy. The ABRIXAS mirrors also had this geometry. In order to enhance the effective area at low energies, the 27 outer shells are added thereby doubling the diameter of the mirrors. Each of the mirror module systems contains 54 nested shells. The focal length is 1600 mm. The on-axis resolution is 15" (Half Energy Width, HEW). The geometry of the mirror systems is optimized in order to achieve maximum sensitivity between 0.5 and 10 keV. The optical design of the mirror modules requires shells with a wall thickness between 0.2 and 0.4 mm and diameters between 76 and 358 mm. The length of the paraboloid-hyperboloid pairs is 300 mm. Such mirrors are fabricated in Media Lario Technologies company by using a nickel e-forming improved process similar to the one used for XMM-Newton. In order to enhance the reflectivity, all mirrors are coated with gold.

Like on ABRIXAS the mirror systems still have the hexagonal geometry but are no longer tilted with respect to each other.

X-ray baffle are foreseen for avoiding single reflections, and a thermal baffle is placed in front. The x-ray baffle also provides a thermal shielding.

Figure 3-16. The entrance apertures of the seven telescopes (ABRIXAS flight model).

3.2.5 Focal Plane Assembly

eROSITA will carry seven individual CCD-detectors, each mounted in its own housing and equipped with its own electronics (in a separate box). The CCD has 384×384 pixels and size of 28.8×28.8 mm^2 corresponds to a field of view of 61 arc minutes. The CCDs have to be cooled down to -60°C for optimum operation and energy resolution.

MPE has developed in the semiconductor laboratory the cameras for XMM-Newton and ABRIXAS based on the pn-CCD principle. The camera on XMM-Newton has been operated successfully since early 2000. The eROSITA CCD are already fabricated; they are an advanced version of the pn-CCD with smaller pixel sizes (75×75 μm^2 instead of 150×150 μm^2) and faster readout. The latter is achieved by combining the proven technology with a frame store area. First tests with these novel devices show quite promising results: both the response at low energies and the CTE (charge transfer efficiency) could be dramatically improved with respect to the XMM-Newton camera (Figure 3-17). In order to suppress the internal background generated by fluorescent X-rays, the detectors will be equipped with graded shields, whose design is currently being developed. Events generated by minimum ionizing particles (MIPS) can be removed by the high energy response of the CCDs according to the mechanism developed for the XMM-Newton camera.

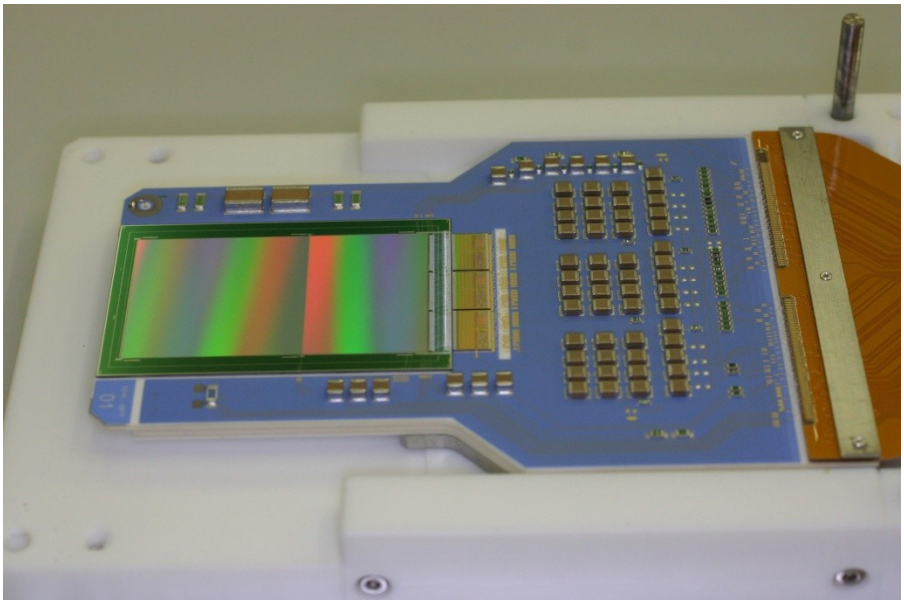

Figure 3-17. CCD module with a frame store pn-CCD, connected to 3 CAMEX chips. Everything is mounted onto a ceramic carrier which, in turn, will be mounted to the cold plate (adapter seen).

3.3 Next future soft /hard missions apart from NHXM and eROSITA

The relevance of the scientific topics of NHXM mission proposal, has already prompted the international community to the approval of three soft/hard x-ray missions. However, because of intrinsic (design) limits, several major goals lie beyond their capability. They are: NuSTAR (USA, due for launch in 2012), with prominent lacking in the soft band (5-80 keV) and angular resolution (60 arcsec HEW at 30 keV); ASTRO-H (Japan, 2014), with a much worse angular resolution (90 arcsec HEW at 30 keV) and separate telescopes to cover the soft and hard x-ray energy band; GEMS (USA, 2014), a non-imaging polarimeter mission which must be rotated to average systematic effects (for a constant source). To fully uncover BH cosmic evolution, accretion physics, acceleration mechanisms and the physics of matter under extreme conditions a more significant leap forward is essential. NHXM is specifically designed to ensure order(s) of magnitude improvements and/or unique features compared to these missions.

Table 3-8. NHXM capabilities compared to other missions. Im=image quality; BB=broad band; IB=internal background; IP=Imaging polarimetry; SSP=Simultaneous broadband spectroscopy & polarimetry. More stars mean better quality.

Topics	NHXM	NuSTAR	Astro-H	GEMS
SMBH cosmic evolution & CXB	★★★★★, Im, IB	★★★	★	-
AGN & GBH hard X-ray emission	★★★★★, BB, SSP, WFXRM	★★	★	★
Galactic center, SgrA* - SgrB2	★★★★★, Im, IB, BB, IP	★★	★	★
PWN B-field topology & e^- population	★★★★★, IP, Im, BB	-	-	★
Blazars	★★★★★ SSP, WFXRM	★	★	★★
Cluster shocks, non thermal emission	★★★★★, Im, IB, BB	★★	★	-
Stellar Coronae	★★★★★, Im, BB, IP	★	★★	★
GR effects, BH spin	★★★★★, BB, SSP		★★	★
Ultra-high B- fields	★★★★★, SSP	-	-	★★★

In addition, it is worth to mention the next soft x-ray IXO/ATHENA mission. In March 2011 ESA announced its decision to reformulate its large mission (L) candidates (IXO, EJSM-Laplace and LISA), and, as part of this reformulation exercise, a new study team was appointed by ESA to look into a new, large x-ray observatory, called ATHENA, candidates for a launch slot in 2020.

In the following the above cited x-ray mission will be briefly presented ordered by the scheduled launch date.

3.3.1 NuSTAR

Nuclear Spectroscopic Telescope Array (NuSTAR) is a planned space-based x-ray telescope that will use grazing incidence mirrors to focus high energy x-rays at 5 to 80 keV from astrophysical sources, especially for nuclear spectroscopy. It is the eleventh mission of the NASA Small Explorer satellite program (SMEX-11) and the first space-based direct-imaging x-ray telescope at energies beyond those of the Chandra X-ray Observatory and XMM-Newton. Mission launch is scheduled for 3 February 2012 (Harrison, 2010).

During a two-year primary mission phase, NuSTAR will map selected regions of the sky in order to:

- take a census of collapsed stars and black holes of different sizes by surveying regions surrounding the center of own Milky Way Galaxy and performing deep observations of the extragalactic sky;
- map recently-synthesized material in young supernova remnants to understand how stars explode and how elements are created; and
- understand what powers relativistic jets of particles from the most extreme active galaxies hosting supermassive black holes.

The payload consists of two co-aligned depth-graded multilayer coated grazing incidence optics focused onto a solid state CdZnTe pixel detectors.

NuSTAR implements a conical approximation to the Wolter-I design and consists of 130 concentric mirror shells coated with Pt/SiC and W/Si multilayers. The NuSTAR optics have an overall length of 450 mm, a maximum radius of 191 mm and a focal length of 10 m. The outer 65 shells consist of 12 pairs of azimuthal segments, the inner 65 of 6 pairs. Each of the 2 mirror modules is expected to have a mass of 24.5 kilograms.

In the following the main parameter of the NuSTAR mission, as best estimate per June 2010, are reported:

- **Energy Band**: 5 - 80 keV
- **Angular Resolution**: 43" (HEW), 7.5" (FWHM)
- **Field of View**: 13' x 13'
- **Effective Area @ 30keV**: ~ 300cm^2.
- **Energy Resolution**: 1.2 keV at 68 keV (FWHM); 600eV at 6keV (FWHM)
- **Sensitivity (3σ, 1Ms):** 2 x 10^{-15} erg/cm^2/s (6-10 keV); 1 x 10^{-14} erg/cm^2/s (10-30 keV)
- **Temporal Resolution**: 0.1 msec
- **ToO response**: < 48 hours
- **Orbit**: 550 km x 600 km, 6 degree inclination

The NuSTAR team has developed a novel approach to building these optics, using the hot slumping approach. The 210 μm thick D263 glass slumped mirror segments are then deposited with a multilayer coating at the DTU-Space at the Danish Technical University in Copenhagen.

The optics are built from the inside out, shell upon shell, spaced apart by graphite spacers and held together by nothing but epoxy. This precision assemblage is done at Columbia University's Nevis Laboratory outside New York City and provides very light and flexible optics.

Figure 3-18. One of the NuSTAR two mirror modules is assembled inside a clean room at Columbia University's Nevis Laboratories in Irvington, N.Y. (www.nustar.caltech.edu).

3.3.2 ASTRO-H

ASTRO-H (also known as NeXT for New X-ray Telescope) is a planned x-ray astronomy satellite under development by the Japan Aerospace Exploration Agency (JAXA). It is expected to be launched in 2014 into a circular orbit with altitude 500–600 km, and inclination 31 degrees or less.

When its telescope is extended in orbit, the satellite will be 14 meters length. The observatory is designed to extend the research conducted by Advanced Satellite for Cosmology and Astrophysics (ASCA) by investigating the hard x-ray band above 10 keV. NASA is participating with this project by committing the High-Resolution Soft X-Ray Spectrometer (SXS). The Netherlands Institute for Space Research (SRON) will build the filter-wheel and calibration source for the spectrometer.

The purpose of ASTRO-H is to explore the structure and evolution of Universe with the following observational capabilities (Takahashi, 2010):

- one of the first imaging and spectroscopic observations with the hard X-ray telescope;
- the first spectroscopic observations with an extremely high energy resolution of the micro-calorimeter;
- the most sensitive wideband observation over an energy range from 0.3 to 600 keV.

Its instrumentation includes four x-ray mirrors: two Soft X-ray Telescopes (SXTs) (see Figure 3-19) for imaging in the 0.3–10 keV band and two Hard X-ray Telescopes (HXTs) for imaging in the 5-80 keV band. In addition to that there are: two Hard X-ray Imager (HXI), one Soft X-ray Spectrometer (SXS), one Soft X-ray Imager (SXI) and one Soft Gamma-ray Detector (SGD)

The HXT has epoxy-replicated aluminium foil mirrors with graded carbon/platinum multilayer reflecting surfaces. The effective area of the HXT is maximized for a long focal length, with current design value of 12 m giving an effective area of ~300 cm^2 at 30 keV.

The HXI consists of four-layers of 0.5 mm thick Double-sided Silicon Strip Detectors (DSSD) and one layer of 0.5 - 1 mm thick CdTe imaging detector. In this configuration, soft x-ray photons will be absorbed in the DSSD, while hard x-ray photons go through the DSSD and are detected by the newly developed CdTe double strip detector.

In addition to the imaging observations below 80keV, SGD will provide a high sensitivity in the soft Gamma-ray region to match the sensitivity of the HXT/HXI combination. The extremely low background will provide sensitive gamma-ray spectra up to 600keV.

In the following the main performance/parameters of the hard x-ray system (HXT/HXI) are given:

- **Energy Band**: 5 - 80 keV
- **Angular Resolution**: 90" (HEW)
- **Field of View**: 9' x 9'
- **Effective Area @ 30keV**: ~ 300 cm^2
- **Energy Resolution**: < 1.5 keV at 60 keV (FWHM)
- **Sensitivity (3σ, 1Ms):** 1 x 10^{-14} $erg/cm^2/s$ (5-80 keV)
- **Timing Resolution:** several 10 μs
- **Diameter:** 450 mm
- **Focal Length:** 12 m
- **Number of Mirror Shells:** 213
- **Number of Mirror Modules:** 2
- **Reflecting Coating:** Platinum / Carbon

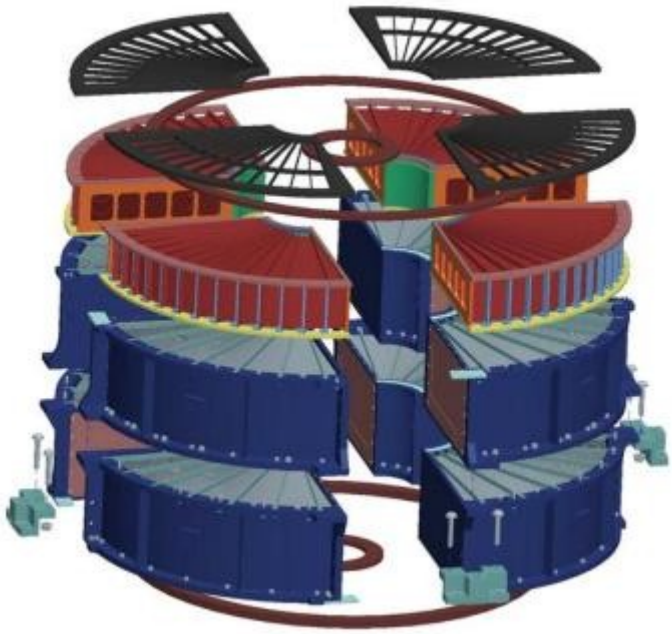

Figure 3-19. Exploded view of the ASTRO-H Soft X-ray Telescope (SXT). The mirror is segmented into quadrants. The main components, from the bottom, are inner and outer lower mounting rings, the two reflection stages, the stray light baffle, the inner and outer upper mounting rings, and the thermal shield (Petre, 2010).

3.3.3 GEMS

The Gravity and Extreme Magnetism SMEX (GEMS) mission is a planned space observatory. The project is an astrophysics program reporting to NASA's Science Mission Directorate (SMD) in Washington, D.C. and it is managed by the Goddard Space Flight Center.

GEMS was one of six Small Explorer missions selected in May 2008 for the NASA Small Explorer (SMEX) Program Phase A study. In June 2009, GEMS was chosen to be the second of these missions to go forward into Phase B, starting in October 2010 for a launch in April 2014 (Jahoda, 2010).

The GEMS project is currently in the definition phase (Phase B). Phase B focuses on requirements definition to design and develop the technical specifications for the spacecraft and instrument. The project completed and successfully passed the Systems Requirements Review (SRR) design review (US Government) in December 2010.

The main scientific goal of GEMS is to be the first mission to systematically measure the polarization of cosmic x-ray sources. The x-ray telescope will be designed to indirectly measure the regions of distorted space around spinning black holes through a measurement of the polarization of x-rays emitted. It will thereby probe the structure and effects of the magnetic field around magnetars and dead stars with magnetic fields trillions of times stronger than Earth's.

GEMS could reveal:

- how spinning black holes affect space-time and matter as it is drawn in and compressed by strong gravitational fields;
- what happens in the super strong magnetic fields near pulsars and magnetars;
- how cosmic rays are accelerated by shocks in supernova remnants.

Current missions cannot do this because the required angular resolution is limited and magnetic fields are invisible.

GEMS will have three identical telescopes, each consisting of foil mirrors and a novel, time projection chamber x-ray polarimeter. The instrument operates in the 2–10 keV band. While the polarimeter is not an imaging instrument, use of an imaging mirror allows accurate placement of a concentrated beam at its small entrance aperture, thus substantially increasing instrument sensitivity. The mirror design is based on the Suzaku design, with the same 4.5 m focal length. Fitting three coaligned telescopes in the SMEX fairing constrains the diameter of each mirror to

be 32 cm. The GEMS mirrors are thus basically a smaller diameter version of the Suzaku mirrors, with 110 nested shells. The same forming and replication mandrels will be used to produce the segments, and the same lightweight housing design will be used, scaled to the smaller diameter. The resulting difference in effective area from the Suzaku mirrors primarily affects the band below 2 keV where the detectors are not sensitive. The angular resolution requirement is 90 arcsec, better than that achieved on Suzaku, but achievable given the smaller size and number of shells and taking advantage of some of the process improvements developed for ASTRO-H (Petre, 2010).

The detector in GEMS will be a small chamber filled with gas. When an x-ray is absorbed in the gas, an electron carries off most of the energy, and starts out in a direction related to the polarization direction of the x-ray. This electron loses energy by ionizing the gas; the instrument measures the direction of the ionization track, and thereby the polarization of the x-ray. The GEMS detector readout will employ a time projection chamber to image the track. The GEMS instrument is about 100 times more sensitive than previous x-ray polarization experiments.

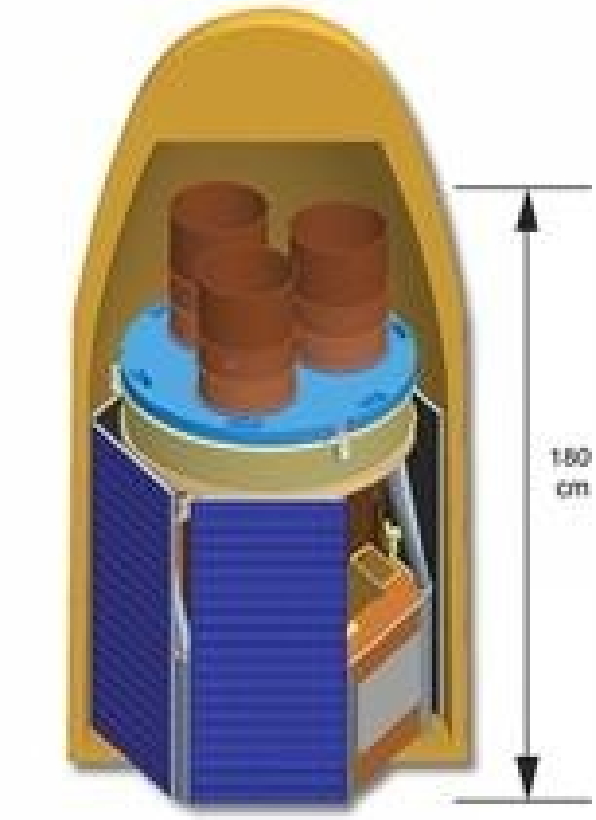

Figure 3-20. GEMS in its stole configuration, design to fit within Pegasus XL class launch vehicle.

3.3.4 IXO/ATHENA

In March 2011 ESA announced its decision to reformulate its large mission candidates (IXO, EJSM-Laplace and LISA) in the light of changing boundary conditions for international participation, particularly from NASA.

IXO was incorporating a single, large diameter mirror module with 20m focal length, 3.3m diameter, and mass of 1750 kg. The effective area at 1.25 keV was to be at least 2.5m^2 with a 3.0m^2 goal and 0.6m^2 at 6 keV. The angular resolution of the entire observatory was to be 5 arcsec.

As part of the reformulation exercise, a new study team was appointed by ESA to look into a new, large x-ray observatory called ATHENA (Advanced Telescope for High ENergy Astrophysics).

The science objectives of ATHENA are to (www.sci.esa.int):

- Explore the extreme physical conditions around supermassive black holes, and determine the contribution of accretion power to the energy budget of the Universe.
- Map the large scale structure of the Universe, and reveal the physical state and cosmic evolution of the hot gas which forms the major baryonic component of the cosmos.
- Determine the importance of and establish the physical mechanism behind cosmic feedback, the process that connects black holes and cosmic structures over 10 orders of magnitude in physical size.

ATHENA is also a powerful, general-purpose observatory**,** able to address a wide range of current astrophysical topics

The ATHENA mission concept is currently under study by ESA, and the mission architecture is, at this stage, in a preliminary state. The baseline concept is, however, as follows (www.sci.esa.int):

- The heart of the Athena mission is a pair of high-throughput x-ray telescopes, based on ultra-lightweight Silicon Pore Optics (SPO) technology developed by ESA. The focal length of each telescope is approximately 11.5m.
- At one focal plane is an imaging calorimeter spectrometer, based on transition edge sensor technology, which provides an unprecedented combination of spectral resolution and effective area in the x-ray band.
- The other telescope feeds a wide field imager, based on Silicon active pixel sensor

technology, which provides a large field of view for broad-band x-ray surveys and imaging, with near Fano-limited energy resolution and high count-rate capability.

ATHENA will be launched into a halo orbit at the Sun-Earth L2 (2nd Lagrangian) point, which provides for high observing efficiency, uninterrupted observations, and a benign thermal environment.

4 Metrological characterization and calibration of X-ray mirrors

This chapter reports and describes the fundamental quantities used to fully characterize the x-ray mandrels and mirrors manufactured and developed in the frame of NHXM and eROSITA projects. The set of dedicated metrological instrumentation used is presented, with reference to the performance and the concept design. **Most of the instruments available in Media Lario Technology company (MLT) and INAF-OAB are custom projects and at the edge of the metrology**, following the principle that you cannot correct what you cannot measure. The instruments are meant to characterize the geometrical shape accuracy (including axial profiles, azimuthal profiles and focal length) and the surface finish (in terms of waviness, roughness, reflectivity and cosmetic defects). **The instruments are being extensively used for the development and manufacturing of the NHXM and eROSITA x-ray mirrors**.

The goal of the metrology is to provide a tool for monitoring the error budget during the manufacturing of the mirror modules and a prediction of the final x-ray performance via indirect measurements. A good prediction of the final x-ray performance is fundamental in this field, because of the logistic complexity to perform direct x-ray measurements. Direct measurement need special facilities with huge vacuum chambers (10^{-6} mbar), with a big diameter to host the mirrors (up to 1 meter) and a suitable length to reproduce as much as possible the condition of paraxial rays from cosmic sources (more than 100 metres). The **PANTER**, of the Max-Planck-Institut für extraterrestrische Physik (MPE) in the Bavarian city of Neuried in Germany, is an example of such a facility that can be considered unique in Europe.

The PANTER facility is being been used by INAF-OAB and MLT for the direct measurements of the effective area and the angular resolution of NHXM and eROSITA mirrors.

4.1 Mirror characterization and image quality prediction

Gazing incidence optical systems operating at x-ray wavelengths pose unique problems in that the traditional long-range (low spatial frequency) surface figure errors and short-range (high spatial frequency) finish do not adequately characterize image quality.

We can thus talk about several different relevant spatial frequency regimes which have distinctly different effects upon image quality as illustrated in Figure 4-1: (*i*) the low spatial frequency regime ("figure" errors) give rise to conventional wavefront aberrations, (*ii*) the high spatial frequency regime ("finish" errors or microroughness) produce wide-angle scattering effects that redistribute radiant energy from the image core into a broad scattered halo without substantially affecting the width of the image core, and (*iii*) the "mid" spatial frequency regime that spans the gap between the traditional "figure" and "finish" errors. For many application, among which x-ray astronomy, the dominating image degradation mechanism is the small angle scatter resulting from mid spatial frequency surface errors (waviness). The resulting requirement to completely characterize surface errors over a very broad spatial frequency domain greatly complicates detailed image quality prediction (Harvey, 1996).

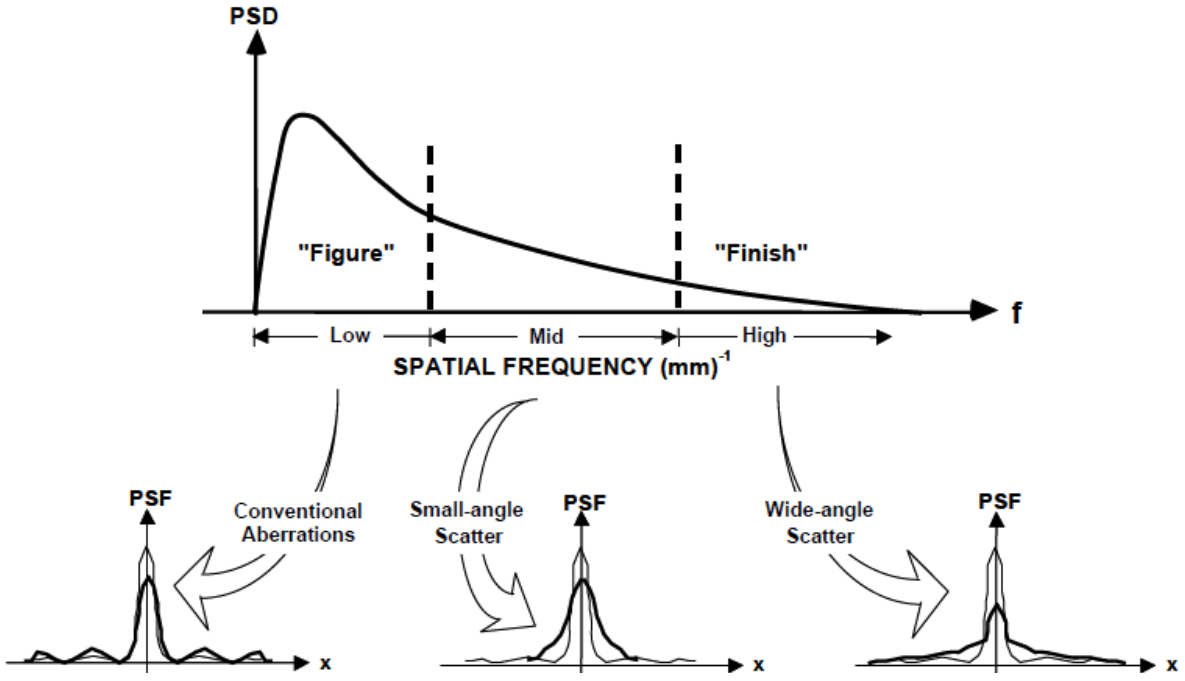

Figure 4-1. Different spatial frequency regimes and their resulting effects upon image quality (Harvey, 1996).

The performance of an optical system is related to surface roughness of the mirrors: the smaller the wavelength of the radiation the bigger the effects of deterioration caused by the surface roughness on the reflection of the incident beam. When light is reflected from an imperfect optical surface, the reflected radiation consists of a specularly reflected component and a diffusely reflected component as illustrated in Figure 4-2. Generally speaking, a surface can be smooth or rough depending on the length scale at which we observe it. In the x-ray, the wavelengths that determine the scattering phenomena are in the range 200-000.1 μm (Aschenbach, 1985).

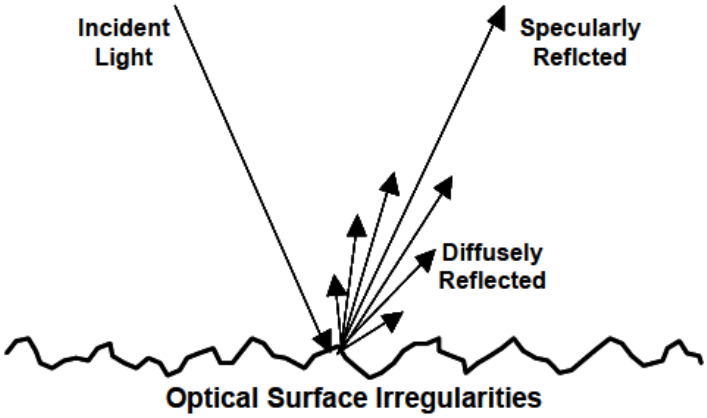

Figure 4-2. Optical surface irregularities produce a specularly reflected beam with a diffusely reflected component that can degrade optical performance in several different ways (Harvey, 1996).

4.1.1 Figure error and ray tracing

The characterization of the optical performance of mirrors in terms of figure error can be performed, in principle, by direct optical resolution measurements under collimate radiation. However, this approach cannot be used for mandrels for which shape metrology must be performed with subsequent post-processing and, possibly, numerical simulation by ray tracing. Of course, the latter approach is applicable to both mandrels and mirrors.

A priori, the best approach for performing this kind of measurements would consist in using a measuring device capable of directly reconstructing the 3D shape of the mirror or mandrel with respect to a single absolute reference system. The alternative approach consists in performing separate 2D measurements with respects to different reference systems each of which gives a partial description of the mirror or master geometrical shape error.

The different error sources affecting the mirror or mandrel image quality can be classified as follows:

- slope error of the axial profiles;
- slope error of the azimuth profiles;
- error in the focal length

The major contribution to the geometrical shape error of x-ray optics normally comes from the axial slope error.

Each error can be effectively measured with metrology equipments that allow the determination of the different contributions separately. Each error term can then be ray traced to estimate corresponding HEW. At first approximation, the different HEWs can be considered statistically independent or at least uncorrelated and the overall performance can be predicted as the root sum squared (RSS) of the separate contributions,

$$HEW_{TOTAL} = \sqrt{HEW_{axial}^2 + HEW_{azimuth}^2 + HEW_{focal}^2} \tag{4.1}$$

The allocation of a measurable error budget for the different error sources can be done by the following geometrical consideration.

Axial Slope Error

The mathematic function "median" can be used to calculate the maximum slope error value containing the 50% of the slope error measured on a profile. This quantity is known as δ^{50} (delta50) and is linked to the HEW by geometrical formulas.

The δ^{50} can be measured on a number of different axial profiles, independently on the parabolic and hyperbolic section. All the δ^{50} measured on the parabola can be averaged to obtain a single value $\delta^{50,P}$ and the same can be done on the hyperbola obtaining the value $\delta^{50,H}$. The HEW is given by the RSS of the parabola and hyperbola contribution, multiplied by a factor 4 taking into account the double reflection and the fact the angle of reflection is doubled w.r.t. to the local slope error of a surface:

$$HEW_{axial\ slope} = 4\sqrt{\left(\delta_H^{50}\right)^2 + \left(\delta_P^{50}\right)^2} \tag{4.2}$$

By allocating axial slope error values $\delta^{50} < 1$ arcsec we can obtain HEW < 6 arcsec.

Azimuthal Slope Error

The δ^{50} can be used also to derive the tolerances for roundness. The roundness (or azimuthal) profiles can be measured on a number of positions on the parabolic and hyperbolic section. All the δ^{50} measured on the parabola can be averaged to obtain a single value $\delta^{50,P}$ and the same can be done on the hyperbola obtaining the value $\delta^{50,H}$ In this case, the HEW given by the RSS of the parabola and hyperbola contribution, has to be scaled for the radius-to-focal length ratio:

$$HEW_{azimuthal\ slope} = r_{med} / F \cdot \sqrt{\left(\delta_H^{50}\right)^2 + \left(\delta_P^{50}\right)^2} \tag{4.3}$$

where r_{med} is the radius at the intersection plane and F corresponds to the focal length.

Focal Length Error

The manufacturing tolerance for the nominal radius and taper error are contributing to a displacement of the focal length. The effects on the HEW values at the best focus are a factor 100 lower than the nominal contribution.

For the absolute radius, the error from the nominal r_{nom} value is averaged over the azimuth and over the z-direction, both for parabola and hyperbola:

$$\delta_P^{radius} = r_P - r_{P,nom} \qquad\qquad \delta_H^{radius} = r_H - r_{H,nom}$$

The HEW contribution is:

$$HEW_{radius} = 1/F \cdot \left|3\delta_H^{taper} - 3\delta_P^{taper}\right| = 1/F \cdot \left|\delta^{radius}\right| \tag{4.4}$$

The focus displacement is given by:

$$\delta F_{radius} \cong 1/2 \cdot ctg(4\alpha)\left|\delta^{radius}\right| \tag{4.5}$$

For the taper, the error from the nominal value is averaged over the azimuth both for parabola and hyperbola.

$$\delta_P^{taper} = (r_{\max,P} - r_{\min,P}) - (r_{\max,P,nom} - r_{\min,P,nom})$$

$$\delta_P^{taper} = (r_{\max,H} - r_{\min,H}) - (r_{\max,H,nom} - r_{\min,H,nom})$$

The HEW contribution is:

$$HEW_{radius} = \frac{4}{L} \cdot \left| \delta_P^{taper} - \delta_H^{taper} \right| = \frac{4}{L} \cdot \left| \delta^{taper} \right| \tag{4.6}$$

Where L is the length of the sections. The focus displacement is given by:

$$\delta F_{taper} \cong \frac{4F\delta^{taper}}{L\sin(8\alpha)} \tag{4.7}$$

Tilt, Decenter an Despace

Other minor contribution to the HEW is given by tilt, decenter and despace of one section with respect to the other.

The angle δ_{tilt} between the symmetry axes of parabola and hyperbola bring to an HEW error of:

$$HEW_{tilt} = 2 \cdot \left| \delta_{tilt} \right| \tag{4.8}$$

The lateral decenter $\delta_{decenter}$ of the hyperbola symmetry axis with respect to the symmetry axis of the parabola brings to an HEW error contribution of:

$$HEW_{decenter} = {}^{1}\!/_{F} \cdot \left| \delta_{decenter} \right| \tag{4.9}$$

The despace $\delta_{despace}$ is the error between the real hyperbola position and the nominal position in the parabola coordinate system. Being α the grazing incidence angle, the HEW degradation can be calculated as:

$$HEW_{despace} \cong 2\,{}^{tg(4\alpha)}\!/_{F} \cdot \left| \delta_{despace} \right| \tag{4.10}$$

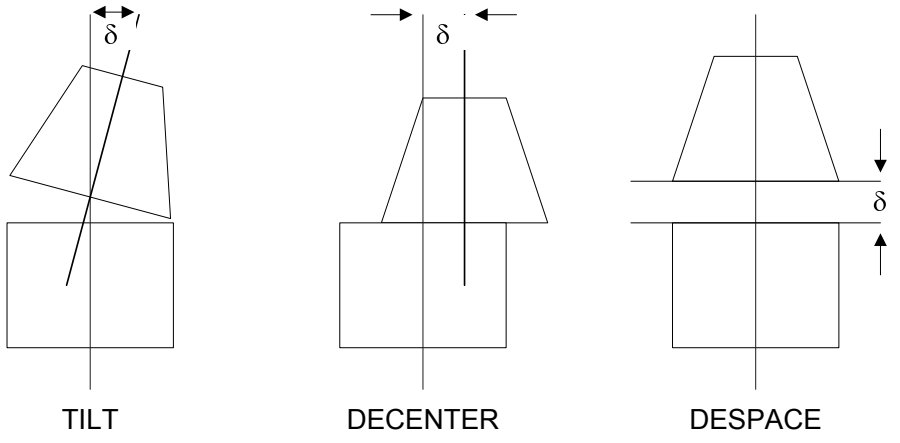

4.1.2 Scattering and Power Spectral Density

Surface scatter effects are merely diffraction phenomena resulting from random phase variations induced upon the reflected wavefront by microtopographic surface features. Most natural surfaces have an inherent roughness (or texture) that results in scattered light. The behavior of light scattered from randomly rough surfaces is dictated by the statistical surface characteristics. The two relevant statistical surface characteristics are the surface height distribution function and the surface power spectral density function.

Variations in height of a surface are usually expressed in terms of a quantity called the **roughness**, the distance between two peaks in the same profile is called wavelength and the reciprocal of the wavelength is the spatial frequency. The profile of any surface, can be described in terms of a Fourier components sum having different spatial frequencies, and the presence of any periodic structures, can be put in evidence in terms of resonance frequency spectrum. The roughness is a necessary but not sufficient way to describe the morphology of a surface, since it is possible to have the same values of surface roughness with totally different morphologies. It is used also a quantity called **slope error**, which describes the distribution of the angle of the tangent to the profile. For a one-dimensional surface profile over a infinite distance L infinite, we can describe the heights above the average surface with a function $z(x)$ where x is the coordinate along the direction of the scan. The reference surface corresponding to the average profile is given by:

$$\bar{z}(x) = \lim_{L\to\infty} \frac{1}{L} \int_{-L/2}^{L/2} z(x)dx \tag{4.11}$$

The roughness is considered as a deviation from that value, and we can distinguish between roughness average value:

$$\delta_a = \lim_{L\to\infty} \frac{1}{L} \int_{-L/2}^{L/2} \left|z(x) - \bar{z}\right| dx \tag{4.12}$$

and root-mean-square (rms) roughness value, i.e. as standard deviation:

$$\delta_{RMS} = \sqrt{\lim_{L\to\infty} \frac{1}{L} \int_{-L/2}^{L/2} \left|z(x) - \bar{z}\right|^2 dx} \tag{4.13}$$

Both σ_a and σ_{RMS} are used to describe the surface roughness of a surface, but, generally, the standard deviation is mainly used to describe the optical surfaces while the arithmetic mean is used for profiles machined with mechanical tools. Values σ_a and σ_{RMS} are similar if the profile does not contain large deviations from the average, otherwise the statistical distribution will be dominated by high values and standard deviation will have higher values. If we now consider the first derivative of average profile $\bar{z}'$, the same considerations can be applied to the errors in the slopes:

$$m_a = \lim_{L\to\infty} \frac{1}{L} \int_{-L/2}^{L/2} \left| \frac{dz}{dx} - \bar{z}' \right| dx \tag{4.14}$$

$$m_{RMS} = \sqrt{\lim_{L\to\infty} \frac{1}{L} \int_{-L/2}^{L/2} \left| \frac{dz}{dx} - \bar{z}' \right|^2 dx} \tag{4.15}$$

Any real measure of the profile of a surface is carried out through a discrete sampling, and, in the equations above, integrals must be replaced with summations. Each measure is defined in a range of spatial frequencies, determined by the maximum length of scan and by sampling in accordance with the critical sampling theorem of Nyquist: if L is the length of scan and d is the sampling interval in acquiring experimental, the minimum and maximum spatial frequency measurement-related will respectively $1/L$ e $1/2d$. Metrological equipments are able to capture the profile of a surface also in two-dimensions: in this case the mathematical procedure to derive the roughness and slope error is nothing more than a simple extension to the two-dimensional case of the previous formulas.

Fortunately, for many cases of interest, the surface heights are normally distributed (i.e.; the surface height distribution function is Gaussian). Although it would be convenient (mathematically) if the surface **autocovariance** function were also Gaussian, in most instances that is not the case. Instead, the surface autocovariance function is material and process dependent. The autocovariance length, l, is defined as the half-width of the autocovariance function at the $1/e$ height. The surface autocovariance function and the surface power spectral density function are Fourier transforms of each other.

The **Power Spectral Density** (PSD) is a mathematical function that describes how the power of a time series varies with the frequency. The surface PSD can be thought of as a plot of surface variance as a function of the spatial frequency of the surface irregularities and can be

defined as the module of the Fourier Transform (FT) of the amplitudes of a profile, normalized to the scan length. In the following a quantitative description of the PSD is provided. The FT of the amplitudes has the effect to go from the space domain to the frequency domain:

$$Z(f_x) = F[z(x)] = \int_{-\infty}^{+\infty} z(x)\exp(-i2\pi f_x x)dx \tag{4.16}$$

The mathematical operation is lawful, since the amplitudes can be considered as the sum of a constant term $\bar{z}$ and an infinite number of sinusoids. The FT can also be evaluated on a finite distance L (referring to the real-case):

$$Z(f_x, L) = \int_{-L/2}^{+L/2} z(x)\exp(-i2\pi f_x x)dx \tag{4.17}$$

The integral shows that the profile can be seen as a function of the bandwidth L and is null outside the interval of integration.

The definition of one-dimensional PSD (units are of cubic length) is derived from the application of Parseval theorem (Spiller, 1994):

$$PSD = S_1(f_x) = \lim_{L\to\infty} \frac{|Z(f_x, L)|^2}{L} \tag{4.18}$$

The PSD is an even function and symmetrical with respect to $f_x = 0$, since the amplitudes $Z(f_x,L)$ are squared. Typically, only the positive frequencies are considered by multiplying by a factor of 2 the equation (4.18) in order to take into account the symmetry. The squared module infer losing the information about the phase of the wave and therefore, in the cases where, as in scattering, the PSD is derived from indirect measures, it is not possible to obtain morphology information. Roughness and slope error are derivable directly from the PSD through the calculation of the first two moments of order:

$$\sigma_{RMS}^2 = \int_{f_{\min}}^{f_{\max}} (2\pi f)^0 S_1(f_x)df_x \tag{4.19}$$

$$m_{RMS}^2 = \int_{f_{\min}}^{f_{\max}} (2\pi f)^2 S_1(f_x)df_x \tag{4.20}$$

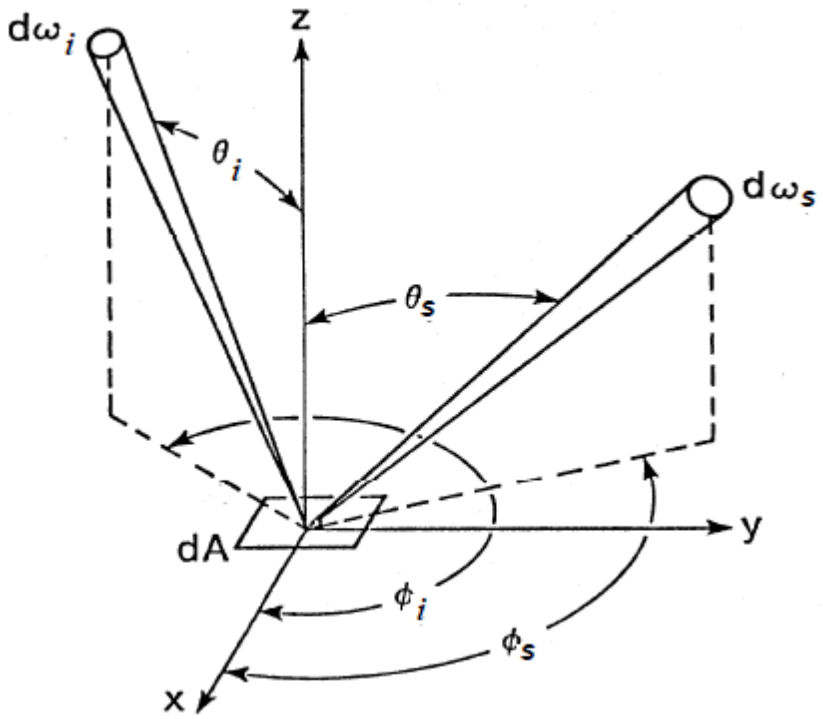

Figure 4-3. Illustration of the defining angles for scattering diagram (Harvey, 1996).

Equation (2.18) tells us that the roughness has the effect of exponentially damping the theoretical amplitude (given by the Fresnel's laws). The reflectivity in the specular direction is linked to the roughness but itself alone can't give a complete characterization of the surface. The comprehensive description of a surface is determined by the interpretation of non-specular reflection (scattering) that occurs in all directions other than the specular direction. There is clearly a relationship between the surface roughness and the amount of light scattered out of the specular beam.

The Rayleigh-Rice vector perturbation theory can explain the **PSD-scattering** link: the main finding of the theory lies in the relationship of proportionality between the intensity distribution of scattering and the PSD of a surface, expressed as a function of spatial frequency of the surface. These results are valid not only in the case of x-ray scattering, but also for scattering at other wavelengths. A typical three-dimensional representation of the phenomenon and grazing incidence scattering is shown in Figure 4-3: the radiation arrives with an angle θ_i, and if the condition of smooth surface

$$2\sigma \sin \vartheta_i << \lambda \tag{4.21}$$

is met, most of the radiation will be reflected in the specular direction. The presence of irregularities on the surface causes the scattering of the radiation in the directions (θ_s, φ_s). If the surface is isotropic, the grazing incidence scattering in the orthogonal plane φ_s is 100 ÷ 1000 times lower then that scattering in the incidence plane θ_s and so it can be neglected. The scattered intensity in a given differential solid angle (normalized by the incident radiant power) is related to one-dimensional PSD from the following approximate equation (Church, 1979):

$$\frac{1}{I_0}\left(\frac{dI}{d\vartheta}\right)_s \approx 4k^3 \cdot \theta_i \cdot \theta_s^2 \cdot R(\theta_s, \theta_i) \cdot \frac{PSD(f_x)}{2\pi} \tag{4.22}$$

where $k = 2\pi/\lambda$ is the wavenumber and $R(\theta_s, \varphi_s)$ is the polarization factor that can be expressed as

$$R(\theta_s, \theta_i) = [R(\theta_i)R(\theta_s)]^{1/2} \tag{4.23}$$

where $R(\theta_s)$ and $R(\theta_i)$ are the Fresnel reflectivity at the angle of scattering and at the angle of incidence. This equation tells us that PSD may be obtained from the diagram of scattering without additional assumptions about the distribution of heights or some form of correlation function. One-dimensional spatial frequencies responsible for the scattering are defined by the angles of incidence and scattering by lattice equation:

$$f_x = \frac{|\cos\theta_{sc} - \cos\theta_{inc}|}{\lambda} \tag{4.24}$$

4.1.3 Roughness and inter-layer diffusion in multilayer

Fresnel and Snell equations allow to accurately describe the behavior of the radiation incident on the interface between two media, if it is assumed that this is perfectly smooth. As in the case of a single surface, the effect of interfacial roughness is to remove the ideal specular intensity and distribute it to other scattering angles. This scattered intensity distribution is therefore intrinsically linked to the type of interface roughness causing the scattering.

Different types of roughness are given by different types of interfacial profiles, the two most commonly used are (Stearns, 1992) (Stearns, 1998):

- The diffusion between two materials that cause a variation of the composition along the

interface;

- the surface roughness due to a sudden change in height of the interface;

The width of a multilayer interfaces can be considered as the combination of both types, namely:

$$\sigma = \sqrt{\sigma_d^2 + \sigma_r^2} \tag{4.25}$$

where σ_d is the interface width due to diffusion, and σ_r that due to roughness. From equation (2.18) we can derive the magnitude of specular reflectivity of an interface of a multilayer:

$$\tilde{r} = r_0 \exp\left(-2k_0 k_1 \sigma^2\right) \tag{4.26}$$

where k_0 is the perpendicular component of the incident wave vector, k_1 the perpendicular component of the diffracted wave and r_0 the amplitude reflected by an ideal surface. The combined effect of surface roughness and scattering produces a reduction in reflectivity of multilayer structure as shown in Figure 4-4.

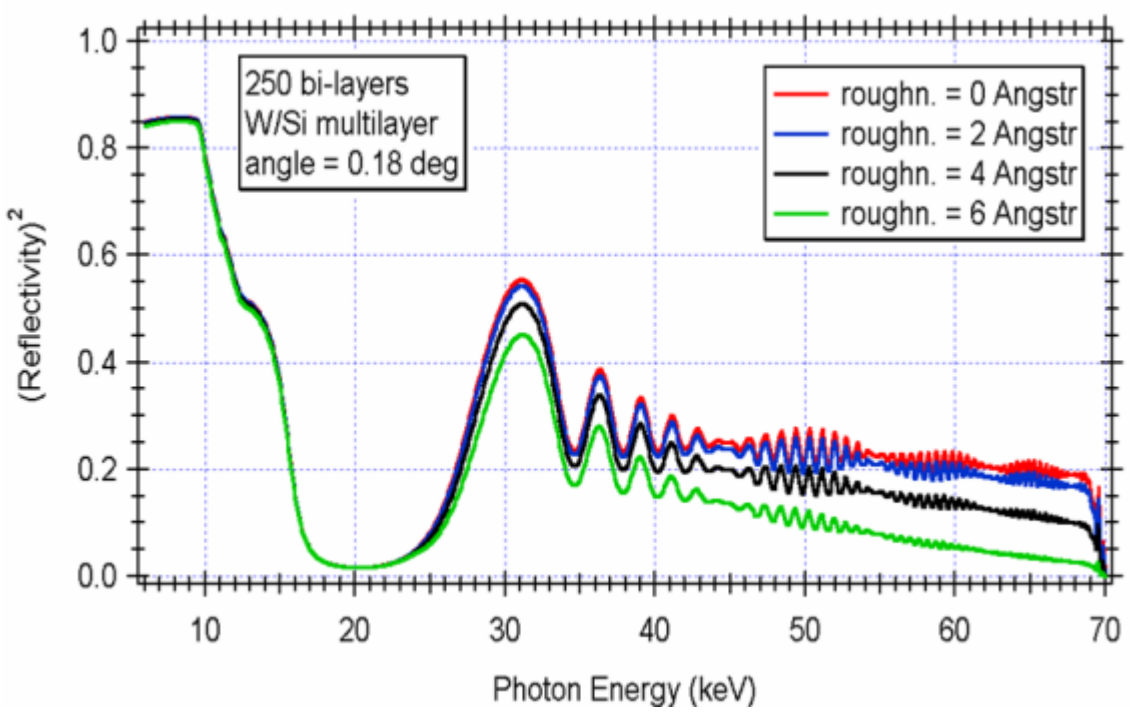

Figure 4-4.Simulation of the reduction in reflectivity in a multilayer due to the roughness/diffusion interface.

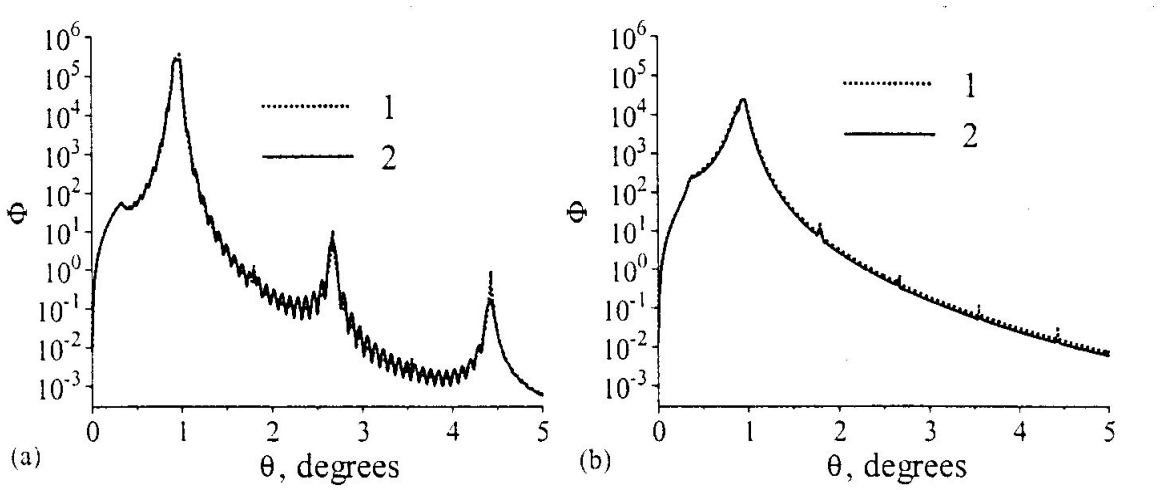

Figure 4-5. Examples of non-specular reflection from semi-infinite (curve 1) and 40 bi-layer (curve 2) multilayers. In the figure (a) it is supposed a completely correlated roughness, whereas in the figure (b) a completely uncorrelated roughness (Kozhevnikov, 2002).

By the expression (4.26) it is clear that the specular reflectivity does not distinguish between the two types of surface roughness, and therefore, to know something about the origin of roughness is necessary to consider also non-specular reflection. In the case of multilayer, the non-specular reflection can be described by a scalar theory known as the Distorted Wave Born Approximation (Sinha, 1994), which treat the roughness as a perturbation of the reflectivity of a surface.

An important factor, for the multilayer scattering, is the way in which the surface roughness propagates along the multilayer itself (see Figure 4-5):

- a roughness completely uncorrelated ($\sigma_{r,uncorr}$) between the layers, distributes the non-specular reflectivity in a uniform halo;
- a perfectly correlated roughness ($\sigma_{r,corr}$) has the behavior of a crystal lattice and order the scattering in structures, obeying the Bragg condition.

The overall roughness can be described as the sum of correlated and uncorrelated roughness:

$$\sigma_r^2 = \sigma_{r,corr}^2 + \sigma_{r,uncorr}^2 \tag{4.27}$$

The uncorrelated component is negligible until the width of Bragg peaks, resulting from the scattering diagram, are of the same width of Bragg peaks of the specular condition. In this case

the correlated surface roughness can be derived from the comparison of the diagram peaks with a theoretical scattering model (Kozhevnikov, 2002). By applying the eq. (4.25) it is possible to get an indirect estimation of the roughness due to interlayer diffusion:

$$\sigma_d = \sqrt{\sigma^2 - \sigma_r^2} \tag{4.28}$$

The deposition of multilayers is characterised by a constant increase of the roughness of the interfaces that are deposited. This is due to the roughness of the starting substrate and the stochastic roughness occurring during the film growth processes.

The profile of a single layer can be described, during its growth, as a function $z(x, y, \tau)$ defined by the following differential equation (Stearns, 1998):

$$\frac{\partial z}{\partial \tau} = -\nu \left| \nabla^n z \right| + \left(\frac{\partial \eta}{\partial \tau} \right) \tag{4.29}$$

which describes the evolution of the surface profile $z(x, y, \tau)$ with the increasing of the thickness τ. The first term is proportional to the derivative of n-th order of the surface profile, through a constant ν, which usually takes negative values resulting in a worsening of the profile. The *n* exponent depends on the mechanism by which growth occurs and can assume integers values between 1 and 4. The η variable is called shot-noise and it is the stochastic factor that causes the increase of surface roughness with the increasing of the thickness τ.

As a first approximation the roughness of the interfaces can be defined by the following sum squared:

$$\sigma_N^2 \approx \sigma_{Sub}^2 + \sigma_{Shot-Noise}^2 \tag{4.30}$$

where σ_N is the roughness of N-th layer, σ_{Sub} is the roughness of the surface on which the layer is grown and $\sigma_{Shot-Noise}$ is the roughness induced by the stochastic growth process.

4.1.4 Stress induced by multilayer coatings

Thin films are often subjected to a tension, called stress. This can in general be seen from the deformation of substrates onto which films are deposited. This stress, σ_f, is to be intended as a force normally-directed to any film section, like the surface tightness of a liquid, and can be

attractive (directed inwards) or repulsive (directed outwards). In the first case, an initially flat substrate will become concave upwards: the stress will then be called tensile, or positive. If the stress is repulsive, the substrate will become convex. Then we speak of compressive (or negative) stress. As σ_f is a force per lateral surface area unit, it is measured in Pascal, or more often in MPa. If t is the film thickness, the product $\sigma_f t$ (force per length unit) represents the surface tightness of the film. In general, the main source of stress is intrinsic, i.e. it is related to the film as deposited, and resulting from the nano-crystalline texture of the film, on the packing density of the atoms, and so on. For example, metallic films deposited by e-beam evaporation develop in general a tensile stress, but the sign can suddenly change if t exceeds the percolation length, beyond which the crystallization state experiences a re-organization with an increase of the crystal size.

If a laterally-homogeneous and isotropic thin film with a thickness t a total stress σ_f is deposited onto an initially-flat substrate with Young modulus E, thickness τ, Poisson ratio ν, it will be bent to a curvature, whose radius R (positive when concave upwards, i.e. on the side of the film) can be computed along with the Stoney equation (Stoney, 1909):

$$\sigma_f = \frac{E\tau}{6(1-\nu)tR} \tag{4.31}$$

This equation was derived, in a mono-dimensional case, by G. G. Stoney in 1909. With respect to that case, the factor $(1-\nu)^{-1}$ appeared due to the partial compensation of stretching/compression along the x and y direction. The factor 1/6 is due to the fact that the stress in the substrate follows:

$$\sigma(r) = \frac{E}{(1-\nu)R}(r - R - r_0) \tag{4.32}$$

where r, the distance from the centre of curvature as it can be seen applying the Young's law. Imposing the forces and torques equilibrium for the system film-substrate, it follows simultaneously $r_0 = \tau 2/3$ and the Stoney equation.

The interpretation of results for the Stoney equation is obvious for the case of single layers. For multilayers, the overall stress results from the stresses of all layers. For this reason, it is convenient to write the Stoney equation in terms of the product $\sigma_f t$. For a multilayer consisting of the alternation of layers h, l (e.g. h = W, l = Si), whose stress is σ_h and σ_l, and where the thickness of layers h and l follows the succession $t_{h,k}$ and $t_{l,k}$, k = 0,1,.., we obtain:

$$\sigma_h \sum_k t_{h,k} + \sigma_l \sum_k t_{l,k} = \frac{E\tau}{6(1-\nu)R} \tag{4.33}$$

under the hypothesis that the stress is constant in layers of the same material. Often σ_h and σ_l have opposite sign, so they tend to partly cancel each other. Note that we cannot derive the values of σ_h and σ_l also knowing the total thickness of the two materials. Indeed, by means of another deposition of a multilayer with the same deposition rate, temperature, and so on, but with a different ratio of the total thickness of the two elements, the previous equation can be solved for σ_h and σ_l. The average stress σ_f of the multilayer, as resulting from Stoney equation adopting for t the total multilayer thickness, is:

$$\sigma_f = \frac{\sigma_h \sum_k t_{h,k} + \sigma_l \sum_k t_{l,k}}{\sum_k t_{h,k} + \sum_k t_{l,k}} \tag{4.34}$$

where the denominator is simply t. Note that, if the multilayer is a periodic one, or if only the layer thickness of the absorber and of the spacer are in a constant ratio, the average stress is a function only of the Γ factor:

$$\sigma_f(const\Gamma) = \sigma_f \Gamma + \sigma_l (1-\Gamma) \tag{4.35}$$

and independent of the number of periods. This was experimentally observed in (Zoethout, 2003). The total surface tightness $\sigma_f t$, indeed, that is directly proportional to the substrate curvature, increases linearly with the number of bilayers.

The Stoney equation can be used also to predict the curvature imparted to a substrate by a thin film with different thickness, Young modulus, and so on, when we know the stress of the film to be applied on it.

4.2 Instruments for metrological characterization at INAF-OAB and MLT

The set of **dedicated metrological instrumentation available in Media Lario Technology company (MLT) and INAF-OAB** is presented, as used for the development and manufacturing of the NHXM and eROSITA x-ray mirrors and mandrels. The instruments are meant to characterize the geometrical shape accuracy (including axial profiles, azimuthal profiles and focal length) and the surface finish (in terms of waviness, roughness, reflectivity and cosmetic defects). The Mandrels 3D Profilometer (MPR) and the Shell Profilometer (SPR) are custom instruments recently developed and installed by MLT.

4.2.1 Mandrel 3D Profilometer (MPR)

The MPR is an integrated metrology equipment that serve to characterize, with a sufficient accuracy and precision, the figuring error and the absolute dimensions of mandrels. The machine is aimed at assessing the mandrel shape in both axial and azimuthal directions while measuring, at the same time, mandrel absolute diameters, thus estimating finally its optical performance in terms of HEW after data processing.

The core of the MPR is its measuring board. The innovation introduced by the MPR stands in its capability of measuring multiple profiles of mandrels both on longitudinal and azimuthal directions using coupled axis system, in such a way that it does not require realignment of the work piece during the whole measuring process. Moreover the adopted position control system allows decreasing the measurements position uncertainties (Sironi, 2010). The design choices making the MPR more performing than single axis measuring profilometers are:

- **Single mounting:** coupling movements along Cartesian axes and a rotation axis allows measuring longitudinal and azimuthal profiles without work piece realignments. This allows 3D surface reconstruction of the master within an unique system of reference.
- **X-Y translation:** the measuring sensor (no-contact) is mounted on a X-Y hydrostatic translation system driven by linear motors. This allows the movement along the tilted mandrel profile on both the conical sections.
- **Null sensor:** the sensor follows the profile of the workpiece and it is used as null-

sensor. This means that the sensor signal is connected in a closed loop control that maintains the sensor distance from the workpiece constant while the sensor moves along the X-axis.

- **Interchangeable sensor:** the mechanical support of null sensor is capable to hold both a contact and non-contact null sensor. In principle, a contact sensor could scratch the surface, for this reason a non-contact optical sensor is used as a baseline while the contact sensor is an optional solution.
- **Two beam laser interferometer:** in the chosen configuration the two-laser interferometer allows measuring the absolute Y coordinate of the null sensor carrier as well as its roll rotation error.
- **Triple beam laser interferometer:** the use of the triple beam interferometer allows recording the absolute X coordinate of the null sensor carrier as well as its pitch and yaw rotation error.
- **Anti-vibrating feet and granite table:** the MPR is placed on a granite table with air bearings feet to eliminate source of vibrations coming from external environment.

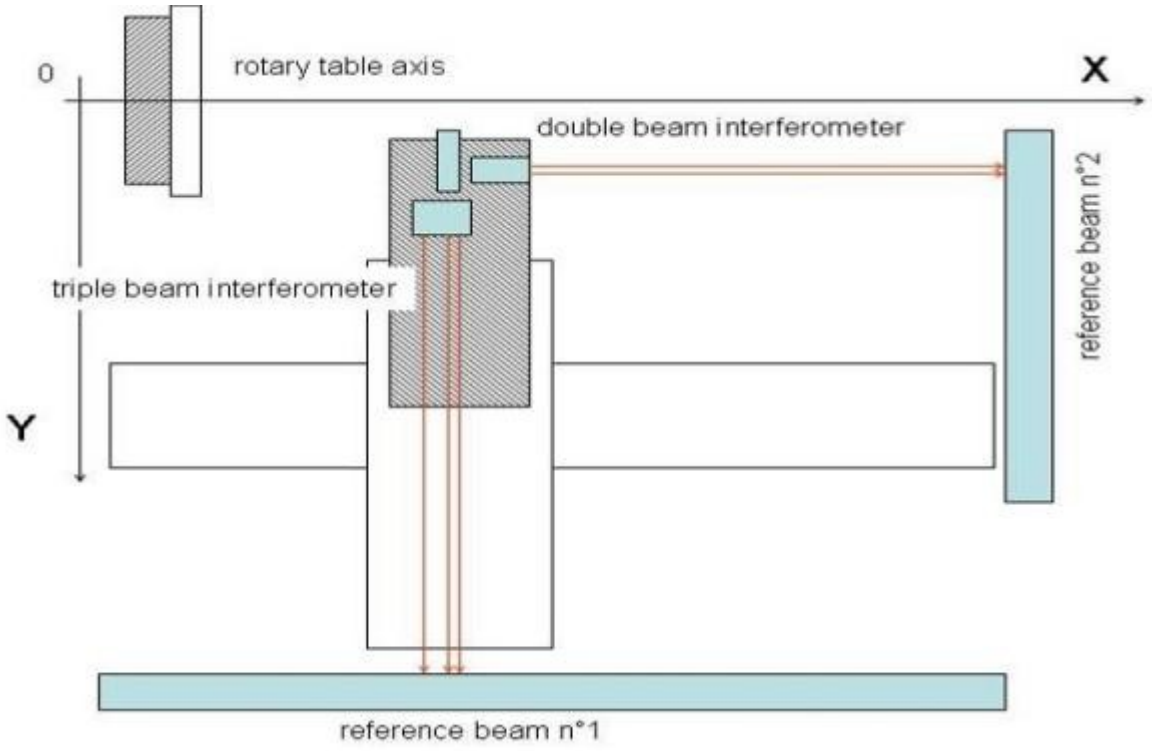

Figure 4-6. Measuring board design choices schematic (Sironi, 2010).

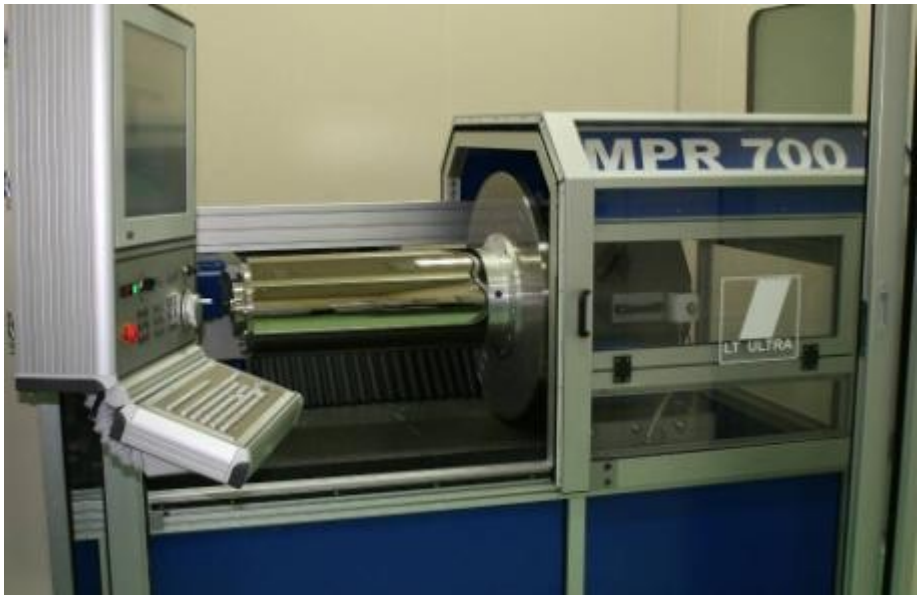

Figure 4-7. Picture of the 600 mm long master assembled on the MPR.

The MPR is installed in a dedicated metrology area. This area is equipped with an air conditioning system keeping a constant temperature for the whole day within the maximum range of ± 0.25°C around a T_0 value. T_0 is set between at 20°C. The temperature in the room is monitored by 2 temperature sensors with sensitivity of better than 0.1°C placed at different positions inside the room volume. In particular, one of these sensors is permanently placed on the top of the covering unit of the MPR and externally to it, and a second sensor placed inside the covering unit.

Additional environmental sensors integrated within the instrument are also installed inside the covering unit. These sensors consist in:

- an integrated environmental sensor monitoring the temperature, the air pressure and the humidity. This sensor is integrated with the controller of the interferometers and serves to correct the wavelength of the lasers;
- a temperature sensor monitoring the oil temperature of the hydrostatic bearing;
- a temperature sensor monitoring the temperature of the X motor;
- a temperature sensor monitoring the temperature of the Y motor.

The main control panel with the SW interface is hosted just outside the metrology area with controlled temperature. A picture of the used MPR setup is shown in Figure 4-7. Mandrels are installed on the MPR though a movable compact crane.

Table 4-1. MPR profilometer performance

Maximum operative diameter	700 mm	**Absolute accuracy**	± 1 µm (limited by the calibration)
Maximum operative length	720 mm	**Position resolution**	10 nm
Profile precision/repeatability	< 15 nm rms	**Vertical Alignment of the work-piece**	< 0.01° (profile error < 10 nm)
Relative profile accuracy	< 20 nm rms	**Measuring time**	<4 min (700 mm profile)

An accuracy better than 20 nm rms is achieved on axial profile measurements over a scanning range of 700 mm by properly taking into account the systematic errors of the machine. In Figure 4-8 the accuracy is shown as measured on a Zerodur bar tilted at different angles.

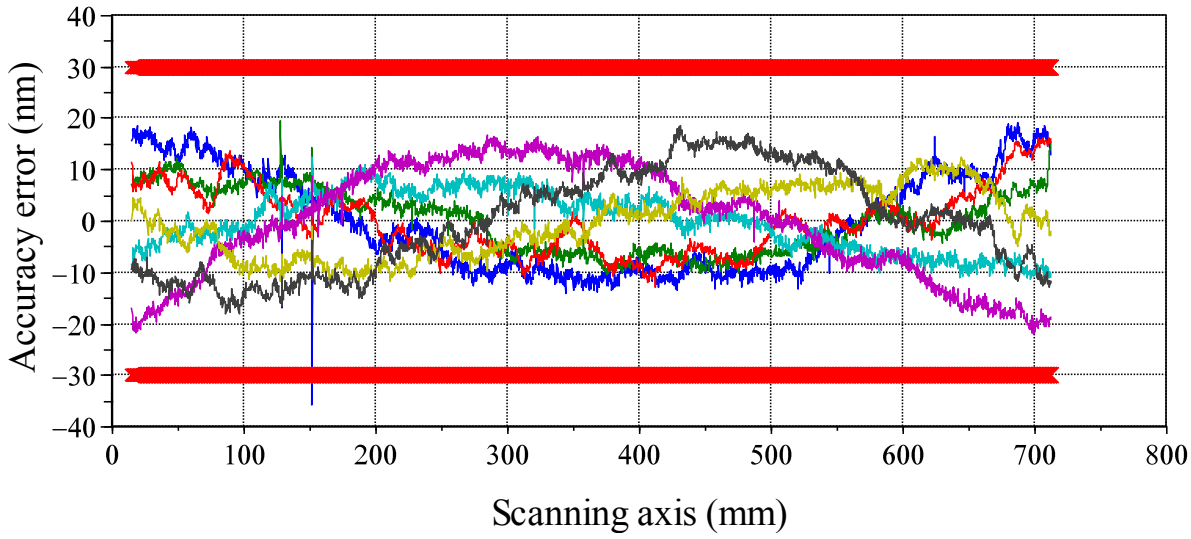

Figure 4-8. Accuracy measurements performed on a Zerodur bar tilted at different angles w.r.t. X-axis.

4.2.2 Mirror Shell Profilometer (SPR)

Due to the high optical performances required by the mirror shell, the characterization of the figuring error becomes mandatory for the optimization of the manufacturing and production processes. For this reason a long trace profilometer called "Shell Profilometer/Rotondimeter (SPR)" has been has been designed and assembled in MLT (Sironi, 2010).

The SPR is able to accurately detect the figuring error of the produced mirror over lengths up to 600 mm and diameters up to 430 mm. The measuring machine is used for the screening and the preliminary acceptance of the mirrors after the replication from the mandrels, and for the debugging of the replication process. The metrological data obtained by the instrument are processed by subsequent software that performs an HEW performance prediction (trough a ray-tracing code) of the mirrors prior to their integration.

The SPR allows the measurement of both integrated and non-integrated mirrors, once the integration structure allows the measuring head (holding pentaprism) to fit the inside. The most critical conditions are imposed by the profile acquisitions on non-integrated mirrors that forces the measuring machine to operate vertically i.e. with the scanning direction parallel to the optical axis of the shell that need to be stand vertically on a properly designed shell holding system. Due to the low mechanical stiffness of a standing mirror shell, a stress-free support structure is used during the metrological process. This is achieved, with minimum deformation of the shell, when it is standing trough a suitable suspension device equipped with flexible holders at one end of the shell, i.e. on the tip of the hyperbola or parabola side. Stated this configuration, the only possible access to the internal surface of the mirror is possible from the bottom side.

The position stability of the standing mirror shell is quite sensitive to the vibrations, both coming from the floor and the air flow and turbulence in the external environment, and, at the same time, from the temperature variations. In order to achieve a certain degree of isolation the motion and detection unit basement are uncoupled from the basement of the support device and these elements are uncoupled from the floor trough suitable dampers and solid granite table. Then, all the setup is placed inside an enclosure box with control temperature variations.

Anyway, it should be considered that, even with these precautions, the achievement of a mirror shell movement as rigid body on the level of less than 100 nm is still very difficult, and so also other considerations have been made in the design phase (Sironi, 2010):

- usage of a profile probing unit having the lowest sensitivity to the rigid body translation of the surface under test;
- usage of additional "soft" vibration dampers to be placed in contact with the mirror shell to reduce residual shell oscillations without deforming the mirror.

The core part of the measuring machine is represented by the motion and detection sub-system, illustrated in Figure 4-9. Its principle of operation is based on the use of a punctual slope measuring sensor coupled to a motion unit (linear translation stage plus a rotation module) that allows the probe scanning the mirror along axial and azimuthal directions. To avoid displacement of the mirror shell during measurement acquisition and damaging of the optical surface, a non-contact optical detection system is used.

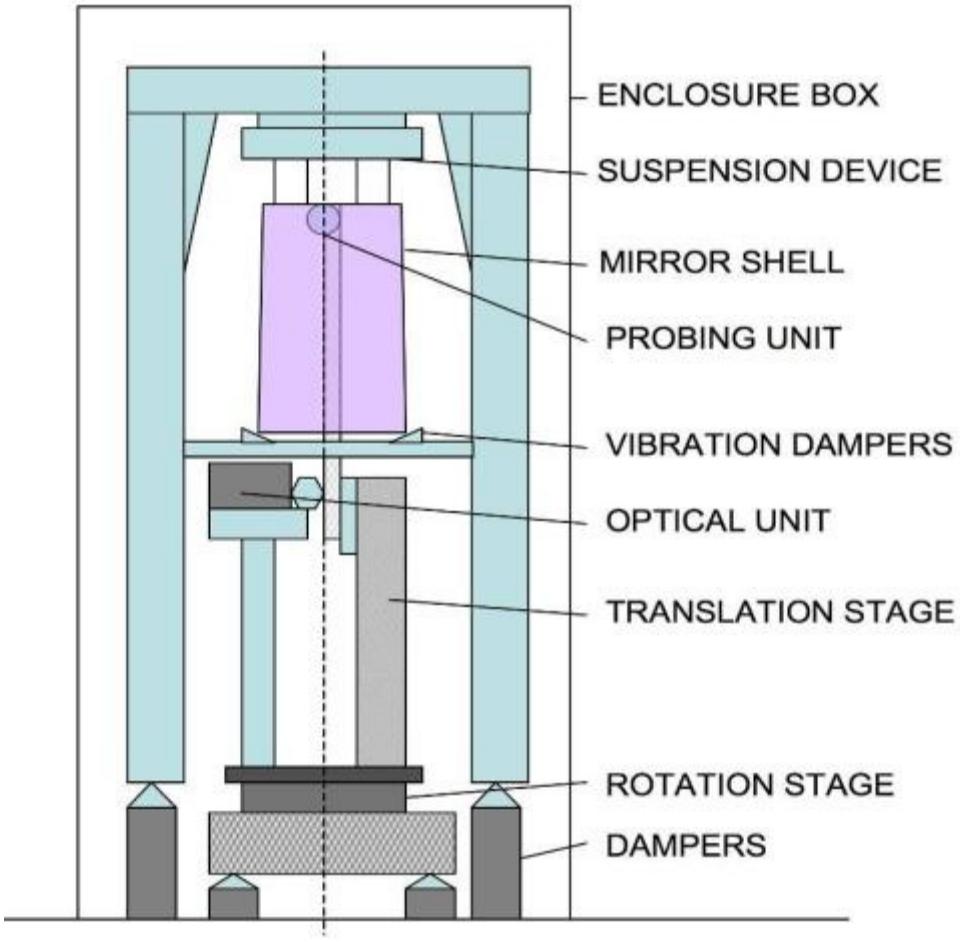

Figure 4-9. Schematics of the SPR Motion and Detection sub-system with air-bearing rotation table with vertical stage on.

In summary, as illustrated in Figure 4-9, the Motion and Detection sub-system consists of:

- A Detection Unit;
- A Vertical Translation Unit;
- A Rotation Unit;
- A Calibration Unit;
- A Supporting Device.

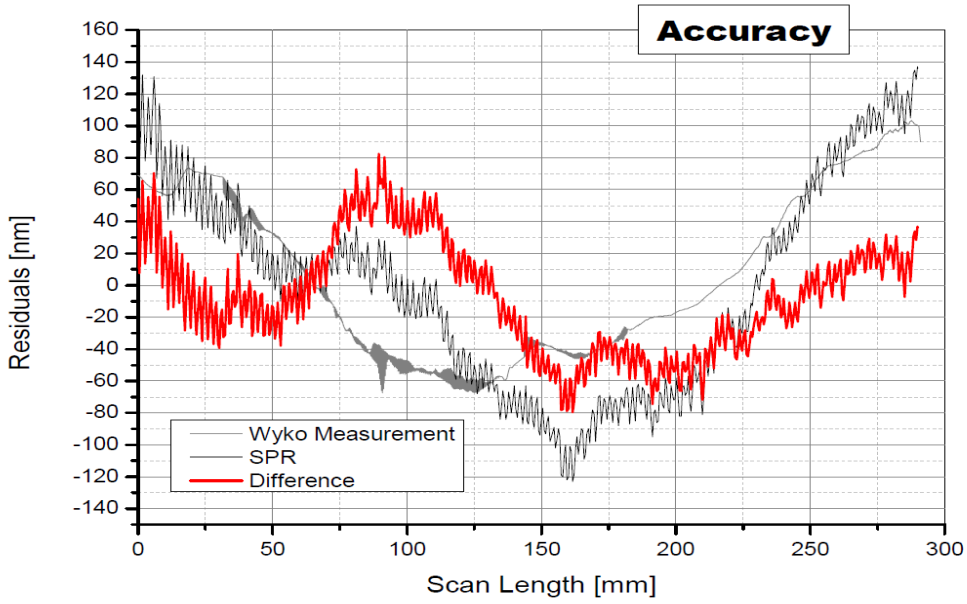

Figure 4-10. Comparison of reference bar measured with the SPR and with WYKO interferometer.

Table 4-2. SPR profilometer performance.

Maximum operative diameter	430 mm	**error on HEW estimation**	< 2 arcsec
Maximum operative length	600 mm	**Position resolution**	1 μm
Profile precision/repeatability	30 nm RMS [2 sigma]	**Vertical Alignment of the work-piece**	n.a.
Relative profile accuracy	Better than 250 nm	**Measuring time**	<5 min/profile (150 mm)

4.2.3 Long Trace Profilometer (LTP)

The LTP is a sensitive slope-angle-measuring instrument, based on the original concept of the pencil-beam interferometer of Von Bieren, and developed by P. Tackacs et al. The LTP measurement principle is simple (see Figure 4-11): two pencil Ne-He laser beams are scan the surface of a mirror and the reflected beam direction changes according to the local surface slope at that position. A Fourier transform lens converts the angle variation of the reflected beam in a variation of position in its focal plane. Another part of the beam is focused on reference surface, in order to subtract the tilting and rotation of the optical head. An advantage of such a configuration is a significant weight reduction of the movable part of the interferometer, and a side-mounting configuration for the surface under test (that greatly reduces the gravity induced deformation). The focused laser beam position is recorded by a linear array detector and, after a proper fit, the local slope of the mirror under test is obtained. With proper environmental conditions and periodic and precise calibrations of the instrument, LTP is able to measure slope profiles, with an accuracy better than 1 μrad rms.

Even if this instrument has a sensitivity to wavelength in the range from meters to millimeters and then cannot really measure the surface roughness, it is very useful in mirror realization as it is able to detect the shape imperfection of mirrors. It turns also to be a basic tool to measure the mirror substrate curvature (e.g. produced by multilayer stresses). The parameters to be optimized are related to environmental changes while measuring (mainly temperature stability and air turbulence along the laser beam path). The whole instrument is mounted on self-stabilizing, air-suspensions. These are necessary for isolation from the sound waves, propagating from the ground.

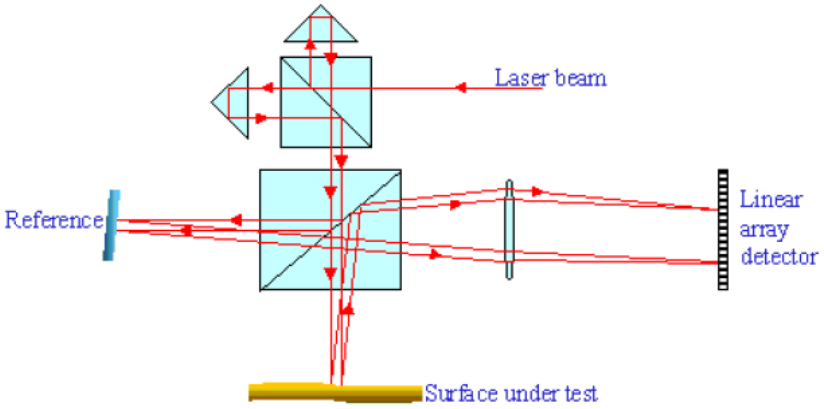

Figure 4-11. scheme of the Long Trace Profilometer LTP (credits: ELETTRA Synchrotron, Trieste).

4.2.4 Optical profilers for roughness (PROMAP, WYKO)

WYKO TOPO 2D profilometer is a 2D optical phase shift interference microscope available in INAF-OAB labs. Polychromatic light is collimated and filtered to be geared towards an interferometer, which produces two beams, one of which illuminates the surface of the sample to be measured and the other illuminates a reference sample. After the reflection, the two beams recombine in the interferometer and the resulting beam is directed toward a position-sensitive CCD detector. The profile of the surface is then obtained from the analysis of interference fringes. The instrument is equipped with 2 objectives having 20x and 2.5x magnifications, which give rise to a sampling of 1024 points on a scanning length of 0.66 mm and 5.28 mm respectively.

MICROMAP PROMAP 512 is a non coherent 3D optical phase shift interference microscope for mid-scale surface error characterization and micro-roughness measurements available in MLT. The instrument is equipped with 2 objectives having 40x and 2.5x magnifications. The main characteristics are:

- height resolution of 0.2 Å for both magnifications;
- repeatability < 1 Å (for 40x magnification) and < 0.6 Å (for 2.5x magnification);
- lateral spatial resolution of 0.55 μm (for 40x magnification) and 3.7 μm (for 2.5x magnification).

Figure 4-12. MICROMAP PROMAP 512 mounted in vertical position for mandrels measurements.

The maximum field of view of measurement is: 150 μm x 100 μm for 40x magnification, and 2.5 mm x 1.8 mm for 2.5x magnification (depending on the curvature of the optic).

4.2.5 Atomic Force Microscope (AFM)

Atomic Force Microscopes (AFM) are very sophisticated tools that enable characterization of optical surfaces on very high spatial frequencies. An atomic force microscope consists of a probe with a metal tip a few micrometers thick, monitored by a laser beam. The probe, by means of careful computer controls, is approached to a position on the sample: the interaction forces between the probe and the atoms of the surface under test cause a deflection of the cantilever where the probe is mounted on. At each height change, the probe changes position/oscillation frequency and phase, and this change may be monitored by a laser lever that amplify the oscillation. By scanning the sample surface, the AFM reconstructs the height 3D profile, with a few angstroms accuracy in height, and an horizontal accuracy up to 2-3 nm. The AFM can work either in "contact mode" (the interaction of the tip to the surface is stronger and the instrument has a better resolution but the surface can be damaged) or in "non-contact" (tapping) mode. The width (and the resolution) of the scans can be set at 100 μm, 10 μm, 1 μm. Every scan covers a 512 x 512 pixel matrix, so that the scan resolution varies between 0.2 μm and 2 nm.

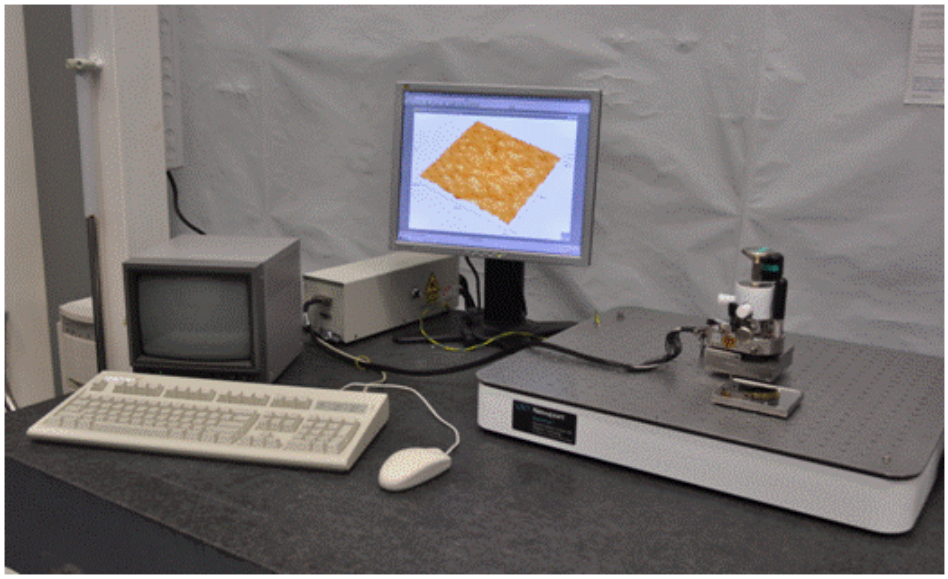

Figure 4-13. Veeco AFM installed in MLT and in INAF-OAB labs.

4.2.6 Phase contrast Nomarski microscope

The Nomarski microscope returns a surface image and it does not permit roughness measurements. Nevertheless, is it widely used to see the roughness of polished samples, and to understand the size and origin of surface defects. The Nomarski microscope produces a polarized, polychromatic light beam, which is split by a Wollaston Prism, producing two correlated beams with perpendicular polarizations. A lens focuses the two beams at two positions on the surface under test, separated by one-micron distance. If a surface defect is present, the two beams will be reflected with two different phase changes. After a further polarization plane rotation, the beams interfere in the image plane. The phase variation appears in the variable brightness of the image, returning a surface map with a sensitivity of 1 nm. The space resolution is near to the used light wavelength, i.e. 0.22 μm. Many magnifications are selectable (from 5x up to 100x) and the phase difference may be shifted in order to highlight the features at the most interesting height.

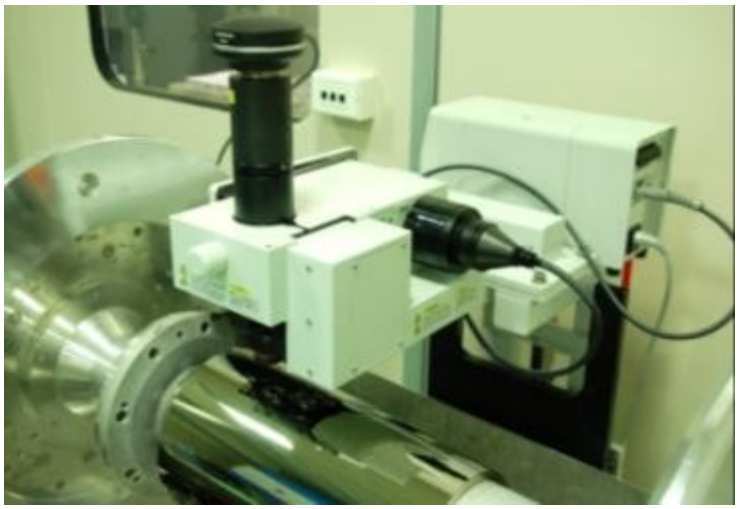

Figure 4-14. Nomarski phase contrast microscope set-up in MLT to inspect the mandrels in horizontal configuration.

4.2.7 X-ray Diffractometer (XRD)

The diffractometer installed at the INAF-OAB is a product of British firm Bede Scientific. It is a three-axis diffractometer, based on a conventional bremsstrahlung x-ray source, by which it is possible to perform scattering and reflectivity measurements. This facility is being particularly

used to test the multilayer samples X-Ray Reflectivity (XRR) as a diagnostic tool to infer the layer thickness and the roughness.

Experimental apparatus

The diffractometer is based on collimated monochromatic pencil beam radiation and consists of an x-ray tube, a series of crystals for the collimation and the monochromatization, a goniometer to attach the samples and an x-ray photon detector.

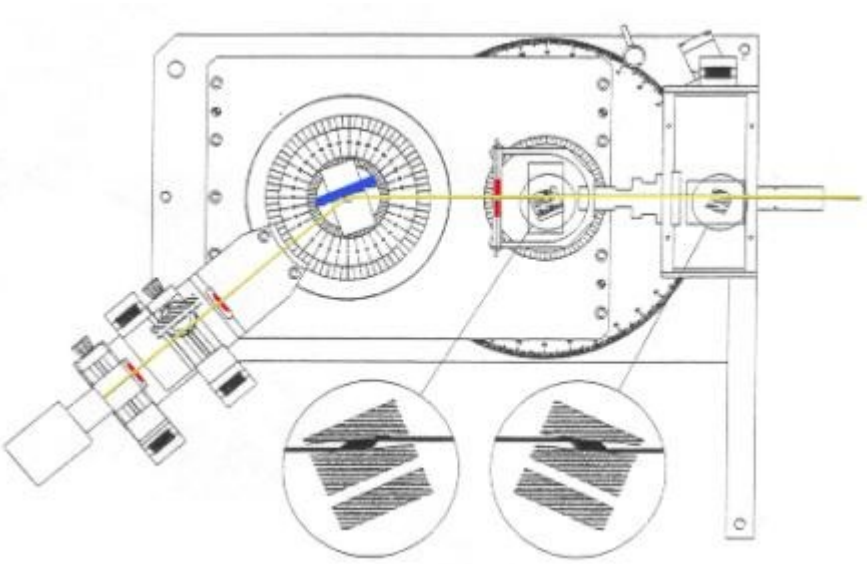

Figure 4-15. Scheme of the x-ray diffractometer Bede installed at INAF-OAB used for the characterization of single and multilayers The yellow line shows the path taken by radiation from the source to the detector, the slits, that are used to determine the size of the beam, are indicated in red and the location of the sample is indicated in blue. Magnification below refers to crystals used for the monocromatization and the collimation of the beam.

Sample and detector can rotate independently to carry out measures of non-specular reflection, or rotate simultaneously in a configuration $\theta/2\theta$ for measurements of specular reflectivity at different incidence angles. The angular size of the slit in front of the detector, is important to determine the maximum angle of non-specular reflection considered.. If *R* is the distance between the sample and the detector and δx are the linear dimensions of the slit, the maximum angle of scattering, measured relative to the normal of the surface of the sample, is given by $\delta\theta = \delta x/2R$.

Röngten type x-ray tube

The radiation source of BEDE diffractometer consists of a Röngten type x-ray tube. The radiation is created inside a vacuum tube, colliding a beam of electrons accelerated by a linearly potential difference against a target, which acts as the anode. If the energy of the electrons is sufficient, x-rays will be produced for bremsstrahlung, consisting of a continuous spectrum plus the characteristics emission line of the material.

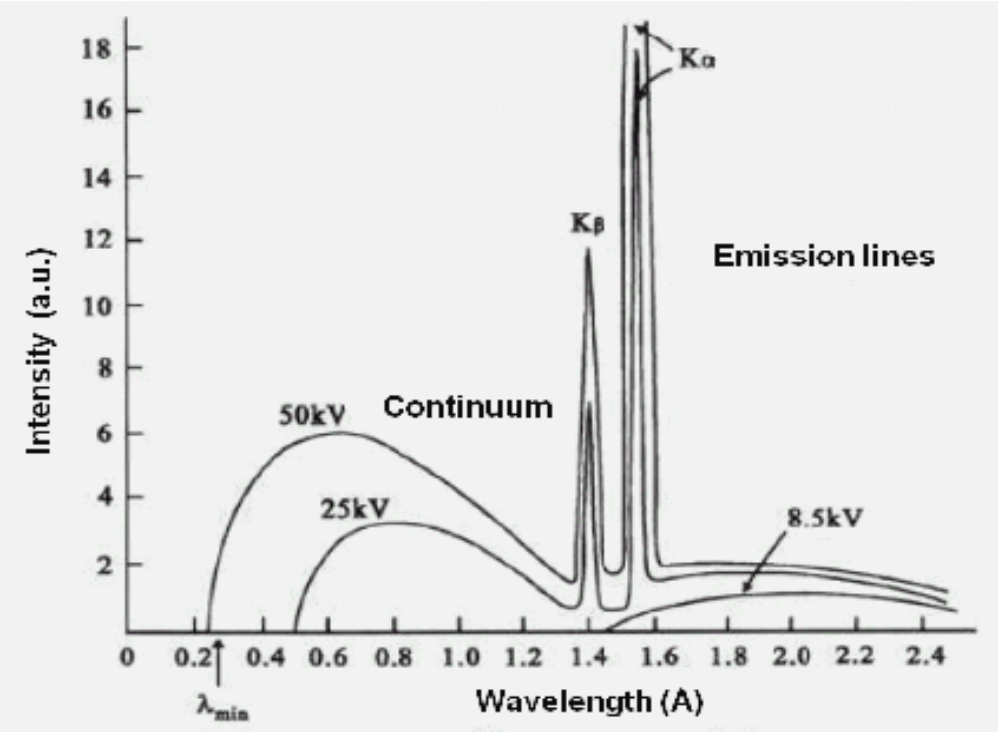

Figure 4-16. Spectra of radiation emitted by bremsstrahlung from a tube type Röngten with copper anode for some values of potential difference. For electrons with energies below about 10 keV you do not have the activation of the K emission lines of copper.

In the system adopted by INAF-OAB there are two sources, one with a copper anode, which K_α line has an energy of 8.05 keV, and a Molybdenum anode, which K_α line has an energy of 17.47 keV. The quite limited distance (90 cm) between the source and detector, and the high energies provided by K_α emission line, are such as to allow of neglecting the absorption of air and therefore to not work in vacuum conditions. Röngten type x-ray tubes are limited to a maximum intensity of radiation around 10^{10} *photons/sec·mrad*^{2}*·mm*^{2}, 9 to 10 orders of magnitude less intense than synchrotron radiation sources.

Collimation and monochromatization system

In order to test the statistical properties of a surface, the continuum radiation emitted from the source needs to monochromatized obtaining a pencil beam consisting solely of the K_α line. The monocromatization is done through the Bragg diffraction, by using one or two Silicon channel cut crystals in non-dispersive geometry, at the energy of the K_α of the anode used.

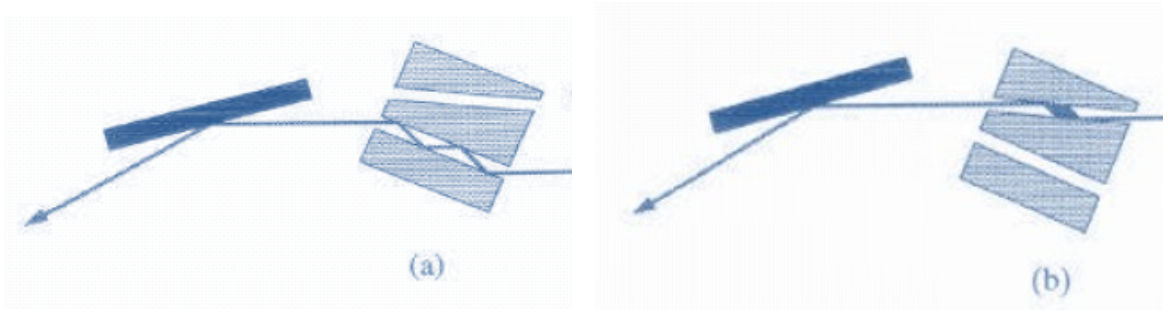

Figure 4-17: Monocromatization through Silicon channel cut crystals (CCC). Two types of channels can be used: a) high-resolution channel; b) high intensity channel.

The Crystal has two channels, one to cut parallel to the (0, 0, 2) orientation of the lattice planes (high intensity channel) and one with an asymmetric cut (high resolution channel). In the high-resolution configuration there are four reflections and at the exit there is a divergence angle of approximately 8 arc seconds (FWHM). In the high intensity configuration, there are only two reflections and the angular divergence is approximately 20 arc seconds (FWHM).

Photons Detector

The detector used is based on a Crystal scintillator YAP(Ce) coupled to a photomultiplier. Detection efficiency can be optimized for two different energies, through the control of voltage and sensitivity thresholds. With a suitable choice of parameters of the detector, you can have a background noise of 0.3 counts per second, over an integration time of 10 seconds. The detector maintains a good linearity up to 300000 counts per second, but can also be used at higher intensities, extracting the exact number of counts, prior to measurement, through the extinction of the beam by a material of known absorption coefficient.

The detector can also be replaced with a camera, very useful to align the optical axis.

4.3 Calibration of the multilayer optics at the PANTER facility of MPE

A facility suitable to calibrate X-ray optics is the PANTER facility in Neuried (DE), an X-ray tube that permits the optics full-illumination with an almost parallel beam up to 50 keV, thus reproducing the approximate operative conditions of the hard x-ray telescopes. The facility was planned in the late seventies to accompany the development and realization of the ROSAT mirror system. The PANTER facility, able to provide a wide, low-divergence x-ray beam for the characterization of x-ray astronomical optics, can be considered unique in Europe. Soon after its construction it turned out that such a facility is absolutely necessary for realizing x-ray telescopes: so the PANTER facility was used for the calibration of x-ray telescopes optics like EXOSAT, Beppo-SAX, ROSAT, XMM, JET-X/SWIFT.

4.3.1 The PANTER facility

For x-ray telescopes calibration, the ideal situation would be an x-ray source at infinite distance. Being this impossible, a wide, collimated x-ray beam can be approximately obtained placing an x-ray source at very large distance. The PANTER (see Figure 4-18) is constituted by a high vacuum tube 125 m long and 1 m wide tube connecting an x-ray source (from 4.5 to 50 keV) to a clean room, where experiments are dealt. The possibility of performing full-illumination tests also up to 50 keV is very important to allow reliable and easy to make calibrations of hard x-ray optics. The low divergence achievable (0.064° for a mirror shell of 300 mm in diameter placed at the entrance window of the testing chamber) is a very important parameter since the typical reflection angles of hard x-ray optics are very small (0.1° - 0.3°). The tube length was adapted to the optical properties of ROSAT and was sufficient for the experiments in the 70s, but now the beam divergence has to be taken into account.

The clean room (class 1000, 12.5 m long and 3.5 m wide) hosts a set of x-ray detectors: the optics under test are placed in the clean room, at the x-ray front end, and their position can be adjusted by a set of manipulators driven by stepper motors. Tube, chamber, source are kept under vacuum (10^{-6} mbar, obtained with turbo-molecular pumps located at four distinct pumping stations). Moreover, two cryopumps connected to the clean room reduce the water vapour partial pressure, in order to avoid the formation of ice on the cooled CCD cameras.

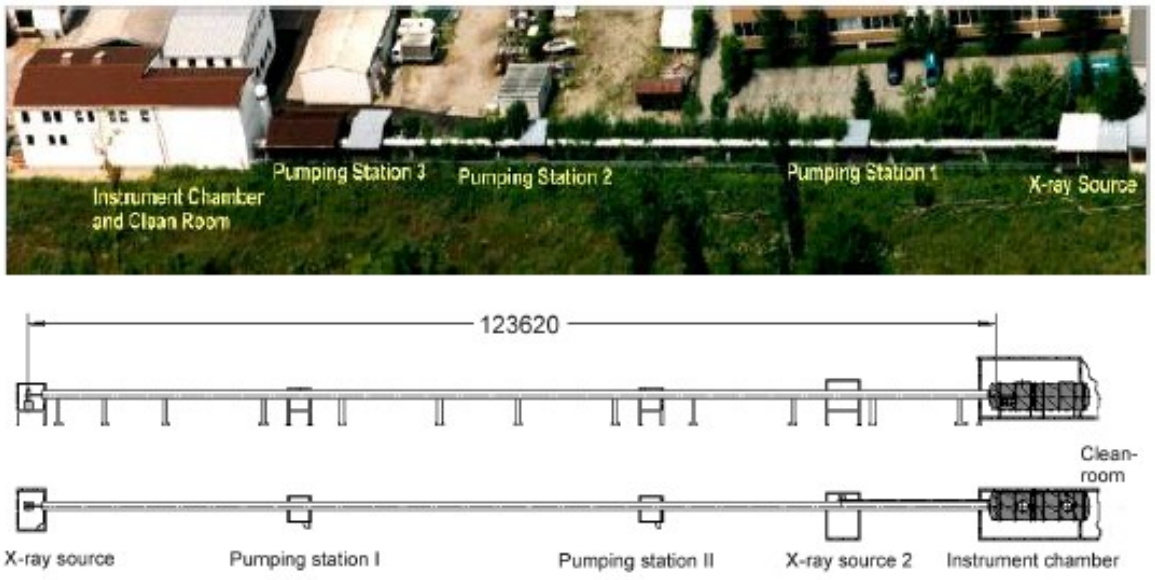

Figure 4-18. (top) Air view of the PANTER facility at MPE (credits: MPE, Max Planck Institut fur Extraterrestrische Physik). (bottom) Scheme of the x-ray tube of the PANTER facility (side and top view). The tube length is 123620 mm (credits: MPE).

4.3.2 X-ray sources

Four different X-ray sources are available at PANTER, with 16 different targets (elements). Typical fluxes are 5000 counts/sec/cm2 in the chamber, depending on the target material. The spectrum of each source is a typical bremsstrahlung one (with a cut-off energy corresponding to accelerating power of the x-ray tube) superposed to the fluorescence lines typical of the adopted target material between 0.28 and 8.05 keV. By means of different absorption filters, the spectrum can be modified by suppressing some part of the continuum or some X-ray fluorescence lines.

For very high fluxes, a commercial (sealed) source is also available. This source provides a couple of x-ray lines between 4.5 and 22 keV, plus a bremsstrahlung component that may cover the spectral range from 4.5 and 50 keV. The continuum component source can be measured with the pn-EPIC detector that, considering its good energy resolution, allows a broad-band measurement (energy-dispersive mode). In our case, the measurements are performed using either the emission lines or the continuum. A preliminary calibration of detectors is usually performed with sharply monochromatic radiation, thus two monochromators are installed at

the PANTER facility. One is a tunable reflection grating and is used as a monochromator covering the energy range 0.2 - 1 keV (or 2 keV, using the second orders), or a tunable double crystal monochromator from 1.5 up to 25 keV; both filter the continuum radiation coming from a Molybdenum or Copper target of an open x-ray source, with a spectral resolution better than 4% .

4.3.3 X-ray detectors

Two energy-sensitive detectors are usually used at the PANTER facility: a model of the ROSAT PSPC (Position Sensitive Proportional Counter, energy resolution 30% at 1.5 keV, spatial resolution 250 μm) working up to 10 keV, and a pn-EPIC CCD camera. The pn-EPIC has a better energy (145 eV @ 6 keV) and spatial resolution (150 μm) than the PSPC and it can operate up to 50 keV. Also a CCD camera with higher spatial resolution may be used (a predecessor of the EPIC MOS camera on-board XMM) but it can operate only up to 8 keV. Others proportional counters are distributed along the vacuum tube in order to monitor the X-ray beam uniformity. For the hard x-rays measurement we have adopted the pn-CCD camera, even if its quantum efficiency rapidly drops after 10 keV (3% at 50 keV) and in spite of its medium spatial resolution, since we were interested mainly in the hard x-ray optics efficiency reflection. The pn-EPIC camera low quantum efficiency beyond 10 keV can be compensated by increasing the exposure time.

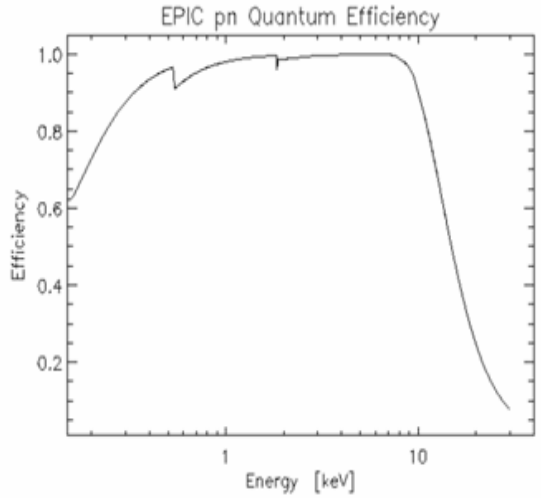

Photon Energy	Quantum Efficiency
10 keV	*89.1 %*
20 keV	*25.1 %*
30 keV	*8.6 %*
40 keV	*4.7 %*
50 keV	*3 %*

Figure 4-19. Quantum efficiency of EPIC pn-CCD detector as a function of the energy.

A very important point to be checked is the x-ray beam uniformity: four detectors (area 36 cm²) at the entrance of the tube are thus used to monitor the spatial constancy of the count rate (one of them can be even be moved in two dimensions to this aim). Another movable detector (area 2.5 mm²) is located at the tube end, near to the x-ray source.

It should be noted that for focal lengths larger than 8 - 9 m the optics to be tested could be placed directly into the x-ray tube connecting the testing chamber to the x-ray source.

Figure 4-20. (left) The mirror shell measurement setup for the x-ray optic reflectivity measurement (focal length < 9 m). The mirror shell is integrated in front of the x-ray beam emerging from a hole in the shutter. A system of screens, driven by motors, can be used to limit the beam. (right) The setup for x-ray optic reflectivity measurement with focal length larger than 9 m. The integrated optic has been mounted inside the x-ray tube, together with a special optic manipulator.

4.3.4 PANTER set-up for measurement in the hard X-ray (> 15 keV)

Two possible setup can be used to extend the operative range of the PANTER facility over 15 keV: the monochromatic x-ray mode and the energy-dispersive mode.

Monochromatic x-ray mode: a monochromatic x-ray source is constituted by a special water-cooled x-ray open tube with changeable anode targets (Cu or Mo), operating up to 50 kV and 60 mA: the size of the anode focus spot is 1 mm diameter, and the emitted x-rays enter the monochromator chamber through a thin Beryllium window (thickness 8 μm, diameter 4 mm, usually closed, but manually removable for low- energy operations). The monochromation is devoted to a couple of crystals that can be rotated to tune the reflected energy: the second

crystal is shifted parallel to the first one simultaneously to the rotation in order to preserve the beam offset. The main limitation to the radiation monochromaticity is the beam divergence (~0.4°): the pair of crystals adopted at PANTER are HOPG (0,0,2), Si (1,1,1). Usually the HOPG crystals are used due to their lower absorption: they are constituted by mosaic structure with mosaic spread 0.3°, able to guarantee a very large integral reflectivity. The choice of a mosaic spread smallest as possible allows to obtain a large intensity of the reflected beam while keeping a large intrinsic energy resolution, which is mainly determined by the beam divergence. HOPG crystals are used over 2 keV, while for energies beyond 15 keV the beam is produced with the Mo anode and monochromatized at the 2nd Bragg peak, returning a resolution of 3%: typical intensities provided by the HOPG monochromators are 100 *counts sec^{-1} cm^{-2}* at 3.5 keV and 600 *counts sec^{-1} cm^{-2}* at 8 keV for the first order at the entrance of the test chamber.

Energy-dispersive mode: it is a very practical way to operate in hard X-rays; a broad-band x-ray beam illuminates the optics to be tested, and the focused photons are collected by the pn-CCD camera. The very good energy resolution of this device (2.5 % at 6 keV and improving proportionally to the square root of the photon energy) allows to derive a broad-band mirror reflectivity with a single exposure. The poor quantum efficiency of the pn-CCD camera can be compensated by long integration times and high incident fluxes, like those produced by the x-ray source with Tungsten anode, operating up to 60 kV (see Figure 4-21). The bremsstrahlung component of this source is thus perfectly suitable to cover the hard x-ray spectrum from 4.5 to 50 keV (with achievable fluxes of 3500 *photons sec^{-1} cm^{-2}* in the 10 40 keV energy range).

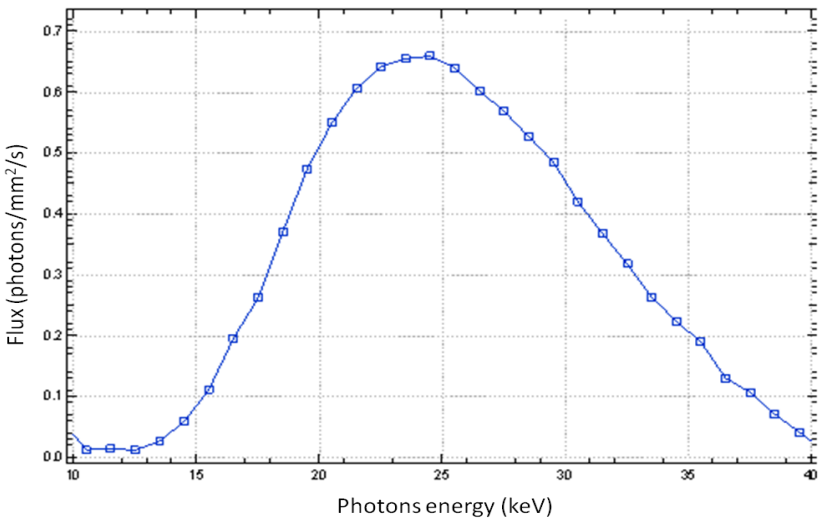

Figure 4-21. Tungsten anode bremsstrahlung continuum emission.

4.3.5 Effects of finite distance in PANTER

Although the PANTER facility is now the best available approximation of an x-ray celestial source, the finite distance has some important the effects on the optical properties of x-ray Wolter I mirror shells.

- Focal length displacement: for a source at infinite distance (case of celestial point source), the angle defined by the direction of the focused beam with the optical axis is equal to 4α, and the focal length is given by:

$$f_{\infty} = r / tg(4\alpha) \tag{4.30}$$

where is the angle of incidence on the mirror and r is the medium radius of the mirror. Now, if the source point is located at a finite, the angle defined by a focused photon and the optical axis is equal to 4α-β (see Figure 4-22), thus leading to:

$$f = r / tg(4\alpha - \beta) \tag{4.31}$$

At the PANTER facility the distance X_S between the x-ray source and the mirror is about 123 m and the angle of divergence β depends on the medium radius of the mirror $\beta = r / Xs$. Consequently in PANTER there is an increase w.r.t. the nominal focal length of the mirror.

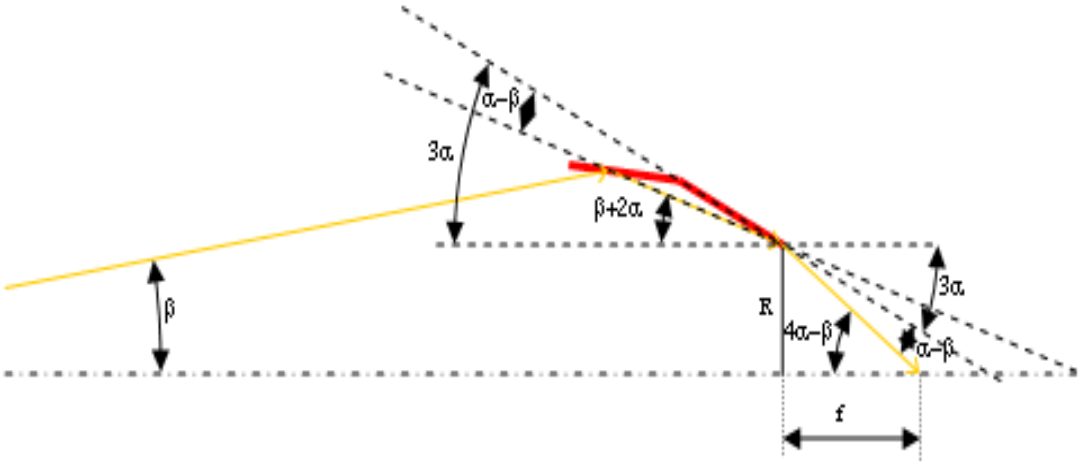

Figure 4-22. Incidence angles in the case of finite source distance. The source is located at the left side and the photons trajectory is represented by the yellow line (the mirror is the red line).

- Effective area reduction: Wolter I optics are usually designed to reflect at the same grazing incidence angle on both paraboloid and hyperboloid, and the two segments have the same length, so that all the on-axis incident rays on the paraboloid are reflected also by the hyperboloid. If the source has a finite divergence, the reflected rays at the paraboloid front, that should strike the hyperboloid back, miss the reflection on the hyperboloid (see Figure 4-23), thus they are not collected in the optics focus (they would be concentrated in a point at a distance 2*f*, but in a complete optic, the dense shell nesting would stop these single-reflected rays), thus a fraction of the optics effective area would be lost. The percentage of the lost geometrical area A_L can be calculated with the following formula:

$$A_L = 1 - \frac{X_S - 4f}{X_S + 4f} = 1 - \frac{\alpha - \beta}{\alpha + \beta} \tag{4.32}$$

This formula tells us that the higher the divergence β the higher the percentage of area that we are losing. For example, for a mirror having an incidence angle of 0.2° and a diameter of 300 mm, the percentage of the lost geometrical area can reach the 50%.

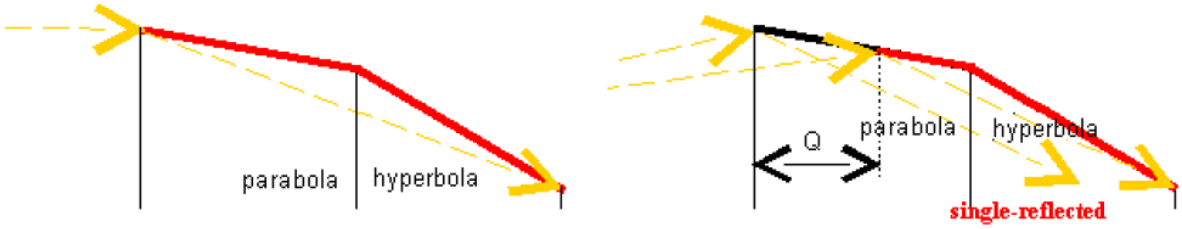

Figure 4-23. Lost illuminated area (Q) by effect of the finite source distance.

- Incidence on the paraboloid and hyperboloid at two different grazing angles: x-rays that undergo a double reflection incise on the paraboloid and on the hyperboloid at two different grazing angles: in particular if α is the incidence angle for a source at infinite distance and β is the beam divergence, the incidence angle on the paraboloid will be α+β and on the hyperboloid α-β.
  For single-layer coated optics, this is not a serious problem, provided that both angles are lesser than the layer critical angle: since the grazing angles at the two surfaces vary in opposite directions, the product of the two reflectivity remains more or less constant.
  For broad-band multilayer coated optics, the situation can be not so critical also, since

the incidence angle variation shifts the energy band of the reflectivity curves, but the product of the two single reflectivity will be non-zero if the band shift is small with respect to the overall multilayer bandwidth, thus the zero-divergence effective area can be recovered from data. The situation is different, instead, for narrow-band multilayer coatings, and since the two Bragg peaks can be located at two different energies, the product of the two reflectivity can vanish: thus, in this case it would be impossible to derive a mirror characterization in hard x-rays.

- Focal point blurring: the finite source distance causes also an intrinsic image blurring. The rms σ_D of the point image (i.e. the angular radius including 68 % of the collected energy) may be expressed by the approximate, semi-empirical formula (Van Speybroeck, 1972):

$$\sigma_D = 4\frac{L_P}{f}\tan\left[\alpha\left(\frac{f}{X_S}\right)^2\right] \tag{4.33}$$

where α is the grazing incidence angle and L_P the length of the single reflection surface (either paraboloid or hyperboloid). The measured rms σ_m is thus $\sigma_m^2 \approx \sigma_D^2 + \sigma_\infty^2$. Here σ_D is the true rms that would degrade the image of a celestial x-ray source, thus the true optical performances can be better than the observed ones in the calibration with full-illumination setup: this effect can be important in the calibration of high-resolution optics, like those of Chandra (HEW ~ 0.5 arc seconds) or the future IXO/ATHENA optics (HEW ~ 5 arc seconds).

5 Development of an advanced polishing technique for X-ray mandrels

The mandrels manufacturing holds a crucial role in the process of mirrors fabrication via the replication techniques. As one can expect, the angular resolution and the reflectivity of the replicated mirrors are strongly affected by the mandrel starting quality. The basic mandrels manufacturing tolerances can be derived from some general consideration on the x-ray mirror performance requirements:

- the waviness and the roughness of the mirrors has to be lower than 0.5 nm rms (for spatial wavelength below 2 mm). Hence the surface finish of the mandrels shall not be higher than 0.3 - 0.4 nm rms (in the same spatial wavelength range);
- the angular resolution of the mirrors shall be 15 arc seconds HEW or better. Replicated mirrors with performance in this range have been obtained in the past by using mandrels with superior accuracy (i.e. typically a factor of two or more better).

I worked on an evolution of the approach used for the manufacturing of the **past mission** x-ray mandrels (e.g. XMM-Newton) in the last years for enabling the eROSITA and NHXM missions. Within that past approach the mandrels were machined from a solid block of a special aluminum alloy and coated with a Nickel-Phosphorous (NiP) alloy before being grinded/shaped and superpolished.

The **multistep surface finishing process I worked on and here described**, consists in the replacement of the classical machining/grinding of the mandrels in favour of Single Point Diamond Turning (SPDT), and in the implementation of a sequence of 2 polishing steps including the classical superpolishing:

- with the SPDT technology it is possible to obtain, at the same time, a good angular resolution (< 10 arcsec HEW) and a low surface roughness (~ 15 nm rms);

- with the first polishing step it is possible to remove the Diamond Turning (DT) marks and to improve both the angular resolution (< 5 arc seconds) and the surface finish (~ 1.5 nm rms);
- with the second polishing step it is possible to improve the mid-frequencies and the roughness, down to the requested values, without degrading the angular resolution.

The benefit of the newly developed process can be seen in Table 5-1 by comparing the performance of some mandrels manufactured using the new approach (NHXM 297, NHXM 350 and eROSITA 25) with some of the past mandrels manufactured without DT and without corrective polishing (NHXM 291 and NHXM 286).

The HEW performance of the mandrels manufactured using the new approach is now consistently below 6 arc seconds, and the roughness is maintained to the required level and in some cases improved due also to the higher quality NiP coating implemented.

Table 5-1. Shape and roughness performance comparison between some mandrels manufactured with the new approach described in this thesis (NHXM 297, NHXM 350 and eROSITA 25) and some previous mandrels (NHXM 291 and NHXM 286)

Mandrel	**HEW**	**PROMAP** [2mm]	**AFM 100** [100 μm]	**AFM 10** [10 μm]	**AFM 1** [1 μm]
NHXM 291	13.1"	0.81 nm	0.38 nm	0.30 nm	0.20 nm
NHXM 286	8.2"	1.07 nm	0.52 nm	0.43 nm	0.35 nm
NHXM 297	4.7"	0.40 nm	0.36 nm	0.31 nm	0.22 nm
NHXM 350	5.9"	0.45 nm	0.32 nm	0.28 nm	0.21 nm
eROSITA 25	5.3"	0.33 nm	0.38 nm	0.36 nm	0.22 nm

5.1 Mandrels blanks preparation

5.1.1 NiP coating

The core material of the x-ray mandrels consists of aluminium; this is because the thermal expansion of the aluminium is higher w.r.t. to the electroless Nickel of the mirror shells and this permits the separation of the mandrel from the mirror shell by cooling. Anyhow, **the mandrel** surface **shall be superpolished** down to nanometric level, and **aluminium does not permit** to reach such roughness quality. **This is the reason why the mandrel is coated with electroless NiP coating, a material well suitable for superpolishing**.

Electroless-nickel plating is also known as chemical or autocatalytic nickel plating. **In contrast to the electroplating (galvanic) technique, electroless-nickel plating baths work without an externally applied electric current. The plating operation is based on the catalytic reduction of Nickel ions onto the aluminium mandrels.** The electroless-nickel process deposits uniformly hard amorphous coatings on any section of a part exposed to fresh plating solution. NiP quality depends on the characteristics of the substrate used and on the post-deposition thermal treatment. The NiP coating must be free of porosity, that can come from the gas released during the process. These imperfections can cause problem during the replication of the mirror shell, through the sticking forces that they could create in the correspondence of these points.

A good quality NiP coating can be defined by the following parameters:

- thickness uniformity;
- low porosity;
- homogeneous hardness;
- limited nodular growth;
- high adhesion to the substrate;
- high content.

The NiP coating is an industrial process but the specifications for the x-ray mandrels application are very stringent. **I worked on the qualification of a suitable NiP coating and on the definition of the procurement specification**. The process is an electroless process generating high percentage Phosphorous amorphous coating material with no particular nodular growth.

In order to qualify the NiP coating process, I used the flight-quality mandrel NHXM 297. The mandrel has been successfully polished (by using the approach described in this Chapter, see also § 6.1) down to about 0.4 nm rms - between 2 mm and 0.05 mm wavelengths range - and 0.2 nm rms - between 0.2 mm and 0.002 mm wavelengths range. These results show that the necessary texture level can be obtained by using a NiP coating having the above characteristics.

In the past, due to the fact that the mandrels are subjected to temperature change between 10°C and 50 °C during the mirror shell production cycle, there has been some evidence of print-through effect coming up from the aluminium blank to the NiP surface, reflecting in a degradation of the texture. The absence of this print-through effect has been verified by now, by subjecting the NHXM 297 mandrel to 5 thermal cycles between 5°C and 60°C as depicted in the graph here below (Figure 5-1).

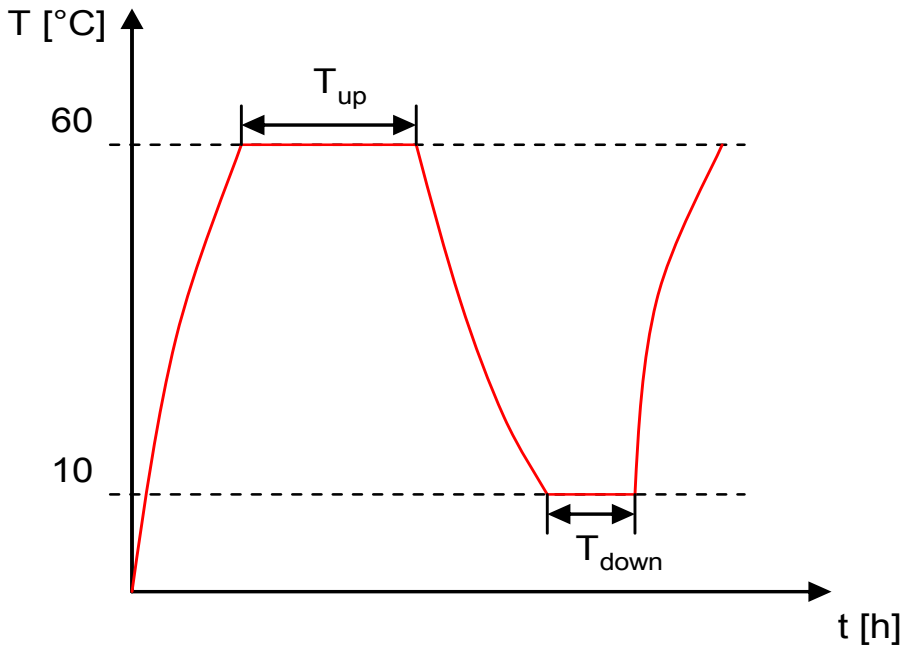

Figure 5-1. Thermal cycle applied to the prototype NiP coated mandrel

The mandrel has been installed in a climatic chamber inside its own transport container under Nitrogen atmosphere. Two thermocouples have been installed at the centre and the top of the mandrel for recording the temperature. A picture of the mandrel with the thermocouples is provided below (Figure 5-2) as the tracks recorded during the thermal cycling (Figure 5-3).

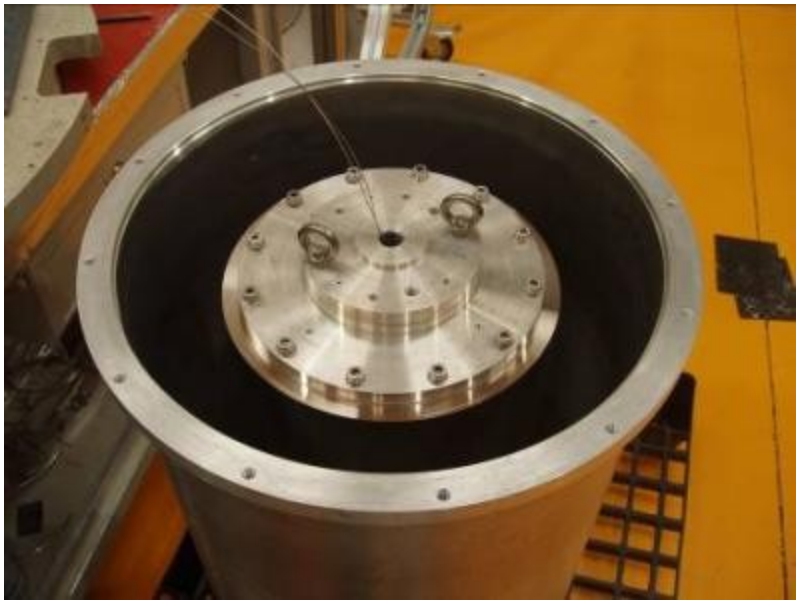

Figure 5-2. Installation of the thermocouples on the prototype mandrel for the thermal cycle.

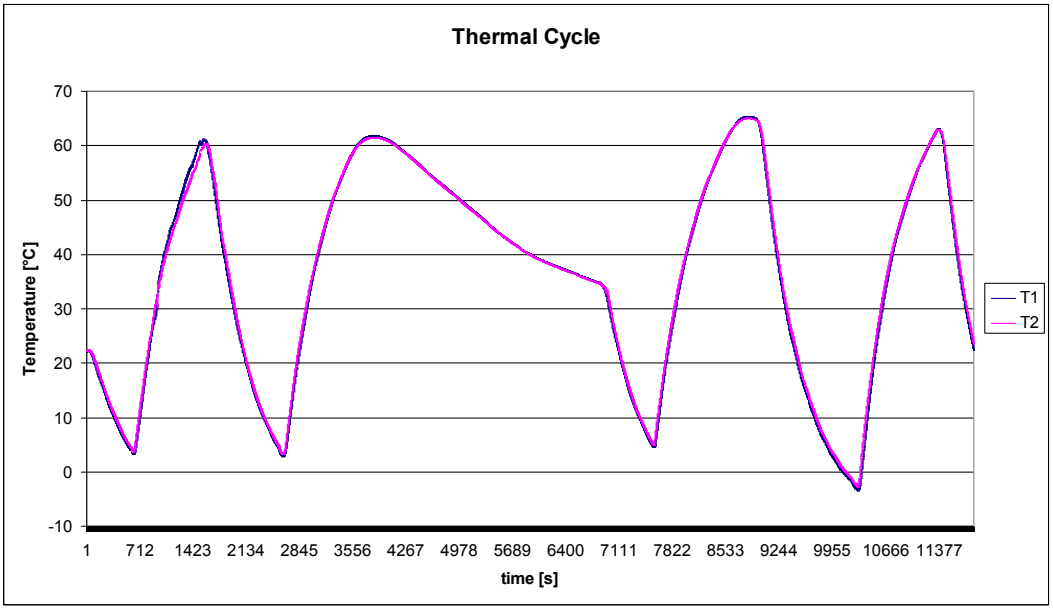

Figure 5-3. Temperatures recorded by the thermocouples placed on the mandrel.

Based on the results from PROMAP measurements on significant areas of the mandrels (shown in Figure 5-4 and Figure 5-5) it can be observed that the coating roughness is not affected by temperature cycling.

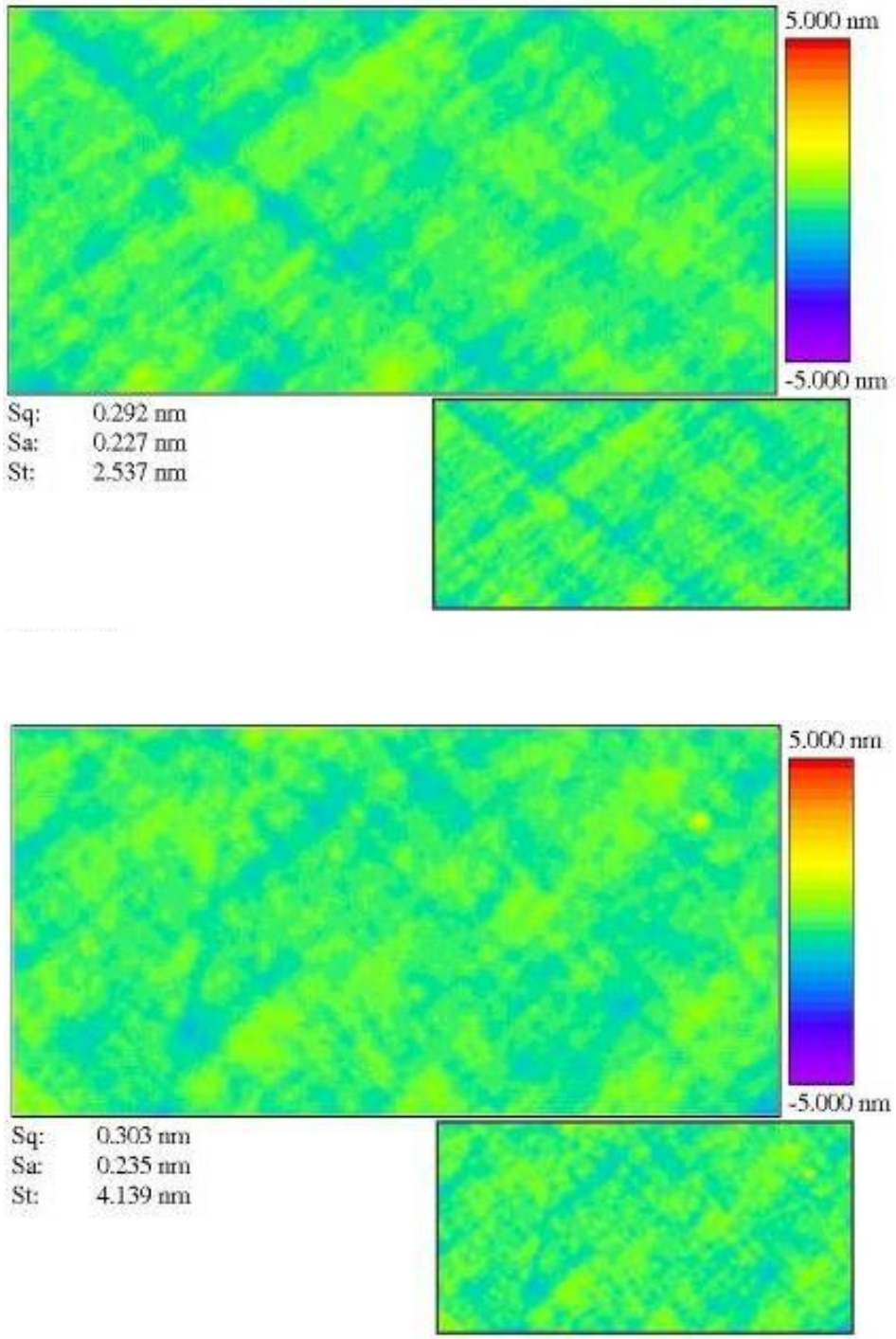

Figure 5-4. Roughness measurements PROMAP 2.5x (2mm x 1mm area) before (picture above) and after the 5 thermal cycling (picture below).

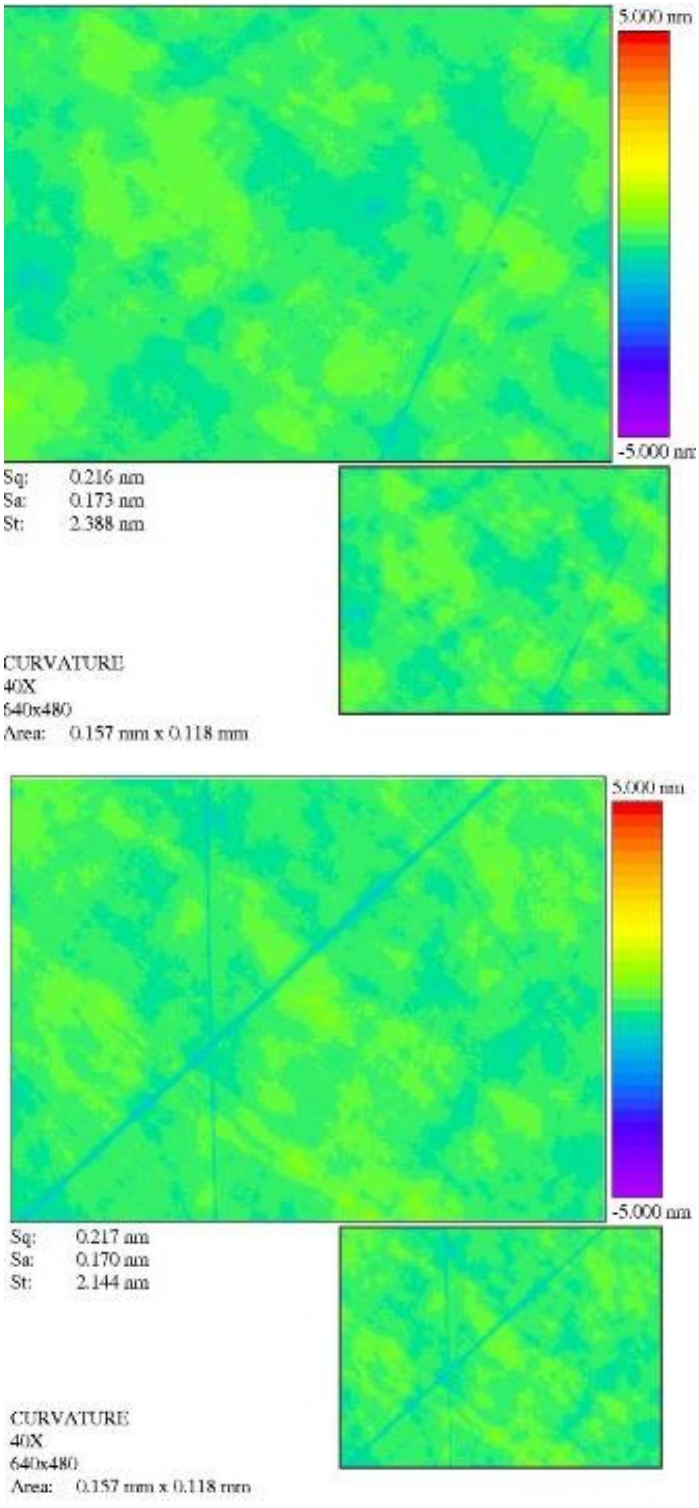

Figure 5-5. Roughness measurements PROMAP 40x before (picture above) and after the 5 thermal cycling (picture below).

5.1.2 Diamond Turning

Single-Point Diamond Turning (SPDT) is a machining process making use of a monocrystal diamond cutting tool which possesses nanometer edge sharpness, form reproducibility and wear resistance. The depth of cut in SPDT is in the order of the micrometers. The Diamond Turning (DT) is the process aimed to ensure high profile accuracy together with low surface roughness on NiP coated mandrels. The surface roughness is driven by the depth of the DT marks. Stringent thermal controls are mandatory during this operation to reduce figuring errors due to tool positioning and mandrel thermal expansion.

I worked on the development of DT technology and its extension to the x-ray mandrels geometry and requirements. Accuracy of DT has been assessed in order to validate the feasibility study of the process. Improvements and adjustments to the process has been identified and implemented directly on the DT machine. The main objective was to characterize the axial slope error accuracy of the DT when applied to the x-ray mandrel geometry.

A flight quality mandrel, representative of the weight and dimension of x-ray mandrels for NHXM has been subjected to DT with subsequent in-house metrological inspection. The axial profile accuracy has been measured by using high accuracy profilometer available at INAF-OAB labs. The mid-spatial frequencies and the roughness have been measured with PROMAP instruments:

- The accuracy of the DT machining is remarkable with a typical error of ± 150 nm over 300 mm length of the mandrel, with some residual features in the range of 10 mm wavelength (see Figure 5-8). Another remarkable aspect is the accuracy in the cylindrical symmetry leading to almost identical axial profiles; this is an ideal starting condition to perform the corrective polishing (Figure 5-6).
- The axial slope error distribution after DT is provided in the Figure 5-9; the median of the slope error (δ50) is 1.4 arcsec leading to HEW prediction of 8 arcsec.
- The roughness of the surface after DT is in the order of 15 nm rms, and it is dominated by the grooves left by the diamond tool. The Peak-to-Valley of the surface is below 100 nm and the pitch of the grooves is 10 μm. In Figure 5-10 some roughness measurements taken with PROMAP 40x objectives are reported; the field of view of these measurements is 0.15 mm x 0.1 mm.
- The mid frequencies (mm range) after DT are below 10 nm rms. The Peak-to-Valley of the surface is below 100 nm and the pitch is between 1.5 and 0.5 mm. In Figure 5-11

some roughness measurements taken with PROMAP 2.5x objectives are reported, the field of view of the measurements is 2.5 mm x 1.8 mm. Figure 5-12 shows a profile extracted along the optical axis direction from the PROMAP 2.5x measurements, where the mid-frequency error are clearly visible.

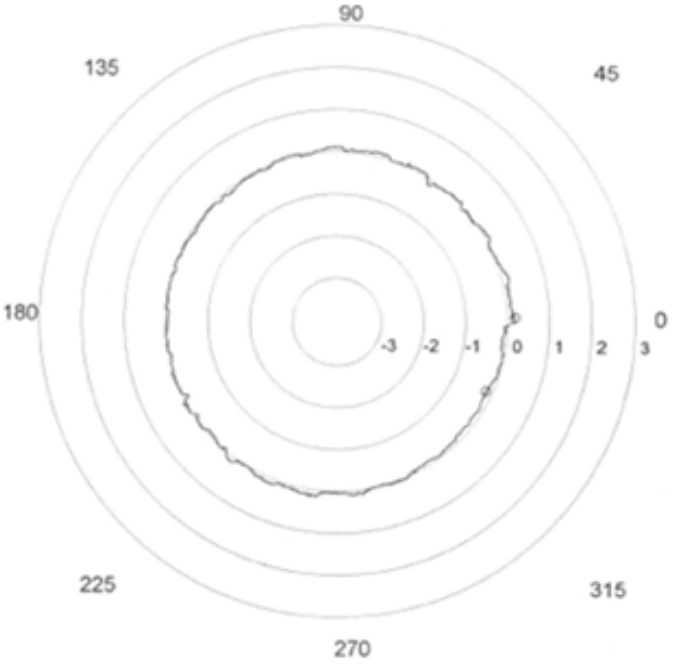

Figure 5-6: Out of roundness measurements giving 0.2 μm PtV.

Figure 5-7. Prototype mandrel after DT, the rainbow effect of the grating is visible.

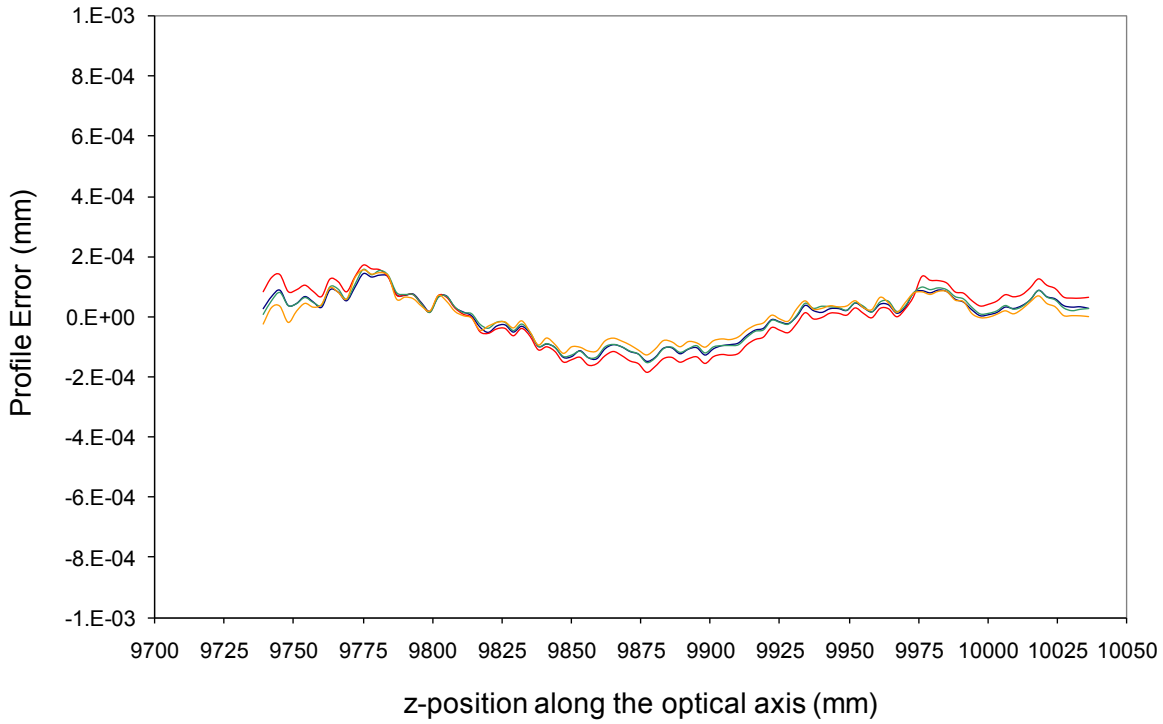

Figure 5-8. Axial profile errors measured after the DT along 4 axes (0, 90, 180 and 270 deg).

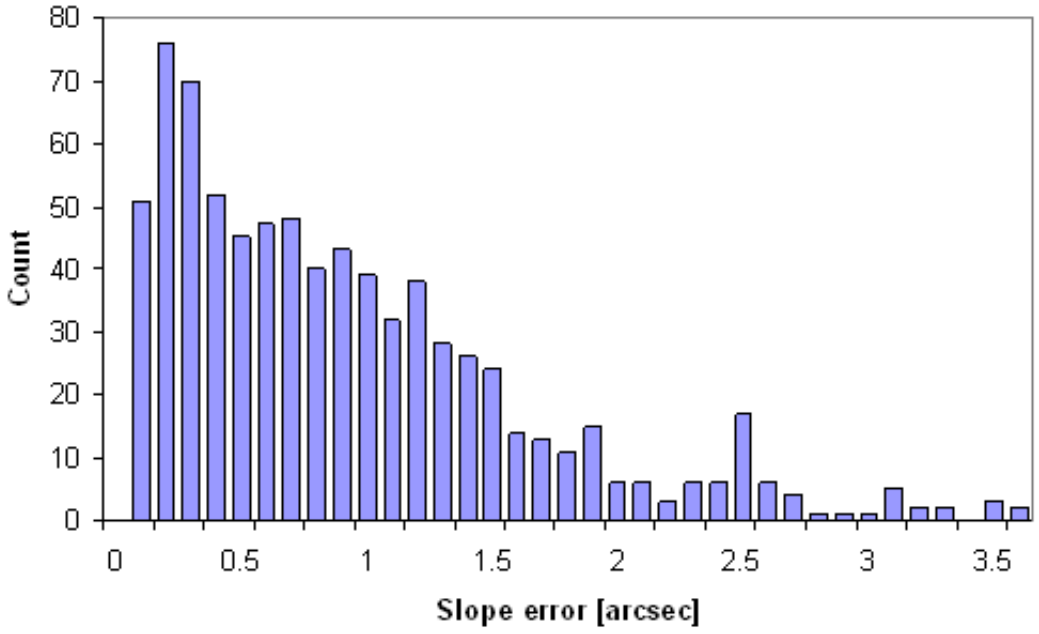

Figure 5-9. Axial profile slope error distribution after the DT.

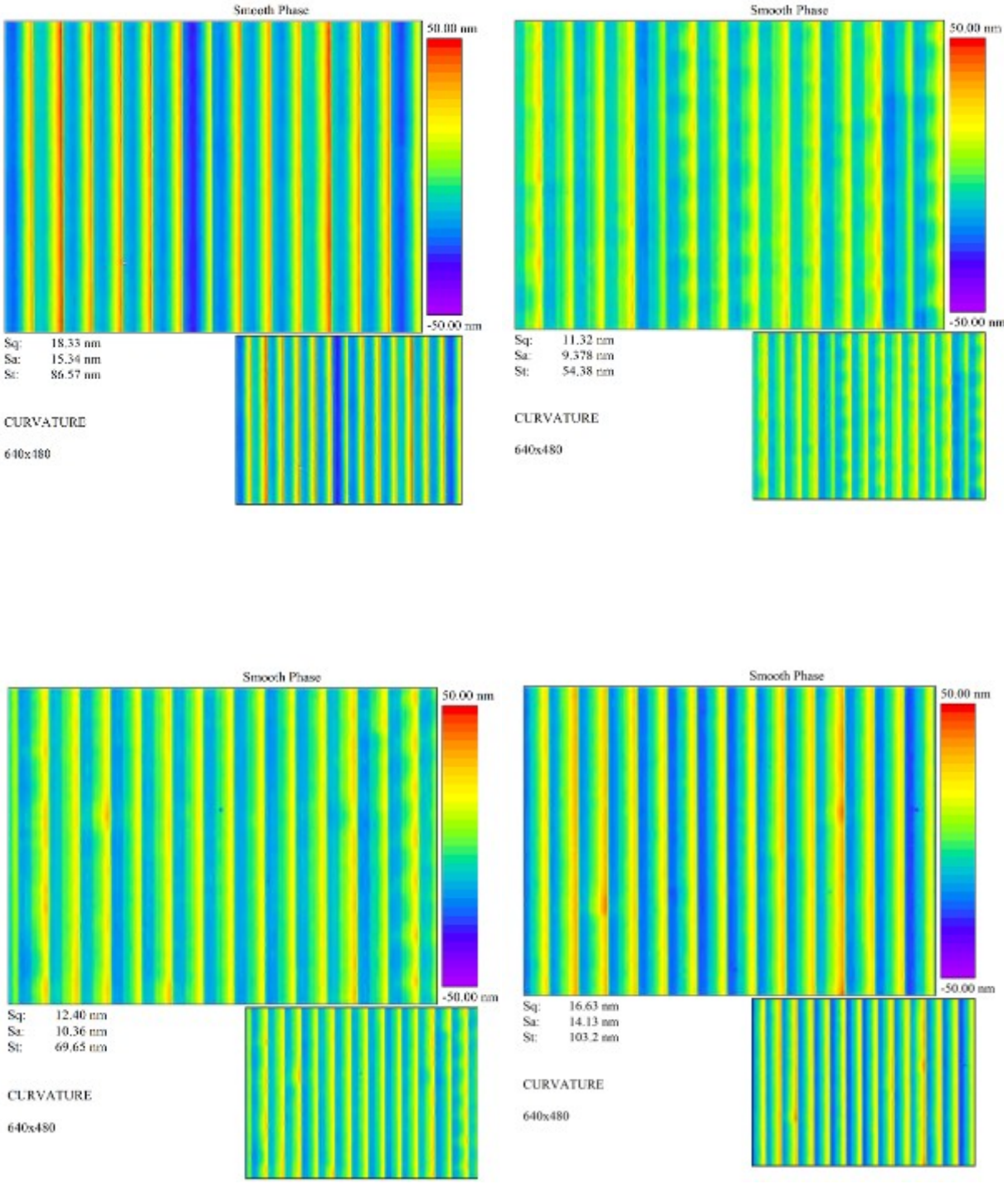

Figure 5-10. PROMAP 40x images (0.15 mm x 0.1 mm area) of different zones of the mandrel.

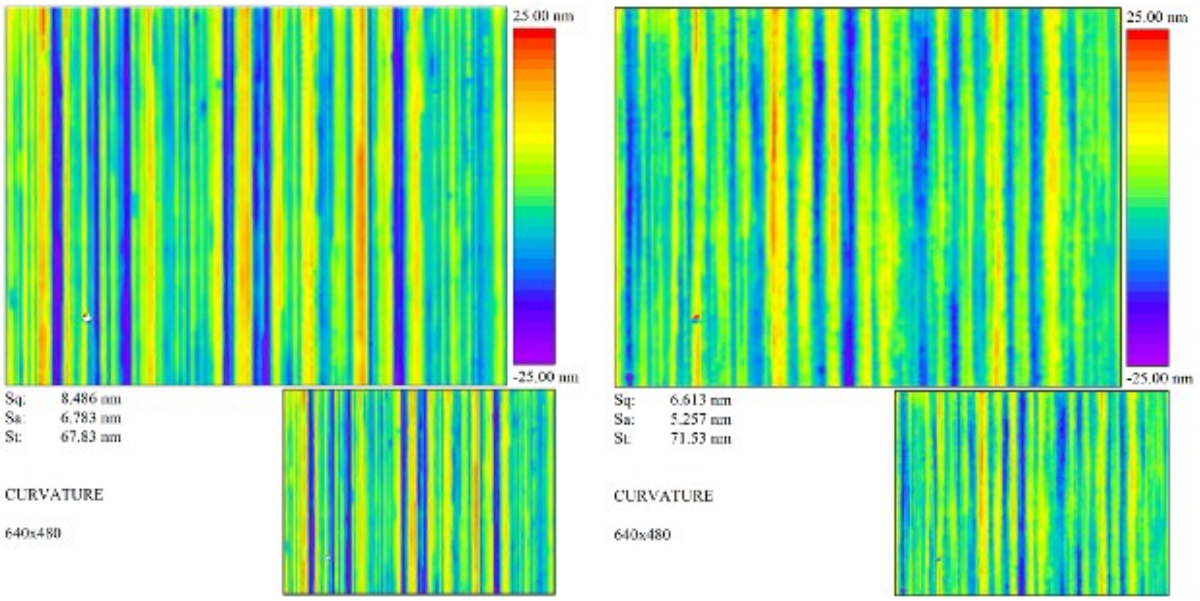

Figure 5-11. PROMAP 2.5x images (2.5 mm x 1.8 mm area) of different zones of the mandrel.

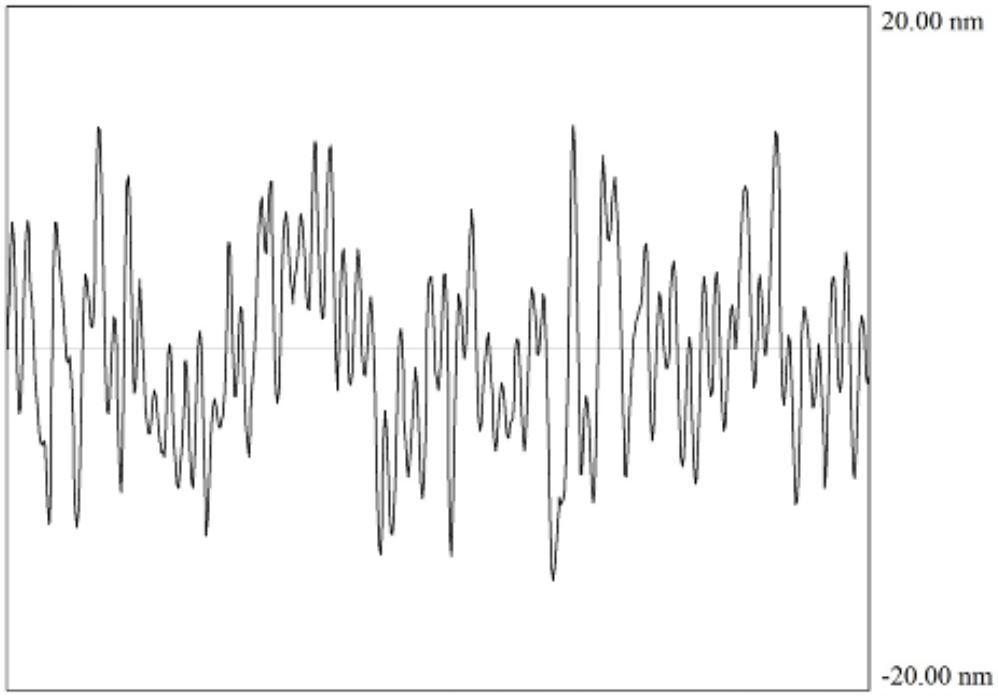

Figure 5-12. Profile extracted from the 2.5x image showing the mid-spatial in the 2.5 mm length.

From the roughness measurements performed on the diamond turned mandrel it is possible to calculate the mono-dimensional PSD. In the PSD (Figure 5-13) the 10 μm pitch of the DT marks can be seen, together with the additional n-the order of the diffraction pattern.

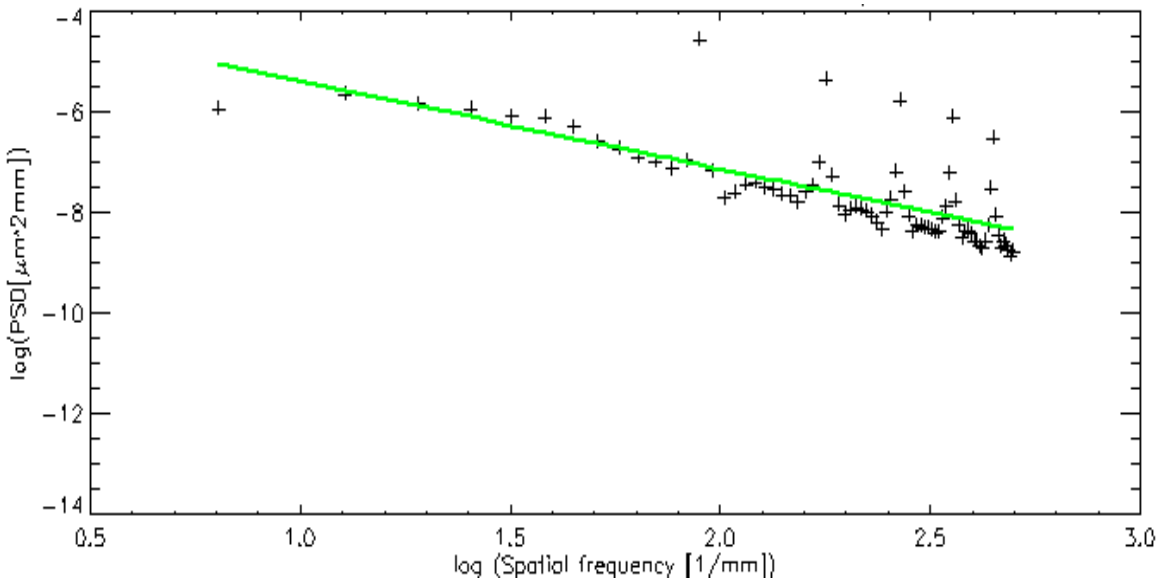

Figure 5-13. Spectral analysis of the PROMAP 40x measurements on the DT mandrel. The peak near the value log = 2 on the x-axis correspond to 10 μm.

5.2 Mandrels figuring and polishing

The traditional mandrel polishing process used so far for x-ray mandrels (i.e. stochastic polishing using rigid polishing tools) is not likely to improve the axial slope errors, especially when the curvature of the shape is more pronounced (i.e. big diameters and short focal lengths). The process is then qualitative and iterative, with many cycles of metrology and processing required converging on final HEW. This is because of the unpredictability of manual polishing, mitigated only in part by the skill of opticians. Based on these considerations, the drive for the design of the advance polishing technology has been identified, as a technique capable to apply a uniform roughness reduction together with the possibility to work deterministically. The uniform reduction of roughness is intended to remove DT marks and to reduce the improve the surface texture. The capability to work deterministically on different mandrel sections reflects into the possibility to maintain and/or improve the angular resolution of the mandrel.

The technique that I studied is a polishing process, which uses a bridge based, 7 axis CNC optical polishing/figuring machine. **No machine was available on the market** and the polishing machine **IRP 1200X** has been procured from an external supplier (Zeeko Ltd) according to x-ray mandrels specifications based on a **common development in which I participated**. This kind of machines are used for traditional spiral, raster, and free-from polishing of normal incidence mirrors/lenses. **I defined the specification of the x-ray mandrels and work on the development of the polishing process**, due to the fact that Zeeko has few, or none, experience on the polishing of grazing incidence NiP coated mandrels.

The baseline of the process is a physical sub-diameter tool operating in the presence of a polishing slurry (Walker, 2003). The tool comprises an inflated, bulged rubber membrane of spherical form (the "bonnet"), covered with one of the usual polishing surfaces familiar to opticians. The membrane moulds itself around the mandrel, retaining good contact also on aspheric surfaces. Such a membrane has the property that the polishing pressure (tool hardness) and the contact area (polishing spot size) can be varied independently by changing:

1. the internal pressure of the working fluid within the tool;
2. the axial position of the tool with respect to the mandrel, and therefore the degree by which the membrane is compressed against it.

The variable spot size might be 5-15% of the diameter of the mandrel optical area, although this is not a limit. In order to achieve a high volumetric removal rate despite the small area in contact, the tool is spun about its axis (at up to 1500rpm) to increase surface speed.

A static pole-down spinning tool exhibits zero surface-speed at center, rising linearly to a maximum at the periphery. This influence function does not lend itself to effective form control, on account of the "cross talk" between zones on the part that are separated by the diameter of the contact-spot.

For this reason, the rotation-axis of the tool is inclined to the surface local-normal. The tool polishes on the side of the bulged membrane, and the zero-point of surface-speed is shifted outside the contact spot. The tool-axis is then precessed in discrete steps about the local-normal to the surface of the part. The rotation-axis of the tool is orientated in space with respect to the local slope of the part by two rotation axes (A and B, see Figure 5-16) which coincide at the virtual pivot P, located at the center of curvature of the bonnet (see Figure 5-14). Changing the A and B angles then preserves the same location of the polishing spot on the surface of the part.

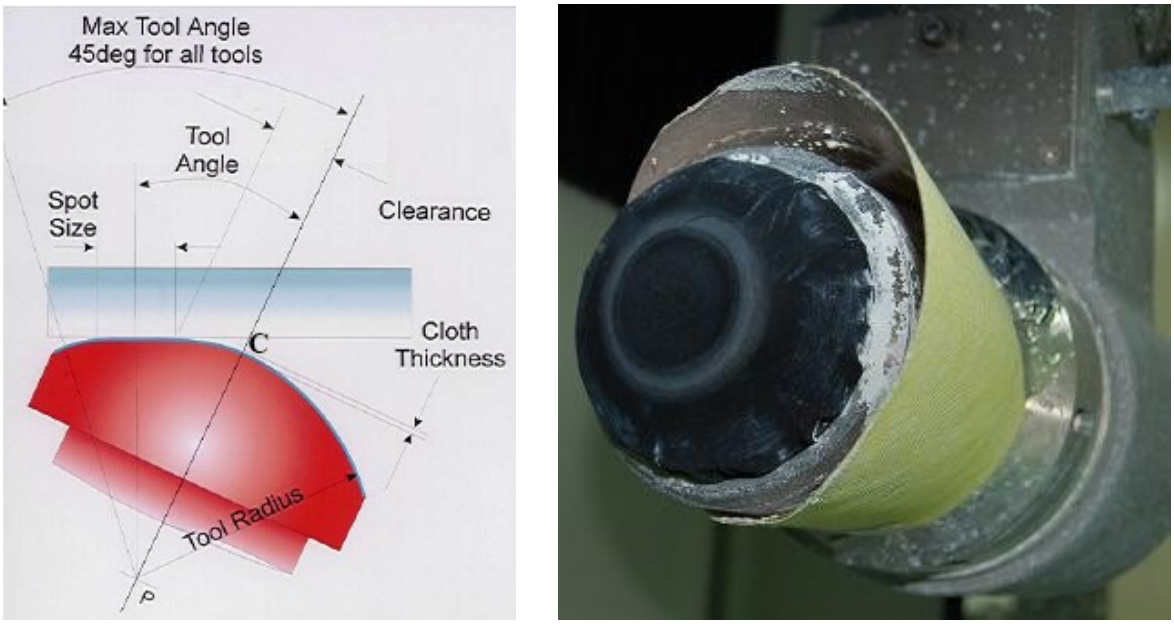

Figure 5-14. Precessing bonnet: scheme and picture.

The distance shown as "Clearance" in Figure 5-14 is then the clearance between the edge of the contact-spot on the part, and the axis of rotation of the tool. This clearance must always be positive, in order to prevent "double polishing" on either side of the rotation axis, which would distort the influence removal function.

Following from Preston's law, the depth *D(r)* of material removal is given by:

$$D(r) = k \cdot P(r) \cdot S(r) \tag{5.1}$$

where *P(r)* and *S(r)* and *k* are respectively the pressure and speed distributions, and Preston's constant. The value *r* is the radial distance from the point C of zero speed (see Figure 5-14). Now, *S(r)* is linear with *r*. As a consequence, the form of *D(r)* – the influence removal function – is dominated by the pressure distribution *P(r)* exerted by the bonnet. The surface speed (revolutions per minute) can then be used to moderate the depth of the mandrel profiles without significantly affecting its form.

Bonnets are available in different size and having radius R80, R40 and R20. They can be chosen according to the required removal rate and desired footprint onto the mandrel surface.

The process here developed uses bonnet polishing, permitting stable removal rate, elimination of diamond turning "record groove" marks, form correction and texture improvement.

The effectiveness of following sequence of activities has been proven on the diamond turned NiP coated mandrels:

- Constant removal DC runs for eliminations of diamond turning marks and surface damage;
- Corrective polishing of the mandrel axial profiles for improving the geometrical HEW by using R80, R40 or R20 bonnet according to the dimension of the error to be corrected;
- Constant removal DC runs for the improvement of the mid-frequencies and of the roughness.

5.2.1 IRP 1200X custom polishing machine adoption

The IRP1200X machine (see Figure 5-8) is the bridge based, 7 axis CNC optical polishing/figuring machine designed to process parts up to 1200 mm diameter, and 800 mm in height. **The equipment is an evolution of the standard Zeeko Ltd IRP1200 machine, that I contribute to customize allowing the polishing of grazing incidence x-ray mandrels**.

Figure 5-15. IRP1200X polishing machine installed at INAF-OAB and MLT site (Center of Excellence).

The IRP1200X machine is built on a 6000 kg polymer-granite cast base, which gives excellent stability and damping. Two symmetrical "X" slide-ways carry a hollow polymer-granite bridge. The bridge carries the pair of "Y" slide-ways and drive/encoder system. The Z-axis carriage is mounted off the Y-axis, and carries the virtual pivot assembly, which, in turn, support the tool-spindle ("H" axis). The A and B axes intersect at a point in space ("virtual pivot") located on the axis of rotation of the tool spindle, and the new design allows for full hemisphere coverage. The centre-of-curvature of the spherical polishing membrane ("bonnet") is arranged to coincide with the virtual pivot.

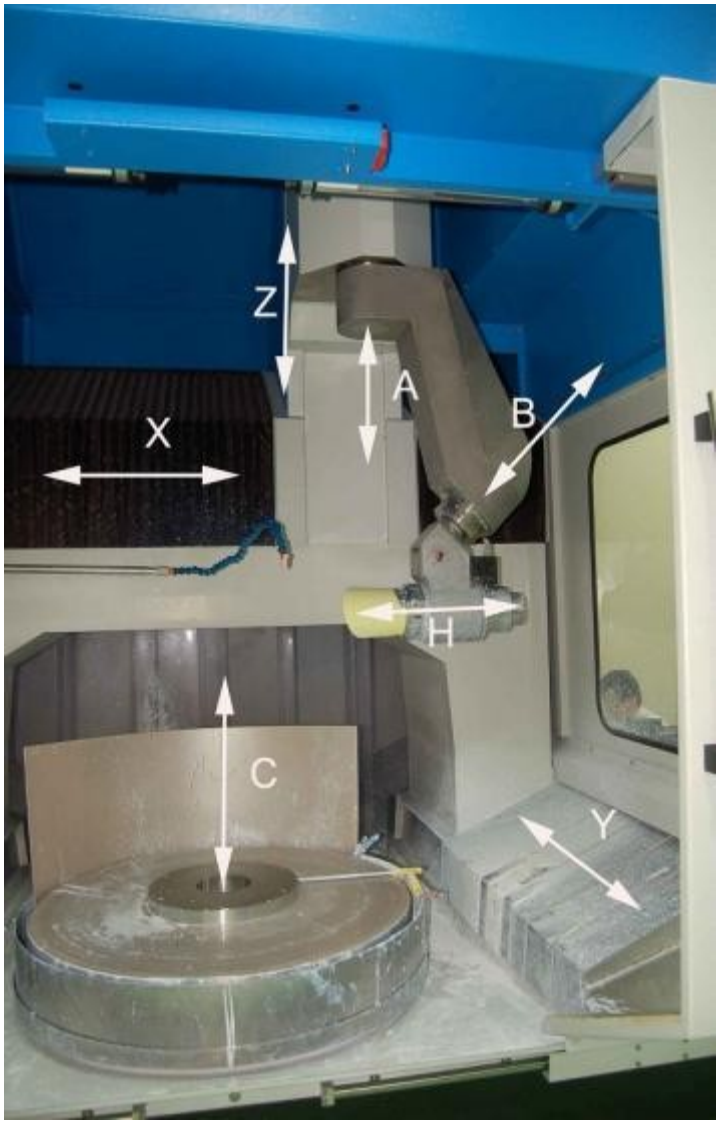

Figure 5-16. IRP1200X machine axes nomenclature reference.

Beside the standard testing (tests A and B in the following), **I performed a specific verification of the capability of the machine to polish x-ray mandrels (test C)**.

In order to ensure that the machine was fulfilling all the requests, an acceptance divided into two phases was performed: pre-acceptance at the supplier site and final acceptance after installation at MLT and INAF-OAB site (Centre of Excellence - CoE).

In the test A the geometric features of the polishing machine were investigated with Zeeko Ltd standard Ball Bar test and Laser test.

In the test B the functionality of the machine has been verified with the standard "Pass-Off" test derived from the Zeeko Ltd procedure. Pass-Off test consists in corrective polishing of two glass samples, a nominally flat one and a nominally spherical one.

In the following Table 5-2 and Figure 5-17 the polishing results are presented: in both cases the results were in line with the standard polishing capabilities of the IRP1200X machine.

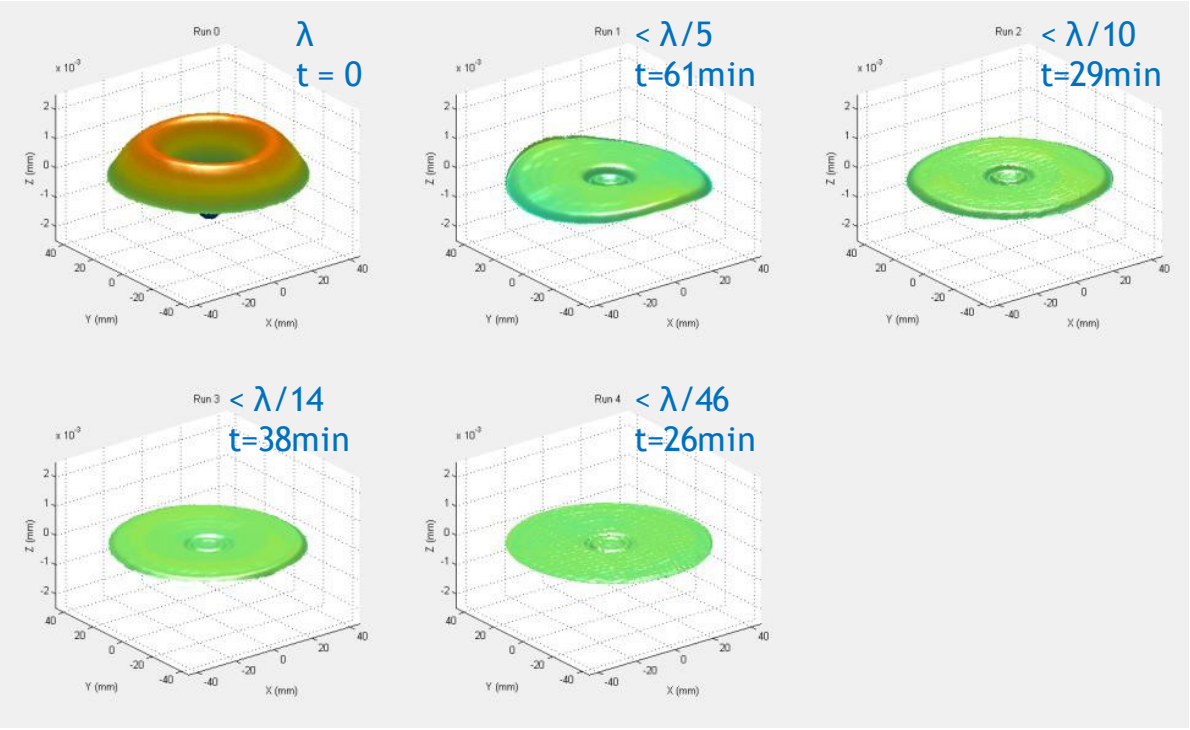

Figure 5-17. Polishing runs evolution on the spherical glass sample with indication of the shape accuracy (λ/n rms) and the duration of each run.

Table 5-2: Test B - Standard corrective polishing capability tests summary.

B	Standard Polishing Capability Verification	Test	Specification	Measured
B1	Polishing of an 80 mm flat sample made of BK7	ZYGO Interferometer	surface error to $\lambda/40$ rms over 95% of the useable area	$\lambda/42$
B2	Polishing of a ∅100 mm circular spherical sample made of BK7	ZYGO Interferometer	surface error to $\lambda/40$ rms over 95% of the useable area	$\lambda/46$

The test C is the final test to verify the polishing capabilities when applied on the NiP coated grazing incidence mandrels. The test mandrel (150 mm diameter and 340 mm height) was Diamond Turned to a nominal roughness of 15 nanometers, in order to reproduce conditions of the flight quality mandrels, and polished following the status-of-the-art experience as to reach best results. The mandrel was polished to the requested performance, namely an angular resolution below 6 arcsec HEW and a mid-frequencies/roughness level below 1.5nm rms. The polishing process did not introduce peculiar patterns and the marks due to the Diamond Turning were removed.

Table 5-3 below show the results obtained and compares them with the requirements separated between the Parabolic and Hyperbolic sectors of the mandrel. Figure 5-18 shows a CCI image (instruments similar to PROMAP) of the mandrel texture after the polishing.

Table 5-3. Test C – Mandrel polishing tests summary.

C	Mandrel Polishing Capability Verification	Test	Specification	Measured
C1	Mandrel shape (HEW)	PGI Profilometer	< 6 arcsec	5.9 arcsec on HYP 5.6 arcsec on PAR
C2	Mandrel texture (rms)	CCI Interferometer	< 1.5 nm rms	0.91 nm on HYP 1.01 nm on PAR

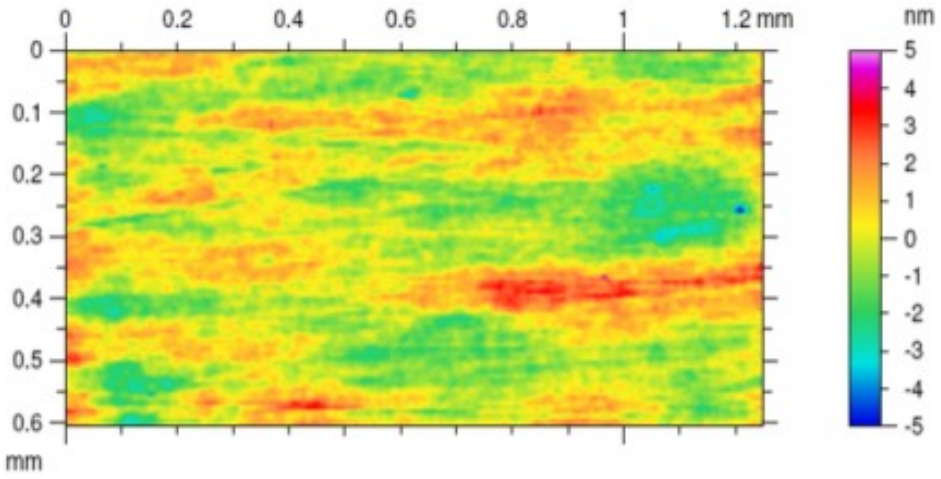

Figure 5-18. CCI interferometer measurement of MLT mandrel (Sq = 1.1 nm, St = 10.7 nm).

5.2.2 Diamond Turning marks removal

The first polishing step, developed to be performed with the IRP1200X machine, is for removing the Diamond Turning marks from the NiP coated mandrel surface. We have seen in the paragraph 5.1.2 that the depth of the DT marks is typically in the order of 100 nm and the characteristic pitch is in the order of 10 μm.

In order to remove these DT marks, in principle it would be sufficient to remove a constant amount of material (DC) having a thickness of 100 nm. In the practice this does not happen, because the bonnet polishing, due to its intrinsic degree of softness, is going to remove material not just on top of the DT peaks but also in the DT valleys. More than 100 nm of material shall thus be removed to get rid of the DT marks.

The development I performed, permitted the adoption of the most suitable polishing cloth and the identification of the proper polishing parameters settings. The main operational parameters that have been considered are the followings:

- **Head speed**: it is the rotational speed (rpm) of the bonnet mounted on the machine H-axis.
- **Turntable speed**: it is the rotational speed (rpm) of the mandrel mounted on the machine C-axis.
- **Tool offset**: it is the offset (mm) of the bonnet compressed on the surface to be

polished.

- **Feed-rate**: it is the linear speed (mm/min) of the bonnet in the Z-axis direction.
- **Bonnet radius**: it is the radius (mm) of the bonnet tool.

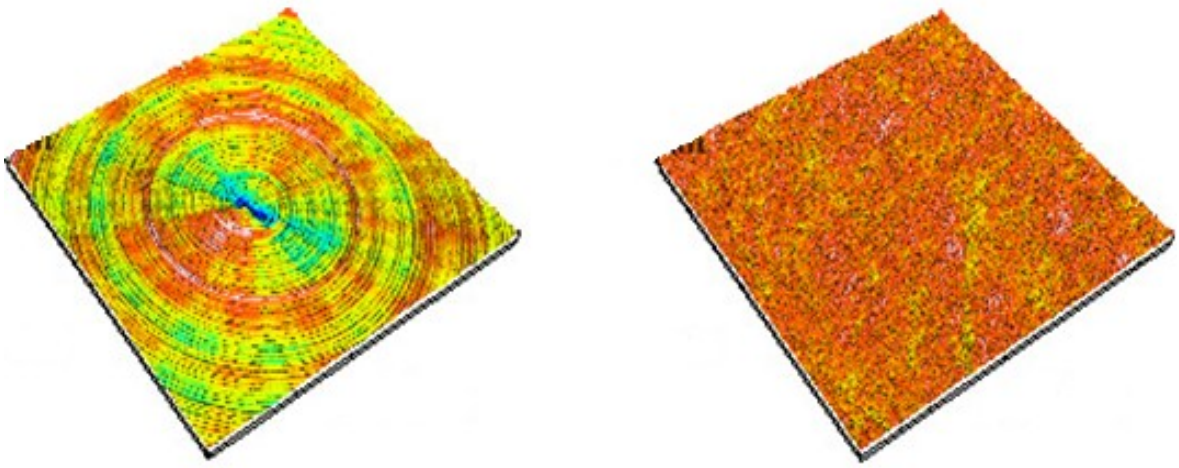

Figure 5-19. CCI measurements (3.5 mm x 3.5mm) showing the DT removal from a flat puck.

I performed the development activities on a set of hardware, including some flat samples and some test mandrels:

- 3 Flat Pucks having 90 mm clear aperture diameter;
- 2 Test Mandrels representative of x-ray mandrels design;

The entire set of items was made of the same materials (aluminium core + NiP coating), has been manufactured with the representative flow and by using the qualified suppliers.

In the Figure 5-19 it is possible to see the results obtained on the DT marks removal from one of the flat pucks, as measured by CCI instruments. In the Figure 5-20 it possible to see the comparison of Nomarski images acquire before and after the polishing runs on one of the two test mandrel. The effectiveness of the identified operational parameters in removing the DT marks can be appreciated.

5.2.3 Shape corrective polishing

The second polishing step, to be performed with the IRP1200X machine, is for improving the angular resolution of the mandrels. The level of correction is dictated by the axial profile

accuracy provided by the DT, and in most cases it is limited to a maximum value of 1 μm.

The very good roundness of the mandrels after the DT (see paragraph 5.1.2) allows to correct the shape by just imputing the axial correction.

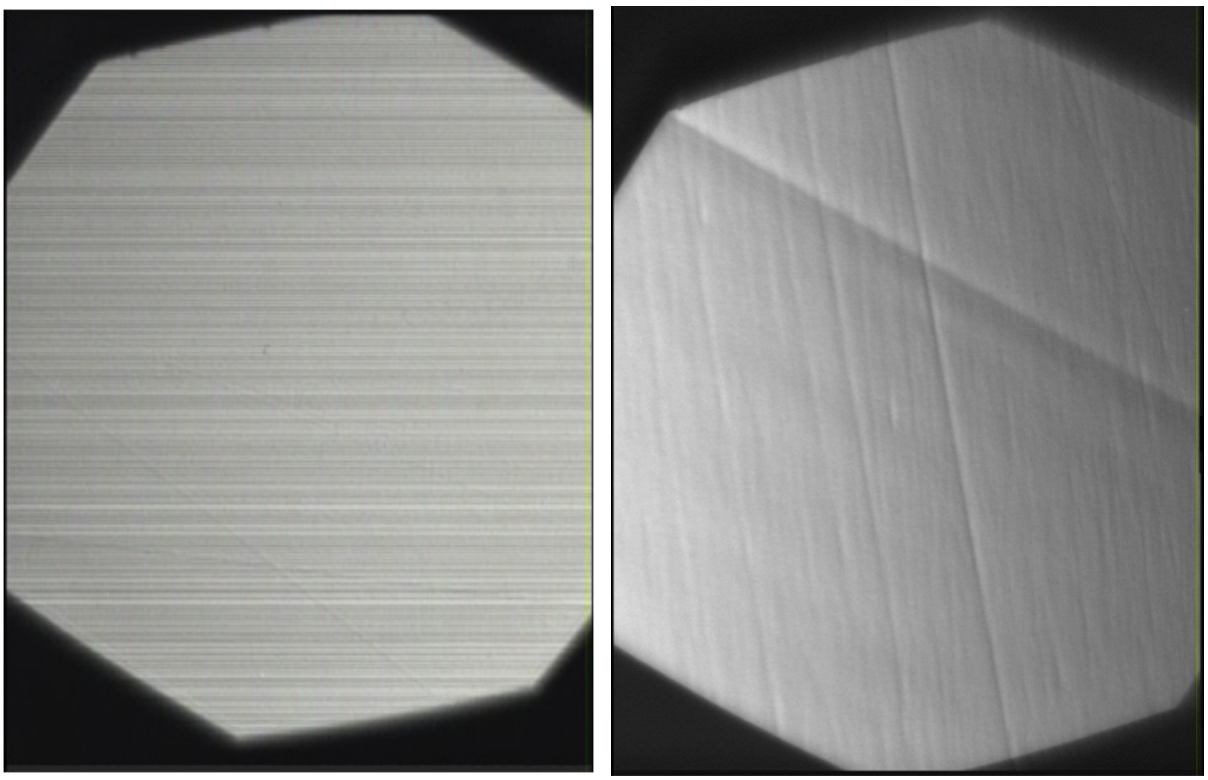

Figure 5-20. Nomarski microscope measurements (0.6 mm x 0.5mm) taken on the test mandrel after the DT and after the bonnet polishing. The mandrel optical axis corresponds to the vertical direction.

The trade-off here performed, permitted the adoption of the same polishing cloth used for the DT marks removal and the identification of the proper combination of the polishing parameters. The main operational parameters that have been considered are:

- **Head speed**: it is the rotational speed (rpm) of the bonnet mounted on the machine H-axis.
- **Turntable speed**: it is the rotational speed (rpm) of the mandrel mounted on the machine C-axis.
- **Tool offset**: it is the offset (mm) of the bonnet compressed on the surface to be polished.

- **Feed-rate**: it is the linear speed (mm/min) of the bonnet in the Z-axis direction.
- **Bonnet radius**: it is the radius (mm) of the bonnet tool.

The different combination of the operational parameters are affecting the removal function, and in this case the most important parameter is the bonnet radius. The radius determines, together with the tool offset, the footprint size of the bonnet onto the mandrel surface, giving constrains to the spatial wavelengths range that one can correct. Bonnets are available in different radius: R80, R40 and R20. They can be used, as a first approximation, for the following spatial wavelengths ranges:

- R80 → can be used to correct spatial wavelengths higher than 20mm;
- R40 → can be used to correct spatial wavelengths higher than 10mm;
- R20 → can be used to correct spatial wavelengths higher than 5mm.

Once the removal rate is defined, the shape correction is obtained with fine modulation of the feed-rate during the polishing run. The modulation in the feed-rate defines a modulation in the total amount of polishing to be perform in each single points of the mandrels. The input for the calculation of the feed-rate, comes from the axial profile measurements, properly averaged and filtered according to the error to be corrected.

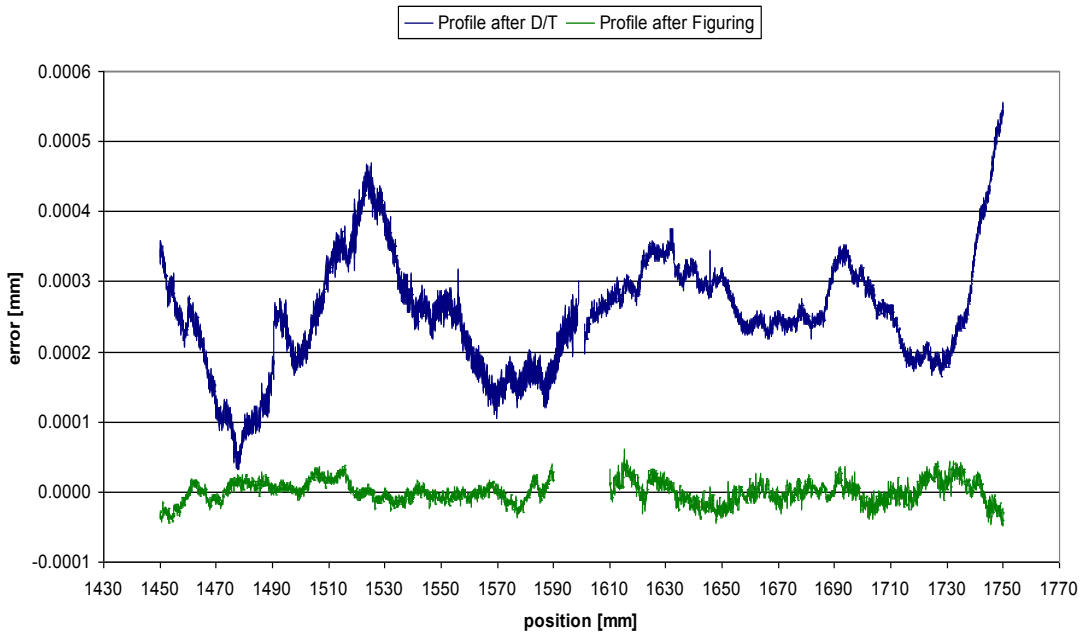

Figure 5-21. Corrective shape polishing improving the axial slope error after the DT (blue line); the final results after the figuring is the green line.

The correction obtained on a test mandrels, representative of the current level of knowledge, is presented in Figure 5-21. The blue line represents the axial profile error of the mandrel after the DT (and also after the DT marks removal) and the green line represents the axial profile error after the corrective polishing. The starting PtV error of 500 nm has been reduced to 60 nm, and in terms of HEW we are talking of 5 arc seconds against the starting 9 arc seconds.

5.2.4 Texture improvement

After the corrective polishing, the texture of the mandrels is not homogeneously distributed. This is a consequence of the feed-rate modulation defining a differential amount of polishing along the optical axis.

The third polishing step, to be performed with the IRP1200X machine, is for improving the texture homogeneity and the roughness level in general. The roughness/waviness limit of the bonnet polishing technique has not been clearly verified, but the plateau seems to be at 1.5 nm.

The different combination of the operational parameters are here tuned following the principle of slowing the reciprocal velocity of the mandrel and bonnet. The iteration of the Bonnet polishing sessions brought the roughness Sq level (measured on 1.6mm squared area) down to 1.5 nm rms before encountering the plateau. The improvement in terms of Sq through the different polishing runs is reported in the graph of Figure 5-22.

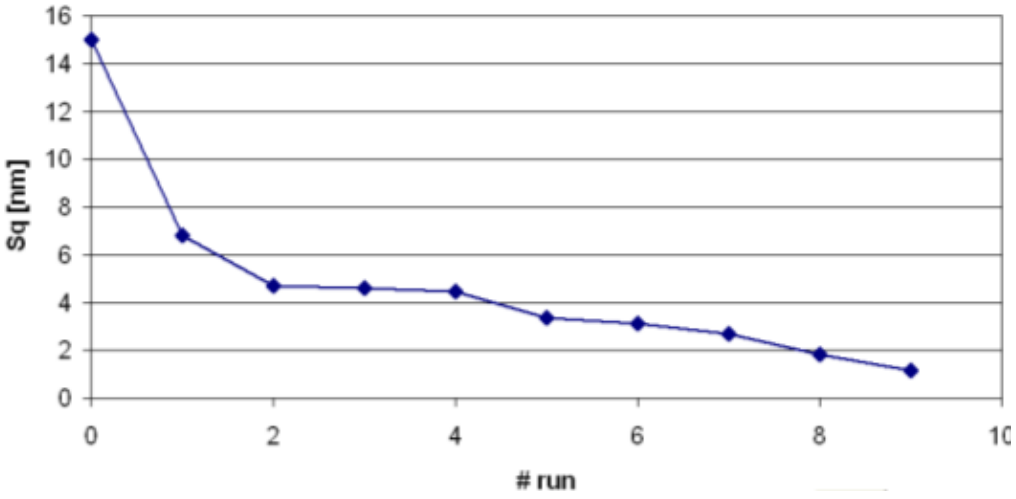

Figure 5-22: Sq roughness level of the test mandrel against the polishing runs.

Figure 5-23. Close picture of the mandrel during the bonnet polishing process.

5.3 Mandrels superpolishing

As results of the first polishing step, the diamond turning marks are removed from the mandrel and the geometrical shape HEW is properly corrected. Anyhow, with the bonnet polishing is not possible reaching the final medium/high scale roughness requirements of the grazing incidence x-ray mandrels.

The mandrels are therefore superpolished (SP) by using the traditional polishing machine. Starting from the good roughness left by the first polishing step, the amount of material to be removed is very low and consequently the risk to degrade the shape of the mandrel is limited.

The superpolishing process is performed by using:

- standard slurry of nanometric grain size
- reciprocating rigid polishing tools positioned, with some load-pressure, onto the surface of the mandrel kept in rotation (see Figure 5-24).

My experimental work has been concentrated on finding the most suitable process parameters for the superpolishing (slurry, rotation and translation rates, load pressure). **I also defined a proprietary design of the polishing tool**, that guarantees an excellent finishing both in the mid-frequency range (mm range) and in the high frequency range (μm range).

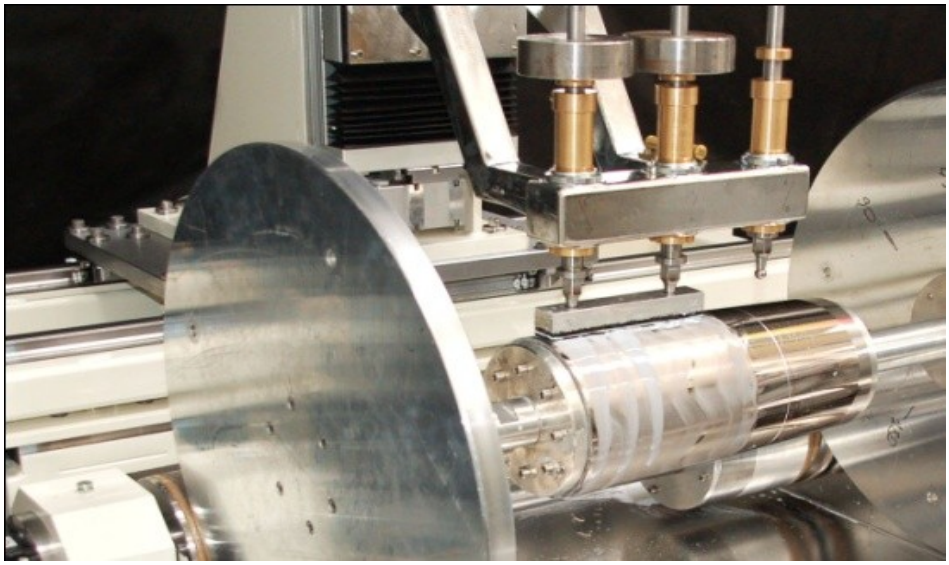

Figure 5-24. Flight-quality eROSITA mandrel during superpolishing.

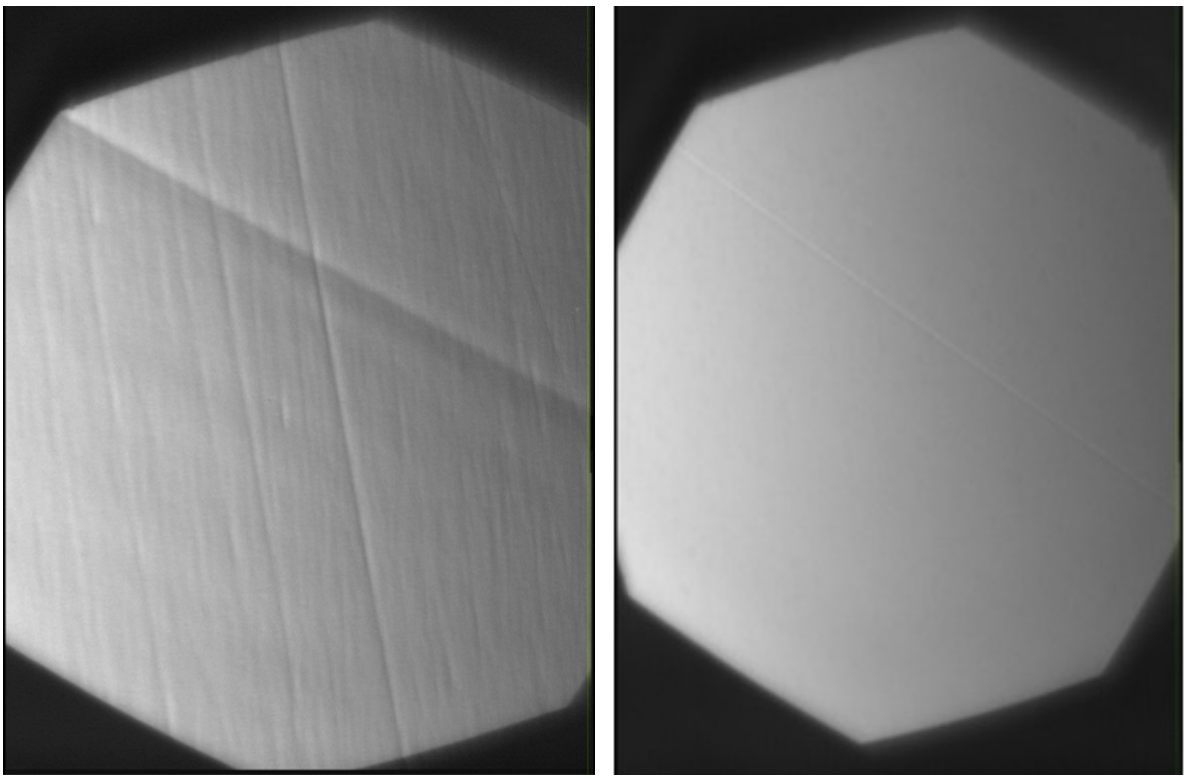

Figure 5-25. Nomarski measurements (0.6 mm x 0.5mm) on the mandrel before (left) and after (right) the SP. The mandrel optical axis corresponds to the vertical direction.

5.4 Centre of Excellence for the advanced polishing

The Centre of Excellence (CoE) has been established in March 2010 via INAF-OAB and MLT Memorandum of Understanding and is fully operational since June 2010. The centre has been established by the two parties with the intention to:

- design and fabricate mandrels/optics exploiting the technological know-how developed in scientific field and leveraging off for commercial applications;
- consolidate and develop partnership with Italian and worldwide top level scientific, technology and industrial entities;
- establish a facility with top level equipment, instrumentations and skilled personnel.

The CoE is 120 m^2 clean room with a full comprehensive set of polishing and metrology equipments (see Figure 5-26) and is currently operating for the manufacturing of the flight-quality eROSITA mandrels, for the prototyping of the NHXM mandrels and for the manufacturing of normal incidence mandrels for different applications.

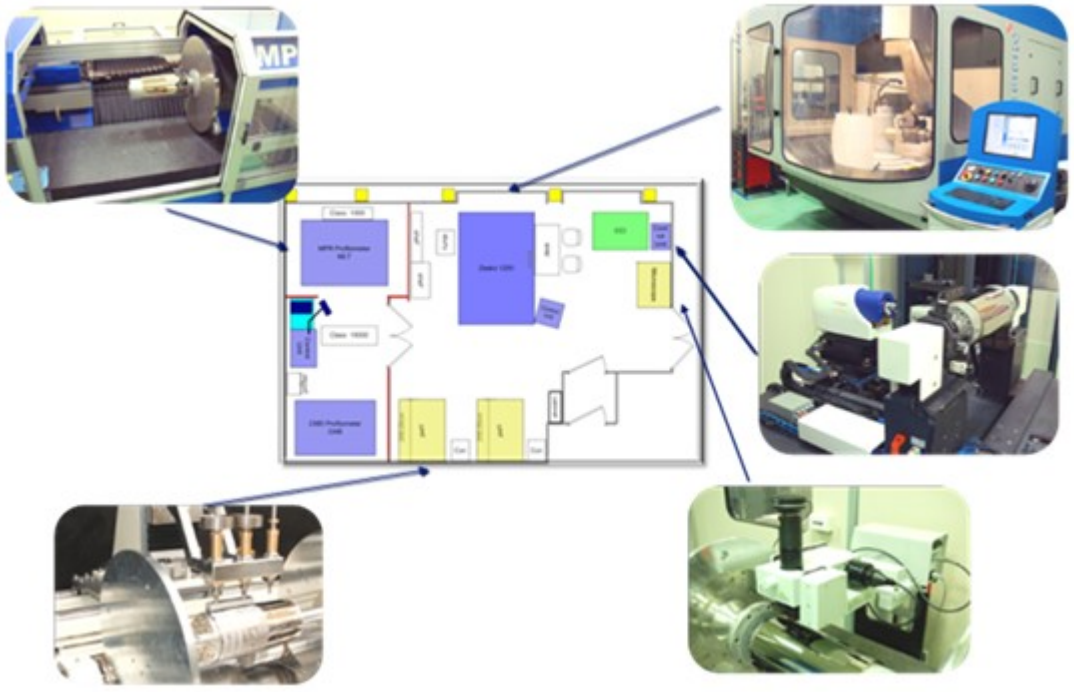

Figure 5-26. Layout of the CoE, from the top-left corner and going clockwise it is possible to see pictures of: MPR profilometer, IRP1200X machine, CCI roughness profiler, Nomarski microscope stage and one of the superpolishing machine.

The polishing and metrology commercial and proprietary equipments currently available at the CoE are:

- IRP1200X polishing machine;
- IRP600 polishing machine;
- Superpolishing traditional machine (x3);
- MPR profilometer for 3D free-form measurements;
- Nomarski contrast phase microscope inspection stage;
- CCI and PROMAP roughness profiler;
- AFM Veeco Explorer measuring device;
- WYKO 600 interferometer.

5.5 Conclusions

The results obtained in the development study for an advance polishing technology for grazing incidence x-ray mandrels are here summarized.

- NiP coating shows good uniformity ensuring good response during the polishing. No defects of adhesion or print-through effects have been found on the mandrels;
- the Diamond Turning (DT) is defined and proven as one of the basic processes to manufacture the x-ray mandrels. The DT process provides an excellent azimuthal symmetry, useful for the subsequent corrective polishing step;
- a dedicated custom CNC polishing machine, the IRP 1200X, has been adopted;
- the DT record marks can be effectively removed by bonnet polishing;
- a suitable corrective polishing, which is the bonnet polishing, has been identified and further developed to extend it to the x-ray mandrel case;
- in order to achieve the final finishing, the classical superpolishing is necessary.

6 Characterization of mandrels manufactured with the advanced polishing technique

6.1 NHXM mandrel M297

6.1.1 Mandrel design and manufacturing

To further develop the advance polishing technique **I followed the manufacturing** of a prototype mandrel for NHXM as **technical/scientific responsible**. The NHXM mandrel is named M297, it is ~ 297 mm in the medium diameter (*Φmid*) with ~ 10 m focal length (*F*) and hence with an incidence angle α = 0.21176 deg. The mandrel is designed with Wolter I geometry and the optical area is 600 mm long (300mm parabolic section and 300mm hyperbolic section). The design parameters are summarized in Table 6-1.

Table 6-1. Design parameter of the NHXM mandrel M297.

Design Parameter	Type / Value
Mandrel Material	Aluminium core + NiP
Optical Design	Wolter I
Medium Diameter	296.800 mm
Incidence angle (α)	0.2118 deg
Focal length	10037.5 mm
Mandrel length	600 mm

The mandrel blanks consists of a **NiP** coated aluminum core, the **Wolter I** geometrical shape has been generated by using the **Diamond Turning** (DT). I performed the polishing of this mandrel directly with the traditional **superpolishing** equipments, without passing through the IRP1200X machine for figuring/polishing. This is because, at the time of mandrel manufacturing, the IRP1200X was not yet available. Nevertheless, the angular resolution of the mandrel after the DT was already very good, and so no particular shape correction was needed.

Figure 6-1. NHXM mandrel M297 during visual inspection in the MTL clean room facilities.

6.1.2 Mandrel geometrical shape

I effectively measured the shape accuracy error with 2D and 3D metrology equipments that allow the determination of the different contributions separately. The final HEW is calculated by the Root Sum Square (RSS) of the contributions.

The **axial profile error** has been measured by using the high accuracy LTP profilometer (see chapter 4) at 8 equally spaced azimuthal angles (i.e. each 45deg), because the MPR profilometer was still under procurement. The raw data have been Fourier filtered with a low-pass 3.5mm

cut-off corresponding to the noise limit of the instrument (see Figure 6-2). The axial slope error contribution to the HEW has been calculated by ray-tracing. The 50% of the encircled energy gives a $\boldsymbol{HEW_{axial}}$ **= 4.64 arc seconds**. The spot diagram, at best focus position, resulting from the ray tracing simulation is reported in Figure 6-3 (left side) together with the encircled energy (left side).

The **out-of-roundness** has been measured on 6 different positions along the optical axis (3 on parabola and 3 on hyperbola). The typical roundness error is shown in Figure 6-2 (left side) with error in the order of 0.3μm. The azimuthal slope error distribution has been calculated for defining the median value containing the 50% of the errors both for parabola and hyperbola (δ50). The HEW contribution coming from the out-of-roundness error has been calculated by using the median values scaled for the focal length according to the 4.3 formula:

$$HEW_{roundness} = \frac{\Phi_{MID}}{F} \cdot \sqrt{\delta_{50,HYP}^2 + \delta_{50,PAR}^2} = \frac{148.4}{10037.5} \cdot \sqrt{0.89^2 + 0.73^2} = 0.02''$$

The absolute value of the **mandrel radii** has been measured by using UPMC 3D coordinate machine before final superpolishing. The contribution to the HEW of the error in the absolute radius is almost a homogeneous defocusing w.r.t. the nominal Wolter I profile with optical aberration giving HEW_{radius} = 0.12 arcsec. The **focal length** is F = 10041.1 mm

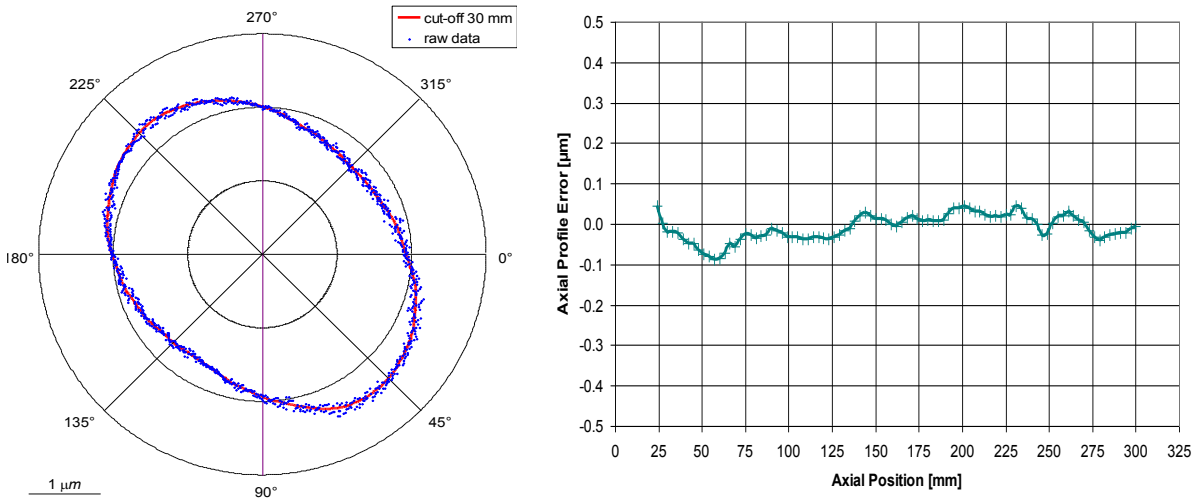

Figure 6-2. Out-of-roundness (left side) and axial profile error (right side) of the NHXM mandrel M297 measured after the final superpolishing.

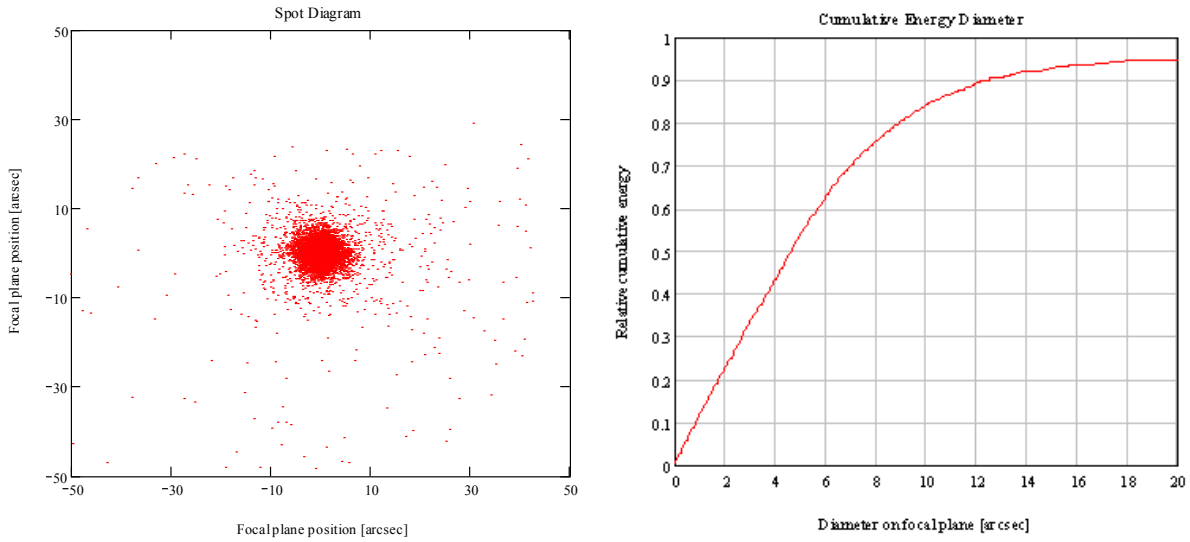

Figure 6-3. Spot diagram (left side) and encircled energy (right side) from ray-tracing of the axial profile error data.

The axial slope error, has expected, acts as the dominant source of error for the geometrical HEW of the mandrel. In fact, if we calculate the Root Sum Squared of the different HEW contributions coming from axial profile error, azimuthal error and absolute radii error, the result does not differ significantly from the one obtained considering only the axial profile error (i.e. 4.65 arc seconds).

The single HEW contributions and the result of the Root Sum Squared are summarized in the next Table 6-2.

Table 6-2. Geometrical HEW breakdown error and RSS of the single contributions.

Error Source	HEW (arcsec)
Axial slope (cut-off 3.5 mm)	4.64”
Out of roundness	0.02”
Absolute radius (best focus)	0.12”
Root Sum Squared	**4.65”**

6.1.3 Mandrel roughness

The metrological characterizations of the superpolished mandrel mid-scale error and micro-roughness have been performed, over spatial wavelength range between 2mm and 10nm, by using the non-destructive metrological systems available in MTL and INAF-OAB: atomic force microscopy, phase shift interferometry and contrast phase microscopy Nomarski.

I was able to superpolish the mandrel surface down to the remarkable roughness level of **Sq = 0.21 nm** as calculated by averaging the PSDs from 24 measurements acquired over the mandrel optical area with PROMAP 40x (157 μm x 118 μm area). Also the mid-spatial frequencies error has been brought to the desired value of **Sq = 0.40 nm** as calculated by averaging the PSDs from 24 measurements taken randomly over the mandrel optical area with PROMAP 2.5x (2 mm x 1 mm area).

The AFM measurements is giving a microroughness < 0.2 nm rms for the 1 μm scanning, and roughness between 0.2 nm – 0.4 nm rms for the 10 and 100 μm scanning. In the Figure 6-4 (left panel) a 100 μm scanning measurement is reported.

The smoothness of the mandrel surface is confirmed by inspection performed with contrast phase Nomarski microscope. In the Figure 6-4 (right panel) a 0.6mm x 0.5mm image is reported. The diagonal light scratch (having only few microns width) can be used as reference for appreciating the smoothness of the surrounding area.

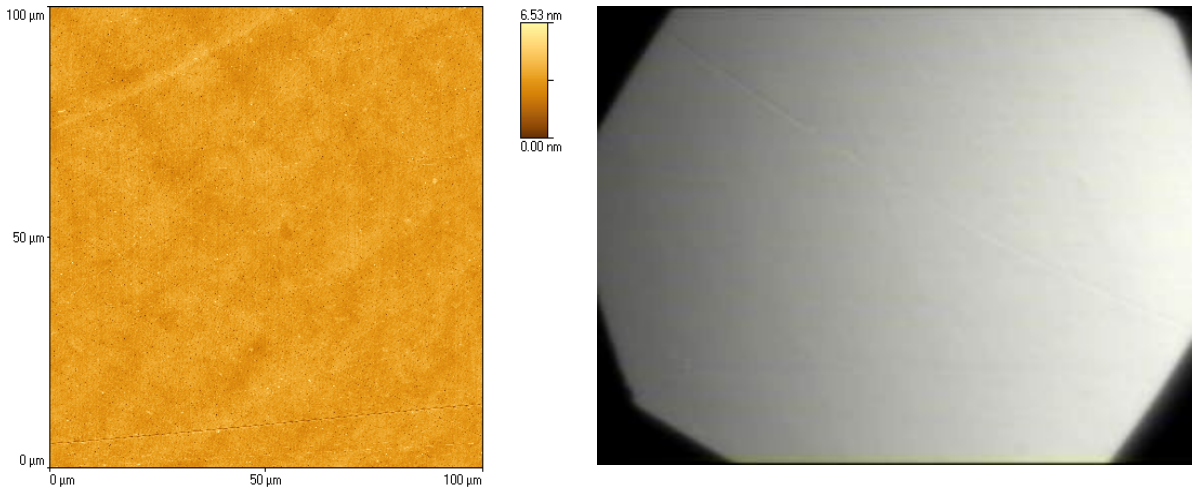

Figure 6-4. AFM 100x measurement of the superpolished mandrel (left side) and Nomarski picture of the finished surface in a 0.6mm x 0.5mm area (right side).

6.2 NHXM mandrels M350

6.2.1 Mandrel design and manufacturing

To qualify the developed advance polishing technique **I followed the manufacturing** of a flight mandrel for NHXM as **technical/scientific responsible**. The NHXM mandrel is named M350, it is ~ 350 mm in the medium diameter (*Φmid*) with ~ 10 m focal length (*F*) and hence with an incidence angle $\alpha = 0.2497$ deg. The mandrel is designed with Wolter I geometry and the optical area is 600 mm long (300mm parabolic section and 300mm hyperbolic section). The design parameters are summarized in Table 6-3.

The mandrel blanks consists of a **NiP** coated aluminum core, the **Wolter I** geometrical shape has been generated by using the **Diamond Turning** (DT) process. I performed the polishing of this mandrel IRP 1200X machine for removing the DT marks and for improving the geometrical angular resolution to HEW < 7 arc seconds. The surface finishing has been optimized by using the traditional **superpolishing** equipments.

This is a fully representative NHXM mandrel manufactured with the complete advanced polishing technique.

Table 6-3. Design parameter of the NHXM mandrel M350.

Design Parameter	Type / Value
Mandrel Material	Aluminium core + NiP
Optical Design	Wolter I
Maximum Diameter	352.605 mm
Medium Diameter	350.000 mm
Minimum Diameter	342.145 mm
Incidence angle (α)	0.2497 deg
Focal length	10037.5 mm
Mandrel length	600 mm

6.2.2 Mandrel geometrical shape

The M350 mandrel geometrical shape accuracy has been measured with the newly developed MPR profilometer (Sironi, 2010), allowing to measure the absolute error w.r.t. the nominal design. The axial slope error, the roundness error and the radius error are meshed reconstructing the 3D shape error. The **HEW** has been calculated by ray-tracing of the 3D shape error, giving **11.3 arc seconds** after the DT, **5.1 arc seconds** after the corrective polishing and **5.9 arc seconds** after the superpolishing. The best focus is at the **focal length** F = 10042.0 mm.

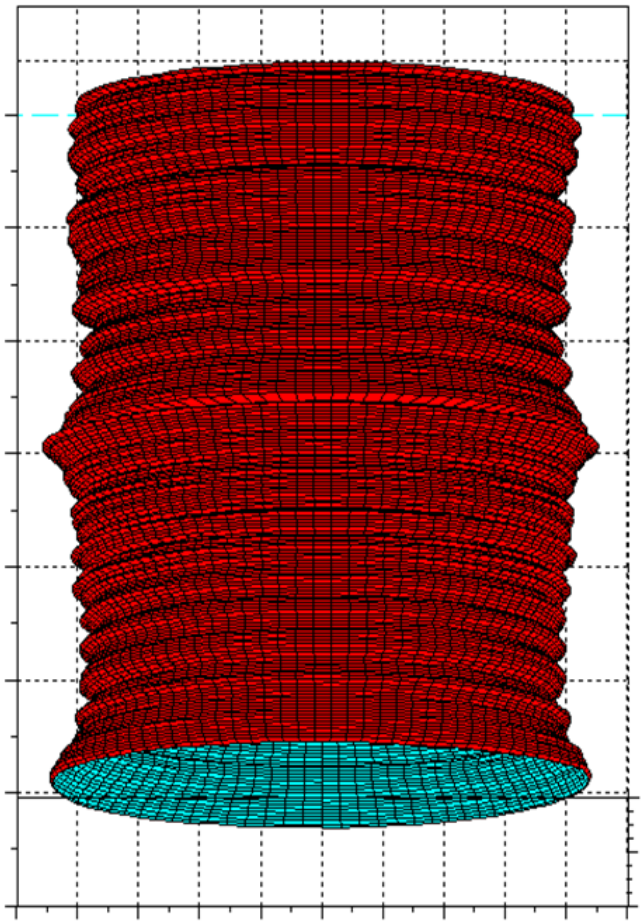

Figure 6-5. MPR 3D measurements of NHXM mandrel M350. The absolute values of the mandrel diameter have been removed from the graph to emphasizes the roundness and axial slope errors. The roundness error is within 0.3 μm PtV and the axial profile error is within 0.1 μm PtV.

The **axial profile error** after the DT process was giving a pronounced residual error, especially for the parabolic section. With the IRP 1200X we was able to correct this error, bringing it down to PtV values below 0.1 μm against the starting 1.5 μm (see Figure 6-6).

The **out-of-roundness** after the DT process was already very good (< 0.3 μm PtV), and it has been preserved towards polishing and superpolishing processes.

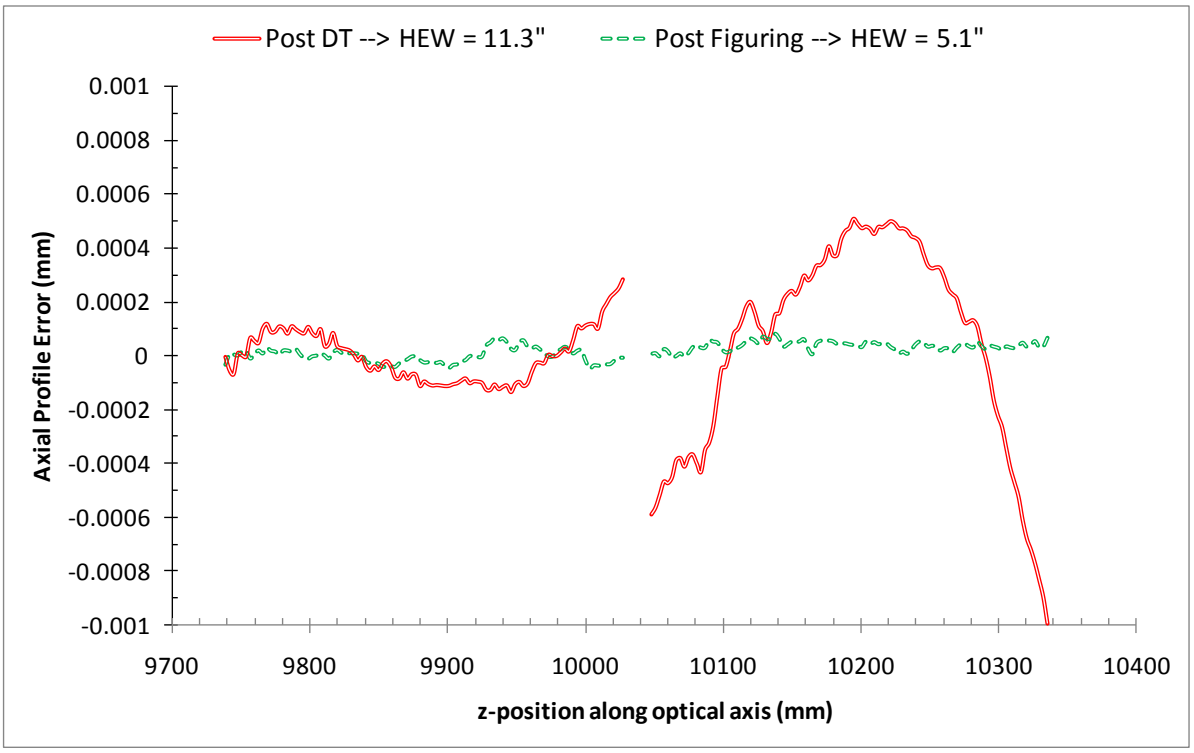

Figure 6-6. Comparison of the M350 axial profile after the DT process (red-solid line) and after the corrective polishing performed with the IRP 1200X machine (green-dashed line).

6.2.3 Mandrel roughness

The metrological characterizations of the superpolished mandrel mid-scale error and micro-roughness have been performed, over spatial wavelength range between 2mm and 10nm, by using the non-destructive metrological systems available in MTL and INAF-OAB: atomic force microscopy, phase shift interferometry and contrast phase microscopy Nomarski.

The surface has been superpolished to the roughness level of **Sq = 0.22 nm** as calculated by averaging the PSDs from 24 measurements acquired over the mandrel optical area with

PROMAP 40x (157 µm x 118 µm area). Also the mid-spatial frequencies error has been brought to the desired value of **Sq = 0.45 nm** as calculated by averaging the PSDs from 24 measurements taken randomly over the mandrel optical area with PROMAP 2.5x (2 mm x 1 mm area). The AFM measurements is giving a microroughness ~ 0.2 nm rms for the 1 µm scanning, and roughness between **0.2 nm – 0.4 nm** rms for the 10 and 100 µm scanning.

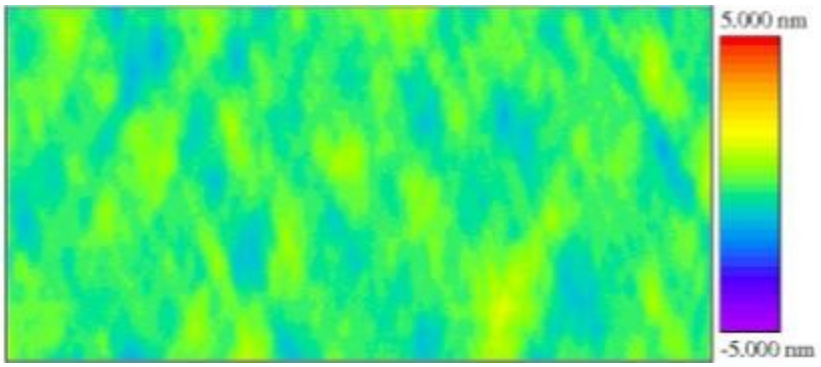

Figure 6-7. M350 PROMAP 2.5x image (2mm x 1 mm area), giving midscale error Sq = 0.41 nm.

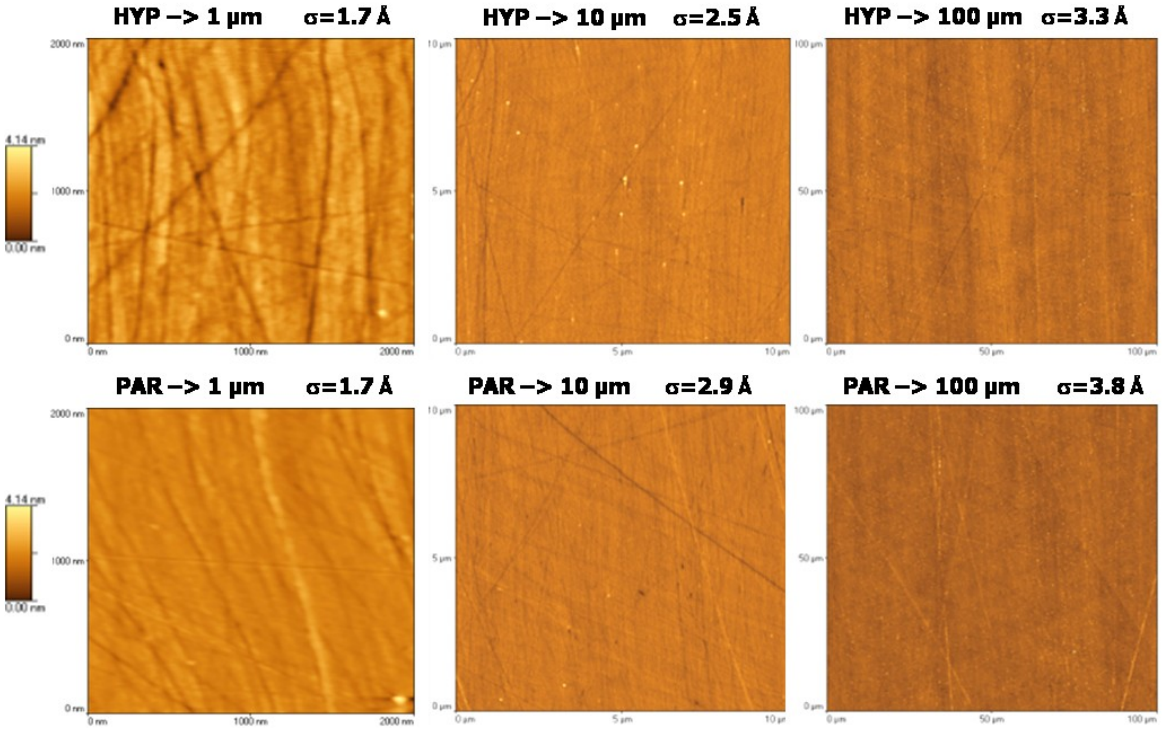

Figure 6-8. AFM measurements performed on NHXM mandrel M350 with 100, 10 and 1 scanning length, The height scale is identical for all the pictures and the roughness value is indicated above.

6.3 eROSITA mandrels

The eROSITA x-ray mirror modules are extended versions of the ABRIXAS modules with the same focal length but with double diameter by adding 27 outer mirror shells. This similarity in the design allows re-using the existing ABRIXAS mandrels for the replication of the inner mirror shells. In 2010 MPE institute commissioned to MLT company the manufacturing of the additional outer 27 mandrels, **after the successful accomplishment of the pilot development program in which I participated as technical/scientific responsible.**

The deviation of Wolter geometry from the double cone is much more pronounced when the focal length is short. In the case of eROSITA the deviation of the parabolic/hyperbolic profiles from the double cone is in the order of 10-20 μm. When applied to the traditional polishing equipment used so far (rigid reciprocating polishing pad), this characteristic entails a tendency to rapidly degrade the shape accuracy. For the eROSITA development program a flight-quality mandrel (eROFM25) has been manufactured by MLT with the advance polishing technique in 2010. This mandrel has been replicated for x-ray testing in PANTER, obtaining excellent performance (HEW ~ 12 arcsec, see Chapter 8).

Currently (at June 2011) MLT has manufactured nearly half of the 27 mandrels set, and all the available mandrels are with HEW < 6 arcsec and roughness ~ 0.3 nm rms.

6.3.1 Mandrels design and manufacturing

The existing 27 ABRIXAS mandrels that are foreseen to be utilized for the eROSITA project have a focal length of 1600 mm. From that it is clear that the new 27 mandrels required by the project must have the same focal length. The following formulas are defining the mandrel design at temperature of 20°C:

Parabola $$r_P = \sqrt{a \cdot (z - b)}, \qquad 1770 < z \le 1600;$$

Hyperbola $$r_H = e\sqrt{\left[(z + c)^2 / d^2\right] - 1}, \qquad 1600 \le z < 1430.$$

where z is the direction of the optical axis and $r_{P,H}$ the radius of a mandrel point. The focal length is 1600 mm with the focus at the position z = 0 mm. The parameters *a, b, c, d, e* for all mandrels are listed in Table 6-4.

Table 6-4. Optical Design parameters for the eROSITA mandrels.

#	*a*	*b*	*c*	*d*	*e*
1	9.44637	-1611.82121	804.72981	802.36473	61.65148
2	8.91622	-1611.04036	804.40566	802.17366	59.88222
3	8.41187	-1610.85293	804.37498	802.26882	58.17085
4	7.93902	-1610.48707	804.25116	802.26325	56.51186
5	7.49356	-1608.77675	803.45168	801.57679	54.85657
6	7.07244	-1608.52586	803.37887	801.60917	53.29505
7	6.67422	-1607.70963	803.02054	801.35091	51.75623
8	6.29811	-1608.36214	803.39381	801.81726	50.30604
9	5.94461	-1607.28939	802.90162	801.41422	48.84931
10	5.61284	-1606.54561	802.57120	801.16717	47.45197
11	5.29615	-1607.02079	802.84838	801.52292	46.11432
12	4.99735	-1606.50564	802.62815	801.37764	44.78645
13	4.71915	-1605.03775	801.92898	800.74896	43.48788
14	4.45373	-1604.64374	801.76516	800.65159	42.24207
15	4.20057	-1605.36540	802.15763	801.10673	41.04726
16	3.96548	-1604.89583	801.95223	800.96028	39.87482
17	3.74282	-1604.17791	801.62110	800.68514	38.72586
18	3.53057	-1604.44654	801.78195	800.89880	37.62182
19	3.33407	-1603.16732	801.16690	800.33347	36.53406
20	3.14545	-1604.16868	801.69116	800.90429	35.51092
21	2.96839	-1603.21480	801.23635	800.49414	34.47932
22	2.79977	-1603.08643	801.19324	800.49318	33.48564
23	2.64313	-1602.47138	800.90530	800.24458	32.52536
24	2.49399	-1602.57386	800.97518	800.35166	31.59860
25	2.35204	-1603.42178	801.41688	800.82848	30.70451
26	2.22060	-1603.60520	801.52503	800.96940	29.83943
27	2.09660	-1602.63653	801.05619	800.53186	28.97855

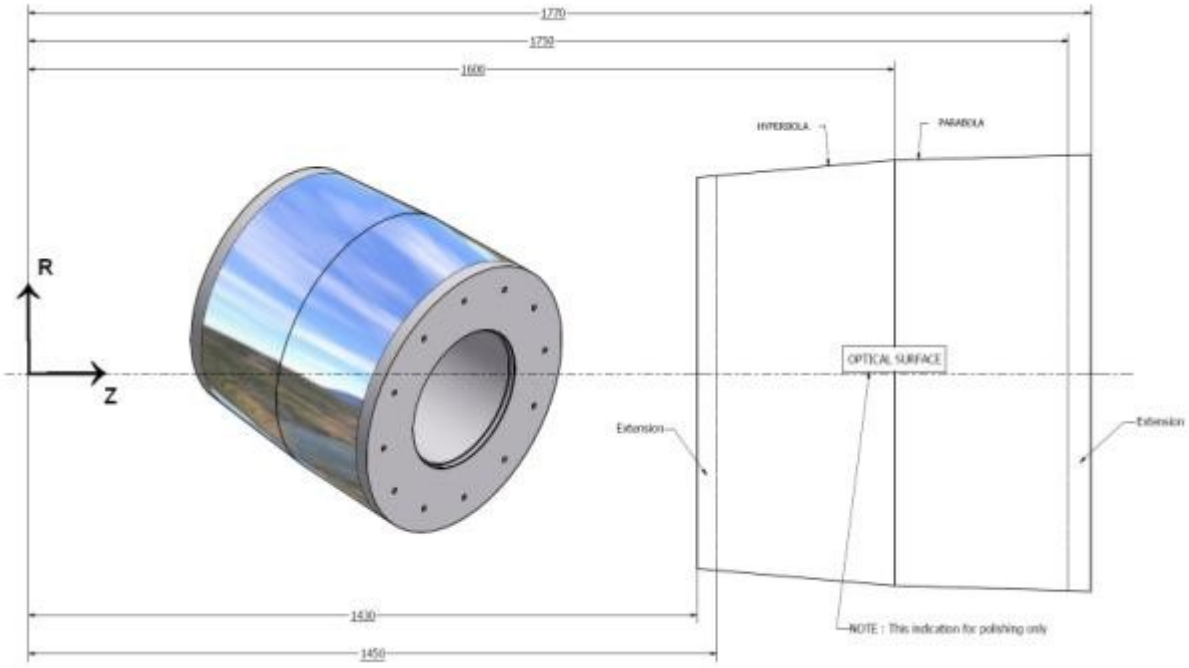

Figure 6-9. eROSITA mandrels mechanical design.

The biggest mandrel is the number 1 (eROFM1) with a medium diameter of 356..41 mm. The smallest (of the new mandrel series) is the number 27 (eROFM27) with a medium diameter of 167.68 mm. The grazing incidence angles vary from ~ 0.7 deg (for the mandrel eROFM27) to ~ 1.5 deg (for mandrel eROFM1).

The mandrels are constituted of a single piece (no assembly) consisting of two continuous sections (parabola and hyperbola – Wolter I). Each section of the mandrel is 170 mm long. The extension of 20 mm, with respect to 150 mm required for the mirror shell replication, is to permit a continuity of the surface during polishing process. The extension is shielded during the electroforming process.

The mandrel blanks consists of **NiP** coated aluminum cores, the **Wolter I** geometrical shape is generated by using the **Diamond Turning** (DT) process. The polishing of this mandrel has been perform with the IRP600 machine for removing the DT marks and for improving the geometrical angular resolution to HEW < 6 arc seconds. The surface finishing has been optimized by using the traditional **superpolishing** equipments.

The IRP600 machine is a smaller version of the IRP1200X machine, procured by MLT company specifically for the production of the eROSITA mandrels.

6.3.2 Mandrels geometrical shape

The shape accuracy error has been effectively measured with 2D and 3D metrology equipments that allow the determination of the different contributions separately. The final HEW is calculated by the Root Sum Square (RSS) of the contributions, and the dominant contribution is from the axial profile errors.

The **axial profile error** has been measured by using the high accuracy LTP and/or MPR profilometer (see chapter 4) at 8 equally spaced azimuthal angles (i.e. each 45deg). The raw data have been Fourier filtered with a low-pass 3.5mm cut-off. The axial slope error contribution to the HEW has been calculated by ray-tracing software, giving prediction consistently below < 6 arcsec (see Figure 6-10 and Table 6-5).

The **out-of-roundness** has been measured on 6 different positions along the optical axis (3 on parabola and 3 on hyperbola). The typical roundness error is in the order of 0.3μm. The HEW contribution coming from the out-of-roundness error has been calculated by using the median values (δ50) scaled for the focal length according to the formula as per eq. (4.3).

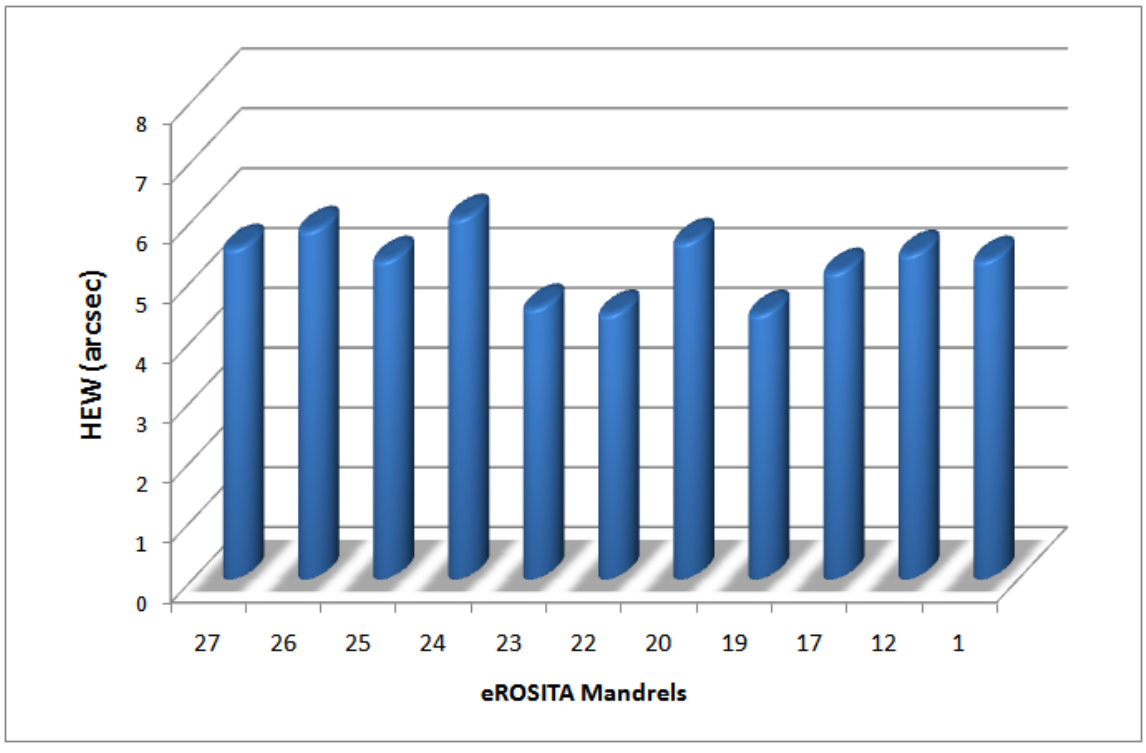

Figure 6-10. HEW axial slope error contribution of the eROSITA mandrels.

The absolute value of the **mandrel radii and taper angle** has been measured by using UPMC 3D coordinate machine before final superpolishing. The contribution to the error in the absolute radii is almost a homogeneous defocusing w.r.t. the nominal, and has negligible effect on the HEW. The **focal length** of the eROSITA mandrels is $F = 1600.0 \pm 0.5$ mm.

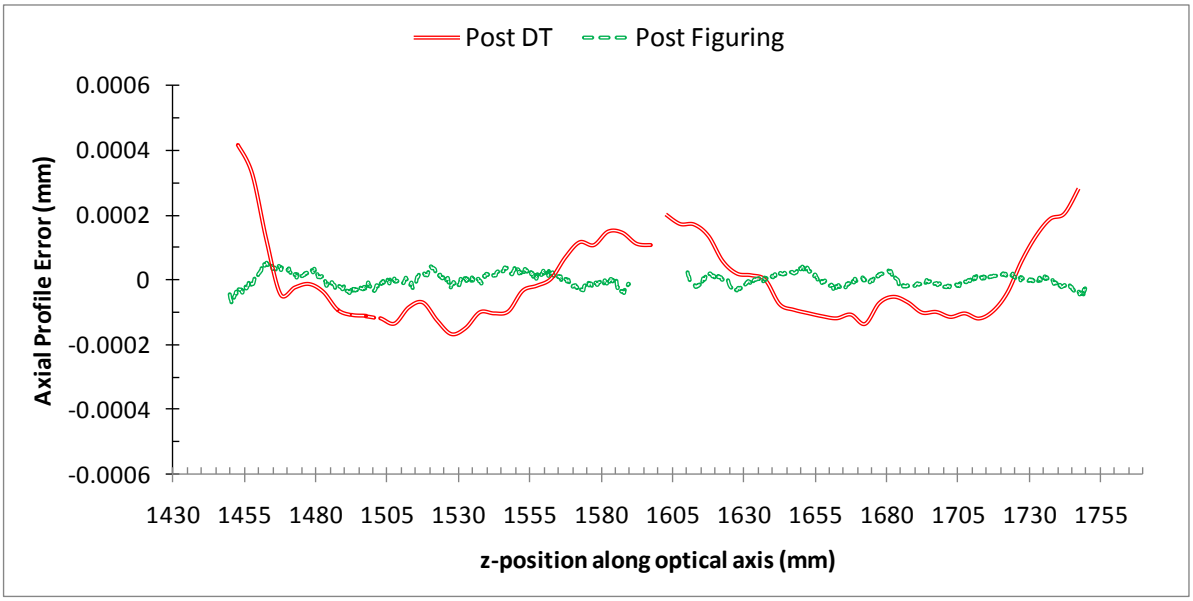

Figure 6-11. Profile error of eROSITA mandrel eROFM1 after the DT process (red-solid line) and after the corrective polishing performed with the IRP 600 machine (green-dashed line).

6.3.3 Mandrels roughness

The metrological characterizations of the superpolished mandrel mid-scale error and micro-roughness have been performed, over spatial wavelength range between 1.25mm and 0.002mm, by using the non-destructive metrological systems available in MTL: PROMAP phase shift interferometry and contrast phase microscopy Nomarski.

The surface has been superpolished to the roughness level of **~ 0.2 nm** as calculated by averaging the PSDs from 6 measurements acquired over the mandrel optical area with PROMAP 40x (157 μm x 118 μm area). Also the mid-spatial frequencies error has been brought to the desired value of **~ 0.3 nm** as calculated by averaging the PSDs from 12 measurements taken randomly over the mandrel optical area with PROMAP 2.5x (1.25 mm x 0.6 mm area). The roughness of the eROSITA mandrels is summarized in Table 6-5.

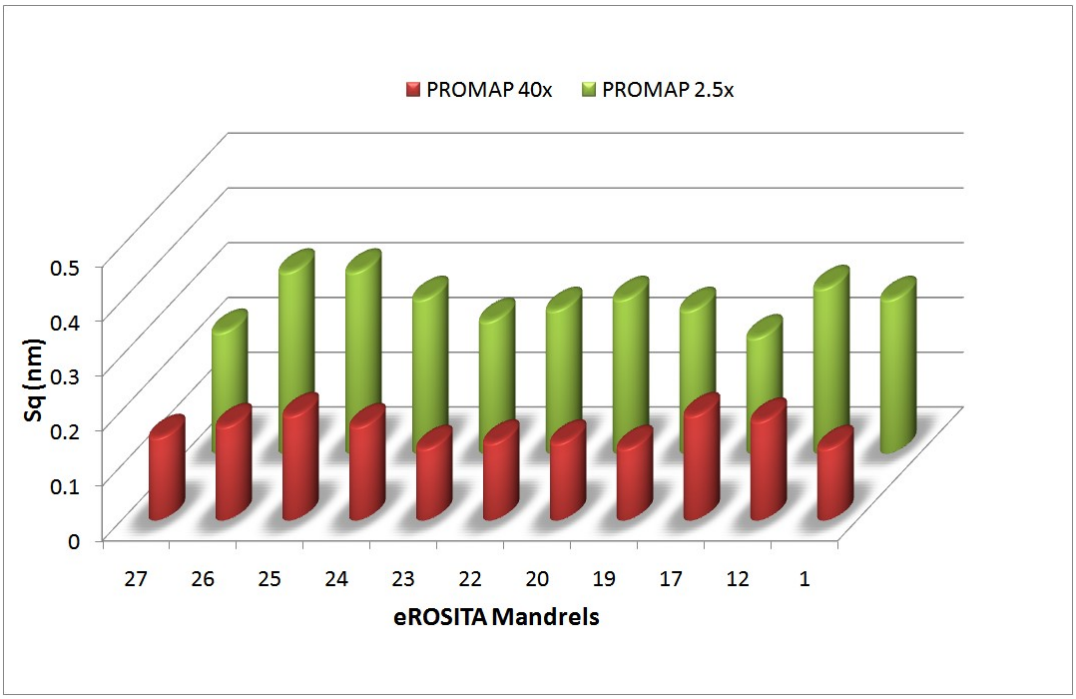

Figure 6-12. PROMAP 40x and 2.5x roughness of the eROSITA mandrels.

The AFM measurements are not mandatory for the eROSITA mandrels, since the mission will operate in the soft x-ray band. The AFM measurements have been performed just for the mandrel eROFM25 giving a microroughness between **0.2 nm – 0.4 nm** rms.

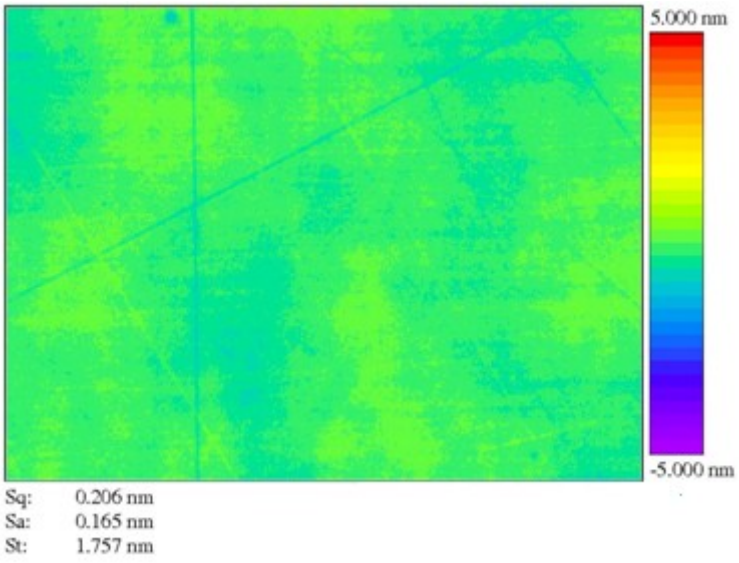

Figure 6-13. eROFM25 PROMAP 40x image (157 μm x 118 μm area), giving roughness Sq = 0.21 nm.

Table 6-5. Summary of eROSITA mandrels performance.

Mandrel	Shape accuracy		Mid-scale errors and roughness	
	HEW cut-off 3.5mm	W90 cut-off 3.5mm	PROMAP 2.5x	PROMAP 40x
	[arcsec]	[arcsec]	[nm]	[nm]
27	5.5	14.6	0.22	0.15
26	5.8	14.0	0.33	0.17
25	5.3	15.0	0.33	0.19
24	6.0	14.4	0.28	0.17
23	4.5	12.9	0.24	0.13
22	4.4	11.1	0.26	0.14
20	5.6	13.9	0.28	0.14
19	4.4	13.8	0.26	0.13
17	5.1	13.6	0.21	0.19
12	5.4	15.3	0.30	0.18
1	5.3	14.4	0.28	0.13

6.4 Mandrels performance summary

In the figure and table below it is provided comparison of the PSDs and performance of the main mandrels I manufactured whit the advance polishing technique.

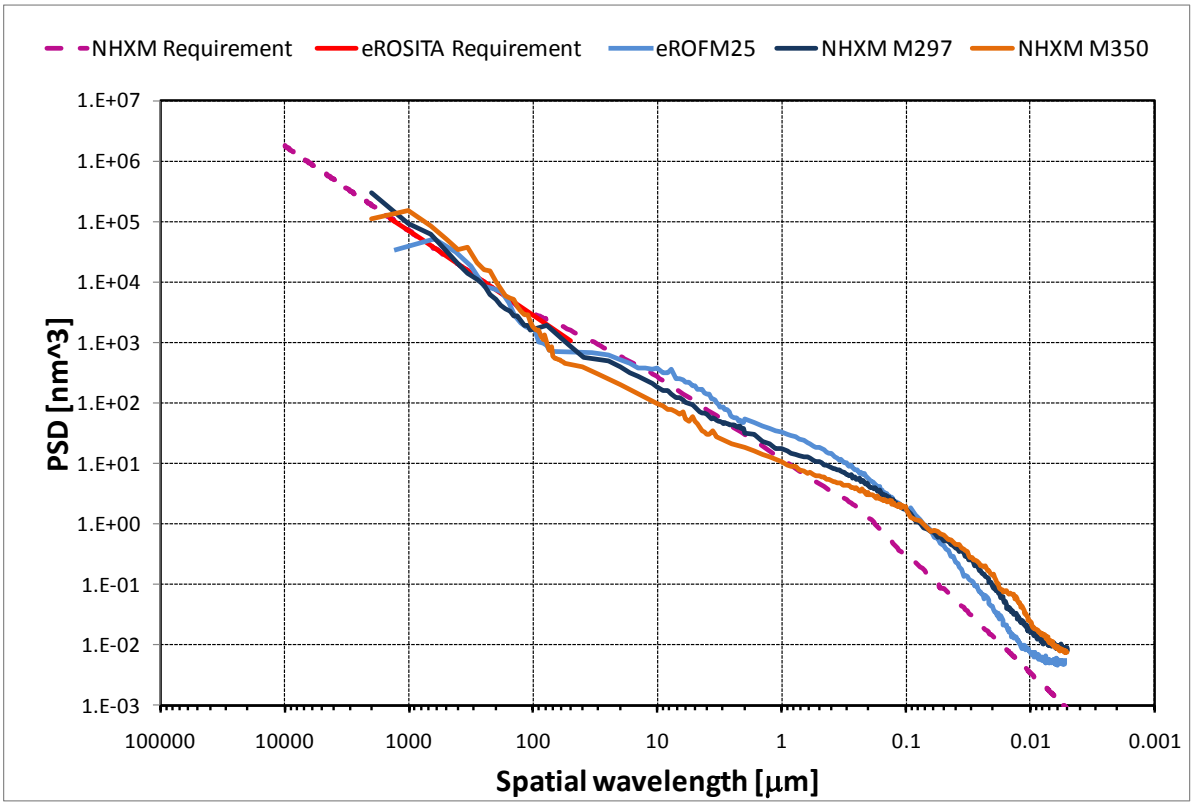

Figure 6-14. PSDs of NHXM mandrels (M350, M297) and one eROSITA mandrel (eROFM25).

Table 6-6. Summary of mandrels performance obtained with the advance polishing technique.

Mandrel	HEW	PROMAP 2.5x	AFM 100 µm	AFM 10 µm	AFM 1 µm
	[arcsec]	[nm]	[nm]	[nm]	[nm]
eROFM25	5.3	0.33	3.8	3.6	2.2
M350	5.9	0.45	3.2	2.8	2.1
M297	4.7	0.40	3.6	3.1	2.2

7 Development status of the NHXM mirror module assembly

The development status here presented is part of the study contracts financed by ASI in 2009 for a Technology Development Program (ASI-TDP) aiming at improving the technology readiness level, with in-house adoption of hardware for the metrology/manufacturing of the multilayer x-ray optics.

The baseline for 4 identical NHXM Mirror Modules is based on nested electroformed Nickel-Cobalt alloy (NiCo) thin mirror shells with multilayer coating. For the NHXM mirrors, a number of core technological improvements have been studied, including:

- manufacturing techniques to obtain mandrels with high accuracy and low roughness for replication by electroforming and related metrology systems **(already described in the previous chapters and relevant part of my PhD activity)**;
- e-forming technique for the innovative NiCo alloy and the studies on the gold separation layer;
- the W/Si and Pt/C multilayer (both deposition machine and technique), mandatory to obtain reflectivity up to 80 keV;
- the integration of the mirrors into modules by using an improved Vertical Optical Bench (VOB) aimed at minimizing diffraction effects and at obtaining a better prediction of the optical performance (HEW).

The feasibility of the technologies is demonstrated by the manufacturing of 2 Technology Demonstration Models (TDMs), integrating NiCo mirror shells (coated with W/Si and Pt/C multilayer), **produced by using the mandrels manufactured under my supervision**.

The TDMs have been tested at the PANTER-MPE x-ray calibration facility demonstrating the feasibility of the technologies for the focusing optics of the NHXM mission.

7.1 Nickel-Cobalt (NiCo) e-forming of the mirror shell

The mirror shells thickness is one of the main parameters tuned in this study. Mass reduction is fundamental in every space missions and all x-ray missions are characterized by the mass-to-collecting area ratio. It is well known that for a quasi-cylindrical shell, the deformation due to a generic load is indirectly proportional to the cubic power of the thickness. A strong reduction of the thickness increases the risks to have plastic deformation during the separation of the shell from the mandrel and possibly during the handling and integration process of the shells. Moreover the internal stress of the electroforming bath and the electrical field distribution over the mandrel optical surface, need to be kept under control in a more stringent way with respect to thicker mirror shell.

The introduction, development and optimization of the Nickel-Cobalt (NiCo) alloy instead of pure Nickel for the electroforming of the mirror substrate is meant to the maximization of the mechanical properties of the alloy and optical performance of the mirror. Internal stress, surface roughness and cobalt percentage have been the main characteristics observed. The most important requirements cover the Yield Strength, the Microyield and Young's module of axial to radial direction of the shell. The advantages in using the NiCo alloy than pure Nickel are:

- The NiCo alloy has the microyield point about 3 times higher than that of pure nickel;
- The NiCo alloy has a higher hardness than the pure nickel;
- The NiCo alloy has the higher Ultimate Tensile Stress (UTS) compared to pure Nickel;
- The NiCo alloy has higher yield strength than pure Nickel.

The Nickel Cobalt alloy (NiCo), obtained by electroforming process, is a relatively new material and the literature does not provide enough information which can be used to define unequivocally the physical and mechanical specifications of the alloy.

The electroformed Nickel-Cobalt alloy developed in MLT company has been fully characterized and demonstrated to have better mechanical performances w.r.t. to pure Ni has reported in Table 7-1.

The NiCo shells have been realized with nominal thickness of alloy equal to 0.26 mm. Different electroforming parameters have been applied, in order to optimize the NiCo electroforming process, principally in term of Residual Internal Stress (RIS). The mirrors obtained are characterized by mass, thickness and chemical composition in agreement with the expected 5%

variation as shown in Figure 7-1.

The benefit of using NiCo alloy as electroforming material for shell substrate is highlighted by the optical performance of replicated shells as measured in full illumination under UV light on a Vertical Optical Bench (VOB). The validation of the process has been performed by replicating a series of Nickel and NiCo mirror shells with 0.26 mm thickness by using the flight-quality NHXM mandrels M297. The improvement of the mirror shells HEW is reported in Table 7-2, showing the better optical performance of NiCo shell w.r.t. pure Nickel.

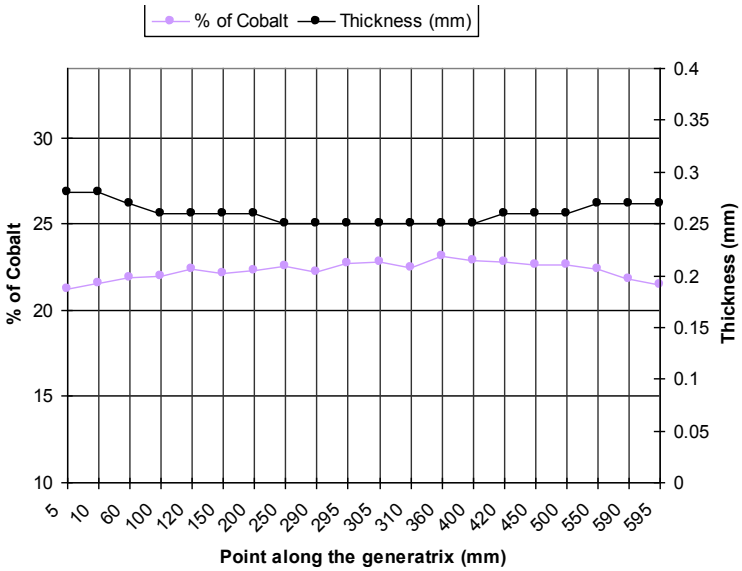

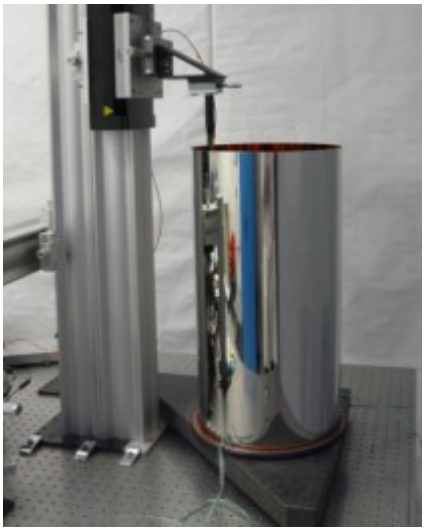

Figure 7-1. Thickness (dark line) and chemical composition (violet light line) along the axis of a 0.26mm thick NiCo mirror shell (on the left) and a NiCo shell during axial profile measurement (on the right).

Table 7-1. Comparison of Nickel-Cobalt alloy and pure Nickel properties as per MLT e-forming.

MATERIAL	HARDNESS [HV 0.3]	YIELD (0.2%) [MPa]	UTS [MPa]	MICRO YIELD [MPa]	YOUNG'S MODULUS [GPa]
Nickel	300	500	800	70	150
Ni-Co	500	1000	1600	160	160

Table 7-2. HEW performance (express in arcsec and measured with VOB) of NiCo and Ni mirror shells (MS) replicate from the M297 mandrel.

NICKEL – COBALT (NiCo)			PURE NICKEL (Ni)
MS 1 (M297R2)	MS 2 (M297R3)	MS 3 (M297R4)	MS 4 (M297R5)
14.5”	14.8”	13.6”	16.3”

Also surface roughness measurements have been performed on the mirror shells replicated from the NHXM flight quality development mandrel M297. Objective of the tests was to characterize the surface roughness of the e-formed shells in order to verify that the NiCo is able to provide similar texture performance w.r.t. to the pure Ni. Pure Ni electroforming process is known to provide good replication of the mandrels roughness.

Four 2-inches diameter samples have been derived from each mirror replicated from the mandrel, and they have been measured with AFM (100, 10 and 1 μm) and PROMAP (2.5x and 40x) instruments. A couple of measurements result is provided in Figure 7-2 and the complete set is summarized in Table 7-3 together with the reference values of the M297 mandrel.

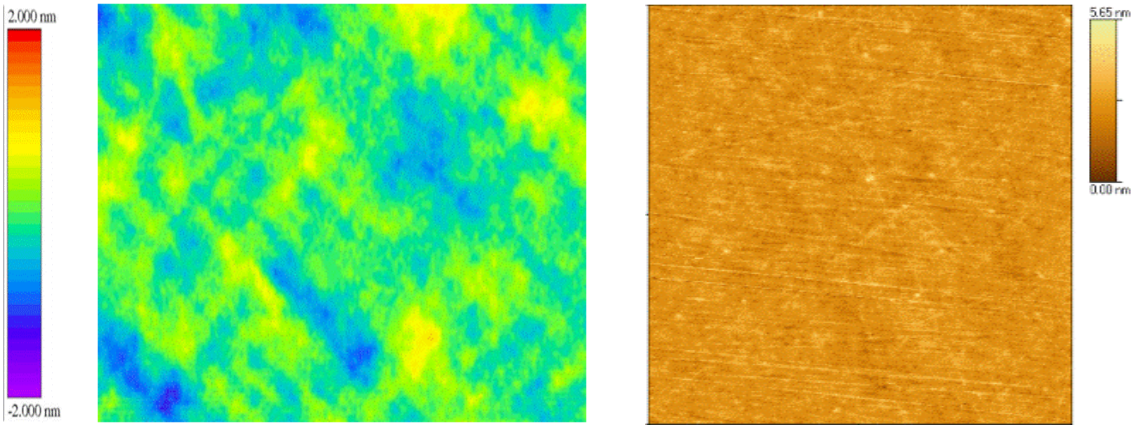

PROMAP 2.5x (2.509 mm x 1.882 mm)

Sq = 0.38 nm

AFM 10 μm x 10 μm

Sq = 0.48 nm

Figure 7-2. Roughness measured on MS 1 (M297R2) with PROMAP and AFM instruments.

Table 7-3. Roughness of the Ni and NiCo mirror shells replicated from the M297 mandrel. Measurements performed with AFM (100, 10 and 1 μm) and PROMAP (2.5x and 40x) instruments.

Mandrel / Mirror Shell	**Roughness**				
	100 μm	**10 μm**	**2 μm**	**2.5X**	**40x**
	σ rms [Å]	**σ rms [Å]**	**σ rms [Å]**	**σ rms [Å]**	**σ rms [Å]**
Mandrel M297 before replicas	3.9	3.4	2.3	2.9	2.1
MS1 (M297R2) NiCo	5.5	4.8	2.8	3.8	2.8
MS2 (M297R3) NiCo	6.1	5.6	3.1	3.6	2.7
MS3 (M297R4) NiCo	6.1	5.9	3.8	2.7	2.8
MS4 (M297R5) Ni	6.3	5.1	2.7	3.1	2.4
Mandrel M297 after replicas	4.0	4.3	3.0	3.1	2.3

7.2 Multilayer deposition on mirror shells

During the Phase A of the NHXM project completed in 2008, the multilayer activities were focused on the retrofitting of the existing PVD machine available in MLT company and the development of a-periodic W/Si coating with 95 bi-layers to be deposited on the two demonstrator mirror shells. After the coating with 95 bi-layers, a first test consisted in the deposition of depth graded coating with 200 bi-layers has been done.

The main components designed for NHXM phase A retrofitting are reported below:

- two vertical axially mounted magnetron sources equipped with cylindrical automatic shutters;
- a dedicated gas injection system in order to assure uniformity of gas pressure inside the chamber;
- a completely new top flange with an integrated lifting mechanism;
- a differentially pumped quadrupole mass spectrometer, for the characterization of the

residual atmosphere before, during and after the deposition;
- two digital storage oscilloscopes equipped with high voltage and current probes for monitoring the electrical process parameters in the pulsed current operation mode;
- PC for data logging and control.

In order to meet one of the main objective of the NHXM project, that is to improve, by means of a multi-layer coating, the reflectivity for x-rays in the energy band from 10 to 80 keV, an improved design for W/Si multi-layer stack (200 bi-layers) must be defined, at the same time new couple materials must be considered and investigated.

As far as the materials are concerned, several studies have already been performed in the past to define the best couple of high and low density materials. Good candidates are the couples Pt/C, W/Si, Mo/Si and Ni/C, which are well known for their chemical stability and the high reciprocal contrast of the refraction indexes in the x-ray region. The broader reflectivity in total reflection regime and the extended operative range free of absorptions make Pt and C material the best choice for the NHXM development program.

Moreover, the NHXM project foresees that the PVD machine must be able to house and coat mirror shells with the diameters ranged between 150 mm $\leq \varnothing \leq$ 350 mm. Therefore, the following "hardware" improvements have been now faced:

- design of a new set of linear miniaturized sources;
- a new system for precise positioning of magnetrons has been designed in order to change the distance between target and shell substrate.

The paragraph reports the W/Si design for the development of a high performance a-periodic 200 bi-layers, the new hardware designed for the development of Pt/C multi-layer coating and the design for the development of a brand new Pt/C a-periodic 200 bi-layers.

Big efforts have been spent in order to understand the minimum lateral dimensions of the source due to the small diameters of the inner shells to be coated. Moreover, source dimensions have been chosen based on trade-off between target cooling capabilities, axial homogeneity of deposition on 600mm length, and to allow high rate deposition of Pt and C. Two solutions have been investigated: "single body" source, "dual body" source.

Single body magnetron source

The "single body" source is a linear magnetron 850 mm long (see Figure 7-3), made by two

independent cathodes joined back to back; each cathode have a different targets that sputter in opposite directions. To minimize the dimensions, the source presents a single anode (Figure 7-3, top view) and has the advantage to allow depositions starting from the shell with a diameter of 160mm (without shutter). Due to the design of the anode, built as a single and indivisible component, the main drawback is represented by the impossibility to separate the two cathodes and therefore to position the magnetrons in order to have the appropriate target to substrate distance (TSD).

It is worth to highlight this aspect as the TSD represents a fundamental parameter for the process that must be properly varied and studied during the development of the multilayer in order to select the best process condition for multi-layer growth; for this reason, this design has been rejected.

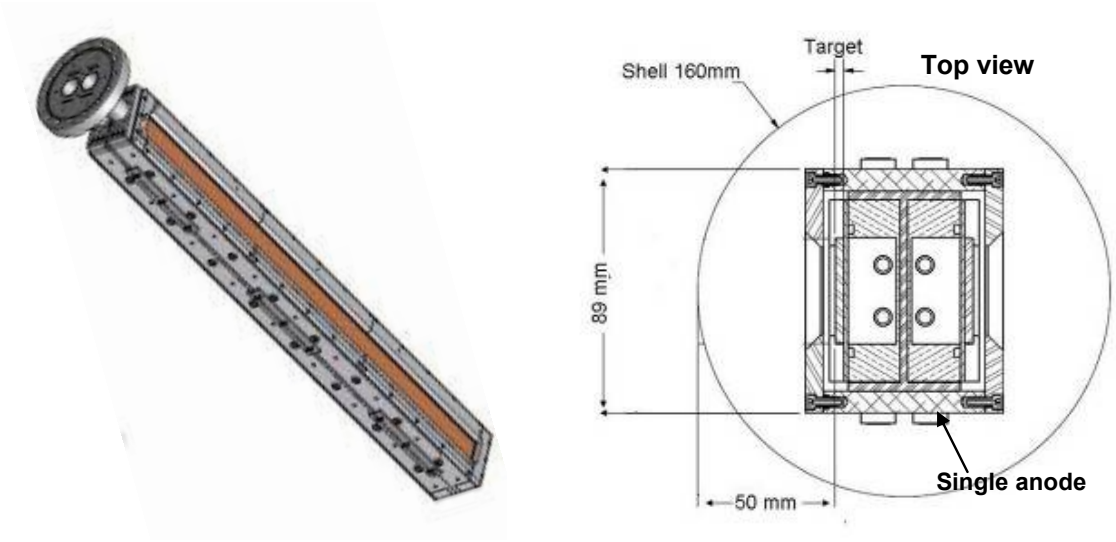

Figure 7-3: Lateral and top view of "single body" source, in the top view is visible the single anode, the 160mm diameter shell is reported.

Dual body magnetron source

The "Dual body" source is very similar to "single" body being a linear magnetron with length of about 850 mm (Figure 7-4, lateral view): the main difference consists in the possibility to separate the two cathodes allowing to change the target to substrate distance (Figure 7-4, top view). In fact, the anode is not a single and indivisible piece but is made by two independent parts joined together by a system of screws as shown in Figure 7-4.

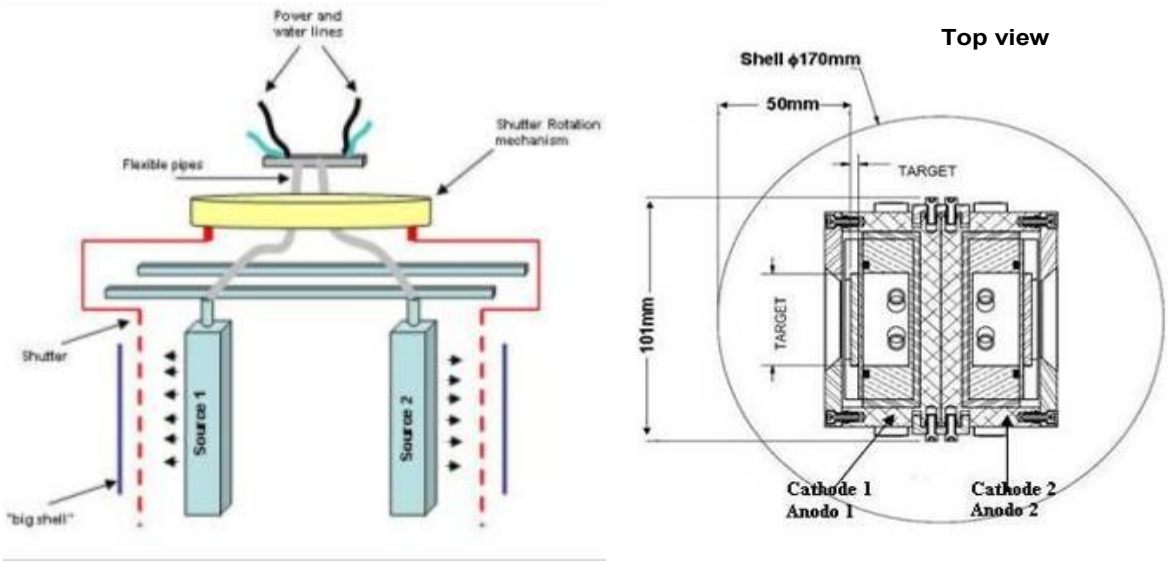

Figure 7-4: Lateral and top view of "dual body" source: in the top view is visible the "separable" anode. The shell of 170 mm diameter is sketched.

The drawback of this design is that the minimum diameter of shell that can be coated is 170 mm without the shutter. The capability to change the TSD parameter, placing the magnetrons in different positions, together with the chance to coat the innermost shells (150 ≤ diameter (mm)< 180) with a Pt monolayer, is the reason that has pushed to accept this solution as the new source for NHXM program.

7.2.1 W/Si multilayers

The W/Si multilayers are deposited using the dedicated facility at MLT company. The facility testing and calibration has been done with XRR tests (see section 4.2.7) performed on W/Si samples deposited onto small Silicon wafer pieces. This kind of non-destructive investigation enables not only the direct measurement of reflectivity performances, but also to extract the characteristic parameters of the stack like thickness, density values, roughness, by means of a very accurate fit of the reflectivity. This was achieved, in turn, using the PPM computer simulation program (Spiga, 2007). The resulting feedback to the multilayer manufacturing allowed the tuning of the facility to deposit wideband multilayer coatings for focusing x-rays up to 50 keV that have been tested at the PANTER facility.

W and Si single layers

Some XRR measurements were performed onto single layers samples deposited with the same deposition facility to be used to perform multilayer depositions. This was mainly aimed at determining the density of multilayer materials, that in turn affect the reflectivity and – to a lesser extent – the peak position. In fact, the analyses of XRR curves always returned density values lower (by 10-15%) than the bulk ones. This is not surprising in principle, because several voids can remain in a thin film structure while it is grown. In particular, it is the W density that affects the reflectivity, which is proportional to the difference of the optical constants. In addition, it is known that density variations result in a small Bragg peak shift due to refraction. This is, indeed, also affected by the Γ factor of the stack; therefore a firm estimation of the layer density ought to be confirmed by measurements on single layers.

HS23 samples (graded, 200 bi-layers)

This set of samples has obtained by depositing a 200 bilayers W/Si multilayer stack. Different samples HS23_1, HS23_7, HS23_13 have been located, respectively, at the parabolic end, the intersection plane, and the hyperbolic end of a mirror shell simulator. The XRR scan of the HS23_7 sample at 8.045 keV is reported in Figure 7-5 (very similar to HS23_1 and HS23_13).

Also plotted is the best fit reached with PPM, adopting a single power-law model superposed to oscillations grouped in blocks of 10 layers: in spite of the simplicity of the model adopted, it can be seen that the fit performed very well, even if not all details are reproduced. The power law parameters are reported in Table 7-4. Fluctuations of the fitted parameters w.r.t. the nominal do not exceed **2-3 Å**.

Table 7-4. power law parameters of the HS23_7 sample.

HS23_7	Parameters for SI	Parameters for W
Power Law parameters	a=54.55, b= -0.612, c=0.213	a=32.9, b= 2.19, c=0.24813

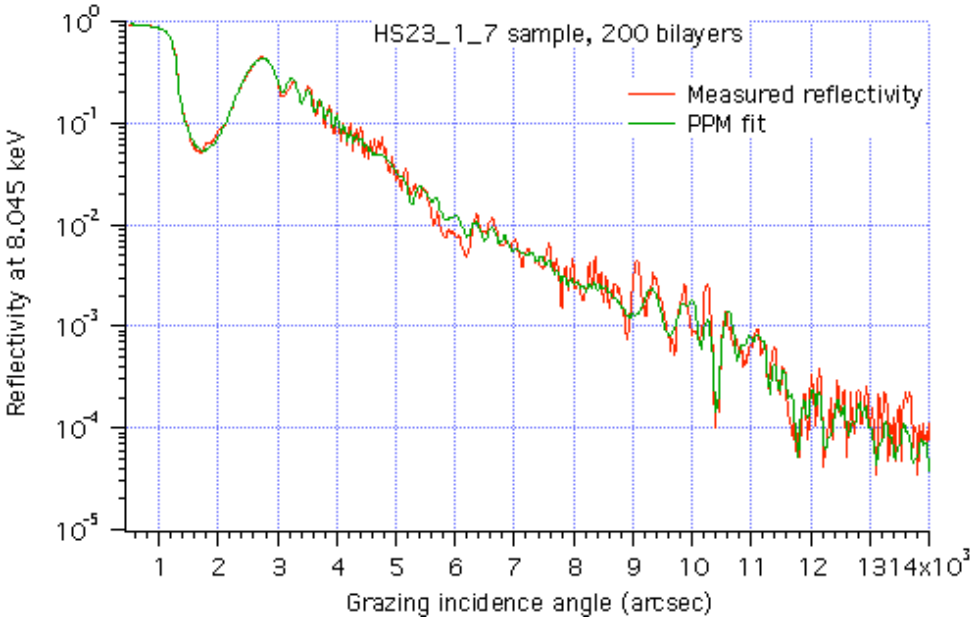

Figure 7-5. the XRR curve at 8.045 keV of the HS23_1_7 W/Si sample, superposed to the best fit obtained with PPM software.

Other findings from the PPM fit are: the density of Tungsten is **18.5 g/cm^3** and that of Silicon **2.2 g/cm^3**, while the interfacial roughness that is inferred from fit is **3.5 Å**, very close to that of the substrate.

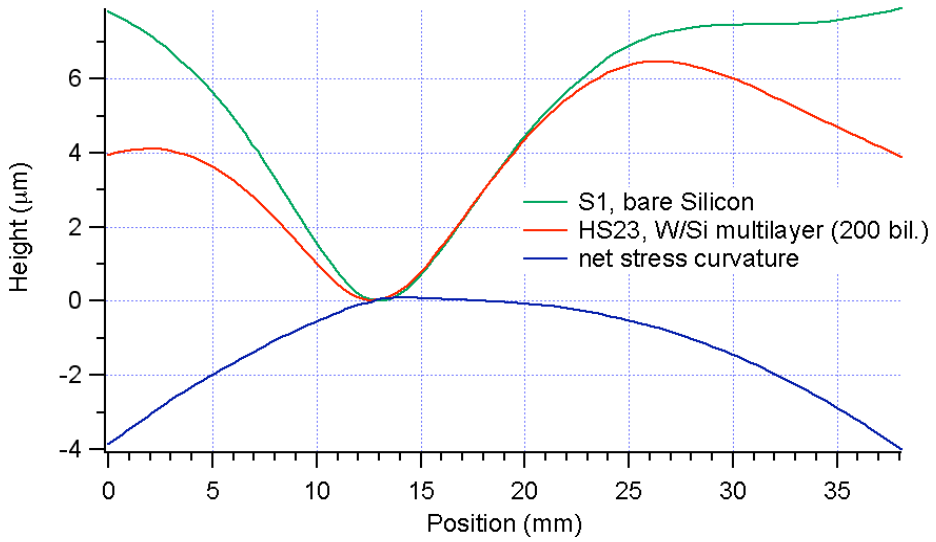

Figure 7-6. LTP stress measurement on the HS23 sample. The difference of the two profiles is almost parabolic, excepting the minimum point.

The stress measurement performed with LTP profilometer onto the graded multilayer deposited in the HS23 run is shown in Figure 7-6. The profile of the Silicon wafer (named S1) before coating has been reported in green and the profile after coating is also plotted in red. The difference of the two profiles (blue) is the net curvature induced by the multilayer stress. The net curvature is concave downwards, because the stress is **compressive**, i.e., it tends to expand the substrate. In other words, when this multilayer is applied to a Wolter-I mirror shell, it will cause a slight enlargement of the diameter of the mirror, which will result, multiplied by the f-number of the mirror, in a focal length increase. This is what we actually observe in absolute focal length measurements at PANTER.

The difference of the two profiles is almost perfectly parabolic, which means, as expected, that the stress is uniform. Only in correspondence of the minimum there is a deviation, probably due to a difficult data acquisition because the sample was heavily deformed in transverse direction. The total deformation is 4 μm over a scan length of almost 40 mm, while the measurement error (estimated along with a stability scan) is less than 20 nm, peak to valley. The parabolic fit of the profiles difference returns a curvature radius of 45.179 m. The total thickness of Silicon is 0.445 μm, the total thickness of Tungsten is 0.177 μm, and therefore the Stoney formula (eq. 4.30) yields a stress measurement of -***370 MPa***.

The **W/Si** multilayer development has reached a very good level, also because it took the benefits of the previous phase A NHXM development. The results of tests performed onto W/Si multilayers can be summarized as follows:

- the **thickness control** and the compliance to the nominal recipe has attained good levels, with random deviations of ± 2 Å at most in the thickness;
- the **repeatability** of the stack deposition is very good, with a 1% of variation of the stack structure on average;
- the **lateral uniformity**, when measured, is within 6% over the shell length, Vs. a 5% tolerance;
- the **layer density** of Tungsten (18.5 g/cm3) is lower than its nominal value (19.3 g/cm3). This is a negative point, because it conveys a reflectivity reduction. The density of Silicon is also slightly lower but this does not relevantly affect the reflectivity;
- the multilayer **stress** is compressive, and close to -370 MPa for a thickness ratio of ~0.36;
- the growth of the **roughness** and the layer interdiffusion are very low, because the final roughness replicates almost exactly the one of the Si wafer substrate.

7.2.2 Pt/C multilayers

The Pt/C multilayers are deposited using the same dedicated facility at MLT company, already used for the W/Si deposition. The facility testing and calibration has been done with XRR tests (see section 4.2.7) performed on Pt/C samples deposited onto small Silicon wafer pieces. This kind of non-destructive investigation enables not only the direct measurement of reflectivity performances, but also to extract the characteristic parameters of the stack like thickness, density values, roughness, by means of a very accurate fit of the reflectivity. This was achieved, in turn, using the PPM computer simulation program (Spiga, 2007).

The resulting feedback to the multilayer manufacturing allowed the tuning of the facility to deposit wideband multilayer coatings for focusing x-rays up to 50 keV that have been tested at the PANTER facility.

Pt and C single layers

Some XRR measurements were performed onto single layers samples deposited with the same deposition facility to be used to perform multilayer depositions. This was mainly aimed at determining the density of multilayer materials, that in turn affect the reflectivity and – to a lesser extent – the peak position.

The **Carbon** measured density is consistent with the known value, and the roughness, though uncertain, is sometimes larger than that of the Si substrate, due to the thickness of these layers, much larger than the one used for multilayers. The nominal density value we hereafter refer to is the one of amorphous Carbon (**2.1 g/cm^3**). It should be pointed out that the density of Carbon could be also much lower, down to 1.8 g/cm3 or even less.

Also for **Platinum** the measured density is always close to its nominal value (**21.1 g/cm^3**) within a few percent, although with some uncertainty due to some alignment errors on the BEDE XRD. Like for Carbon, the high surface roughness is probably related to the unusual large thickness of these layers, even though the presence of a surface oxide layer makes the roughness estimation quite uncertain.

HS79 samples (graded, 100 bilayers)

Deposition HS79 represents a 100 bi-layer depth-graded Pt/C multilayer coated on samples mounted on the mirror shell simulator corresponding to mirror shell M350.

Only the first 100 bi-layers taken from the nominal recipe have been taken (see Table 7-5). Different samples, from HS79_1 to HS79_6, have been positioned on the shell simulator:

- Samples HS79-1, HS79-2 and HS79-3 have been positioned on the 0° axis, respectively on the top, the medium and the bottom part of the shell.
- Samples HS79-4, HS79-5 and HS79-6 have been positioned on the 180° axis, the first on the top, the second on the medium and third on the bottom part of the shell.

The PPM fit results (power-law parameters, density and roughness) tell that in general the nominal recipe is well reproduced, with a good lateral uniformity (**6%**) excepting one sample, whose XRR is much less structured and could be fitted poorly, always because of a probable lateral gradient of thickness over the sample surface.

The roughness values inferred from the fit (**3.5 – 4 Å rms**) are in general good because they are close to that of the substrate (3 Å rms), meaning a low roughness introduced by the process itself, excepting the sample n. 2, which undoubtedly exhibits a higher roughness (6.5 – 7.0 Å rms).The density values are ~ **20 g/cm^3** for Platinum and **2.0 g/cm^3** for Carbon (the density of Pt is somehow lower than the bulk value, but in this case this is doubtful).

The reflection performance in hard x-rays has also been checked at 5 to 40 keV, finding a confirmation of the low roughness and the multilayer structure found with PPM (as can be seen in Figure 7-7).

Table 7-5. Power law parameters of the HS23_7 sample. The Γ ratio is equal to 0.42.

HS79	Parameters for C	Parameters for Pt
Power Law parameters	a=37.7, b=-0.943, c=0.223	a=27.3, b=-0.943, c=0.223
Power Law parameters	Maximum thickness: 71.5 Å. Min thickness of 11.6 Å	Maximum thickness: 51.7 Å. Min thickness of 8.4 Å

Table 7-6. Density and roughness values inferred from XRR scans for samples of HS79 series.

Samples	Pt parameters a, b, c	C parameters a, b, c	Pt density (g/cm^3)	C density (g/cm^3)	XRR roughness rms (Å)
HS79_1	26.3, -0.94, 0.22	37.8, -0.97, 0.22	19.6	2.0	4.1
HS79_2	27.6, -0.85, 0.29	37.8, -0.75, 0.19	19.6	2.4	6.4
HS79_3	27.2, -0.95, 0.21	39.6, -0.98, 0.21	20.7	1.9	5.1
HS79_4	27.5, -0.95, 0.21	38.1, -0.97, 0.22	19.6	2.0	3.6
HS79_5	26.6, -0.94, 0.22	38.8, -0.97, 0.22	19.6	2.3	4.5
HS79_6	28.2, -0.93, 0.23	39.4, -0.97, 0.22	20.8	1.9	3.3

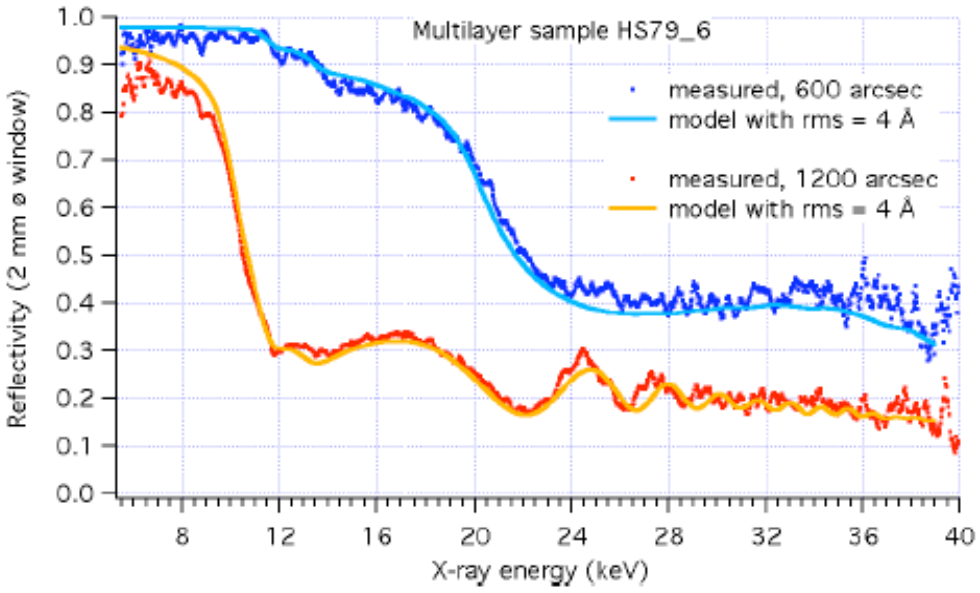

Figure 7-7. XRR curves of the HS79_6 at 5 to 40 keV, at incidence angles close to those of the hyperbolic and parabolic segments of the mirror shell MS350 in the PANTER configuration.

Also some stress measurements were performed for the HS79 deposition run. The difference of the profiles is almost perfectly parabolic. From the curvature radius, the total film thickness, the wafer thickness, we derive, using the Stoney equation, a compressive stress of ~ **-400 MPa**, a value similar to those of the HS64 samples.

The deposition of **Pt/C** multilayers exhibited more complex problems than the one of the W/Si, as expected, because this kind of multilayer was never deposited with the PVD deposition machine of MLT, before this phase:

- the **thickness control** and the compliance to the nominal recipe were optimal at the beginning of the development. The subsequent tests yielded alternate results at this regard, but the thickness stability was reduced soon to acceptable values (< 2 Å). The nominal recipe is reproduced to within a few percent;
- the **repeatability** of the stack deposition has probably reached good levels (a ~5% variation), even if it should be further investigated;
- the **lateral uniformity** is close to 6% over the shell length, Vs. a 5% tolerance;
- the **layer density** of Platinum (20.6 g/cm3) is - on average - very close to its nominal value (21.4 g/cm3), an important aspect because a density reduction would have affected the reflectivity performance. The density of Carbon is also similar to the nominal value, even if this has a lesser impact;
- the **multilayer stress** is compressive. Initial measurements yielded a very high stress value of -1000 MPa (0.44 thickness ratio): subsequent measurements returned a compressive stress of -400 MPa (0.42 thickness ratio), more similar to the one of W/Si multilayers;
- **roughness** growth and layer interdiffusion: XRR data highlighted soon a problem with the surface roughness. The first graded sample, though thinner than the nominal recipe, is much rougher than its substrate. The subsequent periodic samples, moreover, systematically show a surface roughness that increases with the total thickness. The roughness inferred from the XRR data is correlated to the measurement performed with the AFM. The XRR-AFM data matching allows ruling out a significant contribution of the interdiffusion of layers, which could not be distinguished from the sole XRR dataset. From last samples, the interfacial roughness has been improved, partly because the number of graded bilayers has been reduced to 100, but the real reason of the improvement is to be clarified yet. In spite of the undoubted improvement, there always remain one or two samples per deposition run showing

evidence for growth of roughness. Because the different samples are located at different positions in the coating chamber, the multilayer deposition might have an inhomogeneous roughness, i.e., scattering properties variable from point to point, which is clearly a negative point. Future developments of the Pt/C multilayer in the context of this project should be aimed at understanding the reason of the roughening of the multilayer interface and correcting it, improving thereby the reflectance/focusing performances of the coating.

7.3 Mirror Module integration

After the manufacturing of the mirror shells and the coating with multilayer films, the optical elements have to be assembled in a specially-designed mirror case that endows them with the necessary stiffness and allows the optical module handling with a minimization of the shells deformation. The mirror shells integration into the mechanical structure is a particularly delicate operation since the mirror shells are very thin and the risk to induce deformations is very high. For this reasons it is also necessary the adoption of special designed front and rear spiders, with a large number of arms (20 or more), as derived by previous studies. In order to handle the thin mirror shells, and to restore the best roundness profile to the pseudo-cylinders, for each mirror shell it is necessary to precisely machine two metallic stiffening rings to be mounted at the top and bottom of the shell. The two rings are close to the two edges of the shell. With these rings, that have a radial thickness of about 20mm, it is not possible to put in the mirror module the other shells. Therefore the shells must be glued to a temporary structure that gives the needed stiffness and that it will be taken out at the end of the integration, when both spiders are glued

The VOB is the facility that allows to measure, optically in full illumination, the mirror shells and to align (integrate) them in the mirror module. The VOB measures the HEW of a shell by direct imaging of its focus, i.e. using the same approach adopted at the PANTER facility for the measurement at x-ray wavelength. The use of a UV source allows the VOB to better predict the HEW value at 1.5 keV measured at PANTER, roughness effects not included. The HEW measurements aims also at the monitoring of the integration steps. In fact, in order to achieve the best performances, the geometrical HEW of the mirror must be carefully measured before, during, and at the end of the integration procedure. Possible deformations arising during the integration process are promptly indicated by VOB and can immediately be corrected.

UV source radiation is used to minimize the contribution of diffraction effects that blur out the focus image. The shorter the wavelength, the lower the contribution of diffraction, the more reliable the measurement. According to a preliminary test, the shorter wavelength usable is in the range of **220 nm**, since shorter wavelength are absorbed by the ozone in the air. The existing VOB allows the measurement and integration of mirror shells with maximum diameter of 500 mm with any focal length between 8 and 12 meters.

The VOB is constituted by an optical collimator (diameter 750 mm) for full illumination of mirror shells; the light reflected by the mirror shell is focused on a CCD for the measurement of the optical performance; each mirror shell can be aligned to the mirror module pre-positioned on the optical bench and fixed (integrated) to it. The control room is provided with the electronics to control the mechanical actuators for the positioning of the source, the CCD in the focal plane of the mirror shells, the alignment of the mirror shells and the managing of the CCD in the focal plane of the mirror shells, including the software dedicated for the real-time analysis of the focal plane.

The VOB "product tree" is presented, together with an overview of the system, in Figure 7-8.

<u>VOB Inner Room subsystem</u>

- Cassegrain collimator
  - Mirrors
  - Optical sources
- MM Support structure
  - Integration adapter
  - Suspension device
- MM Positioner (crane)
- Main tower
  - Folding mirrors

<u>VOB Control Room subsystem</u>

- Motion control electronics and S/W
- CCD electronics and dedicated S/W
- Metrology and analysis S/W

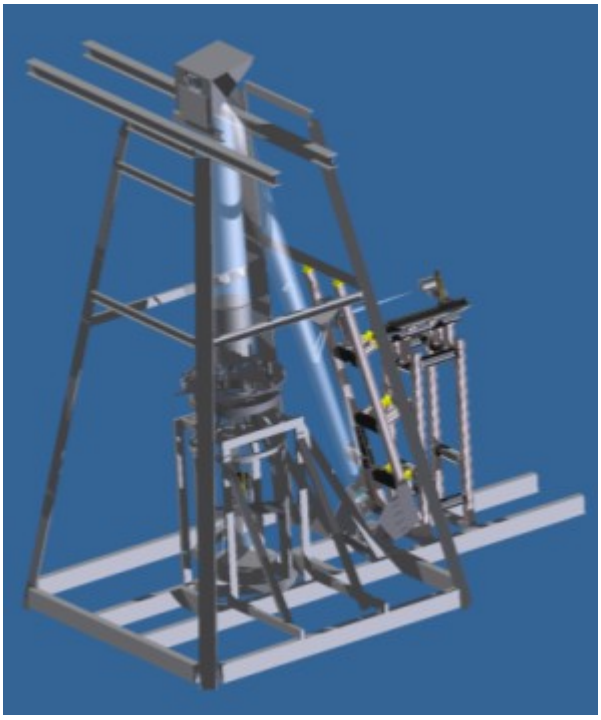

Figure 7-8. Product Tree and structure overall view of the VOB installed at MLT.

Two different Technological Demonstrator Models (TDMs) each composed by 3 mirror shells have been integrated. TDM1 by making use of the VOB facility of INAF-OAB, TDM2 by making used of the specifically developed VOB facility available at MLT (above described). The two VOBs mainly differs in the UV source (373nm for the former, 220nm for the latter) and the mirror holding system (actuators for the former and suspension for the latter).

7.3.1 TDM 1 integration

The main steps of the integration process can be summarized as follows:

1. positioning and alignment of the case, spider, central tube and actuators/suspensions;
2. positioning of the shell;
3. alignment of the shell;
4. gluing the shell to the lower spider;
5. gluing the shell to the temporary structure;
6. removing the stiffening rings for the glued shell;
7. shifting outside the actuators/unhook of the suspensions;
8. repeating from step 2 to step 6 for the next shell;
9. gluing all the shells to the upper spider;
10. removing the temporary structure.

For the TDM1 the only difference between the planned integration sequence and the applied process is the fact that no temporary structure has been used. This was based on the results of some preliminary tests showing that the fixation was leading to a negligible improvement. Three NiCo mirror shells, replicated from mandrels having different diameters in the range of the NHXM optical modules (400 – 150 mm), have been integrated. The mirror wall thickness is 0.26 mm, the mirrors are 600 mm long, exactly like those of NHXM. The mirror shells are:

- MS286-R4 (4th replica of mandrel M286);
- MS291-R9 (9th replica of mandrel M291);
- MS297-R1 (1st replica of mandrel M297).

All the three mirrors have been coated with a graded W/Si multilayer to enhance their reflectivity in the hard x-ray band, up to 50 keV. These multilayer coatings are made with a 200 bilayers W/Si multilayer deposited by RF magnetron sputtering at the MLT *ad hoc* PVD facility.

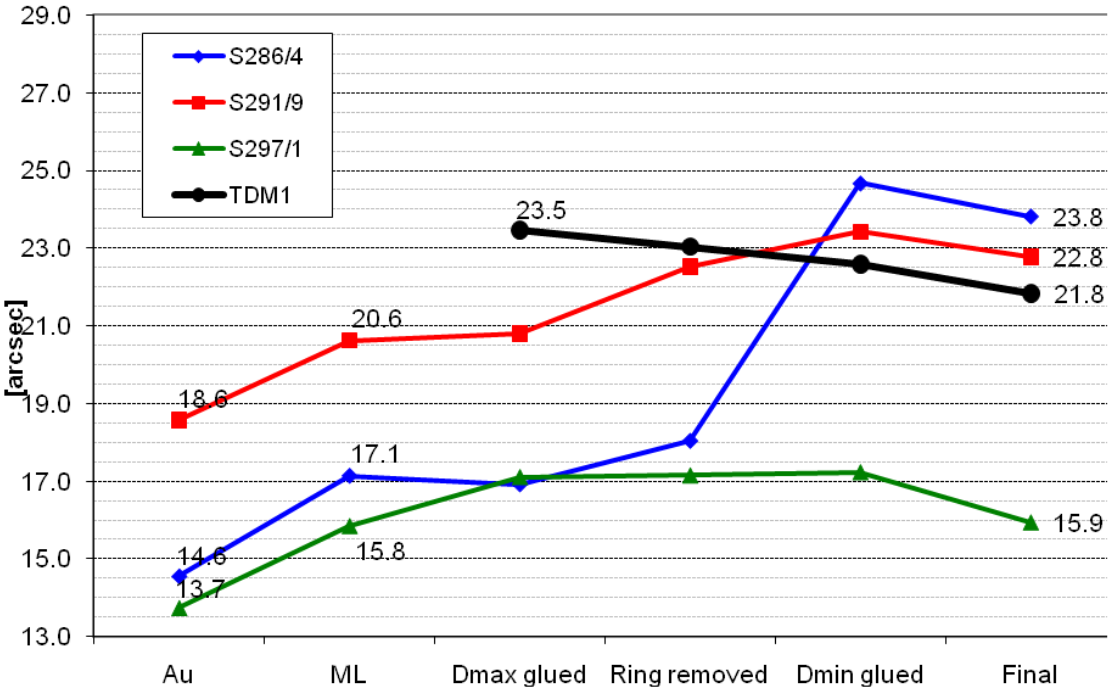

Figure 7-9. HEW evolution during integration of TDM1 starting from the measured value after replication and multilayer coating. The HEW is given for the individual mirror shell and for the mirror module as a whole.

Summarizing the behaviour of the three shells, the effect of each integration step is shown in the Figure 7-9 and here below commented:

- The increase of HEW of shell 286-R4 (from 18 arc seconds to 23.8 arc seconds) has occurred after its gluing on the upper spider. It is not known whether the cause is linked to the troubles induced on the shell by the operations performed to secure the fixation of shell 297-R1, or to some interference during the installation of the upper spider. In the hypothesis that the problem is the upper spider, its interference with the shell could be avoided by using a device that assures high centering tolerances of the upper spider or re-introducing the virtual spider.
- The **removal of the reinforcing integration rings** has caused a mean degradation of HEW of 1 arcsec on each shell. This could have been reduced probably with the use of the central shaft and the virtual spider.
- The **Focal lengths**, after the multilayer coating, showed an increase of 20 mm as average value.

7.3.2 TDM 2 integration

The integration of the demonstrator TDM2 has been performed on the new MLT VOB, aligning the shells using a suspension system, i.e. acting from top. For the TDM2 the full planned integration sequence and the applied process has been used, including the temporary structure.

Three NiCo mirror shells, replicated from mandrels having different diameters in the range of the NHXM optical modules (400 – 150 mm), have been integrated. The mirror wall thickness is between 0.2 and 0.3 mm, the mirrors are 600 mm long, exactly like those of NHXM. In the following we shall refer to them as:

- MS185-R2 (2nd replica of mandrel M185);
- MS297-R9 (9th replica of mandrel M297);
- MS350-R1 (1st replica of mandrel M350).

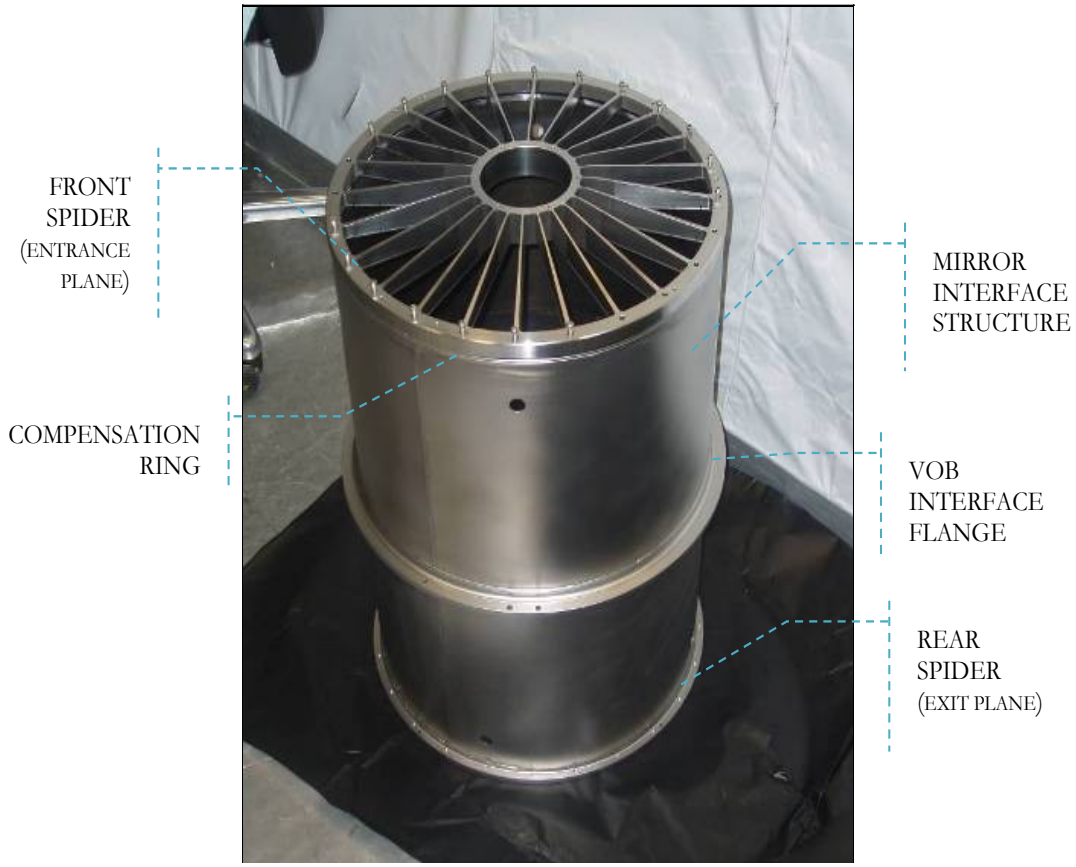

Figure 7-10. Mirror Module structure parts (note: the structure is upside down).

Like for the previous prototypes TDM1, the mirrors have been coated with a graded multilayer to enhance their reflectivity in the hard X-ray band, up to 50 keV. These multilayers are different from shell to shell: the well-experimented 95 bilayers W/Si multilayer has been deposited onto the MS297, whilst the MS185 and the MS350 are coated, for the first time, with two 100 Pt/C graded bilayers coating, with slightly different recipes. All multilayers are deposited using the magnetron sputtering facility developed *ad hoc* at MLT.

Summarizing the behaviour of the three mirror shells, the effect of integration is reported in the Table 7-7 and commented here below:

- the improvement (-0.3 arcsec) of HEW of shell 185 is within the metrology accuracy;
- the degradation (+3.4 arcsec) of HEW of shell 297 is due (≈ +3 arcsec) to the fact that the temporary bridge has not maintained the shape of the shell when its small rounding ring has been removed, and to the torque of the rear spider (≈ + 1 arcsec);
- the degradation (+1.7 arcsec) of HEW of shell 350 is due (≈ +1 arcsec) to the re-positioning of the small rounding ring before placing the temporary bridge, and to the torque of the rear spider (≈ + 0.5 arcsec).

Figure 7-11. TDM2 view with the rear spider integrated. The temporary structure has been already removed.

In view of multishell telescope to be integrated in the future, the following improvements should be considered:

- the number of actuators/suspensions for mirror shells must be optimized for the different diameters;
- reduce the temperature range to 20°C ± 0.5°C to avoid detachment between rounding rings and mirror shells (a variation of 3°C has shown change of HEW due to detachments);
- install on-line temperature recording system provided with visual alert system for the technicians in case of non conformances;
- the temporary spider must be attached to the front spider after the curing of the glue of the innermost shell to avoid torque too strongly the interface screws that may distort the spider itself and therefore the mirror shells;
- the positioning of the bridges on the temporary spider is very critical and tests to improve process reliability should be performed.

Table 7-7. HEW of TDMs before and after integration for single mirrors and for the complete modules; the HEW of the complete modules before integration is calculated as weighted average of the single mirror shells.

MIRROR SHELL	MODEL	HEW BEFORE INTEGRATION	HEW AFTER INTEGRATION	HEW WORSENING [arcsec]
MS 286- R4	TDM1	17.1”	23.8”	6.7”
MS 291-R9	TDM1	20.6”	22.8”	2.2”
MS 297-R1	TDM1	15.8”	15.9”	0.1”
MS 185- R2	TDM2	19.9”	19.6”	-0.3”
MS 297-R9	TDM2	16.2”	19.6”	3.4”
MS 350-R1	TDM2	15.3”	17.0”	1.7”
All	TDM1	17.9”	21.8”	3.9”
All	TDM2	16.7”	18.6”	1.9”

7.4 Technology Demonstrator Models (TDMs) tested at PANTER

7.4.1 TDM 1

The present section reports the results of measurements performed at the x-ray facility MPE-PANTER on the 1st Technological Demonstrator Model (TDM1) optic prototype for the NHXM development project.

The integration of the 3 mirror shells of TDM1 has been described in the section 7.3.1, together with the HEW prediction from VOB measurements. In the following we shall refer to the mirror shells as *MS286/4* (4th replica), *MS291/9* (9th replica) and *MS297/1* (1st replica), or simply MS286, MS291, MS297. Nevertheless, of the 3 shells, the MS286 has not been measured in order to concentrate the tests on the two more performing mirrors - i.e. the MS291 and MS297, those with the arguably best surface roughness. The MS297 and the MS291 are measured separately and together at their best align and focus. The mirrors have been coated with a graded 200 bilayers W/Si multilayer deposited by magnetron sputtering.

In the following one can find the measurements results of effective areas and angular resolution performed on the TDM1 at PANTER at 1 to 45 keV, using the PSPC in monochromatic setup at low energies (< 10 keV) and TRoPIC at high energies (> 10 keV) in polychromatic setup.

Figure 7-12. (left) View of the TDM1 mounted on the manipulator used at PANTER. (right) the TDM1 is inserted into the 1 m wide tube at PANTER (credits: MPE).

Table 7-8. Geometric properties and coating of the mirror shell 291 in TDM1.

Parameter	***Symb.***	***Value***
Maximum mirror diameter (parabola)	$2R_M$	293.2 mm
Median mirror diameter	$2R_0$	291 mm
Minimum mirror diameter (hyperbola)	$2R_m$	284.5 mm
Mirror length (parabola + hyperbola)	$2L$	600 mm
Mirror walls thickness	τ	260 μm
Nominal, on-axis, incidence angle at the median diameter	a_0	0.208 deg
Measured focal length with the VOB (after integration)	f_V	(0.989 ± 0.02) m
Measured HEW at the best focus of the VOB	H_0	22.8 arcsec
Focal distance for a source at infinity	f	(10.07 ± 0.01) m
Actual focal distance at PANTER	f'	(10.98 ± 0.01) m
Distance of the x-ray source at PANTER	D	(120.89 ± 0.03) m
X-ray beam divergence (at the mirror front-end) at PANTER	δ	0.069 deg
Incidence angle on the parabola at PANTER	α_1	0.277 deg
Incidence angle on the hyperbola at PANTER	α_2	0.139 deg
Lost area fraction of parabola for double reflection at PANTER	Q	49.8%
Mirror obstruction by spider (at 1 keV)	V	11.7%
Supermirror parameter for Si and W (from witness samples)	a	60.5; 38.8
Supermirror parameter for Si and W (from witness samples)	b	-0.31; 2.48
Supermirror parameter for Si and W (from witness samples)	c	0.23; 0.29

Table 7-9. Geometric properties and coating of the mirror shell 297 in TDM1.

Parameter	***Symb.***	***Value***
Maximum mirror diameter (parabola)	$2R_M$	299.2 mm
Median mirror diameter	$2R_0$	297 mm
Minimum mirror diameter (hyperbola)	$2R_m$	290.3 mm
Mirror length (parabola + hyperbola)	$2L$	600 mm
Mirror walls thickness	τ	260 μm
Nominal, on-axis, incidence angle at the median diameter	α_0	0.212 deg
Measured focal length with the VOB (after integration)	f_V	(0.988 ± 0.02) cm
Measured HEW at the best focus of the VOB	H_0	15.9 arcsec
Focal distance for a source at infinity	f	(10.03 ± 0.01) m
Actual focal distance at PANTER	f'	(10.94 ± 0.01) m
Distance of the x-ray source at PANTER	D	(120.89 ± 0.03) m
X-ray beam divergence (at the mirror front-end) at PANTER	δ	0.070 deg
Incidence angle on the parabola at PANTER	α_1	0.282 deg
Incidence angle on the hyperbola at PANTER	α_2	0.142 deg
Lost area fraction of parabola for double reflection at PANTER	Q	49.8%
Mirror obstruction by spider (at 1 keV)	V	11.4%
Supermirror parameter for Si and W (from witness samples)	a	64.0; 35.5
Supermirror parameter for Si and W (from witness samples)	b	-0.64; 3.27
Supermirror parameter for Si and W (from witness samples)	c	0.25; 0.26

The PSPC and TRoPIC views

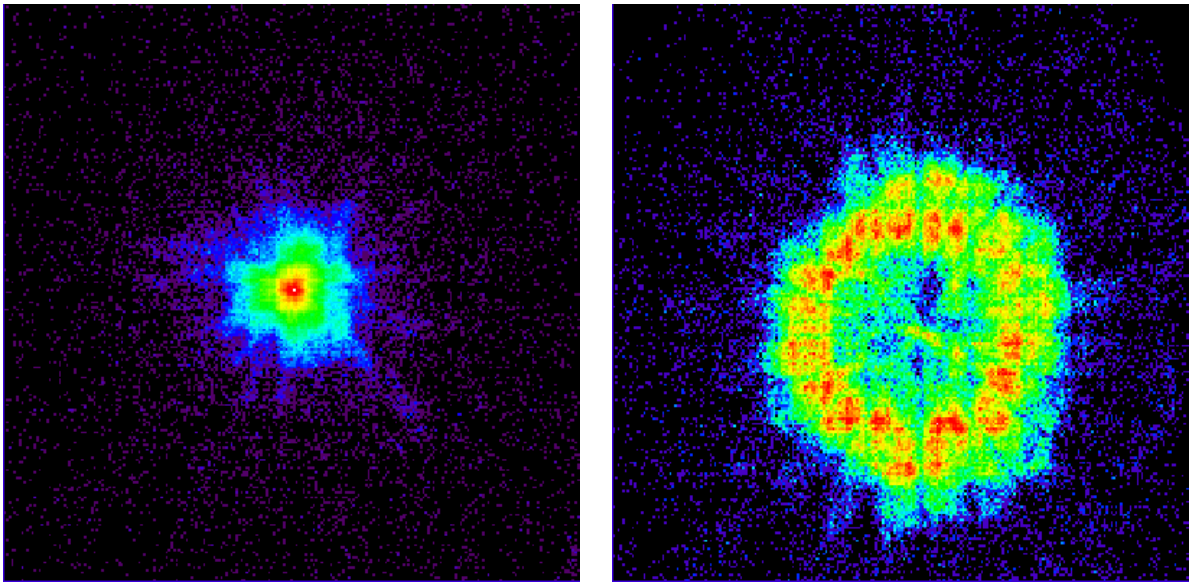

Figure 7-13. The on-axis focal spot of the TDM1 at 1.49 keV (the Al-Kα line), as seen by the PSPC. Logarithmic colour scale. (left) in focus, (right), 30 cm intra-focal.

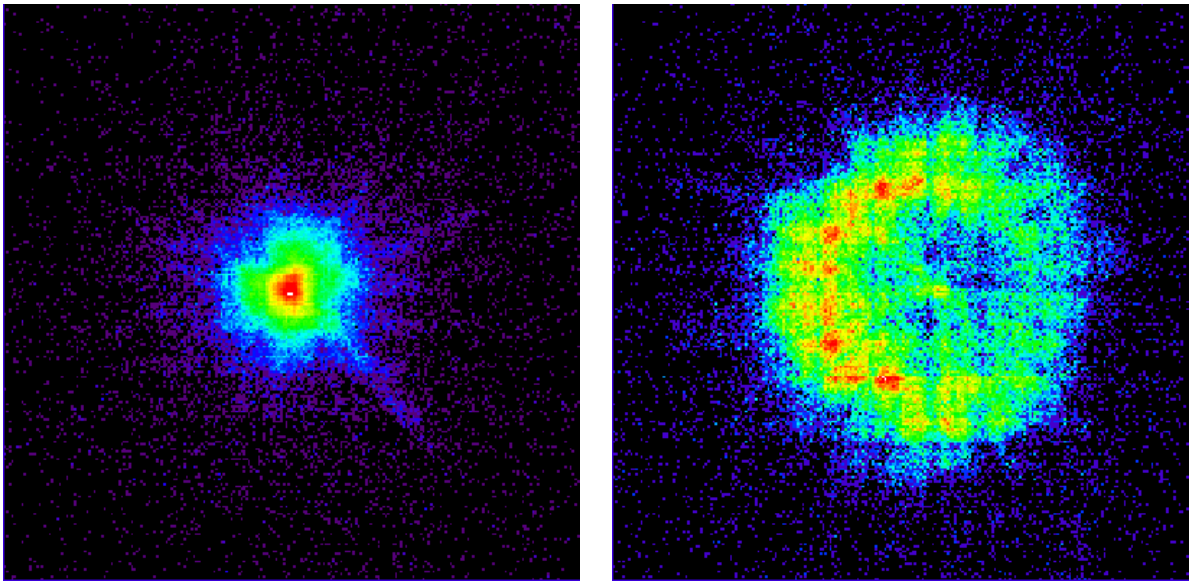

Figure 7-14. The +4 arcmin off-axis focal spot of the TDM1 at 8.05 keV (the Cu-Kα line), as seen by the PSPC. Logarithmic colour scale. (left) in focus, (right), 30 cm intra-focal.

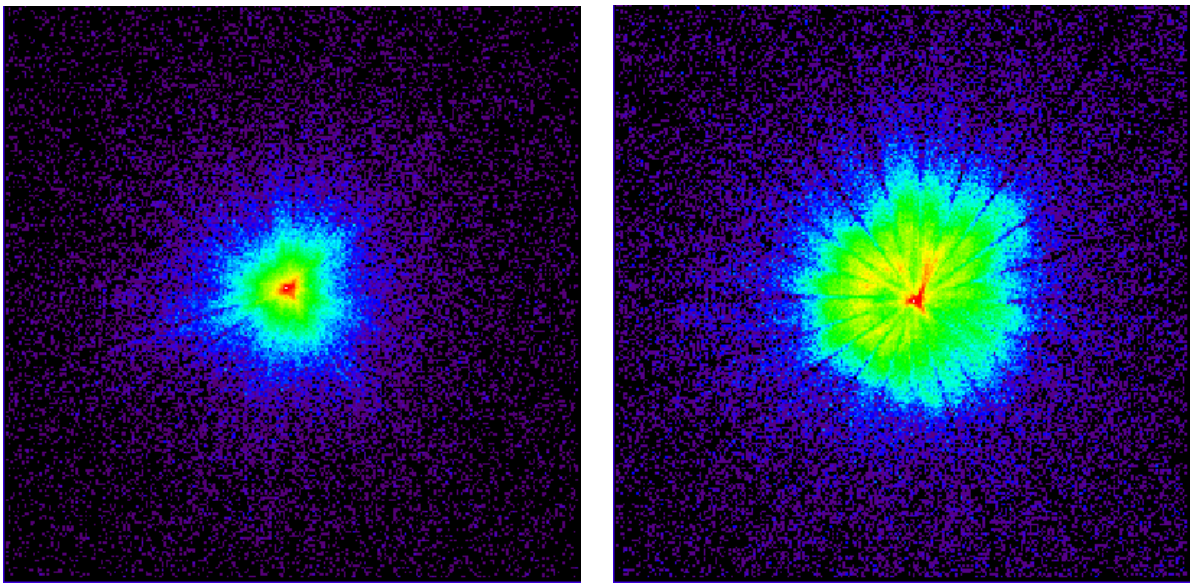

Figure 7-15. The on-axis focal spot of the TDM1 at seen by TRoPIC, with the x-ray source in 50 kV setup. Logarithmic colour scale. (left) in focus, (right), 15 cm intra-focal.

Effective Areas

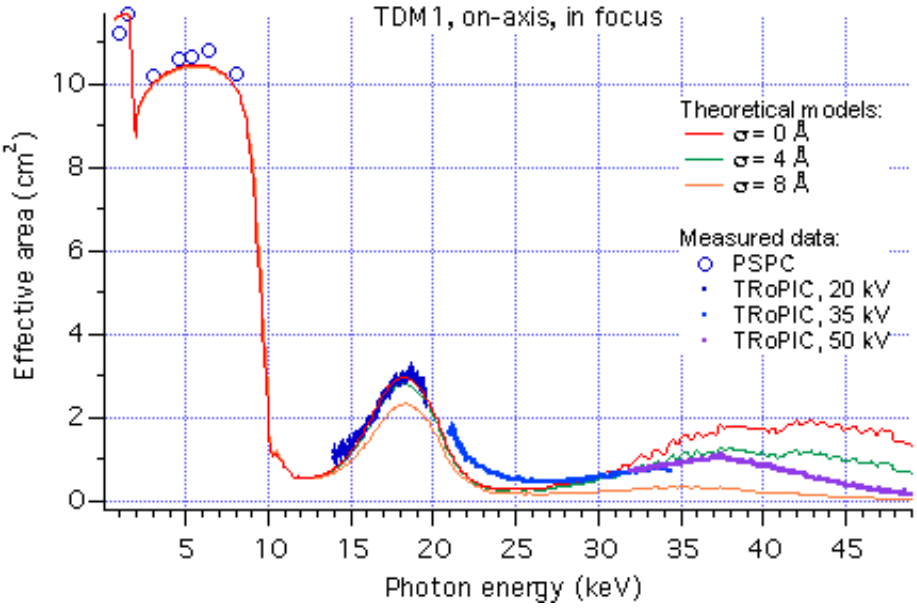

Figure 7-16. The EA of the TDM1 on-axis, as a function of the x-ray energy. Theoretical model curves are over-plotted.

Angular Resolution (HEW)

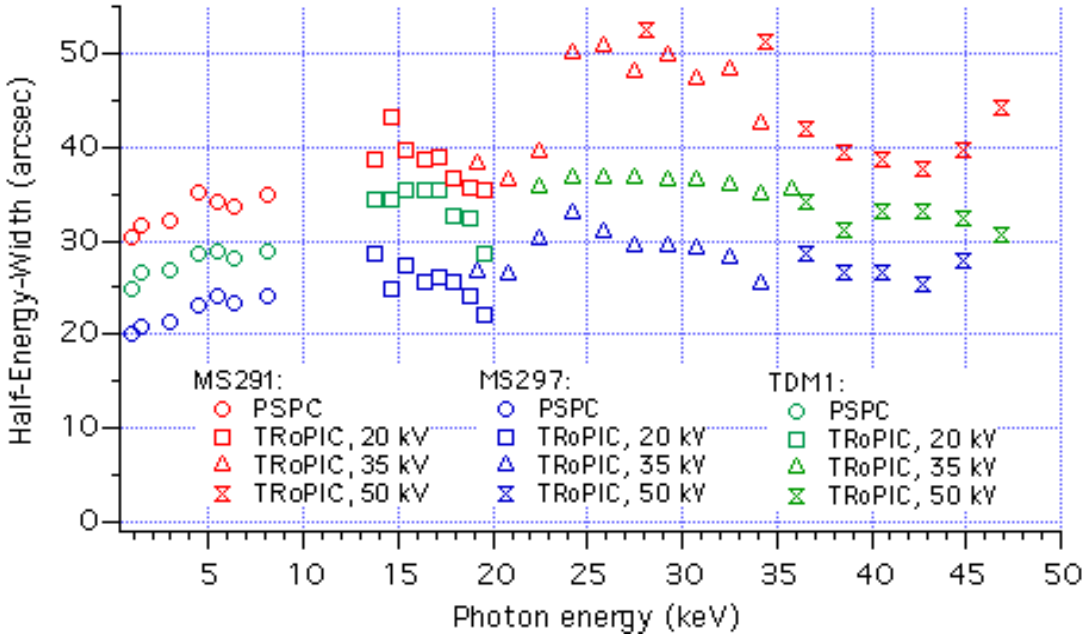

Figure 7-17. Comparison of the on-axis HEW for the MS291, MS297, TDM1, as a function of the x-ray energy. Data are uncorrected for the lost area, therefore they are reliable up to 32 keV, beyond this limit they are underestimated. The TDM1 HEW falls almost exactly in between of the HEW of the two shells.

Conclusions

- Both mirror shells of the TDM1 exhibits worse optical performances than expected from the VOB measurements in UV light prior to PANTER tests. For the MS297, this has been probably caused by an accidental damage occurred during the transportation to PANTER.
- The HEW of the MS297 increases slowly with the X-ray energy, excepting for some oscillations due to the x-ray scattering modulation in the multilayer structure, up to 32 keV. The increase for the MS291 is larger.
- The measured effective area (by integrating the focal spot in TRoPIC area) matches with the expectations up to 32 keV. After this limit, the effective area loss starts to be visible.
- The HEW of the TDM1 roughly matches the average of the HEW of the two shells.

7.4.2 TDM 2

The present section reports the results of measurements performed at the x-ray facility MPE-PANTER on the 2nd Technological Demonstrator Model (TDM2) optic prototype for the NHXM development project.

The integration of the 3 mirror shells of TDM1 has been described in the section 7.3.2, together with the HEW prediction from VOB measurements. In the following we shall refer to the mirror shells as *MS185/2* (2nd replica), *MS297/9* (9th replica) and *MS350/1* (1st replica), or simply MS185, MS297, MS350. The mirrors have been coated with a graded multilayers different from shell to shell: the well-experimented 95 bilayers W/Si multilayer has been deposited onto the MS297, whilst the MS185 and the MS350 are coated, for the first time, with two 100 Pt/C graded bilayers coating, with slightly different recipes.

Because 3 remote-controlled shutters could not be mounted on the manipulator, the measurement campaign has been divided into 2 parts: in the first week, two shutters select/shut the beam from the MS185 and the other covers both MS297 and MS350, which are selected/shut together. Then the vacuum has then been broken, a fixed shutter has been mounted on the MS185 and the shutters are replaced with other two with different diameters, one for the MS297 and the other for the MS350 to measure them separately.

In the following one can find the measurements results of effective areas and angular resolution performed on the TDM2 at PANTER at 1 to 45 keV, using the PSPC in monochromatic setup at low energies (< 10 keV) and TRoPIC at high energies (> 10 keV) in polychromatic setup.

Figure 7-18. (left) View of the TDM2 mounted on the manipulator used at PANTER. (credits: MPE).

Table 7-10. Geometric properties and coating of the mirror shell 185 in TDM2.

Parameter	***Symb.***	***Value***
Maximum mirror diameter (parabola)	$2R_M$	186.4 mm
Median mirror diameter	$2R_0$	185 mm
Minimum mirror diameter (hyperbola)	$2R_m$	180.9 mm
Mirror length (parabola + hyperbola)	$2L$	600 mm
Mirror walls thickness	τ	200 μm
Nominal, on-axis, incidence angle at the median diameter	a_0	0.132 deg
Measured focal length with the VOB (after integration)	f_V	(10.07 ± 0.01) m
Measured HEW at the best focus of the VOB	H_0	23.3 arcsec
Focal distance for a source at infinity	f	(10.09 ± 0.02) m
Actual focal distance at PANTER	f'	(11.01 ± 0.02) m
Distance of the x-ray source at PANTER	D	(120.90 ± 0.03) m
X-ray beam divergence (at the mirror front-end) at PANTER	δ	0.044 deg
Incidence angle on the parabola at PANTER	α_1	0.176 deg
Incidence angle on the hyperbola at PANTER	α_2	0.088 deg
Lost area fraction of parabola for double reflection at PANTER	Q	50%
Mirror obstruction by spider (at 1 keV)	V	10.0%
Supermirror parameter for C and Pt (from witness samples)	a	44.9; 32.5
Supermirror parameter for C and Pt (from witness samples)	b	-0.943; -0.943
Supermirror parameter for C and Pt (from witness samples)	c	0.223; 0.223

Table 7-11. Geometric properties and coating of the mirror shell 297 in TDM2.

Parameter	***Symb.***	***Value***
Maximum mirror diameter (parabola)	$2R_M$	299.2 mm
Median mirror diameter	$2R_0$	297 mm
Minimum mirror diameter (hyperbola)	$2R_m$	290.3 mm
Mirror length (parabola + hyperbola)	$2L$	600 mm
Mirror walls thickness	τ	260 μm
Nominal, on-axis, incidence angle at the median diameter	a_0	0.212 deg
Measured focal length with the VOB (after integration)	f_V	(10.05 ± 0.01) m
Measured HEW at the best focus of the VOB	H_0	21.1 arcsec
Focal distance for a source at infinity	f	(10.05 ± 0.01) m
Actual focal distance at PANTER	f'	(10.97 ± 0.01) m
Distance of the x-ray source at PANTER	D	(120.90 ± 0.03) m
X-ray beam divergence (at the mirror front-end) at PANTER	δ	0.070 deg
Incidence angle on the parabola at PANTER	α_1	0.282 deg
Incidence angle on the hyperbola at PANTER	α_2	0.142 deg
Lost area fraction of parabola for double reflection at PANTER	Q	50%
Supermirror parameter for Si and W (outer 20 bilayers) Supermirror parameter for Si and W (inner 50 bilayers)	a	54.6; 52.3 58.1; 20.3
Supermirror parameter for Si and W (outer 20 bilayers) Supermirror parameter for Si and W (inner 50 bilayers)	b	-0.87; -0.47 39.7; 0.46
Supermirror parameter for Si and W (outer 20 bilayers) Supermirror parameter for Si and W (inner 50 bilayers)	c	0.36; 0.30 0.25; 0.26

Table 7-12. Geometric properties and coating of the mirror shell 350 in TDM2.

Parameter	***Symb.***	***Value***
Maximum mirror diameter (parabola)	$2R_M$	352.6 mm
Median mirror diameter	$2R_0$	350 mm
Minimum mirror diameter (hyperbola)	$2R_m$	342.2 mm
Mirror length (parabola + hyperbola)	$2L$	600 mm
Mirror walls thickness	τ	300 μm
Nominal, on-axis, incidence angle at the median diameter	a_0	0.249 deg
Measured focal length with the VOB (after integration)	f_V	(10.07 ± 0.01) m
Measured HEW at the best focus of the VOB	H_0	18.8 arcsec
Focal distance for a source at infinity	f	(10.04 ± 0.01) m
Actual focal distance at PANTER	f'	(10.95 ± 0.01) m
Distance of the x-ray source at PANTER	D	(120.90 ± 0.03) m
X-ray beam divergence (at the mirror front-end) at PANTER	δ	0.083 deg
Incidence angle on the parabola at PANTER	α_1	0.332 deg
Incidence angle on the hyperbola at PANTER	α_2	0.166 deg
Lost area fraction of parabola for double reflection at PANTER	Q	50%
Mirror obstruction by spider (at 1 keV)	V	10.0%
Supermirror parameter for C and Pt (from witness samples)	a	38.1; 27.6
Supermirror parameter for C and Pt (from witness samples)	b	-0.943; -0.943
Supermirror parameter for C and Pt (from witness samples)	c	0.223; 0.223

The PSPC and TRoPIC views

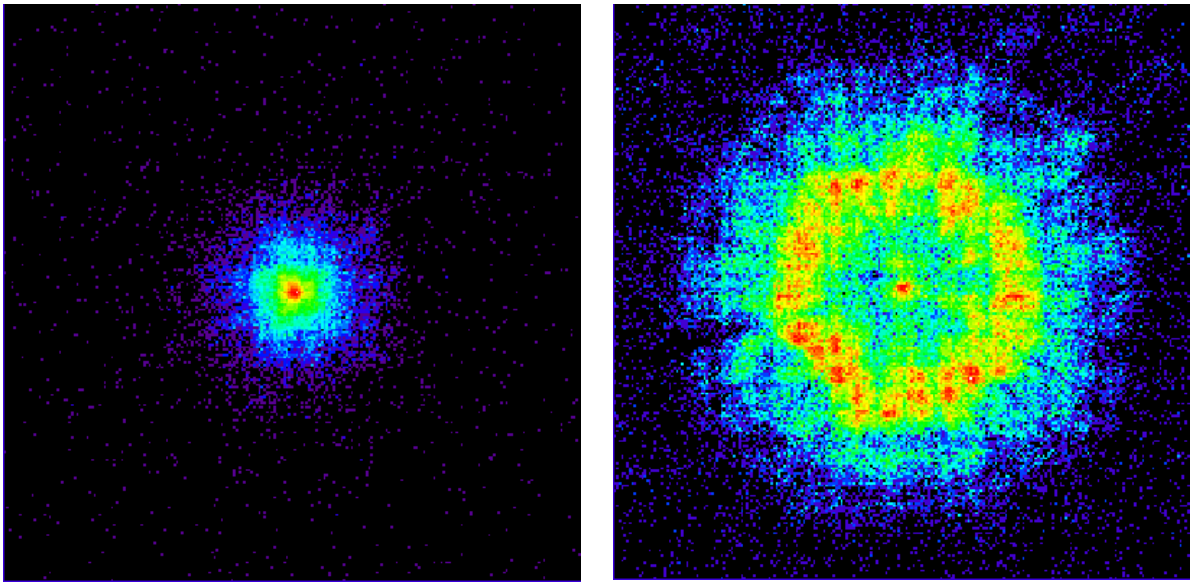

Figure 7-19. The on-axis focal spot of the TDM2 at 0.93 keV (the Al-Kα line), as seen by the PSPC. Logarithmic colour scale. (left) in focus, (right), 30 cm intra-focal.

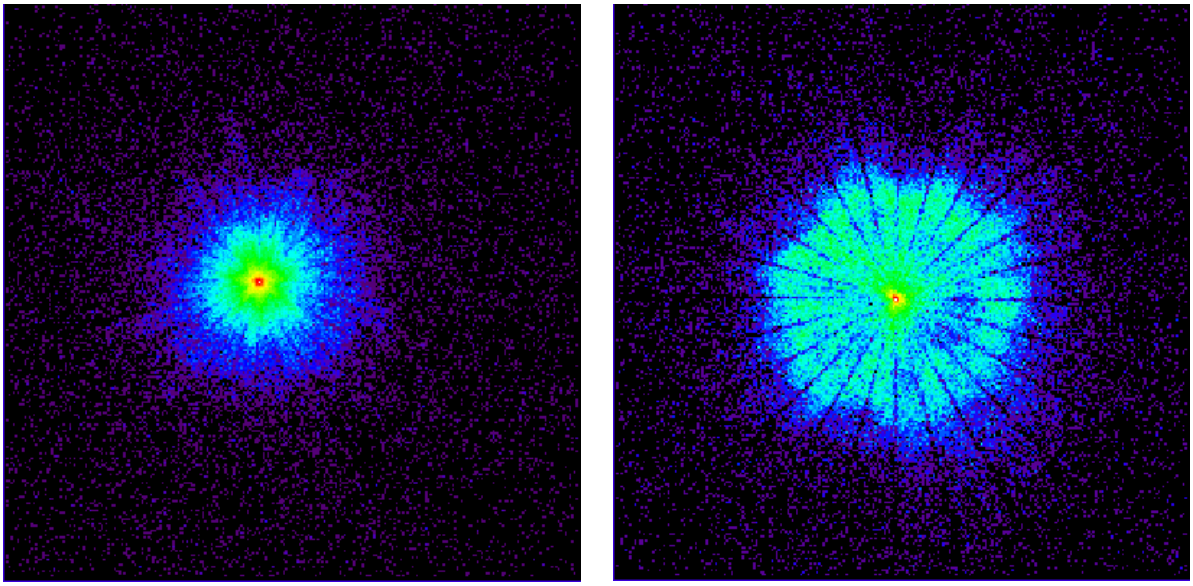

Figure 7-20. On-axis focal spot of the TDM2 at seen by TRoPIC, with the X-ray source in 35 kV setup. Logarithmic colour scale. (left) in focus, (right), 25 cm intra-focal.

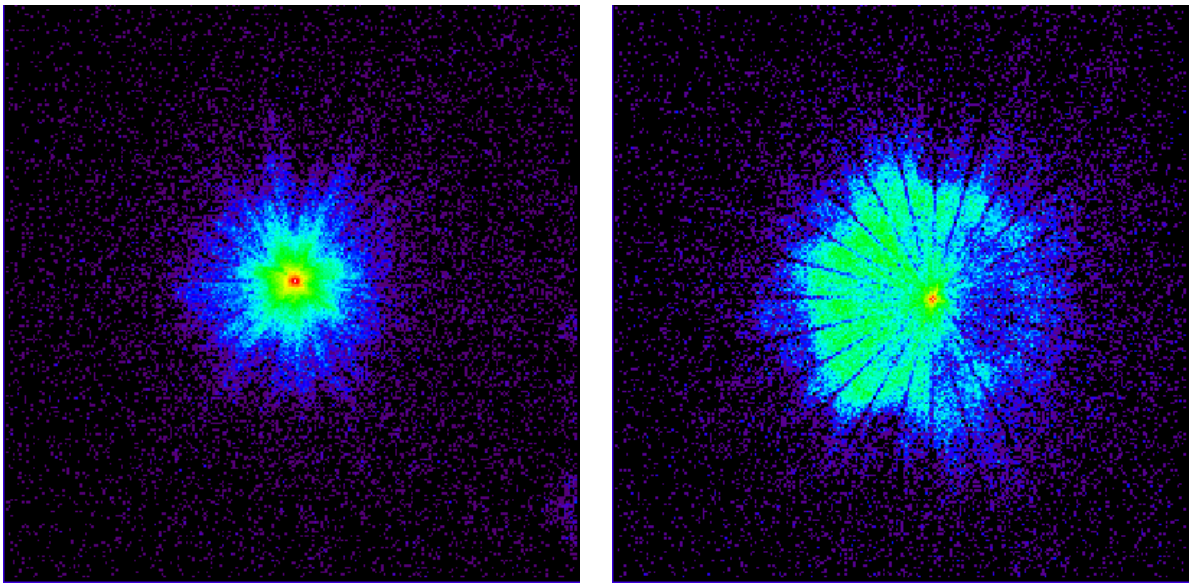

Figure 7-21. The 3 arcmin off-axis focal spot of the TDM2, as seen by TRoPIC, source at 35 kV. Logarithmic colour scale. (left) in focus, (right), 25 cm intra-focal.

Effective Areas

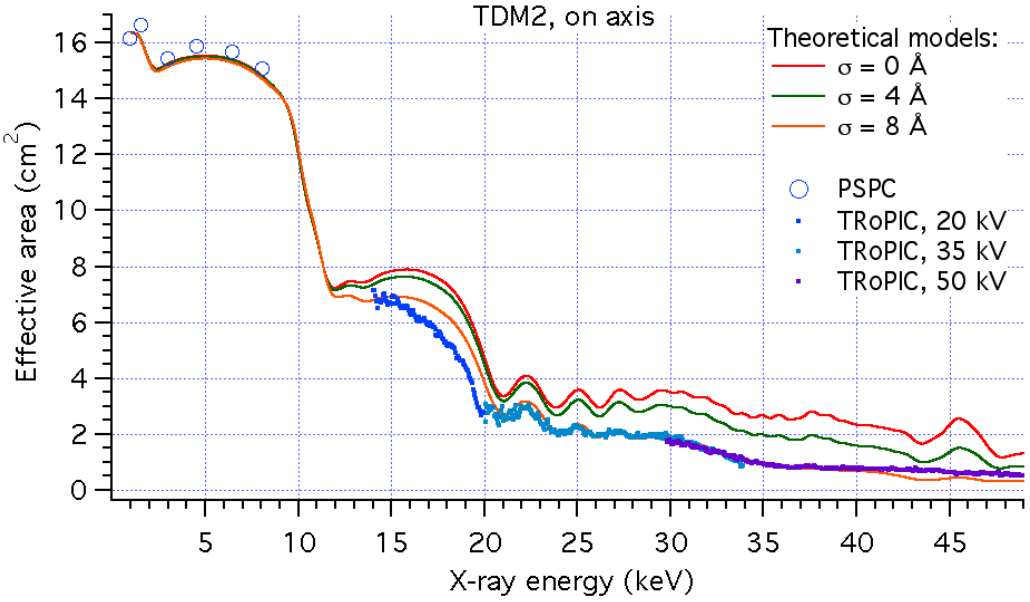

Figure 7-22. the EA of the TDM2 on-axis, as measured in monochromatic setup with the PSPC and in energy-dispersive setup with TRoPIC, The performances are the average of the 3 shells.

Angular Resolution (HEW)

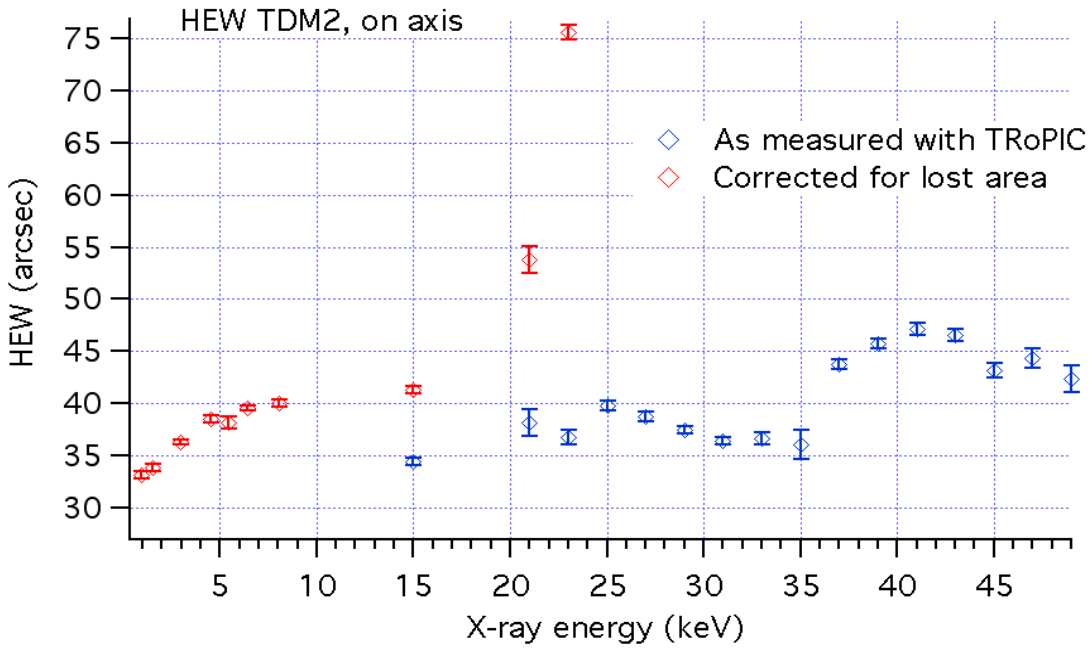

Figure 7-23. the on-axis HEW for the TDM2, as measured with the PSPC in monochromatic setup, and with TRoPIC in energy-dispersive setup. The corrected curve, using the total effective areas measured, increases very rapidly.

Conclusions

- The MS297 has discrete performances in terms of effective area, but still too much area is lost at large scattering angles.
- The MS297 is the only mirror shell with a good angular resolution HEW at low energies, and similar to the HEW measured in UV light.
- The HEW of the MS297, after correction for the lost area, is 35 arcsec at 30 keV, i.e. out of specification (20 arcsec).
- The MS185 has bad HEW performances at low and high energies, but the effective area is still measurable.
- The MS350 has a bad HEW at low energies and a roughness so high that also the effective area at high energies is nearly zero.
- The Pt/C coating is identified as the most probable cause for the bad performance of M185 and M350 mirror shells.

7.5 Conclusions

The 2 TDMs have been tested at the PANTER-MPE x-ray calibration facility demonstrating the feasibility of the technologies for the focusing optics of the NHXM mission

Some considerations and conclusions can be drawn from the different core technologies that have been studied.

Mirror replication:

- innovative NiCo alloy studies showed the improvement of the mirror shell mechanical properties w.r.t. to pure Nickel;
- the gold separation layer optimization permitted obtaining much better replication of the mandrel roughness.

Metrology

- the MPR profilometer, for the grazing incidence mandrels form measurements, has been designed, manufactured and tested. The MPR is now being studied to verify the performance in measuring free-form optics;
- the SPR profilometer, for the grazing incidence mirror-shells form measurements, has been designed, manufactured and tested.

Multilayer

- a miniaturized solution for the multilayer coating of small diameter mirror-shells (i.e. 170mm), with the possibility to set the distance between the sources and the mirrors, has been implemented.
- the W/Si multilayer (both deposition machine and technique) is a consolidated solution for the NHXM mirrors;
- the Pt/C multilayer, that would be preferable to W/Si, needs to be further studied for the lay-out of the deposition machine and for the process itself.

Integration

- the integration of the mirror modules emphasised the need for the temporary stiffening rings for the mirrors.
- the HEW worsening occurred during integration is due to unrecoverable damages and not to the process itself;
- even with the implementation of the UV source, the VOB predictions of the x-ray performance have not been accurate enough, particularly for the TDM2 mirror module

8 Status of the eROSITA Flight Mirror Modules

Some of the eROSITA mandrels, **manufactured under my supervision by using the advanced manufacturing technique** described in Chapter 5, have been used by Media Lario Technology company and MPE to produce some preliminary mirror shells and verifying the overall compliance with eROSITA x-ray performance requirements.

After the successful demonstration of the possibility to obtain mirror shells with angular resolution below 15 arc seconds HEW (up to 8.05 keV), the production of the Flight Modules (FMs) started. The FM1 is currently (at July 2011) the most advanced in production, with the mirror shells ranging between 24 and 54 positions already integrated; at this stage it has been x-ray calibrated at PANTER facility by MPE to have a further confirmation of the HEW performance.

A description of the eROSITA mission is provided in Chapter 3, whereas the optical design and the metrological characterization of the eROSITA mandrels is provided in Chapter 6.

8.1 PANTER x-ray test on single mirror shells

8.1.1 Mirror shell form mandrel eRO25

For the eROSITA development program a flight-quality mandrel (eROFM25) has been manufactured with the newly developed polishing technique. This mandrel eROFM25 has been replicated for x-ray testing in PANTER (MPE), obtaining remarkable performance **(HEW ~ 12 arc seconds)**. The mirror shell geometrical parameters are summarized in Table 8-1.

The in-focus image measured in PANTER and the encircled energy diagram are shown in Figure 8-1 (the image is in logarithmic scale).

These results permitted the qualification of the mandrel manufacturing process and so the starting of the production of the eROSITA flight-quality mandrel set.

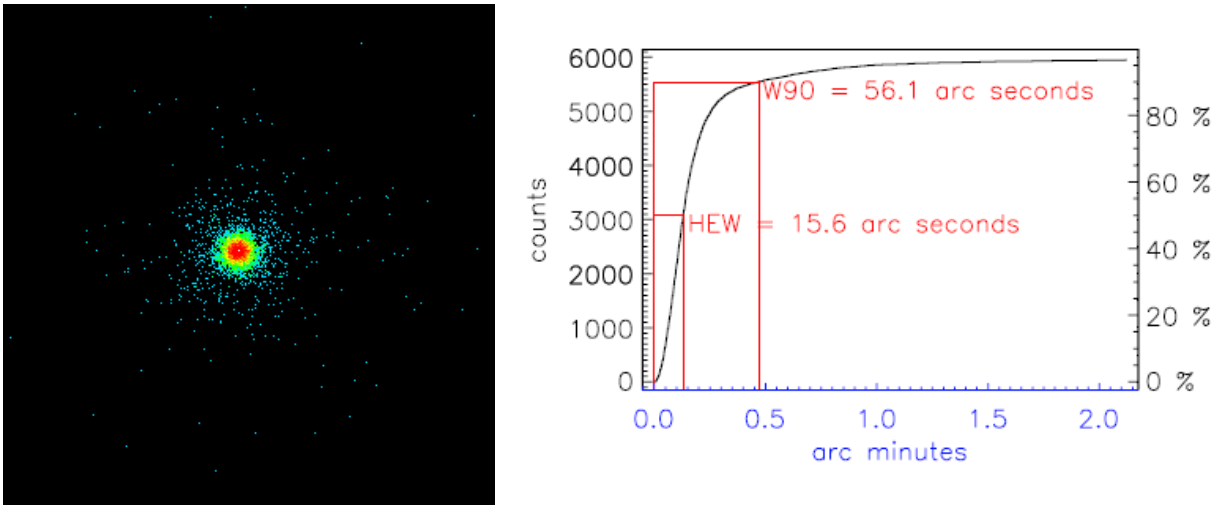

Figure 8-1. eRO25 mirror shell: HEW @ 1.49 keV 15.6"/12.1" (without and with sub-pixel resolution); HEW @ 5.41 keV 16.6" (without sub-pixel resolution). Focal plane (left) and encircled energy (right).

Table 8-1. Geometric properties of the mirror shell eROFM25.

Parameter	***Symb.***	***Value***
Maximum mirror diameter (parabola)	$2R_M$	177.681 mm
Median mirror diameter	$2R_0$	173.661 mm
Minimum mirror diameter (hyperbola)	$2R_m$	161.405 mm
Mirror length (parabola + hyperbola)	$2L$	300 mm
Mirror walls thickness	τ	270 μm
Nominal, on-axis, incidence angle at the median diameter	a_0	0.7763 deg
Nominal focal length	f_V	1600.528 m

8.1.2 Mirror shell form mandrel eRO12

In order to demonstrate the scalability of the newly developed process also to bigger diameters, the manufacturing of a medium size mandrel (eROFM12) has been anticipated w.r.t. the schedule.

This mandrel eROFM12 has been replicated for x-ray verification in PANTER, obtaining excellent performance **(HEW ~ 13 arc seconds)**.

The Nickel mirror shell geometric properties are summarized in

Table 8-2 here below. The thickness is 470 μm.

The in-focus image measured in PANTER and the encircled energy diagram for Al-K (1.35 – 1.60 keV) and Ag-L (2.75 – 3.50 keV) emission lines are shown respectively in Figure 8-2 and Figure 8-3 (the focal plane images are in logarithmic scale).

Table 8-2. Geometric properties of the mirror shell eROFM12.

Parameter	***Symb.***	***Value***
Maximum mirror diameter (parabola)	$2R_M$	259.114 mm
Median mirror diameter	$2R_0$	253.255 mm
Minimum mirror diameter (hyperbola)	$2R_m$	235.389 mm
Mirror length (parabola + hyperbola)	$2L$	300 mm
Mirror walls thickness	τ	420 μm
Nominal, on-axis, incidence angle at the median diameter	a_0	1.1309 deg
Nominal focal length	f_V	1600.528 m
Effective Area @ 1.5 keV	*Aeff*	14.04 cm^2
Weight	-	0.88 kg

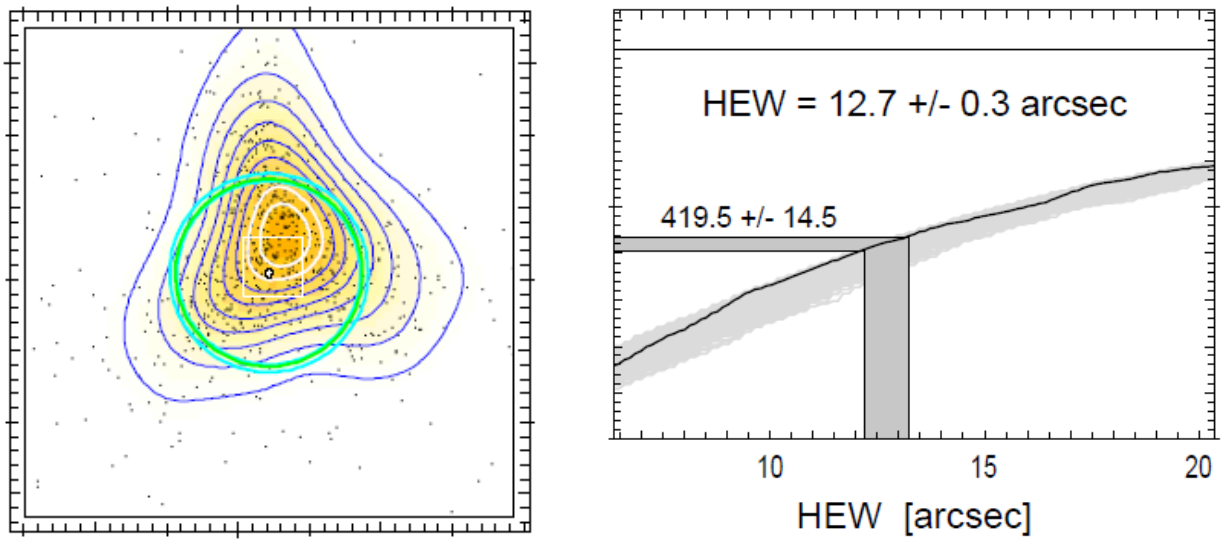

Figure 8-2. eRO12 mirror shell: HEW @ 1.35 – 1.60 keV 12.7" ± 0.3"(with sub-pixel resolution). Focal plane image in logarithmic scale (left) and encircled energy graph (right).

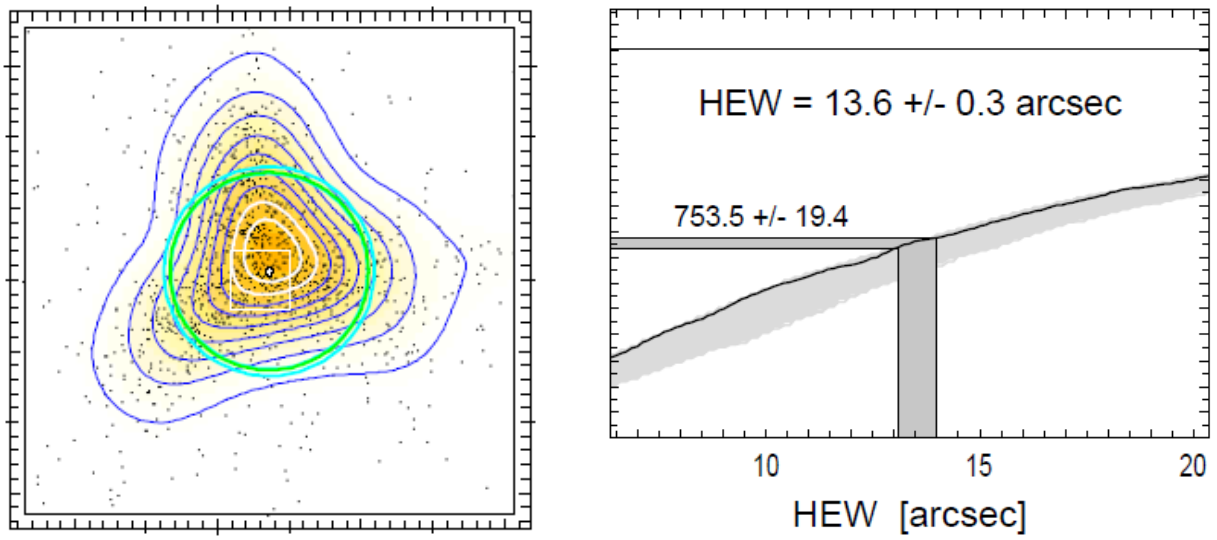

Figure 8-3. eRO12 mirror shell: HEW @ 2.75 – 3.50 keV 13.6" ± 0.3"(with sub-pixel resolution). Focal plane image in logarithmic scale (left) and encircled energy graph (right).

8.2 PANTER x-ray calibration of Mirror Module FM1

The mirror shell integration of mirror module FM1 are being completed in three (or more) steps in order to check the optical performance of integrated shells as early as possible. After integration of 31 mirror shells (from #24 to #54) a x-ray test has been performed, the shells from #28 to #54 are replicated by existing MPE mandrels whereas the shells from **#24 to #27** are replicated by **new mandrels manufactured under my supervision**. The test took place in June 2011 in the MPE x-ray test facility PANTER.

Performance criteria are point spread function (PSF), effective area – both for different photon energies – alignment, and focal length. The emphasis was on the PSF (Point Spread Function) measured in terms of HEW, W90, and scattering fraction. Furthermore, the alignment of groups of shells has been studied.

The x-ray test of FM1 with 31 shells has been considered successful. The integration of the next mirror shells into FM1 and other FMs are now continuing.

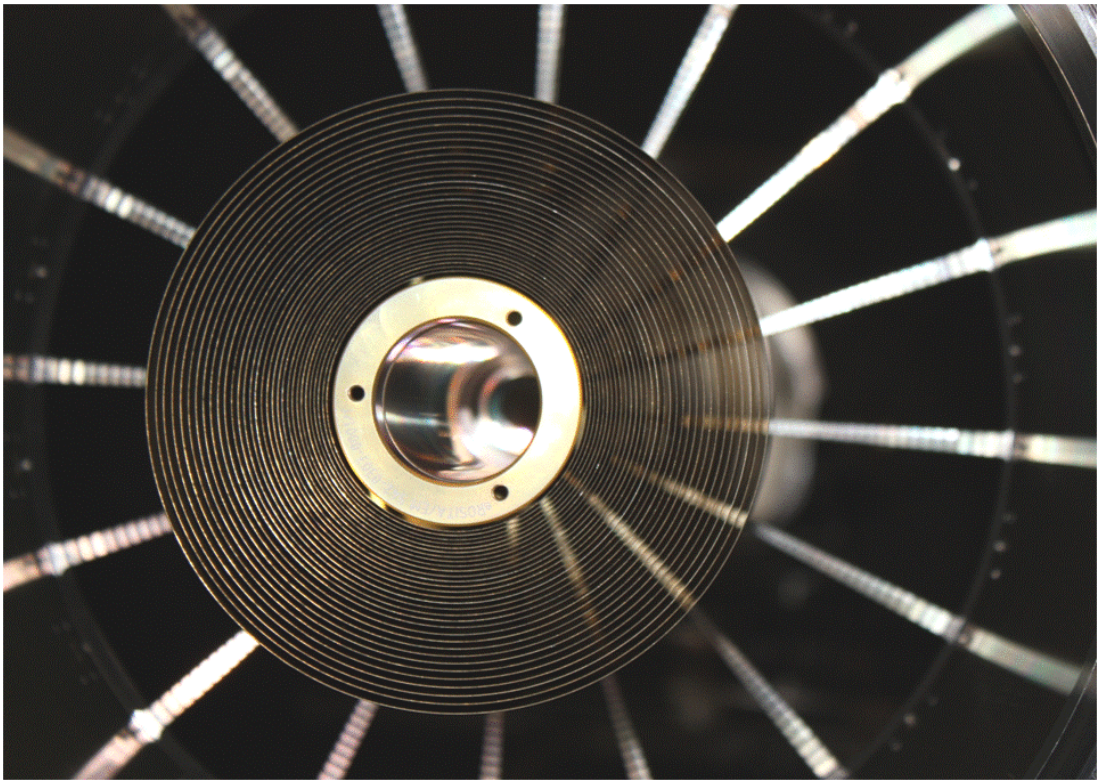

Figure 8-4. Front view of the 31 shells FM1 mirror module tested at PANTER.

The measured PSF is close to or within the specification at both specified energies, 1.49 keV and 8.04 keV.

Table 8-3. Summary of PSF performance of eROSITA FM1 composed by 31 mirror shells at different energies ranging from 1.49 keV and 8.04 keV.

Target	**Energy**	**PSF**		
		HEW	**W90**	**scattering**
Al-K	1.49 keV	16.0 arcsec	74.3 arcsec	5.1%
Ag-L	2.98 keV	16.3 arcsec	92.8 arcsec	6.9%
Cr-K	5.41 keV	17.0 arcsec	130.3 arcsec	9.5%
Cu-K	8.04 keV	15.6 arcsec	140.9 arcsec	11.8%

Table 8-4. Summary of PSF performance of eROSITA FM1 as measured by sub-dividing the shells into smaller groups.

Group	**Energy**	**PSF**		
		HEW	**W90**	**scattering**
Shells 40-54	1.49 keV	13.8 arcsec	43.5 arcsec	2.5%
Shells 24-39	1.49 keV	17.8 arcsec	94.6 arcsec	5.2%
Shells 34-39	1.49 keV	19.5 arcsec	101.6 arcsec	9.0%
Shells 28-33	1.49 keV	17.3 arcsec	100.6 arcsec	8.4%
Shells 24-27	1.49 keV	16.5 arcsec	84.5 arcsec	3.2%
Shells 24-27	5.41 keV	20.9 arcsec	186.7 arcsec	14.3%

A relative large lack of effective area at all energies has been observed for the 15 innermost shells and not for the outer shells. The assumption here is that the loss is most likely caused by geometric factors, i.e. alignment of the optical axes and partial shadowing rather than by reflectivity of the gold coating. A loss of ~10% with respect to the theoretical numbers which is measured for the complete 31 shells is in agreement with the specification.

Table 8-5. Summary of Effective Area performance of eROSITA FM1 composed by 31 mirror shells at different energies ranging from 1.49 keV and 8.04 keV.

Target	**Energy**	**Effective Area**		
		measured	**calculated**	**loss / win**
C-K	0.28 keV	113.299 cm^2	119.89 cm^2	-5.5%
Al-K	1.49 keV	106.770 cm^2	118.38 cm^2	-9.8%
Cr-K	5.41 keV	57.714 cm^2	63.69 cm^2	-9.4%
Cu-K	8.04 keV	24.350 cm^2	28.84 cm^2	-15.6%

Table 8-6. Summary of Effective Area performance of eROSITA FM1 as measured by sub-dividing the shells into smaller groups.

Target	**Energy**	**Effective Area**		
		measured	**calculated**	**loss / win**
Group 40-54	1.49 keV	28.322 cm^2	34.29 cm^2	-17.4%
Group 24-39	1.49 keV	79.655 cm^2	84.09 cm^2	-5.3%
Group 34-39	1.49 keV	21.876 cm^2	23.83 cm^2	-8.2%
Group 28-33	1.49 keV	30.594 cm^2	32.45 cm^2	-5.7%
Group 24-27	1.49 keV	26.004 cm^2	27.81 cm^2	-6.5%

The x-ray focal plane images and the encircled energy of the FM1 composed by 31 mirror shells taken at 1.49 keV and 8.04 keV are reported in Figure 8-5 and Figure 8-6.

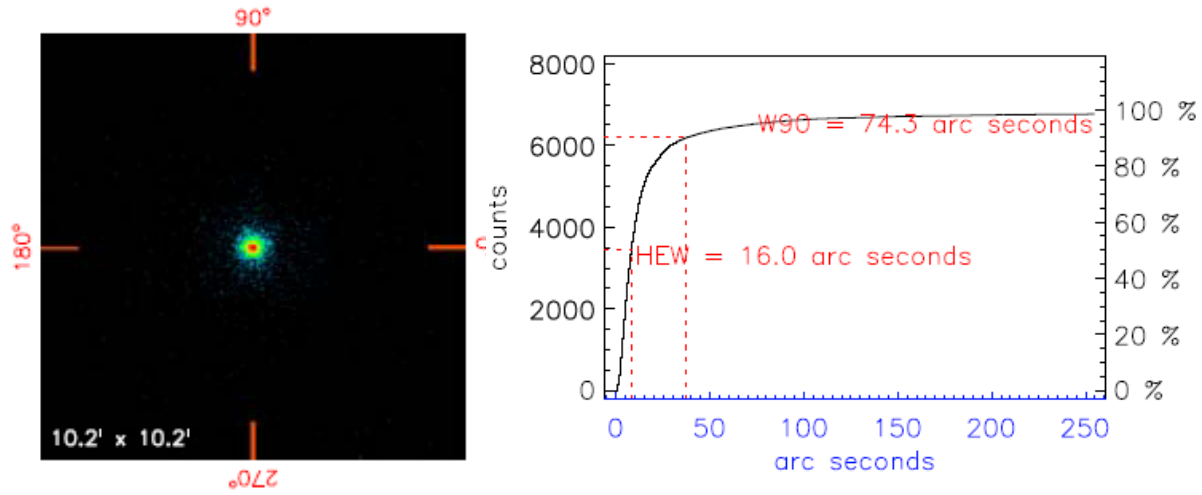

Figure 8-5. 31 mirror shells FM1 HEW @ 1.49 keV is 16.0"(with sub-pixel resolution). Focal plane image in logarithmic scale (left) and encircled energy graph (right).

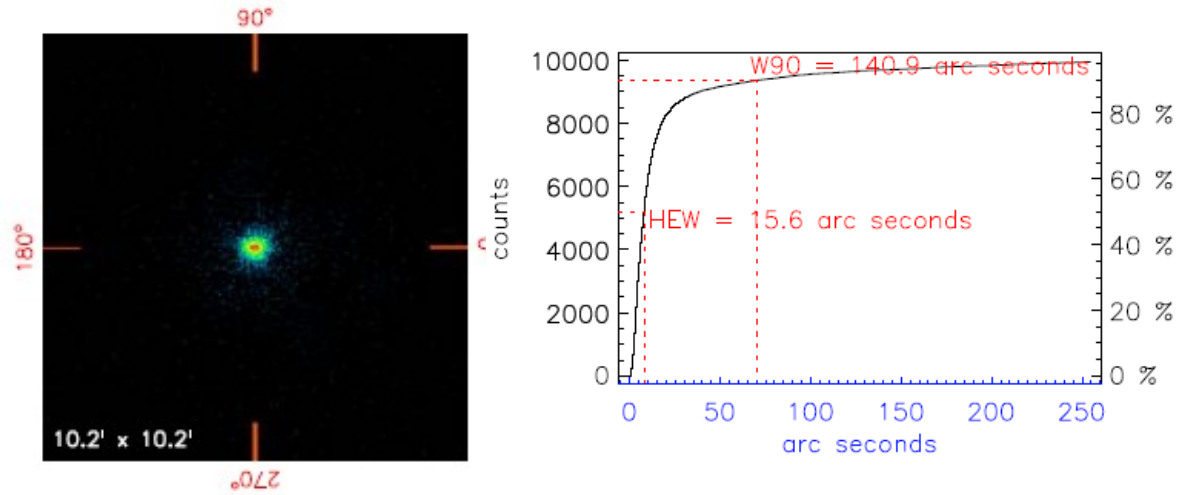

Figure 8-6. 31 mirror shells FM1 HEW @ 8.04 keV is 15.6"(with sub-pixel resolution). Focal plane image in logarithmic scale (left) and encircled energy graph (right).

9 Glass Mirrors by Cold-Slumping for IACTs (Imaging Atmospheric Cherenkov Telescopes)

For the **MAGIC II telescope** (one of the larger IACTs) 236 one squared meter mirrors have been manufactured, the first 136 mirrors have been realized with an improvement of the technique already adopted for the MAGIC I telescope (Bastieri, 2007) (Doro, 2009), whereas the remaining **104 mirrors** have been manufactured with **the glass cold-slumping technique**. **The development and qualification of this technique has been relevant part of my PhD activities**. This Chapter starts with an overview of the IACTs technique, then it concentrates on the MAGIC telescope system and more specifically on the glass segmented mirrors solution.

9.1 Overview of the VHE gamma-ray ground-based telescopes

9.1.1 Historical and scientific overview

The emission of the gamma-ray by cosmic sources was predicted by scientists long before the real experimental detection. Theoretical works by E. Feenberg and H. Primakoff in 1948 (Feenberg & Primakoff, 1948), S. Hayakawa in 1952 (Hayakawa, 1952), and P. Morrison in 1958 (Morrison, 1958) had led scientists to believe that a number of different processes, which were occurring in the universe, would result in gamma-ray emission.

High-energy gamma rays are probing the "non-thermal" Universe. They can be produced by all those acceleration processes at work in extreme conditions that can be found in the proximity of black holes or in the very energetic shock waves created in stellar explosions. Otherwise they can be obtained from decays of heavy particles such as the hypothetical dark matter particles or

cosmic strings, both relics which might be left over from the Big Bang. The flux and energy spectrum of the observed gamma rays bring important information on the emission processes and the physics producing them.

The first true astrophysical gamma-ray sources were solar flares, which revealed the strong 2.223 MeV line predicted by P. Morrison. Significant gamma-ray emission from our galaxy was first detected in 1967 by the gamma-ray detector aboard the OSO-3 satellite (Kraushaar, 1968). Perhaps the most spectacular discovery in gamma-ray astronomy came in the late 1960s and early 1970s from a constellation of defense satellites which were put into orbit for a completely different reason. Detectors on board the Vela satellite series, designed to detect flashes of gamma-rays from nuclear bomb blasts, began to record bursts of gamma-rays not from the vicinity of the Earth, but from deep space (Strong, 1974). Today, these Gamma Ray Bursts (GRB) are seen to last for fractions of a second to minutes and then fading after briefly, constituting one of the prevalent topics of modern astrophysics.

Gamma rays at MeV-GeV energies have been typically observed with space-based instruments but at higher energies those instruments are completely unusable. With the advent of the IACTs in late 1980's, ground-based observation of TeV gamma-rays came into reality and, since the first source detected at TeV energies in 1989 the number of gamma-ray sources has rapidly grown up to over eighty now as shown in Figure 9-1 (see (Volk, 2009) and (de Angelis, 2008) for an extended review). Such high energy photons interact high up in the atmosphere and generate an air shower of secondary particles. These particles emit the so-called Cherenkov light, a faint blue light. The Cherenkov light illuminates an area of about 250 m diameter on the ground and a telescope located somewhere within the light will detect the air shower, provided that its mirror area is large enough to collect enough photons. The image obtained with the telescope shows the track of the air shower, which points back to the celestial object where the incident gamma-ray originated.

The IACT technique for the detection of VHE gamma rays (in the energy range 100 GeV - 10 TeV) was first pioneered by the Whipple experiment since 1985 leading to the discovery of TeV gamma-rays from the Crab Nebula in 1989 (Weekes, 1989). This first result was followed by the discovery of the TeV emission from the first extragalactic source (Mrk 421) (Punch, 1992), showing that acceleration processes are taking part in AGNs too. The third source, discovered in 1996, was still an extragalactic object (Mrk 501) which showed a violent flaring activity observed by the European experiment HEGRA.

The recent discovery of flux variability on the time scale of few minutes from Mrk 501 and PKS 2155-304, obtained in 2007 by MAGIC (Albert, 2007) and by HESS (Aharonian, 2007) respectively, has shown that the observed γ-rays are coming from the innermost region of the central part of the AGN giving important information on the physical processes at work. The discovery of TeV emission from extragalactic objects was of fundamental importance to constrain the density of the Extragalactic Background Light and the transparency of the Universe to TeV photons. In 2002 HEGRA discovered also the first unidentified TeV γ-ray source showing for the first time that some of the celestial objects discovered at these wavelength emit most of their radiation in the VHE band, or are not detectable in any other waveband.

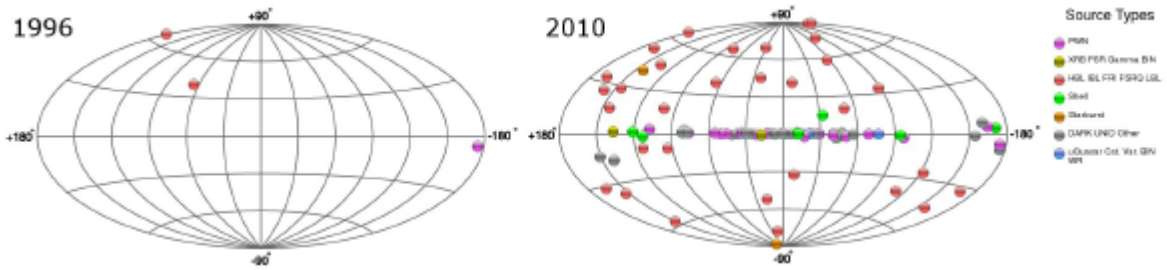

Figure 9-1. The improvement in the VHE astrophysics from 1996 (left panel) to 2010 (right panel). Images created using http://tevcat.uchicago.edu/

The Imaging Atmospheric Cherenkov Telescope (IACT) is the technique that currently achieves the highest sensitivity in the VHE gamma-ray observations covering the observational gap between 10 and 300 GeV (Saggion, 2002). Gamma-ray astronomy has experienced a major breakthrough with the impressive astrophysical results obtained mainly by the current generation of Cherenkov experiments like HESS (Hofmann, 2000) (Bernlohr, 2003), VERITAS (Krawczynski, 2008), MAGIC (Lorenz, 2000), and CANGAROO (Mori, 2000).

IACT gamma-ray astronomy observations are, for the moment, limited by non-gamma ray backgrounds at lower energies, and, at higher energy, by the number of photons that can be detected. Larger area detectors and better background suppression are essential for progress in the field. Some new experiments, like HESS II (Horns, 2007) and MAGIC II (Moralejo, 2009), have been recently undertaken aiming at improving the capability of the existing IACT observatories. Among the most outstanding results obtained so far by TeV astronomy there is the discovery of pulsed γ-ray emission from Crab Pulsar by MAGIC (Aliu, 2008). This is a very

important result providing a unique insight into the structure of pulsar magnetospheres and the main energy transfer processes at work. In March 2007, the HESS project was awarded by the Descartes Research Prize of the European Commission for offering "A new glimpse at the highest-energy Universe".

Thanks to the two experiments HESS and MAGIC, and to their forthcoming follow-ups HESS-II and MAGIC-II, the European community is now firmly leader in this research field. The impressive physics achievements obtained with the present generation instruments has triggered the initiative of astrophysicists to consider future ground-based gamma-ray observatories, like CTA (Hermann, 2007) and AGIS(Buckley, 2008), consisting in large array of telescopes.

9.1.2 The Cherenkov air showers and the IACT technique

In 1934 the Russian physicist Pawel Alexejewitsch Cherenkov discovered the emission of bluish light from relativistic radioactive particles in water for which he received the Nobel Prize in 1958. Cherenkov radiation is an electromagnetic radiation due to the interaction of fast moving charged particles with other particles. If a particle passes through a transparent medium, the atoms along its trajectory become temporarily polarized and emit electromagnetic waves due to polarization. Usually, these waves interfere destructively. However, if the particle moves at a velocity that is faster than the speed of light in this medium, the waves no longer interfere in a destructive manner, as they develop faster than they extinguish each other. The frequency spectrum of Cherenkov radiation is continuous around the visible spectrum; most Cherenkov radiation is in the ultraviolet spectrum, it is only with sufficiently accelerated charges that it even becomes visible.

These effect is called Cherenkov effect and light is emitted within a Mach cone. One parameter that describes the Mach cone is its angle of aperture φ, which depends on the velocity ν of the particle and the speed of light *c'* of the medium which has the refraction index η. The angle φ can be within the range of 0. 4°-1. 2° for Cherenkov light.

When a γ-ray impinges the top atmosphere, after interaction with the electric field of atmospheric molecules, it pair-produces an electron-positron couple:

$$\gamma(\gamma) \rightarrow e^{+}e^{-}$$

The reaction has an energy threshold of $h\nu = 2m_e c^2 \approx 1MeV$, and therefore normally takes

place for γ-rays in the VHE band. Each electron-positron in turn generates new γ-rays via bremsstrahlung:

$$e^{\pm}(\gamma) \rightarrow e^{\pm}\gamma$$

where the secondary γ-ray takes away in first approximation half of the energy of the electron. Eventually the secondary γ-ray again pair-produces an electron and a positron and so on, and the γ-shower is initiated. A sketch of a schematic view of the shower development is shown in Figure 9-2. The energy of secondary particles produced in the shower decreases as the shower proceeds. When the mean energy of $e^{\pm}$ is below a critical energy E_c which in air is ~ 83 MeV, the dominant energy loss process for electrons becomes ionization, rather than bremsstrahlung.

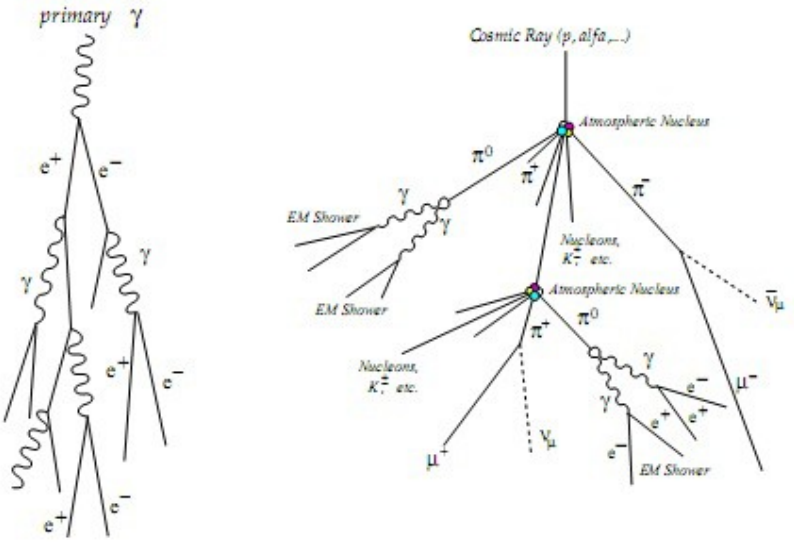

Figure 9-2. Schematic representation of air shower generated by a γ-ray (left) and by an hadron (right).

Almost contemporary, when the mean photon energy decreases below few MeV, the cross-section for Compton scattering and photoelectric absorption becomes dominant over pair-production. Rapidly the showers stop. In addition to γ-showers, the atmosphere is strongly populated also by hadronic showers. They are initiated by hadrons, mainly protons with small amount of helium and heavier elements. They interact strongly with atmospheric nuclei creating pions, kaons and nucleons. The secondary particles keep on multiplying in successive generations until the mean energy per particle drops below the pion production threshold at around 1 GeV. At that point, ionization becomes the dominant process and the shower starts to die out. Heavier nuclei are less penetrating than lighter ones, and therefore they create

showers with larger development. Moreover, the nuclear interaction lengths for hadrons are larger than the radiation length for γ-rays which implies that hadronic-shower has a larger transversal spread than that of a γ-shower of the same energy.

Given the very low fluxes of -rays in the VHE regime, a few photons per m^2 per year above 1 TeV for strong sources, direct detection by space-based instruments is excluded. Ground-based instruments detect secondary products resulting from the development of γ-ray initiated air showers: either particles reaching the ground or Cherenkov light emitted by shower particles in the atmosphere. In contrast to the well-collimated electromagnetic air-showers induced by γ-rays (or electrons), air-showers initiated by cosmic ray nucleons typically feature a number of electromagnetic sub-showers induced by π_o decays and contain muons from charged pion decays. Rejection of the background of showers initiated by charged cosmic rays is a key performance criterion for γ-ray detection systems, and is usually achieved on the basis of shower shape or muon content. The field of ground-based gamma astronomy has been largely driven by the exceptional results obtained with the IACTs. As any other optical or radio telescopes, an IACT consists of three basic elements: a mechanical tracking system, which compensate the Earth's rotation, a collecting surface, which gathers the incident electromagnetic radiation and focuses it, and a receiver element, which converts the collected light in a recordable image of the observed field of view.

A peculiar feature of Cherenkov telescopes is that they do not detect directly the photon flux, but instead detect the Cherenkov light produced in the air shower induced by the primary photon. At the maximum of the shower development, around 10 km above sea level for TeV energies, the Cherenkov threshold for electrons is around 40 MeV and the Cherenkov angle is 0.7° or less. Light emitted at the Cherenkov angle reaches the ground within a circle of 100 m to 150 m radius depending on the height above sea level of the detection system. Multiple scattering angles of shower particles near the Cherenkov threshold are comparable to the Cherenkov angle, resulting in a more or less uniformly filled light pool, with typically 10 detected Cherenkov photons per TeV shower energy and m^2 mirror area for photomultiplier sensors. An optical telescope pointing to the source and located within the illuminated footprint of the shower can detect the air shower against the background light of the night sky, provided the camera is sufficiently fast to integrate the short Cherenkov ash of the order of few nsec. With increasing energy, the central density in the light pool is enhanced due to deeper penetration of showers. Triggering and image reconstruction usually requires 50 to 100 detected photons and sets the scale for the dish size. The pixel size of the detection system should be

matched to the size of features in air-shower images; simulation studies show saturation of performance for pixels much below 0.1° diameter, close to the typical rms width of a γ-ray image at TeV energies. The asymptotic collection area for IACTs is determined by the maximum impact distance for which shower images still fall within a camera and hence by the camera FOV. At 2000 m above sea level the impact distance limitation is approximately 100 m per degree of the opening angle of the camera field of view (for showers close to Zenith).

The Cherenkov technique takes advantage of the shower development information in the image of the telescope camera (see Figure 9-3). It is therefore possible to take a sort of "snapshot" of air showers resolved in space (and time). This information can then be used to distinguish the origin of the air shower (hadronic or γ-ray) using the different spatial development of γ- and hadron-induced air showers. The parameterization of such images is called "Imaging Technique", which dramatically improves the γ/hadron separation power and makes IACTs the most successful instrument for cosmic very high energy γ-ray observations. Moreover, the measurement of the Cherenkov light provides a good indicator of the energy absorbed in the atmosphere, which is in fact acting as a calorimeter. Therefore, the total amount of light contained in the image gives the energy of the primary particle. In addition, orientation and shape of the image also provide information on the incoming direction of the primary particle.

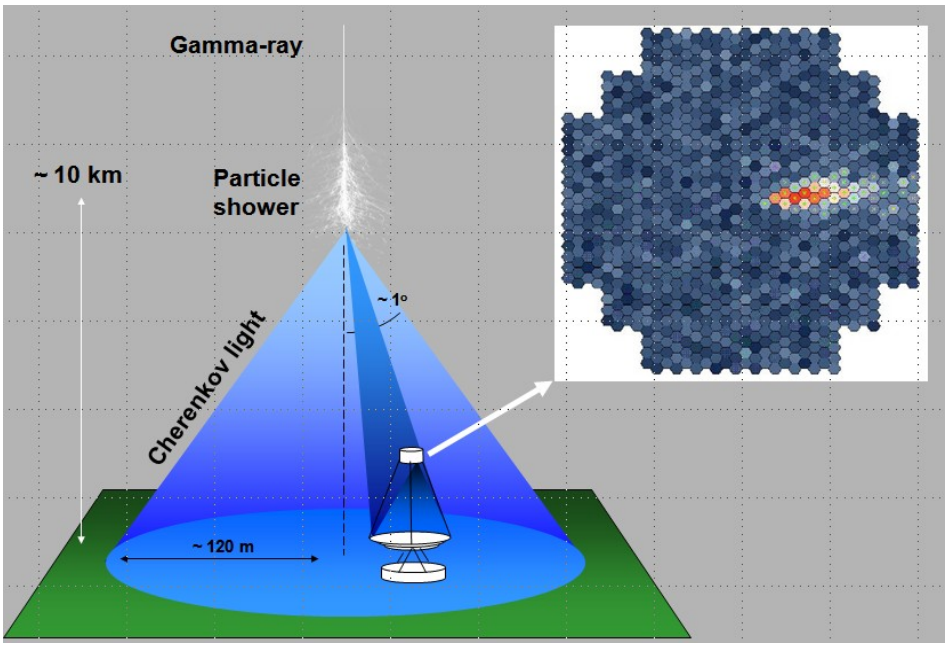

Figure 9-3. Schematic description of the IACT technique: the Cherenkov light pool impinging the reflector and image of the air showers as it appears in the camera. Courtesy of M. Mariotti.

Two main parameters characterize an IACT: its sensitivity, i.e. the minimum detectable γ-ray flux in a given number of observation hours (usually defined as a 5σ excess during 50 hours of observation time), and its energy threshold. Most modern instruments use multiple telescopes (a) to image the air-shower from different viewing angles for improved reconstruction of γ-ray direction and rejection of cosmic ray background and (b) to apply a coincidence requirement rejecting single-telescope triggers caused by cosmic ray muons with impact points close to a telescope mirror, or by night-sky background. Telescope spacing needs to be large enough to provide a sufficient baseline for stereoscopic measurements, but small enough that multiple telescopes fit within the Cherenkov light pool; the exact spacing tends to be uncritical within a range of ~70 m to 150 m. The stereoscopic technique has become the nominal standard for all current and future installations (Canestrari, 2009).

9.1.3 Manufacturing technique of the current IACTs mirrors

All the Cherenkov telescopes use optical systems consisting of large segmented mirrors, focusing the Cherenkov light onto photon detectors made of photomultiplier to resolve the image of the air shower. Task of the optical system of IACTs is to collect Cherenkov light and to focus it onto the detector. The point spread function should ideally be smaller than the pixel size over the entire field of view. Whereas the imaging performance of IACTs is modest compared to normal astronomical telescopes, the cost-effective design and the lightweight of the mirrors of large Cherenkov telescopes is not trivial. Different technologies have been adopted so far for the production of the Cherenkov segmented mirrors. The different technologies can be divided into three main groups:

- aluminized ground-glass mirrors manufactured with standard technique starting from raw blanks;
- composite sandwich structure mirrors manufactured via direct machining of each individual piece;
- composite sandwich structure mirrors manufactured via replication process from a mould.

Ground-glass mirror solution has been often preferred (e.g. HEGRA (Daum, 1997), CAT (Barrau, 1998) HESS, VERITAS) primarily because of its technical maturity, but at cost of a quite long time of production. Moreover, the ground-glass mirrors are quite heavy translating into increasing cost and complexity for the telescope mechanical structure.

Thanks to the limits of the ground-glass technology, the idea to make use of lightweight mirror consisting of composite sandwich structure came to pass since the very beginning of IACT astronomy. In sandwich construction, membranes (such as sheet steel, aluminum, glass, or plastic) are bonded to both side of a core material. This type of construction is widely utilized in products ranging from doors and tables to aircrafts, boats and satellites and is characterized by high strength-to-weight.

The first Cherenkov Telescope employing composite sandwich mirrors had been the MARK 3 experiment, for which a replication process had been developed by making use of aluminum honeycomb core and Alanod® face sheets (Carstairs, 1986). The CANGAROO III telescope, instead, adopts composite sandwich mirrors consisting of rigid foamed core pinched by Fiber Reinforced Plastic sheets; in this case the structure is placed on a mould and curved in an auto-clave for shape replication (Ohishi, 2002). Also the MAGIC mirrors are composite structure, in this case consisting of an aluminum face sheet pre-machined to spherical shape and glued to an aluminum honeycomb inside a thin aluminum box making up the raw blank; each individual raw blank is subsequently polished by diamond milling (Bastieri, 2005) (Doro, 2008).

9.2 Brief description of the MAGIC telescope system

The MAGIC telescope system has been designed and is operated thanks to a collaboration of around 150 physicists from 22 institutes and 7 countries. It is located on the Canary island of La Palma at 2225m. The first telescope has been fully operational since fall 2003 and is currently in its fourth observations cycle. The second has been recently completed. A picture of both telescopes is shown Figure 9-4.

MAGIC belongs to the Imaging Atmospheric Cherenkov Telescope (IACT) class of detectors and is constituted by the world's largest mirror dishes (HESS I and VERITAS telescopes have 12 m dishes, while currently a 28 m diameter telescope, named HESS II is under construction).

The Cherenkov light illuminates nearly uniformly a dish of ~ 120 m radius. If a telescope is located inside this Cherenkov light pool, the light hitting the mirror can then be reflected and focused onto a multi–pixel camera composed of a large number of photomultipliers. An image reconstruction algorithm allows the determination of some major parameters of the primary particles, such as energy and direction, as well as its likeliness to be a hadron or a γ–ray. As lower energy γ–rays produce a lower density of photons at ground, a larger telescope mirror

area is required to decrease the energy threshold of the telescope. In the case of MAGIC, the 17m reflector allows the reconstruction of primary gamma-rays above ~ 70 GeV (zenith angle dependent) with an integral sensitivity above 100 GeV of ~ 10^{-11}ph cm^{-2} s^{-1} in 50 hours of observation and with an effective area, which is of the order of 10^5 m^2 (Saggion, 2006).

Figure 9-4. The MAGIC stereoscopic system of telescopes. On the left, the first MAGIC telescope that has been operating since 2003. On the right, the second MAGIC telescope. While the structures of the two telescopes are very similar, all MAGIC II subsystems are substantially improved (Doro, 2009). Picture from R. Wagner.

Despite the similarity with optical astronomical telescopes, Cherenkov telescopes have one major fundamental difference. Although one tracks in both cases very distant stellar objects, the light emitting sources are very different. In cases of optical astronomical observations one observes stellar light, which originates basically at infinity and is parallel. In the case of VHE gamma-astronomy one detects Cherenkov light emitted by an extended air shower initiated by gammas in the atmosphere. The Cherenkov light is emitted with a small angle off the shower particle tracks, therefore the single photons do not point directly to the source like in optical astronomy, nevertheless, the entire bunch of photons has a symmetry which can be traced back to the source.

In addition, one of the main physics goals of MAGIC, besides the observation of steady or slowly flaring gamma-sources, is the (nearly real time) observation of gamma-ray bursts (GRB) and their prompt afterglow and has much influenced the design of the telescope. This requires the telescope to be repositioned as fast as possible to the sky position provided by an alerting

satellite (typically within 10 s after the start of the outburst). To achieve a positioning time to any position on the sky map within much less than a minute requires both a very lightweight telescope and a fast acting drive system. MAGIC uses therefore, a low weight mirror, as well as a low weight mirror support frame made from carbon fiber reinforced plastic (CFRP) tubes. The space frame weighs only 5.5 tons. Nevertheless, it deforms by a factor 3 less than a steel construction of the same size of 27 tons. Other positive effects of the CFRP tubular construction are minimal thermal expansion and a high damping of oscillations (Doro, 2009).

The main mirror of the MAGIC telescope is quite similar to that of large optical telescopes. Nevertheless, there are quite a few different constraints that influence the mirror design parameters, in comparison to optical telescopes:

- Cherenkov reflectors have a much simpler construction and much lower optical quality demands. The internal fluctuations in the development of atmospheric showers make a higher resolution useless. Converted to the point spread function (PSF) requirements these conditions show that IACT mirrors can have a factor 100 − 500 worse PSF compared to that of optical telescopes. The PSF of the mirror facets typically is 0. 02° and that of the overall mirrors 0. 05°.
- The Cherenkov light flux from VHE showers is extremely low. Therefore, very large mirrors are desirable and the construction of the telescope should minimize the loss of photons in the optical system and their conversion into photoelectrons. The overall photon detection efficiency for state of the art IACTs is only 10–15% when averaged over the spectral range between 290 and 600 nm.
- In order to record the shower image in Cherenkov light one needs a "wide field" camera of at least 3°-5° field of view (FOV). For observing significant sections of the sky one would in principle need an even wider field camera. Unfortunately, this is very difficult to achieve. The use of Schmitt optics or a secondary mirror are both very costly, require much more precise optical elements and would result in an additional loss of photons. The optical image quality at the rim area of the 3°-5° FOV camera should not be degraded too much. This requires a rather large f/D (≤ 1) in cases of single mirror optics. As cameras can be quite heavy, a strong and heavy camera support is needed. The structure has to be anchored to the mirror support dish resulting often in a large local mirror deformation.
- Due to their dimension, larger IACTs have no protective dome. It is constantly exposed to the atmosphere, to wind and rain, temperature and intense sunlight and suffers much

more aging than optical telescopes. The reflectivity of the mirror surface is particularly affected by the impact of constant exposure to the ambient.

9.2.1 A parabolic telescope made of spherical mirrors

Cherenkov photons come as a disk of photons with a width of a few meters which covers an area of around 10 m^2. Therefore, most of the time the light–rays hit the reflector at a tilted angle. While for vertical incidence the best reflective surface for light coming at infinity is a parabola, soon when the impinging light is tilted, the effect of astigmatism and coma aberration become very relevant and deform the reflection at the focal plane. On the other hand, the spherical reflector is affected by very strong spherical aberrations already at vertical incidence and the aberrations increase with the telescope diameter.

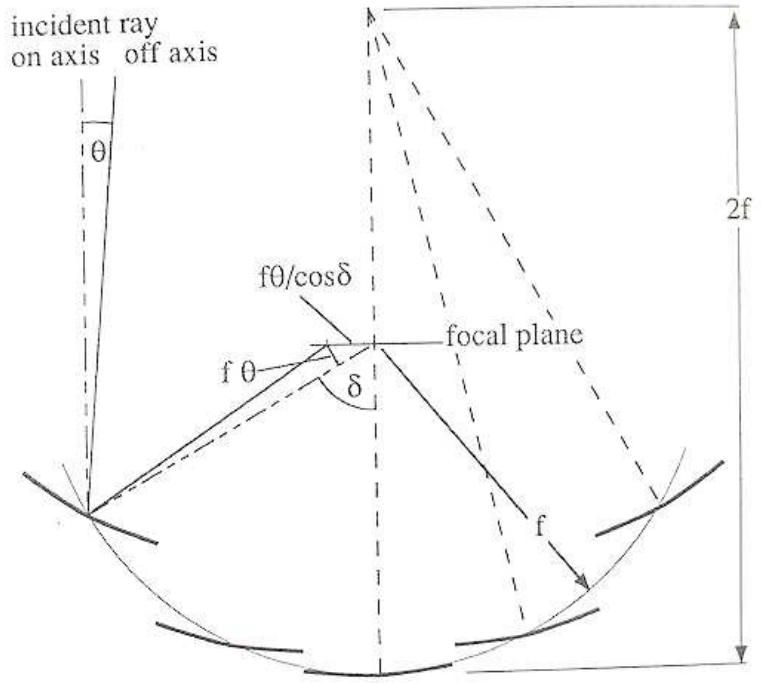

Figure 9-5. The Davies–Cotton mounting (Davies & Cotton, 1957). The spherical mirrors all of focal length f are arranged on a sphere of radius f and focused at 2f distance. This optics was developed for solar concentrators and best performs for Cherenkov telescopes of 10 m. For larger surfaces, as for MAGIC, the arrangement of the tessellated mirrors on a parabola is most recommended to maintain the temporal structure of the showers.

A brilliant solution was found by Davies and Cotton (Davies & Cotton, 1957). They developed a spherical reflector for solar power concentrators composed of mirrors arranged in a smart way, as shown in Figure 9-5. In this configuration, the mirror facets have as radius of curvature twice the radius of curvature of the overall reflector. Furthermore, they are mounted so that they focus at a point twice the telescope focal length. In this way, the center of the mirror, the center of the image in the focal plane and the point at twice the focal length form an isosceles triangle. The alignment is straightforward and the spherical aberration for vertical incidence is strongly reduced.

It was also demonstrated in the study of the optics for the Whipple telescope (Lewis, 1990), that the Davies–Cotton layout is by far better than the parabolic profile even for off–axis light, at least for the Whipple reflector of 10 m diameter and 14.6 m focal plane. On the other hand, the mirror facets in the Davies–Cotton layout are arranged on a sphere and therefore, there is a time delay between light hitting the reflector at different positions, which was up to 6 ns in the Whipple case. For larger surfaces the delay is even larger. While this is of minor importance for the very optical image itself, it strongly competes with background discrimination, both from hadronic showers which develop differently in time, and from the night sky background light which is integrated over a larger time.

9.2.2 The MAGIC I telescope

9.2.2.1 The Mounting and Drive System

The reflector frame is very large and light-weight, it is very stiff and allows for fast repositioning.

The space frame is made from carbon fiber reinforced plastic (CFRP) tubes and has a weight of only 5.5 tons. CFRP is a very strong but light composite reinforced fiber, similar to Fiberglass. The CFRP construction is about three times stiffer and has less than a third of the weight of an equivalent steel construction (Doro, 2009).

The structure of an alt-azimuth design is mounted on a circular rail of 19 m (diameter). The telescope can be moved from -80° to 105° in declination and 450° in azimuth.

The camera at a distance of around 17 m from the reflector is carried by a single aluminum tubular arc. The weight of the camera is around half a ton, and the small bending, unavoidable

during the telescope tracking, is corrected via a re-orientation of the mirror.

Two motors control the motion in azimuth and one motor the zenith motion with a maximum power consumption of ~ 7 kW per motor. The angular positions are controlled by absolute shaft-encoders of 14-bit precision/360°. In addition, a star-guider camera mounted at the centre of the reflector, monitors the positioning of the telescope by viewing both the camera of the telescope and the corresponding section of the sky star-field.

The lightweight structure allows for very fast repositioning of the telescope to any position in the sky within ~ 30 s. This challenging feature was designed to instantly react to Gamma-Ray-Burst (GRB) alerts from dedicated satellites detecting GRBs in the keV/MeV domain.

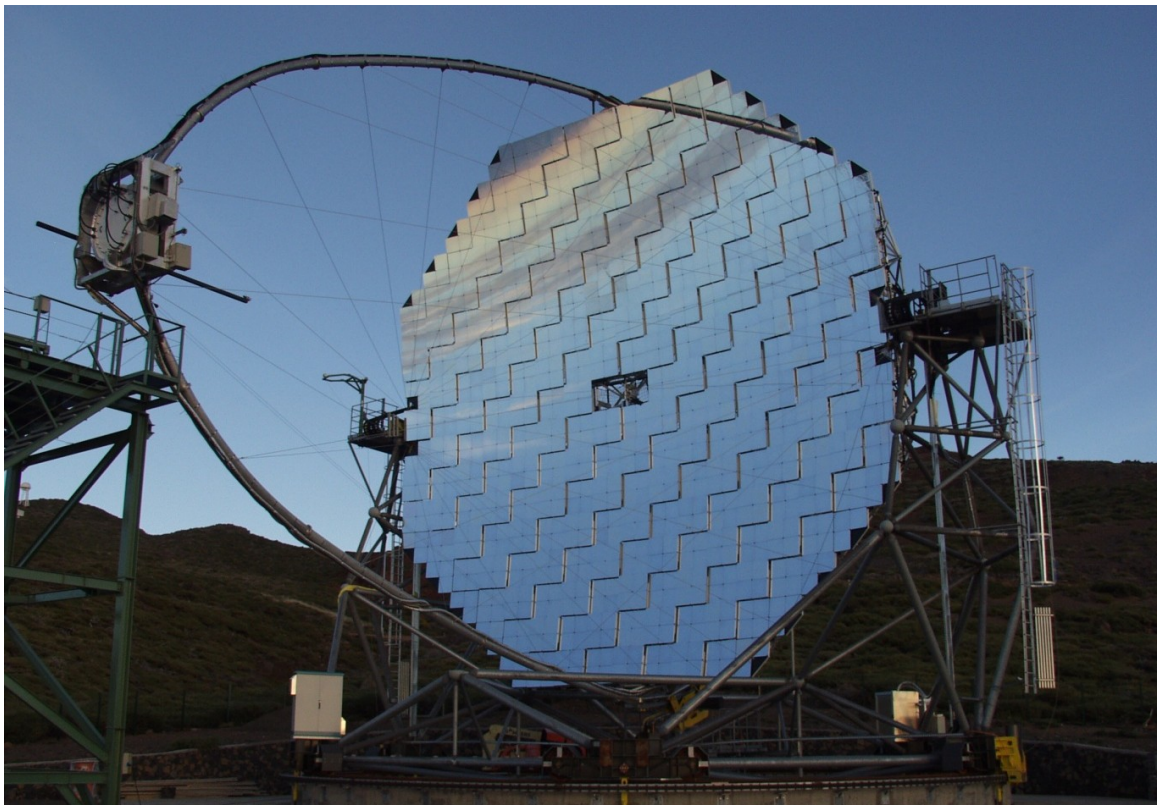

Figure 9-6. The first MAGIC telescope. The reflector dish has a 17 m diameter and the camera is placed at a distance of 17 m (f/D = 1). The reflector is tessellated and composed by 956 mirrors of 0.5 × 0.5 m2 area. The camera weights ≃ 0.5 tons and contains the 576 photomultipliers and the optical converter that transmit the signal through a 160 m optical fibre. The structure is a CFRP space-frame plus some aluminium parts for connections and bearings. The structure is mounted alt-azimuthally and rotates on a 18 m diameter rail. (Doro, 2009).

9.2.2.2 The Reflector

The 17 m diameter reflector (17 m focal distance) follows a parabolic profile which was chosen to maintain the temporal structure of the shower light flashes. The reflector of MAGIC I is tessellated and comprises 956 mirrors with a total area of 234 m^2. Each mirror is a square of 0.495 m side length and has a spherical profile whose radius of curvature is optimized for the position in the telescope to best approximate the paraboloid. MAGIC I mirrors are grouped onto panels of 4 or 3 elements and each panel can be moved by the Active Mirror Control system (AMC) (Biland, 2007). The AMC was designed to correct small deformations of the mirror support dish during telescope positioning and tracking.

The mirrors are an all-aluminum, light weight sandwich construction composed of an Al-skin and an Al-box and filled with a honeycomb structure (Doro, 2008). Two slightly different models were used in MAGIC I: 224 mirrors following a design by MPI-Munich and 740 mirrors designed at INFN-Padova. The skin is a flat square 5 mm thick AlMgSi alloy of 495 mm side, with different Si contamination for the MPI and INFN mirrors. The contamination is an extremely relevant fact to guarantee good machinability and resistance to atmospheric conditions. A heating wire mesh, embedded in the sandwich, can be switched on in cases of dew or ice deposits on the mirrors. The assembly is sandwiched between two heavy aluminum moulds and the ensemble is enclosed in a vacuum plastic bag.

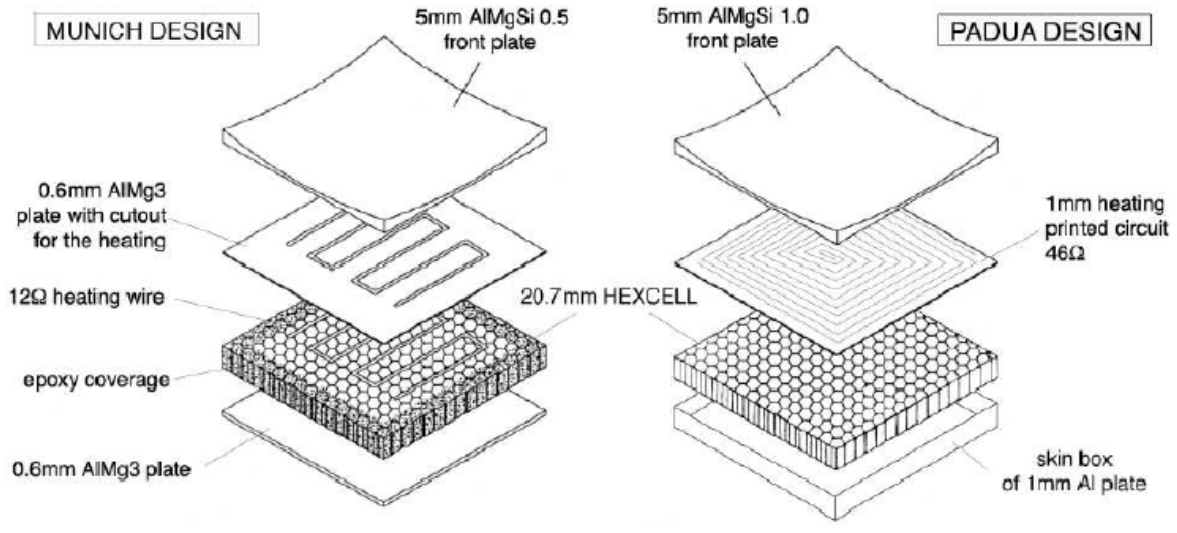

Figure 9-7. The two designs of MAGIC I mirrors: MPI design (left) and INFN design (right).

The packet is put in an autoclave, the air is sucked out of the bag to exert pressure on the sandwich, and then a cycle of high temperature and pressure cures the structural glue: As a result a so-called raw-blank is produced.

After a rough pre-milling that ensures an approximate curvature of 35 m to the aluminum surface, the mirror is milled with precision by using a diamond-milling machine (see Figure 9-8), which provides high reflectivity and a slightly different focal length to fit the overall parabolic shape on the reflector. The final roughness of the surface is around 4 nm and the average reflectivity 85%. In addition, a thin layer of quartz (with some admixture of carbon) around 100 nm thick is vacuum–deposited for protection against corrosion and acid rain. On average, the reflected light of MAGIC I mirrors is focused within 1 mrad corresponding to 17 mm at the camera focal plane. Each mirror has an approximate weight of 3 kg. The mirrors are then grouped into panels of 3-4 elements (see Figure 9-8). This required the construction of an additional panel (also a light-weight honeycomb structure) and foresaw an interalignment procedure of the mirrors within the panel, to be done before the mounting.

After the second winter of operation, some mirrors started to show localized deformations on the upper or lower surface. The reason for the creation of these "bubbles" was water or more likely the humidity entering the mirrors from very small fissures in the sealing. A design variations were considered to solve the problem and some of the mirrors of MAGIC I were replaced (Doro, 2009).

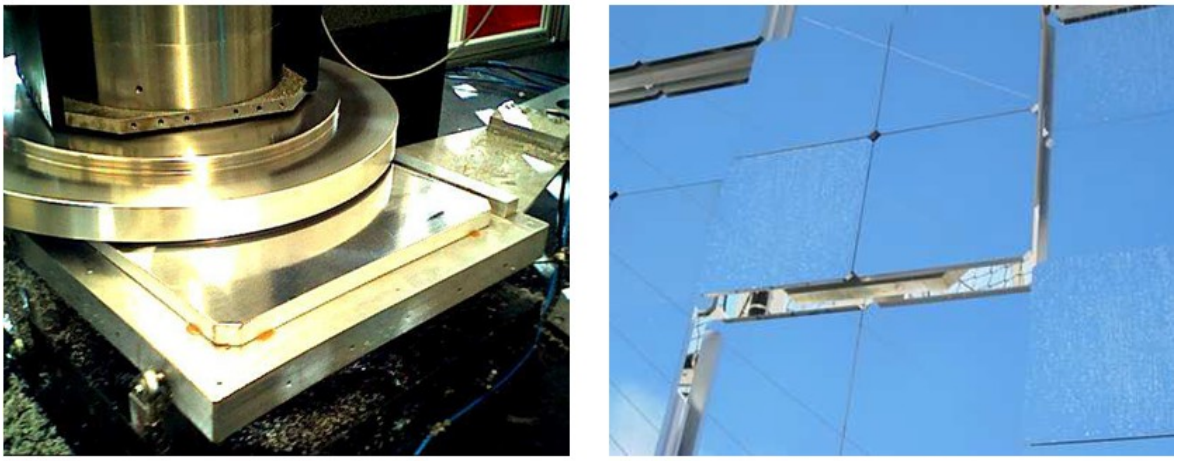

Figure 9-8. The diamond-Milling for a MAGIC I mirror (left) and a panel composed by 4 mirrors mounted on the MAGIC I structure (right).

9.2.2.3 The Camera

The camera of the MAGIC I telescope has a 3.6° field of view (FOV) and comprises 576 photomultipliers (PMTs). The PMTs of a hemispherical cathode were enhanced in QE (Quantum Efficiency) with a diffuse lacquer doped with P-Terphenyl shifting the short wave UV component of the Cherenkov light into the spectral range of larger sensitivity (Paneque, 2004). In order to minimize losses due to the dead space between the densely packed PMTs, hex-to-round light concentrators were used, which added a further increase of the QE by deflecting many photons such that their trajectory passed the semitransparent photocathode twice. The mean QE of the entire system (mirror, camera window, cone, effective PMT QE) between 300 and 600 nm was 15%.

9.2.3 The MAGIC II telescope

The structure of the MAGIC II telescope clone, namely the foundations, and the telescope chassis with the space frame structure, are basically a perfect repetition of MAGIC I. They were assembled and mounted in La Palma already in 2006-07. On the other hand, all the other subsystems were substantially improved. This overall enhancement should substantially increase MAGIC II performance, compared to MAGIC I, and cure some of its design weaknesses.

9.2.3.1 The Reflector

The MAGIC II reflector is composed of two types of mirrors: 143 aluminum mirrors similar to MAGIC I mirrors but with a larger area of 1 m^2 and improved design and 104 cold slumped glass sandwich mirrors (again 1 m^2 area each) developed and manufactured at Media Lario Technologies company and INAF-OAB.

Whereas aluminum mirrors were designed and produced by the Padova group (Doro, 2009), **the work on MAGIC II glass slumped mirrors is relevant to my PhD activity**. This is dealt in greater detail in the following paragraphs of this chapter (see §9.3). In this paragraph, the design of the aluminum square meter mirrors installed in MAGIC II is briefly described.

The design of the aluminum mirrors follows the idea of the full aluminum sandwich structure as for MAGIC I, and in particular the improved design of MAGIC I upgraded mirrors. A sketch of a MAGIC II aluminum mirror can be seen Figure 9-9.

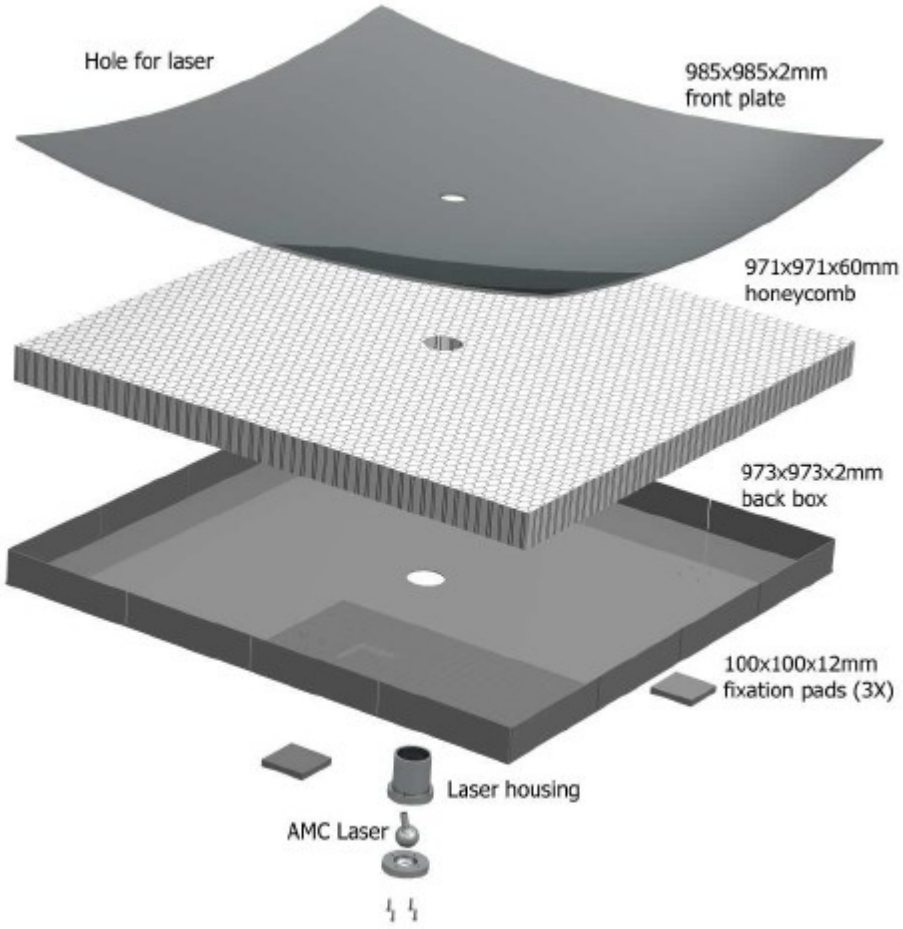

Figure 9-9. Design of the MAGIC II aluminum mirrors. The structure is a sandwich of an aluminum skin 985×985×2 mm made highly reflective by surface diamond milling, a honeycomb panel 971×971×60 mm to provide rigidity, and an aluminum back box 973×973×61.9 mm (2 mm thick) to close the structure. In addition, a hole is drilled at the center to house the laser for mirror repositioning control and three aluminum inserts inside the panel are inserted for mounting (Doro, 2009).

The assembly of the sandwich proceeded as follows:

1. Cleaning. All the aluminum components (top plate, bottom box, inserts) are cleaned with Acetone and hereafter treated with protective gloves in order not to deposit any kind of grease.
2. Assembly. The adhesive film is deposited onto the internal part of the bottom box. The honeycomb and the inserts are introduced into the box. A second layer of adhesive is put over the honeycomb and the top plate is put on the top to complete the sandwich.

3. Mould and Vacuum Bag. The sandwich is put over a curved mould, which has about the same. The entire assembly is put inside a sealed plastic bag and vacuum emptied.
4. Curing Cycle. The sandwich is inserted into an autoclave where a cycle of high pressure and temperature cures the adhesive
5. Preparation. After the raw-blank is produced, some epoxy glue is deposited onto the perimeter of the bottom box where it is fixed to the top plate and over all the small fissures. After this, a hole is drilled in the center of the mirror where the laser housing is inserted and glued. In addition, four holes for the three internal pads are drilled in the back of the mirror corresponding to the position of the AMC actuators.
6. Diamond Milling. The raw-blanks have an average radii of curvature of around 35 m. To reach the exact value of curvature for the position of the mirror in the telescope, which ranges from around 34 m to around 35.5 m, the surface of the mirror is grinded. This is done by a fly-cutting, which operates with a fast rotating diamond head which mills the mirror surface.
7. Quartz Coating At the Fraunhofer Institute (IFAM) in Bremen (Germany), the surface of the mirror was coated through a vacuum deposition of quartz with an admixture of carbon. The technique is called plasma enhanced vapor chemical deposition (PEVCD).

After the mirrors were quartz-coated at IFAM, they were sent to MPI-Munich for individual quality tests before installation on the telescope.

9.2.3.2 The camera

A major effort was made to improve the MAGIC camera photon detection system. First of all, on the market there were already photomultipliers with quite larger quantum efficiency compared to MAGIC I. After a market selection Hamamatsu PMTs were chosen (Photo Multipliers). Their photon conversion efficiency is 32% at 350 nm without lacquer coating,. All the PMTs have the same size of 0. 1°. The number of PMTs has increased from 577 to 1039 in total. Also the triggers have been increased and now comprise 559 PMTs in the central camera. The design of the PMT housing has also been completely renewed. The PMTs are grouped into clusters of 7. Each cluster can be easily removed in case of problems. Inside the cluster, the HV is produced, a sampling signal can be injected to test the electronics after the PMT. The new camera brings an increased effective area, and an increased signal to noise ratio. The MAGIC II camera was designed and realized by F. Goebel at MPI.

9.3 Development of the glass cold-slumping technique

The cold glass slumping is a new method derived from a similar technique proposed for the manufacturing of x-ray optics (Ghigo, 2008), that fits the requirements of Cherenkov telescopes. It has been developed by the Media Lario Technologies (MLT) company in collaboration with INAF-OAB; MLT has been also in charge of the 104 glass panels production and quality control for MAGIC II. **The development and qualification of this technique has been relevant part of my PhD activities**.

9.3.1 Glass sandwich mirror design and fabrication

For Cherenkov Telescopes high collecting area is needed, achievable by the use of a large diameter primary, made of a mosaic of many (possibly light-weight) reflecting facets, like the ones needed for future next generation ground based optical telescopes as E-ELT (Gilmozzi, 2007) telescope studied by ESO (European Southern Observatory). While in both cases a high volume production has to be achieved for making the reflecting panels, for Cherenkov telescopes the angular resolution is not an issue (each panel should present a PSF with a radius at 90% focusing better than 1 mrad, compared to the 0.1 arcsec value requested for each E-ELT panel). However the areal cost and areal density needed for Cherenkov telescopes are quite challenging, since they should maintained <1-3 k€/m^2 and 20 kg/m^2 respectively; for comparison, the same target parameters for E-ELT are 300 k€/m^2 and 70 kg/m^2 respectively.

A thin glass sheet is elastically deformed so as to retain the shape imparted by a master with a convex profile. The master has to be worked with the same optical precision needed for the mirrors, because every defect on its surface will be reproduced on the glass. The master typically is in aluminum and its surface is diamond milled in the same way of the MAGIC I mirrors.

With large curvature radii the glass sheets can be pressed against the master using vacuum suction. In order to provide the necessary rigidity a honeycomb structure is glued on the deformed sheet under the vacuum forces. At last a second glass sheet is glued on the top of the honeycomb structure, in order to obtain a sandwich.

To assure that the optical characteristics required by the telescope design are maintained during operations the mechanical structure of the single panel has been evaluated by FEM analysis.

The final design for the FEM of the glass sandwich panels is the following:

- Dimensions 985 x 985 mm
- Sandwich structure with the following characteristics:
    - reflecting skin 1.7 mm thick (glass)
    - bonding 0.2 mm thick
    - Aluminum honeycomb 20 mm thick
    - bonding 0.2 mm thick
    - backing skin 1.7 mm thick
- Panel total mass: 12 kg
- Three rigid supports glued in the back part of the panel (stainless steel plates 80x80 mm).

The cold slumping technique makes use of the vacuum suction to mechanically bend the reflecting membrane of a composite mirror. The possibility to use glass sheets in sandwich structures was first investigated for Solar concentrators application. If the radius of curvature of the optics is high and the thickness of the glass sheet is sufficiently low, the sheet can be conformed to the shape of the master by means of vacuum action. As previously mentioned, the mirror elements here proposed for Imaging Atmospheric Cherenkov Telescope application have a sandwich like structure where the reflecting and backing glass sheets are bonded to both sides of an aluminum honeycomb core. A schematic illustrating the construction of the sandwich structural mirror is illustrated in Figure 9-10.

The fabrication process is composed by the following steps:

1. Spherical curvature of the surface of an aluminum mould is obtained by diamond milling. Diamond milling is used in order to achieve the best shape accuracy possible without the need for further corrective polishing.
2. The shape of the mould is replicated by the reflecting glass sheet via vacuum suction. A backing glass sheet is assembled with an interposed aluminum honeycomb core element giving the proper rigidity.
3. The connection of the parts is achieved through epoxy resin structural adhesive bonding with curing under elevated temperature while maintaining the vacuum suction.
4. The glass sheets adopted are floating glass available on the market with a very good roughness and do not require any polishing step. The process ensures on the reflecting glass sheet the required shape accuracy after separation from the master and the

preservation of the starting surface roughness of the glass sheets.

5. The reflecting coating is deposited after the manufacturing of the sandwich structure by means of physical vapor deposition in a dedicated high vacuum chamber. The reflecting glass sheet is coated in order to provide a high reflectivity at wavelengths in the range from 300 to 600 nm. Aluminum coating provides the best reflectivity at these wavelengths, especially in the range of short wavelengths (300 to 450 nm) that contains most intensity of the Cherenkov light. To avoid oxidation of the aluminum layer, a protective coating of quartz is also applied.
6. Sealing of the sandwich structure borders is assured by a silicon based sealant. The edges of the sandwich have an external plastic PVC rim. This solution assures higher rigidity and mechanical protection of the mirror corners.

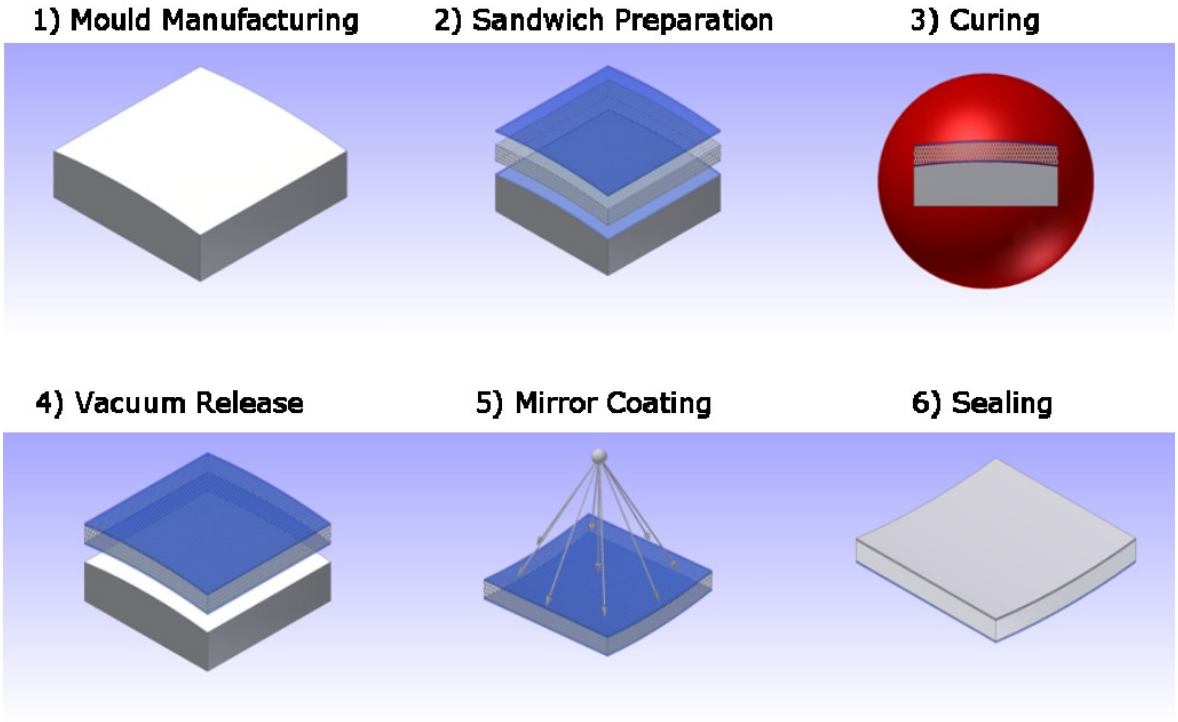

Figure 9-10. Sketch of the cold-slumping mirror manufacturing process.

All the materials within process are off-the-shelf and the higher cost is one time expenditure relevant to the manufacturing of the mould. Moreover the mould is not subjected to significant degradation during the process. In Figure 9-11 the pictures of one of the aluminum master and of glass sandwich mirror are shown.

Figure 9-11. Left: mould shaped by means of diamond milling; right: prototype mirror replicated via cold slumping.

9.3.2 Qualification tests for IACTs

In this session the activities I performed for the environmental qualification of the cold-slumped mirrors for Imaging Atmospheric Cherenkov Telescopes are presented together with their performance in terms of angular resolution and reflectivity. Some qualification tests have been performed at the level of samples (smaller with respect to the final dimension but fully representative of the manufacturing process) and some other test have been performed on 1 squared meter prototypes. In some cases the tests have been performed both on the samples and on the prototype mirrors. In the Table 9-1 the list of the qualification test is reported with the indication whether the test has been performed on small scale samples or on real final dimension prototypes.

Before starting the qualification tests, the angular resolution and the reflectivity of the prototype mirrors have been characterized with two different experimental set-ups. For the Point Spread Function (PSF) measurement, the mirror was placed at the assumed radius of curvature of the mirror in respect to a monochromatic red diode. The diode is simulating a point-like light source. A white sheet of paper was placed into a paper box and located close to the diode, at the same distance to the mirror. The distance from the mirror to the diode and reflecting plane was adjusted until the reflected spot size had its minimum. The reflected spot was imaged with a 16bit CCD camera.

Table 9-1. Summary of the qualification tests with the indication (T) whether the test has been performed on small samples or on real dimension prototypes.

	Qualification Test (Type-Method)	**Test on Samples**	**Test on Prototypes**
1	Angular Resolution	T	T
2	Reflectivity	T	T
3	Angular Resolution after Thermal Cycling (-20°C / +60°C)		T
4	Reflectivity (before and after Weathering Test)	T	
5	Reflectivity (before and after Salt Fog Test)	T	
6	Coating Adhesion test	T	T
7	Sealing Test		T

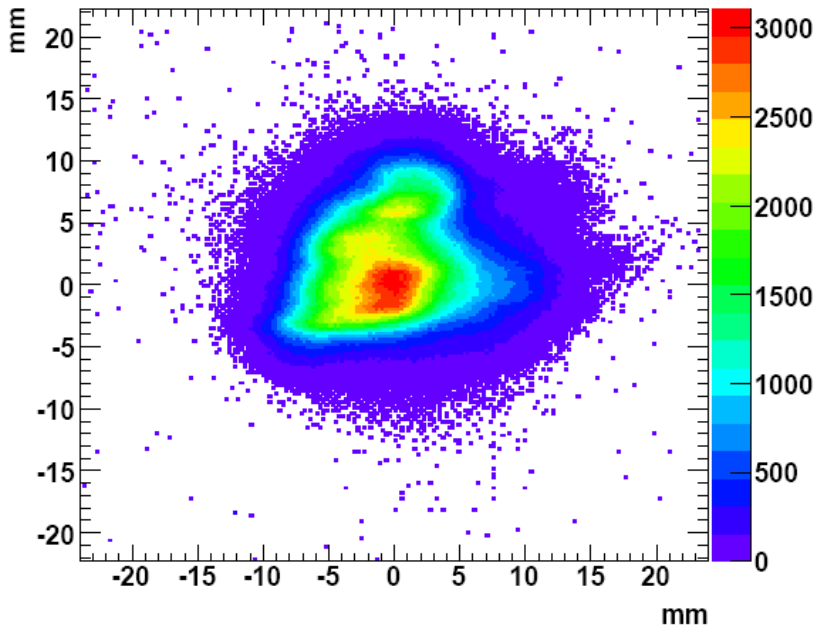

Figure 9-12. Point Spread Function (PSF) of a cold-slumped glass mirror at distance of ~34m. The circle containing 80% of the light has a radius of ~7.4 mm that corresponds to angular radius of ~0.22 mrad (MPI Munich credits).

The spot diagram of a representative cold-slumped glass sandwich mirror is reported in Figure 9-12, where the circle containing 80% of the light has a radius of ~7.4 mm that corresponds to an angular diameter ~ 0.45 mrad.

The focal length of the cold-slumped mirrors is normally slightly shorter than the focal length of the mould from which they are replicated. This aspect of the process, although not expected, is very repeatable and hence the focal length of the mould can be designed in order to take it into account.

For the measurement of the mirror reflectivity I used the portable IRIS 908RS2 instrument. This instrument allows to measure two components of the reflectivity, the direct and the diffuse reflected component, on several position on the mirror reflecting surface. An image of the portable device for the reflectivity measurement is reported in Figure 9-13. The device is operating at four different wavelengths. The four laser diodes have the following characteristics:

1. Blue: λ = 470 nm (FWHM = 30 nm)
2. Green: λ = 530 nm (FWHM = 40 nm)
3. Red: λ = 650 nm (FWHM = 30 nm)
4. Infrared: λ = 880 nm (FWHM = 80 nm)

Figure 9-13. IRIS 908RS2 portable instrument while measuring reflectivity on a glass sample.

The laser diodes focus their beam of light at an inclination angle of 45° in respect to the sample surface. Four detectors are mounted at 0°, +2°, -15° and -45°. The later three are used to determine the scattering component of the reflected light. The maximal relative error of the instrument and therefore the measurement accuracy is 0.5%. The repetitiveness of the reflectivity measurement is 0.1% for 20 measurements. The measured area is 10mm in diameter.

Figure 9-14 shows the measurement of the mirror reflectivity performed on a representative 1 squared meter prototype glass mirror. The reflectivity is well above 80% and peaks in the blue region (where the Cherenkov light emission is higher). The scattering amount of the cold-slumped mirror is typically lesser than 0.1%.

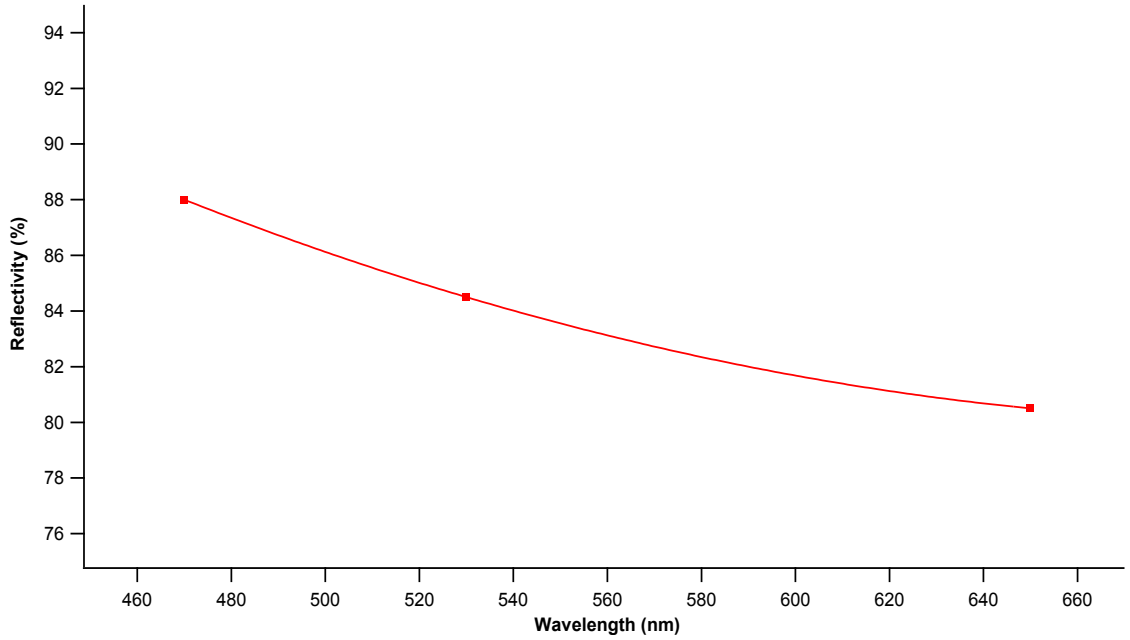

Figure 9-14. Reflectivity measurement at different wavelength of a representative cold-slumped glass sandwich mirror.

Angular Resolution After Thermal Cycling

The measurements of the PSF of the prototype mirrors and the radius of curvature measurements have been performed before and after 5 thermal cycles. These tests aimed at the verification of the maintenance of the optical performance of the mirror in the survival condition. Each thermal cycle has been performed passing quickly from 20°C to -20°C (plateau

of 12 hour) and then from -20°C to 60°C (plateau of 4 hours).

The temperature profile is reported below in Figure 9-15. After each cycle the radius of curvature and the angular resolution (PSF) have been measured showing that no changes occurred with respect to the starting parameter before thermal cycling.

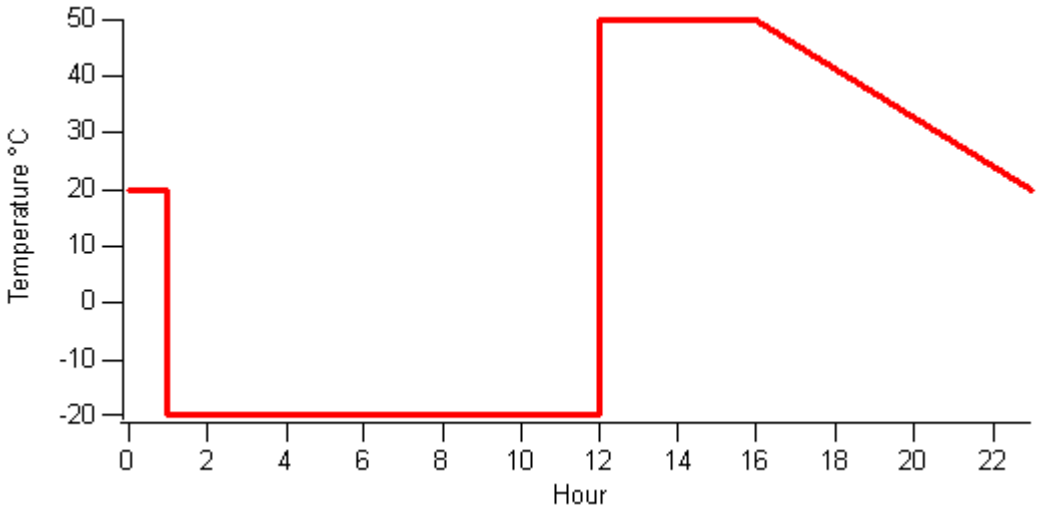

Figure 9-15. Temperature curve of the thermal cycles performed on the prototype mirrors.

Reflectivity Before and After Weathering Test

The reflectivity of 3 samples with dimension 200 mm x 200 mm have been measured before and after accelerated aging test by means of IRIS 908RS2 portable instrument. The accelerated aging test (or weathering test) was 42 days long, with continuous variation of temperature profile, relative humidity profile and ultraviolet radiation power (UVA).

The temperature and humidity profiles are plotted in Figure 9-16.

The UVA power irradiating the samples had been switched during the test between the following 2 values:

- 2.2 mW/cm^2 with the lightening of 5 lamps at distance of 65 cm;
- 4.4 mW/cm^2 with the lightening of 10 lamps at distance of 65 cm.

The reflectivity measurements are reported in the following Table 9-2.

As it can be seen from the table the reflectivity of the mirrors is not significantly affect by the weathering conditions.

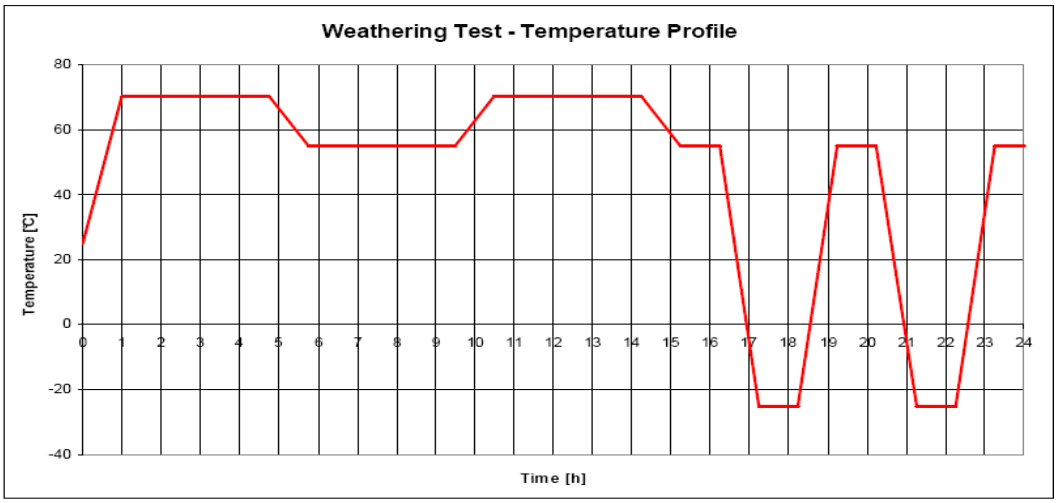

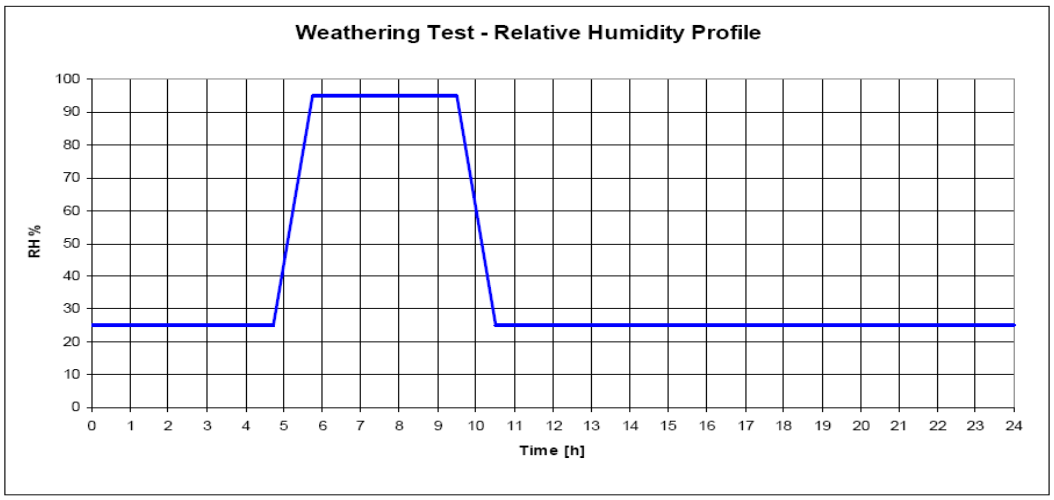

Figure 9-16. Temperature profile (left) and relative humidity profile (right) during weathering test on samples.

Table 9-2. The reflectivity of 3 samples measured before and after accelerated aging test.

Wavelength	Sample 1 Before	Sample 1 After Test	Sample 2 Before	Sample 2 After Test	Sample 3 Before	Sample 3 After Test
470 nm	88.7 %	88.1 %	88.5 %	88.0 %	88.6 %	87.9 %
530 nm	84.4 %	83.7 %	84.1 %	83.6 %	84.3 %	83.8 %
650 nm	80.5 %	80.3 %	80.5 %	80.2 %	80.7 %	80.3 %

Reflectivity Before and After Salt Fog Test

In order to assess the corrosion resistance of the cold-slumped mirror coating, a Salt fog test have been performed on some representative samples. Salt fog test produces an accelerated corrosive attack in order to predict the coating suitability in use as a protective finish on corrosive environments. The Salt fog test has been performed with an atomized fog of water having a high salt content (higher than 5%) for the duration of 24 hours. Even if there is no clear correlation between 24 hours of exposure with a 5% solution to a long period of exposure in an actual corrosive atmosphere, the test has been performed without showing signs of corrosion on the samples. Also the reflectivity of the coating has not been affected by the Salt fog test as measured with the IRIS 908RS2 portable instrument. In Figure 9-17 the experimental set-up is depicted showing the samples installed in the chamber (on the left) also during the execution of the test (on the right).

Figure 9-17. Samples installed in the chamber for Salt Fog Test (left) and during the execution of the Salt Fog Test (right).

Coating Adhesion Test

The adhesion of the coating has been checked by a peel-off test performed both on samples and on prototype mirror. The processes of aluminization and protective quartz layer deposition are performed under high vacuum (~10^{-6} mbar) in a dedicated chamber via physical vapor deposition; the reflecting surface is cleaned through Ion etching before the deposition. Pressure sensitive tape has been applied and removed over different areas in the coating. The areas have been subsequently inspected for removal of coating from the substrate giving no indication of

detachments. Coating adhesion tests have been performed also after Weathering and Salt Fog Test performed on representative samples without giving indication of detachment of the coating.

Sealing Tightness Test

For pressure exchange between sandwich mirror interior and external environment, required by the sealing tightness test, a venting hole has been provided on one side of some prototype mirrors. Sealing tightness of prototype mirror has been tested by means of a vacuum pump. The internal pressure has been reduced from ambient to 0.2 bar and the vacuum circuit has been therefore closed. No leakage has been detected within 15 minutes.

As additional test, some mirror prototypes have been dipped completely into water for the duration of 24 hours. The weight of the mirrors before and after the test was exactly the same giving indication that no penetration of water inside the sandwich structure occurred.

9.3.3 Production of the glass mirrors for MAGIC II reflector

The MAGIC II reflector is composed of two types of mirrors: 143 aluminum mirrors similar to MAGIC I mirrors but with a larger area of 1 m^2 and improved design and 104 cold slumped glass sandwich mirrors (again 1 m^2 area each) developed and manufactured at Media Lario Technologies company and INAF-OAB under my supervision.

According to the position on the telescope, some glass mirrors have an adapted design. In particular:

- 80 glass mirrors are standard
- 16 glass mirrors are square but have a different configuration of the mounting of the actuators to fit in the edge of the parabola
- 8 glass mirrors are not square but have a cut angle in order to not interfere with the structure

The production of the glass mirrors was performed following the manufacturing approach described in the previous chapter §9.3.1. On one corner of each panel a plate designed as holder for a laser has been installed. This laser is used to align the mirror during Active Motion Control (AMC) operations of MAGIC II telescope (Garczarczyk, 2003) (see Figure 9-18).

Figure 9-18. image of the laser with its holder installed on the corner of a glass panel.

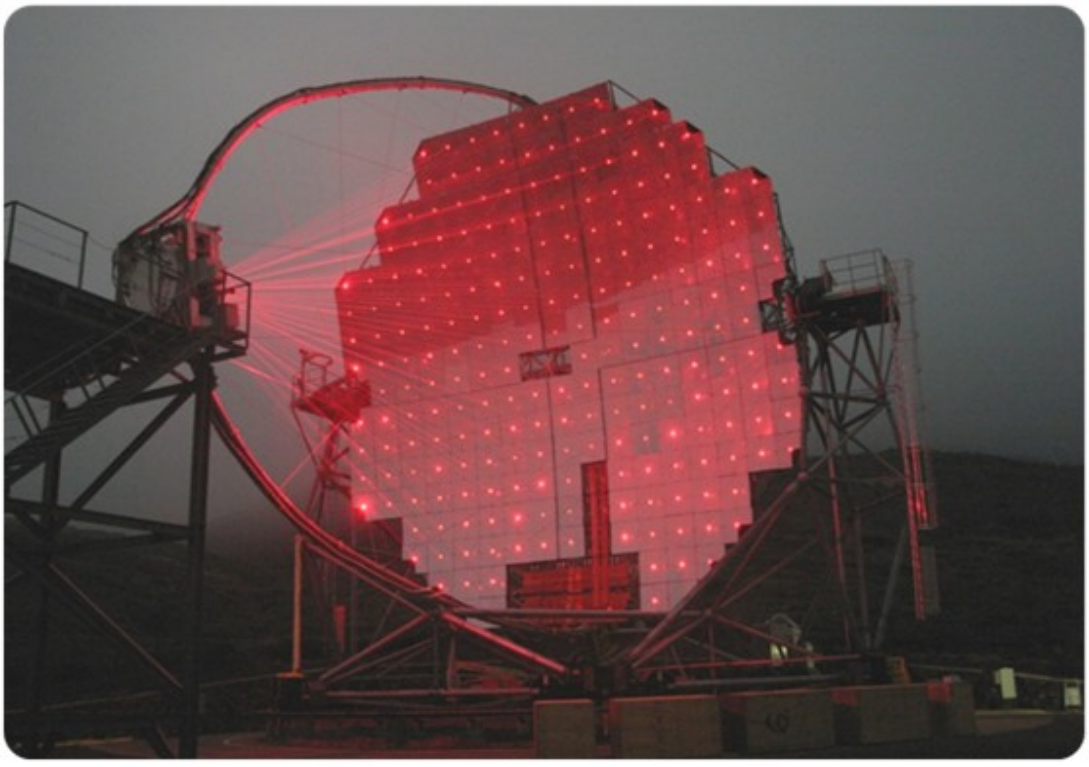

Figure 9-19. MAGIC II telescope during Active Motion Control alignment of the mirrors.

In principle from a single master one could think that only one radius of curvature for the mirror could be obtained. Nevertheless, by a careful control of the spring-back effect during the gluing process, one can obtain several mirrors with curvature different than the master's one. Using this feature, in the case of the **MAGIC II production, to obtain 12 different curvatures (between 35.4 m and 36.3 m) within the angular resolution specifications of 2.5 arcmin only two different radius masters have been used**. The distribution obtained is shown in Figure 9-20. The maximum difference between the required radius and the produced one is of 18 cm, with a mean value of 5 cm and a standard deviation of 6 cm. Considering that the typical error in estimating the curvature radius is between 5 and 10 cm, depending by the quality of the PSF, the distribution fully matches the requirements.

The curvature radii of the panels have been measured illuminating the mirror with a point light source at about 35 m and searching for best the image position on a screen with respect to the panel position (see Figure 9-21). The distance between the mirror and the point source (and between the mirror and the screen) is equal to the nominal curvature radius (or twice the focal length) of the mirror itself, in such a way that a point image is reflected again into a point image. The image obtained on a screen with a CCD camera has been used for the PSF evaluation test.

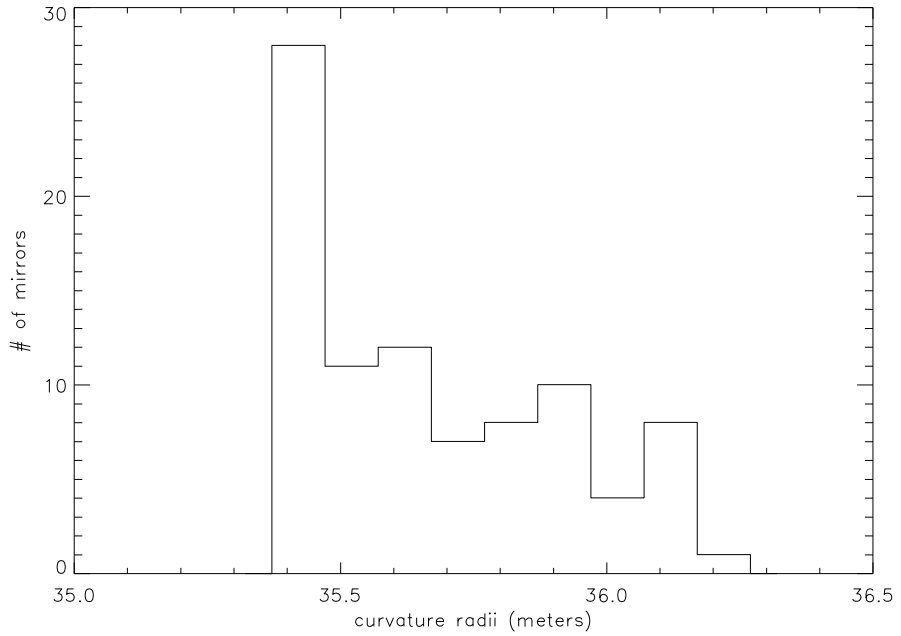

Figure 9-20. Radii distribution for the panel, in the statistics also rejected mirrors are taken into account. This is the reason for the strong left wing of the distribution.

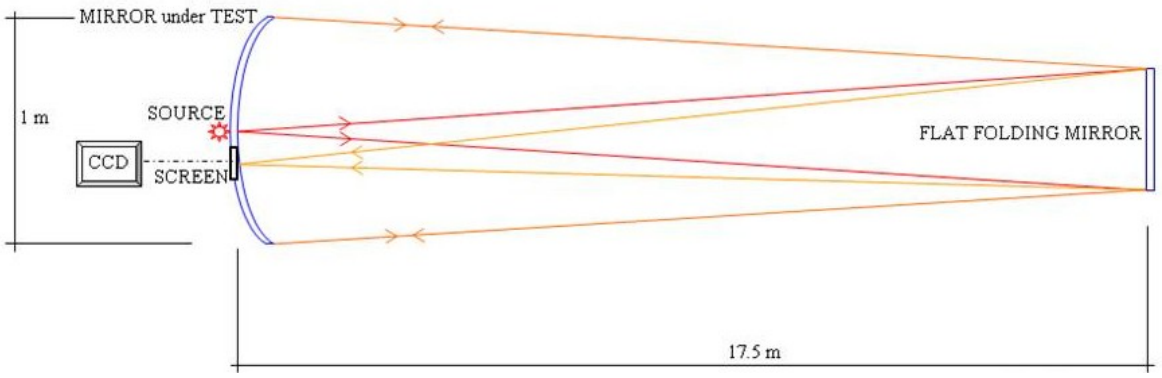

Figure 9-21. Layout of the optical bench used for the measurement of the curvature radius and of the PSF; it is based on a flat folding mirror for achieving the right distance from mirror and source.

The optical quality of each glass mirror for MAGIC II has been verified qualified into two way:

1. Direct measurement of the size of the radius which contain 90% of the light reflected by the mirror (r_90) by using the optical set-up shown in Figure 9-21;
2. Measurement of the local reflectivity (at 4 different wavelengths) on several positions by using the portable instrument IRIS 908RS.

The distribution of the measured r_90 is shown in Figure 9-22. The mean of r_90 at 35 meters is about 12.5 mm (0.7 mrad) with a standard deviation about 2.5 mm.

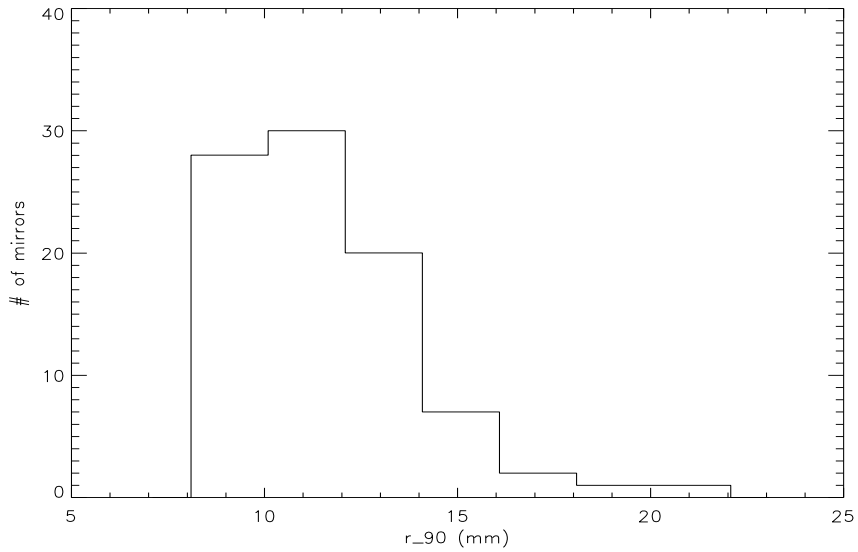

Figure 9-22. Distribution of the r_90 of the glass panels of MAGIC II at 35 meters.

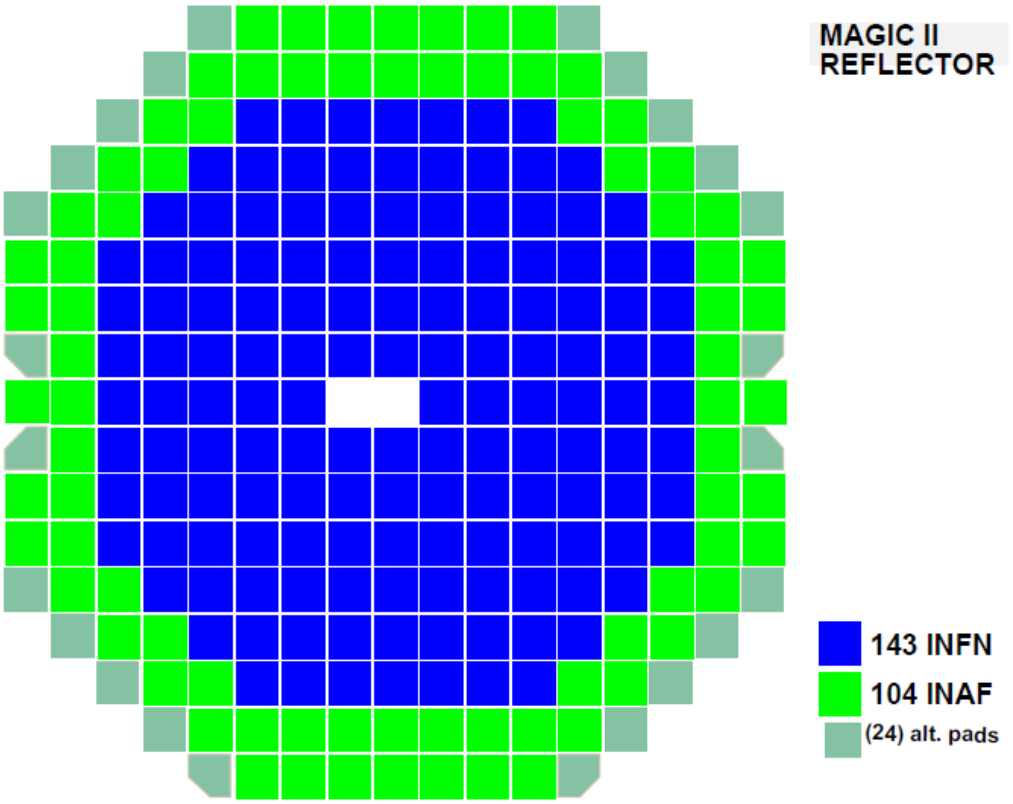

Figure 9-23. Arrangement of full aluminum and glass on MAGIC II. An optimization procedure was set to optimize the positioning of each mirror in order to minimize the difference with the nominal radius of curvature. Dark green mirrors are glass.

The installation of the MAGIC II mirrors has been completed in August 2008. The number of mirrors of each type was decided by budget constraints and political issues. It was decided to use glass mirrors on the edge for two main reasons:

a) 6 of the mirrors on the edge must be cut at an angle. They correspond to the panels in MAGIC I that housed 3 mirrors instead of 4. The angles must be cut to leave space for the telescope structure.
b) Originally, aluminum mirrors were produced before glass mirrors, and it was easier to proceed for installation from the center outwards.

The reflectivity of some aluminum and glass mirrors has been measured 2.5 years after the installation with spectrophotometer. **The reflectivity of the mirrors was still very high, with higher reflectivity for the glass sandwich mirrors** (see Figure 9-24 and Figure 9-25).

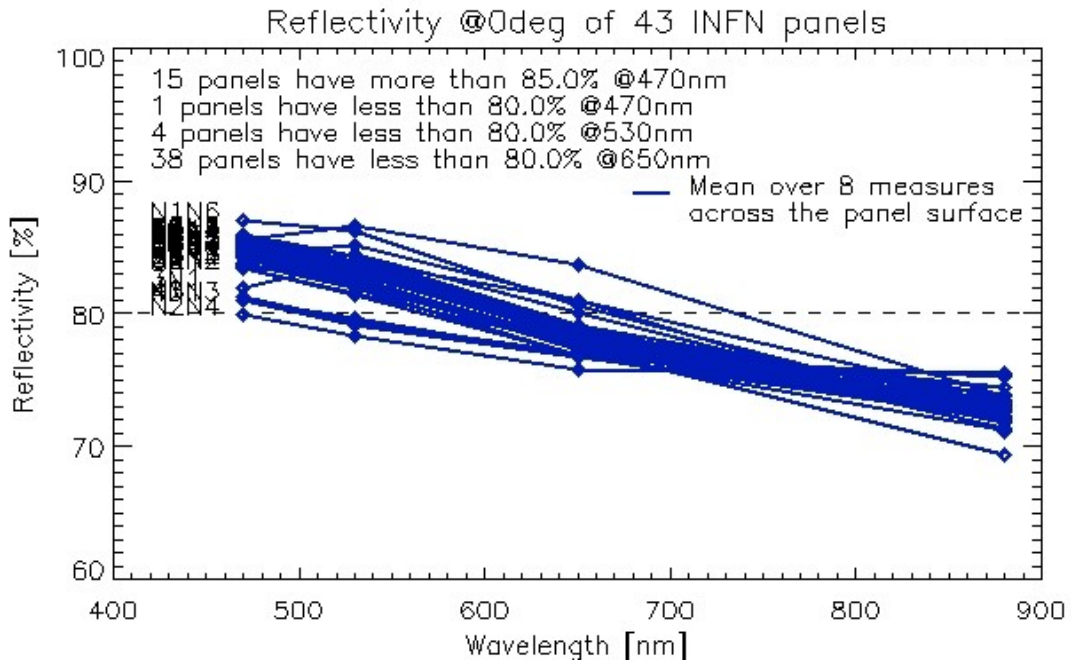

Figure 9-24. Reflectivity measured on 43 INFN diamond milled aluminum mirrors 2.5 years after the installation on MAGIC II telescope.

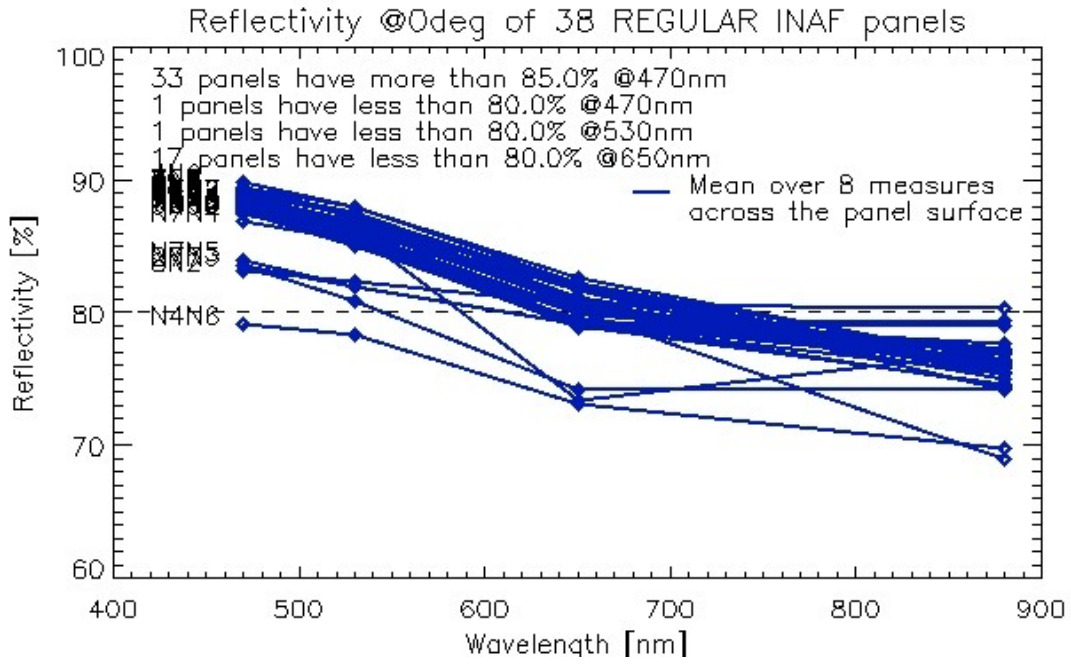

Figure 9-25. Reflectivity measured on 38 glass cold-slumped mirrors 2.5 years after the installation on MAGIC II telescope.

9.4 Conclusions

Cost-effective design of the IACT segmented mirrors and its production rate represent key ingredient for the success of the next generation instrument. During my PhD activity I contribute in the development of the cold slumping technique described in this chapter. It has been demonstrated that, with this technique, it is possible to manufacture lightweight (9.5 kg/m^2) mirrors in quite short time (e.g. 5 mirrors per day if 5 masters are available), with optical quality within the requirements of IACTs, and by using materials available off-the-shelf. I followed a number of environmental tests, that have been successfully performed not showing criticalities within Cherenkov Telescope boundary conditions.

The reflecting surface of MAGIC II, composed by aluminum and glass panels, has been installed on the telescope in August 2008. 104 glass panels commissioned by INAF have been realized and qualified in the time schedule needed to the experiment. The test realized on their optical performances demonstrated that the cold glass slumping is a very promising technique to be applied in the production of the reflecting surfaces of next generation Cherenkov telescopes like CTA. Furthermore, the use of Glassfoam instead of honeycomb inside the mirror could increase the mirror stiffness. All these activities for MAGIC II mirrors are slightly converging into the activities for the future generation of European Cherenkov telescopes, namely for the Cherenkov Telescope Array (CTA) consortium.

10 Conclusions and final remarks

The PhD research activities have been focused on two main topics:

1. the development of an advance polishing technique for the x-ray mandrels to be used as masters for the replication by e-forming of x-ray astronomical mirrors;
2. the development of a cold-slumping technique for VHE gamma-ray astronomical mirrors for Cherenkov Telescopes.

For the former topic, the main goal achieved is the implementation of a process where the mandrels can be manufactured with a high angular resolution (< 6 arc seconds HEW) and a low roughness (< 0.2 nm rms) within a consistent short time.

For the latter topic, the main goal achieved is the implementation of a process where it is possible to manufacture lightweight (9.5 kg/m^2) glass sandwich mirrors in quite short time (e.g. 5 mirrors per day if 5 masters are available).

In the contest of the eROSITA and NHXM x-ray missions, the activities relevant to my PhD can be summarized in the following points:

- an advance polishing technique has been studied and successfully applied to a number of flight-quality mandrels from the NHXM and eROSITA optical design. Some mirror shells produced by using these mandrels were tested at PANTER facility showing that the required x-ray performance can be achieved;
- the Diamond Turning (DT) process has been defined and proven as one basic process for the manufacturing of the x-ray mandrels. The DT process provides an excellent azimuthal symmetry, useful for the subsequent corrective polishing step;
- a new custom polishing machine, the IRP1200X, has been adopted allowing to polish x-ray mandrels with diameter up to 1200 mm and height up to 800 mm;

- the proper polishing parameters settings, of the IRP1200X machine, have been identified for the DT marks removal step, the corrective polishing and the texture improvement;
- the superpolishing technique has been further refined, by studying and implementing new designs of the superpolishing pads.

In the contest of the MAGIC telescope system, the activities relevant to my PhD can be summarized in the following points:

- an advance technique based on glass-cold slumping has been studied and successfully applied to manufacture lightweight (9.5 kg/m^2) mirrors in quite short time;
- a number of environmental tests, that have been successfully performed not showing criticalities within Cherenkov Telescope boundary conditions;
- the reflecting surface of MAGIC II, composed by aluminum and glass panels, has been installed on the telescope in August 2008. 104 glass panels have been realized and qualified in the time schedule needed to the experiment;
- the test realized on their optical performances demonstrated that the cold glass slumping is a very promising technique to be applied in the production of the reflecting surfaces of next generation Cherenkov telescopes like CTA.

During the PhD activity the following papers have been published:

1. **D. Vernani**, G. Borghi, G. Calegari, M. Castelnuovo, O. Citterio, I. Ferrario, G. Grisoni, S. Moretti, G. Valsecchi, H. Brauninger, V. Burwitz, J. Eder, P. Friedrich, P. Predehl, *Performance of a mirror shell replicated from a new flight quality mandrel for the eROSITA mission*, SPIE Vol. 8147-5 (2011)
2. **D. Vernani**, *Manufacturing of precise grazing incidence EUVL/X-ray optics by means of nickel electroforming replica process*, **Keynote Presentation**, EUSPEN 11th International Conference Proceedings, May 23rd – 26th Como, Italy (2011)
3. **D. Vernani**, G. Borghi, R. Binda, O. Citterio, G. Grisoni, J. Kools, F. Marioni, A. Orlandi, A. Ritucci, G. Sironi, G. Valsecchi, S. Basso, G. Pareschi, D. Spiga, G. Tagliaferri, B. Negri, *Technologies for manufacturing of high angular resolution multilayer coated optics for future hard x-ray missions: a status report II*, SPIE Vol. 7732 (2010)
4. **D. Vernani**, G. Borghi, O. Citterio, S. Moretti, A. Ritucci, G. Sironi, M. Riva, S. Basso, G.

Pareschi, G. Tagliaferri, B. Negri, *Performance of supersmooth x-ray mandrels for the new Hard X-Ray Mission*, SPIE Vol. 7437 (2009)

5. **D. Vernani**, G. Borghi, E. Boscolo Marchi, O. Citterio, G. Grisoni, J. Kools, F. Marioni, A. Orlandi, A. Ritucci, M. Rossi, G. Salmaso, G. Valsecchi, S. Basso, G. Pareschi, D. Spiga, G. Tagliaferri, B. Negri, *Technologies for manufacturing of high angular resolution multilayer coated optics for future hard x-ray missions: a status report*, SPIE Vol. 7437 (2009)
6. **D. Vernani**, S. Basso, M. Bello, O. Citterio, G. Grisoni, G. Pareschi, D. Spiga, G. Tagliaferri, G. Valsecchi, *Feasibility study for the manufacturing of the multilayer X-ray optics for Simbol-X,* Memorie della Società Astronomica Italiana, v.79, p.283 (2008)
7. **D. Vernani**, R. Banham, O. Citterio, F. Sanvito, G. Valsecchi, G. Pareschi, M. Ghigo, E. Giro, M. Doro, M. Mariotti, *Development of cold-slumping glass mirrors for imaging Cherenkov telescopes*, SPIE Vol. 7018 (2008)
8. **D. Vernani** and F. Zocchi, *Ray-tracing of shape metrology data of grazing incidence x-ray astronomy mirrors*, SPIE Vol. 7011 (2008)
9. V. Burwitz, P. Friedrich, H. W. Brauninger, B. Budau, W. Burkert, J. Eder, M. Freyberg, G. D. Hartner, E. Pfeffermann, P. Predehl, L. Arcangeli, G. Borghi, A. Borroni, O. Citterio, I. Ferrario, G. Grisoni, F. Marioni, A. Ritucci, M. Rossi, G. Valsecchi, **D. Vernani**, *Development and testing of the eROSITA mirror modules*, SPIE Vol. 8147-6 (2011)
10. S. Basso, G. Pareschi, O. Citterio, G. Tagliaferri, D. Spiga, L. Raimondi, B. Salmaso, V. Cotroneo, G. Borghi, G. Valsecchi, A. Orlandi, **D. Vernani**, R. Binda, F. Marioni, S. Moretti, G. Sironi, P. Attinà, B. M. Negri, *The optics system of the New Hard X-ray Mission: status report*, SPIE Vol. 8147-7 (2011)
11. S. Basso, G. Pareschi, O. Citterio, D. Spiga, G. Tagliaferri, M. Civitani, L. Raimondi, G. Sironi, V. Cotroneo, B. Negri, G. Parodi, F. Martelli, G. Borghi, A. Orlandi, **D. Vernani**, G. Valsecchi, R. Binda, S. Romaine, P. Gorenstein, P. Attinà, *The optics system of the New Hard X-ray Mission: design and development*, SPIE Vol. 7732 (2010)
12. G. Pareschi, G. Tagliaferri, P. Attinà, S. Basso, G. Borghi, O. Citterio, M. Civitani, V. Cotroneo, B. Negri, G. Sironi, D. Spiga, Giuseppe Valsecchi, **D. Vernani**, *Design and development of the optics system for the NHXM hard x-ray and polarimetric mission*, SPIE Vol. 7437 (2009)
13. G. Tagliaferri, S. Basso, G. Borghi, W. Burkert, O. Citterio, M. Civitani, P. Conconi, V. Cotroneo, M. Freyberg, D. Garoli, P. Gorenstein, G. Hartner, V. Mattarello, A. Orlandi, G. Pareschi, S. Romaine, D. Spiga, G. Valsecchi, **D. Vernani**, *Simbol-X Hard X-ray Focusing Mirrors: Results Obtained During the Phase A Study*, SIMBOL-X: FOCUSING ON THE

HARD X-RAY UNIVERSE: Proceedings of the 2nd International Simbol-X Symposium. AIP Conference Proceedings, Volume 1126, pp. 35-40 (2009)

14. P. Friedrich, H. Bräuninger, B. Budau, W. Burkert, J. Eder, M. J. Freyberg, G. Hartner, M. Mühlegger, P. Predehl, M. Erhard, S. Gutruf, D. Jugler, D. Kampf, G. Borghi, O. Citterio, M. Rossi, G. Valsecchi, **D. Vernani**, M. Zimmermann, *Design and development of the eROSITA x-ray mirrors*, SPIE Vol. 7011 (2008)
15. G. Pareschi, P. Attinà, S. Basso, G. Borghi, W. Burkert, R. Buzzi, O. Citterio, M. Civitani, P. Conconi, V. Cotroneo, G. Cusumano, E. Dell'Orto, M. Freyberg, G. D. Hartner, P. Gorenstein, E. Mattaini, F. Mazzoleni, G. Parodi, S. Romaine, D. Spiga, G. Tagliaferri, R. Valtolina, G. Valsecchi, **D. Vernani**, *Design and development of the SIMBOL-X hard x-ray optics*, SPIE Vol. 7011 (2008)
16. G. Pareschi, E. Giro, R. Banham, S. Basso, D. Bastieri, R. Canestrari, G. Ceppatelli, O. Citterio, M. Doro, M. Ghigo, F. Marioni, M. Mariotti, M. Salvati, F. Sanvito, **D. Vernani**, *Glass mirrors by cold slumping to cover 100 m2 of the MAGIC II Cherenkov telescope reflecting surface*, SPIE Vol. 7018 (2008)
17. F. Zocchi and **D. Vernani**, *An Alternative optical design for x-ray telescopes*, SPIE Vol. 6688 (2007)
18. D. Spiga, G. Pareschi, V. Cotroneo, R. Canestrari, **D. Vernani**, A. Mirone, C. Ferrero, C. Ferrari, L. Lazzarini, *Multilayer coatings for x-ray mirrors: extraction of stack parameters from x-ray reflectivity scans and comparison with transmission electron microscopy results*, Opt. Eng.46, 086501 (2007)
19. P. Predehl, R. Andritschke, W. Bornemann, H. Brauninger, U. Briel, H. Brunner, W. Burkert, K. Dennerl, J. Eder, M. Freyberg, P. Friedrich, M. Furmetz, R. Hartmann, G. Hartner, G. Hasinger, S. Herrmann, P. Holl, H. Huber, E. Kendziorra, W. Kink, N. Meidinger, S. Muller, M. Pavlinsky, E. Pfeffermann, C. Rohè, A. Santangelo, J. Schimitt, A. Schwope, M. Steinmetz, L. Struder, R. Sunyaev L. Tiedemann, M. Vongehr, J. Wilms, M. Erhard, S. Gutruf, D. Jugler, D. Kampf, R. Graue, O. Citterio, G. Valsecchi, **D. Vernani**, M. Zimmermann; *eROSITA*, SPIE Vol. 6686 (2007)

Bibliography

Aharonian, F. (2007). An exceptional Very High Energy Gamma-Ray Flare of PKS 2155-304. *The Astrophysical Journal , 664*, L71-L74.

Albert, J. (2007). Variable Very High Energy Gamma-Ray Emission from Markarian 501. *The Astrophysical Journal , 669*, 862-883.

Aliu, E. (2008, November). Observation of Pulsed gamma-Ray Above 25 GeV from the Crab Pulsar with MAGIC. *Science , 322*, p. 1221.

Aschenbach, B. (1985). X ray telescope. *Rep. Prog. Phys. , 48*, 579.

Attwood, D. (1999). *Soft x-rays and extreme ultraviolet radiation.* Cambridge UK: Cambridge University Press.

Barrau, A. (1998). The CAT imaging telescope for very-high-energy gamma-ray astronomy. *Nucl. Instrum. Methods Phys. Res. , 41*, 278-292.

Basso, S. (2010). *SPIE Proc.*, *7732*.

Bastieri, D. (2005). The Mirrors for the MAGIC Telescopes. *29th International Cosmic Ray Conference*, (pp. 101-106).

Bastieri, D. (2007). The reflecting surface of the MAGIC-II Telescope. *ARXIV Contribution to the 30th ICRC.*

Bavdaz, M. (2010). X-ray pore optics technologies and their application in space telescope. *X-Ray Optics and Instrumentation* , 15.

Bellazzini. (2010). *SPIE*, *7732*, p. 116.

Bellazzini, R. (2009). A Sealed Gas Pixel Detector for X-ray Astronomy. *NIMPA , 579*, 853.

Bernlohr, K. (2003). Optical system of the H.E.S.S. imaging atmospheric Cherenkov telescopes. Part I: layout and components of the system. *Astroparticle Physics , 20* (2), 111-128.

Biland, A. (2007). The Active Mirror Control of the MAGIC Telescope. *In Proc. of 30th International Cosmic Ray Conference.* Merıda, Mexico.

Bragg, W. H., & Bragg, W. L. (1918). *X-rays and crystal Structure.* London: Bell and Sons edition.

Buckley, J. (2008). The Advanced Gamma-ray Imaging System (AGIS). *American Physical Society APS Meeting and HEDP/HEDLA Meeting.*

Burrows, D. N. (2000). Swift X-Ray Telescope). *SPIE Proc.*, *4140*, p. 64.

Campana, R. (2011). Imaging performance of a large-area Silicon Drift Detector for X-ray astronomy. *NIMPA , 633*, 22C.

Canestrari, R. (2009). *Thin glass sheets for innovative mirrors in astronomical applications.* (Doctoral Thesis, Università degli Studi dell'Insubria, 2009).

Carstairs, I. (1986). The University of Durham new VHE gamma ray telescopes. *Proceedings of the NATO Advanced Research Workshop Durham*, (pp. 11-15). England.

Church, E. L. (1979). Role of surface topography in x-ray scattering. *SPIE Proc.*, *184*, p. 196.

Citterio, O. (1996). Characteristics of the flight model optics for the JET-X telescope onboard the SPEC-TRUM X-g satellites. *SPIE Proc.*, *2805*, p. 56.

Citterio, O. (2001). Development of Soft and Hard X-ray optics for astronomy: progress report II and consideration on material properties for large diameter segmented optics. *SPIE Proc.*, *4496*, p. 23.

Citterio, O. (1988). Optics for the x-ray imaging concentrator aboard the x-ray astronomy satellite SAX. *Appl. Opt. , 27*, 1470.

Citterio, O. (2000a). Progress on the use of ceramics materials for high throughput light weight X-ray optics. *SPIE Proc.*, *4012*, p. 513.

Comastri, A. (2011). The XMM Deep survey in the CDF-S. First results on heavily obscured AGN. *A&A , 526*, L9.

Compton, A. H. (1923). *Phil. Mag. , 45*, 1121.

Daum, A. (1997). First results on the performance of the HEGRA IACT array. *ASTROPARTICLE PHYSICS , 8*, 1-11.

Davies, J., & Cotton, E. (1957). *J. Solar Energy Sci. and Eng. , 1*, 16.

de Angelis, A. (2008, April). Very-high energy gamma astrophysics. *Nuovo Cimento Rivista Serie , 31*, pp. 187-246.

de Chambure, N. (1999). Lessons learned from the development of the XMM optics. *SPIE Proc.*, *3737*, p. 2.

de Korte, P. (1981). *Appl. Opt. , 20*, 1080.

Debye, P. (1913). *Verh. D. Deutsch. Phys. Ges. , 17*, 389.

Dinklage, J., & Frerichs, R. (1963). *J. Appl. Phys. , 34*, 2633.

Doro, M. (2009). *Novel Reflective Elements and Indirect Dark Matter Searches for MAGIC II and Future IACTs.* (Università Degli Studi di Padova, PhD Thesis, 2009).

Doro, M. (2008). The reflective surface of the MAGIC telescope . *NIMPA , 595* (1), 200-203.

Ehrenberg, W. J. (1949a). *Opt. Soc. Am. , 39*, 741.

Ehrenberg, W. J. (1949b). *Opt. Soc. Am. , 39*, 746.

Feenberg, E., & Primakoff, H. (1948). Interaction of cosmic ray primaries with sunlight and starlight. *Phys. Rev. , 73*, 449.

Fender, R. P. (2004). Towards a unified model for black hole x-ray binary jets. *MNRAS , 355*, 1105.

Fermi, E. (1922). Formazione di immagini coi raggi Röngten. *Nuovo Cimento , 24*, 133.

Feroci. (2010). Monitoring the hard x-ray sky with SuperAGILE. *A&A , 510*, A9.

Fiore, F. (2009). Chasing Highly Obscured QSOs in the COSOS field. *ApJ , 693*, 447.

Fiore, F. (2008). Unvelling Obscured Accretion in the Chandra Deep Filed-South. *ApJ , 672*, 94.

Friedrich, P. (1998). X-ray tests and calibrations of the ABRIXAS mirror systems. *SPIE Proc.*, *3444*, p. 369.

Garczarczyk, M. (2003). The Active Mirror Control of the MAGIC Telescope. *in Proc. the 28th International Cosmic Ray Conferenc*, *5*, p. 2935.

Ghigo. (2008). Slumped glass option for making the XEUS mirrors: preliminary design and ongoing development. *SPIE Proc.*, *7011*.

Ghigo, M. (2009). Hot slumping glass technology and integration process to manufacture a grazing incidence scaled prototype for the IXO telescope modules. *SPIE Proc.*, *7437*.

Ghisellini, G., & Lazzati, D. (1999). Polarization lightcurve and position angleof beamed gamma-ray burst. *MNRAS , 309*, L7.

Giacconi, R. (1979). *ApJ , 230*, 540.

Giacconi, R. (2001). First Results from the X-Ray and Optical Survey of the Chandra Deep Field South. *ApJ , 551*, 624.

Giacconi, R., & Rossi, B. (1960). A telescope for Soft X-ray Astronomy. *J. Geophys. Res. , 65*, 773.

Gilmozzi, R. (2007). The European Extremely Large Telescope (E-ELT). *The Messenger , 127*, 11.

Gorenstein, P. (1988). High throughput x-ray optics: an overview. *Appl. Opt. , 27*, 1433.

Haardt, F., & Matt, G. (1993). Origin of Polarization near Lyman Edge. *MNRAS , 261*, 346.

Hailey, C. J. (1997). Investigation of substrates and mounting techniques for the High Energy Focusing Telescope (HEFT). *SPIE Proc.*, *3114*, p. 535.

Harrison, F. A. (2010). The Nuclear Spectroscopic Telescope Array (NuSTAR). *SPIE Proc.*, *7732*, p. 27.

Harvey, J. E. (1996). Bridging the Gap between "Figure" and "Finish". *OSA Optical Fabrication & Testing Meeting, 3*. Boston, MA.

Hayakawa, S. (1952). Propagation of the Cosmic Radiation through Intersteller Space. *Progress of Theoretical Physics , 8* (5), 571-572.

Hermann, G. (2007). Cherenkov Telescope Array: The next-generation ground-based gamma-ray observatory. *Contribution to the 30th ICRC.*

Hofmann, W. (2000). The High Energy Stereoscopic System (HESS) Project. *AIP Conference Proceedings*, *515*, p. 500.

Horns, D. (2007). H.E.S.S.: Status and future plan. *Journal of Physics: Conference Series*, *60*, pp. 119-122.

Jahoda, K. (2010). The Gravity and Extreme Magnetism Small Explorer. *SPIE Proc.*, *7731*.

Jentzsch, F. (1929). *Phys. Z. , 30*, 268.

Joenson, K. (1995). Design of grazing incidence multilayer supermirror for hard x-ray reflectors. *Appl. Opt. , 34*, 7935.

Joinet. (2008). *ApJ , 679*, 655.

Kirkpatrick, P., & Baez, A. V. (1948). *Bull. Am. Phys. Soc. , 23*, 10.

Kozhevnikov, I. V. (2002). Analysis of X-ray scattering from a rough multilayer mirror in the first-order perturbation theory. *NIMPA , 498*, 482.

Kraushaar, W. (1968). Preliminary results of gamma-ray observations from OSO-3. *Can. J. Phys. , 46*, S414 - S418.

Krawczynski, H. (2008). The VERITAS Gamma-Ray Observatory - Status and Recent Results., *212*, p. American Astronomical Society AAS Meeting.

Kunieda, H. (2001). X-ray telescope onboard Astro-E: optical design and fabrication of thin foil mirrors. *Applied Optics , 40* (4), 553-564.

Laue, M. (1912). *Ann. d. Phys. , 41*, 971.

Lazzati, D., & Begelman, M. (2009). Polarization Signature of Gamma Ray Bursts from Fragmented Fireballs. *ApJ , 700*, L141.

Lewis, D. (1990). Optical characteristics of the Whipple Observatory TeV gamma-ray imaging telescope. *Experimental Astronomy , 1*, 213-226.

Lorenz, E. (2000). The MAGIC Telescope Project. *AIP Conference Proceedings*, *515*, p. 510.

Luo, B. (2008). *ApJ , 179*, 19.

Michette, A. G., & Buckley, C. J. (1993). *X-ray Science and Technology*. London UK: Institute of Physics Publishing.

Moralejo, A. (2009). Status of Magic-II. *arXiv:0912.3673v1 [astro-ph.IM]* .

Mori, M. (2000). The CANGAROO-III Project. *AIP Conference Proceedings*, *515*, p. 485.

Morrison, P. (1958). Solar Origin of Cosmic Ray Time Variations. *Proceedings of the Fifth International Congress on Cosmic Radiation*, *305*.

Motta, S. (2008). *MNRAS , 400*, 1603.

Mushotzky. (2000). Resolving the extragalactic hard X-ray background. *Nature , 404*, 459.

Newell, H. E. (1953). *High Altitude Rocket Researchs.* New York: Academic Pres.

Ohishi, M. (2002). Status of CANGAROO-III. *University of Tokyo Workshop.*

Paneque, D. (2004). A method to enhance the sensitivity of photomultipliers for air cherenkov telescopes by applying a lacquer that scatters light. *Nuclear Instruments and Methods in Physics Research Section A* , 619-621.

Pareschi, G. (2009). *SPIE Proc.*, *7437*.

Petre, R. (2010). Thin Shell, Segmented X-Ray Mirrors. *X-Ray Optics and Instrumentation , 2010*, 16.

Predehl, P. (2010). eROSITA on SRG. *SPIE Proc.*, *7732*.

Punch, M. (1992, August). Detection of TeV photons from the active galaxy Markarian 421. *Nature , 358*, p. 477.

Raban. (2009). Resolving the obscuring torus in NGC 168 with the power of infrared interferometry: revealing the inner funnel of dust. *A&A , 394* (3), 1325.

Ricker, G., & Vallerga, J. (1983). *NIMPA , 213*, 133.

Roentgen, W. C. (1895). Sitzungsberichte der Würzburger Physikalischeb-Medicinischen Gesellschaft.

Saggion, A. (2006). The MAGIC Telescope. *Mem. Soc. Astron. Ital. , 9*, 374.

Saggion, A. (2002). The observational energy gap between 10 and 300 GeV. *Mem. Soc. Astron. Ital. , 73*, 812-820.

Schnittman, J. D., & Krolik, J. (2010). X-ray Polarization from Accreting Balck Holes: Coronal Emission. *ApJ , 712*, 908.

Serlemitsos, P. J. (1995). [Serlemitsos 1995] Serlemitsos P J, Jalota L, Soong Y, Kunieda H, Tawara Y, Tsusaka Y, Suzuki H, Sakima Y, Yamazaki T, Yoshioka H, Furuzawa A, Yamashita K, Awaki H,The X-ray telescope on board ASCA. *Publ. Astron. Soc. Japan , 47*, 105.

Sinha, S. K. (1994). X-ray diffuse scattering as a probe for thin film and interface structure. *J. Phys. III France , 4*, 1543.

Sironi, G. (2010). *Analysis of X-ray telescope angular resolutions: application to NHXM.* (Doctoral Thesis, Università degli Studi dell'Insubria, 2010).

Smirnov, L. A. (1977). *Opt. Spectrosc. , 43*, 333.

Soffita, P. (2010). A set of x-ray polarimeters for the New Hard X-ray Imaging and Polarimetric Mission. *SPIE Proc.*, *7732*.

Spiga, D. (2005). *Development of Multilayer-Coated mirrors for Future X-Ray Telescopes.* PhD Thesis Milano-Bicocca University.

Spiga, D. (2007). Multilayer coatings for X-ray mirrors: extraction of stack parameters from X-ray reflectivity scans and comparison with Transmission Electron Microscope results. *Optical Engineering , 46* (8), 086501.

Spiller, E. (1981). *AIP*, *75*, p. 124.

Spiller, E. (1994). *Soft X-ray optics.* Bellingham - WA: SPIE Press.

Stearns, D. (1998). Nonspecular x-ray scattering in a multilayer-coated imaging system. *J. Appl. Phys. , 84*, 1003.

Stearns, D. (1992). X-ray scattering from interfacial roughness in multilayer structures. *J. Appl. Phys. , 71*, 4286.

Stoney, G. (1909). The Tension of Metallic Films Deposited by Electrolysis. *Proc. Royal Soc. of London*, *82*, p. 553. London.

Strong, B. (1974). Preliminary Catalog of Transient Cosmic Gamma-Ray Sources Observed by the VELA Satellites. *Astrophysical Journal , 188*, L1.

Tagliaferri, G. (2011). The NHXM observatory. *Experimental Astronomy* .

Takahashi, T. (2010). The ASTRO-H Mission. *SPIE Proc.*, *7732*, p. 18.

Tanaka, Y. (2001). Iron line and ASCA. *AAS , 33*, 1427.

Treister, E. (2009). The Space Density of Compton-Thick Active Galctic Nucleus and the X-ray Background. *ApJ , 696*, 110.

Treves, A., & Colpi, A. (1991). *A&A , 241*, 107.

Underwood, J. H., & Barbee, T. W. (1981). Layered synthetic microstructures as Bragg diffractors for X rays and extreme ultraviolet: theory and predicted performance. *Appl. Opt. , 20*, 3027.

Vacchi, A. (1991). Performance of the UA6 large-area silicon drift chamber prototype. *NIMPA*

, 306, 187V.

Van Speybroeck, L. (1979). *SPIE Proc.*, *184*, p. 2.

Van Speybroeck, L. (1972). Design parameters of Paraboloid-Hyperboloid Telescopes for X-ray Astronomy. *Apllied Optic , 11*, 2.

Van Warren. (2010). *Science , 330*, 347.

Vernani, D. (2010). Technologies for manufacturing of high angular resolution multilayer coated optics for future hard x-ray missions: a status report II. *SPIE Proc.*, *7732*.

Volk, H. (2009). Imaging very high energy gamma-ray telescopes. *Experimental Astronomy , 25*, 173-191.

Walker, D. (2003, April 21). The "Precession" tooling for polishing and figuring flat, spherical and aspheric surfaces. *Optical Society of America , 11* (8), p. 958.

Weekes, T. (1989). Observation of TeV gamma rays from the Crab nebula using the atmospheric. *The Astrophysical Journal , 342*, 379-395.

Weisskopf, M. C. (2000). *SPIE Proc.*, *4012*, p. 2.

Weisskopf, M. C. (2000). Chandra X-Ray Observatory (CXO): Overview. *SPIE Proc.*, *4012*, p. 2.

Wolter, H. (1952b). *Ann. Der. Phys. , 10*, 286.

Wolter, H. (1952a). Spiegelsysteme streifenden Einfalls als abbildende Optikenfur Rontgenstrahlen. *Ann. der Phys. , 10*, 94.

Zampa, G. (2011). Room-temperature spectroscopic performance of a very-large area silicon drift detector. *NIMPA , 633*, 157.

Zhang, W. (2008). Constellation-X mirror technology development. *SPIE Proc.*

Zoethout, E. (2003). Stress mitigation in Mo/Si multilayers for EUV lithography. *Spie Proc.*, *5037*.

Acknowledgments

I thank sincerely INAF-Brera Astronomical Observatory (INAF-OAB) for hosting my Ph.D activity in these three years, and in particular G. Pareschi and G. Tagliaferri (INAF-OAB) for the supervision and collaboration in my Ph.D. work. S. Basso, R. Canestrari, O. Citterio, P. Conconi, M. Ghigo, E. Mattaini, G. Sironi and D. Spiga are acknowledged for the support and the collaboration.

I thank sincerely MEDIA LARIO TECHNOLOGIES company (MLT) and Dott. G. Nocerino (MLT-CEO) for supporting and financing my Ph.D work and for the manufacturing and metrology facilities availability. I thank in particular R. Banham, G. Bianucci, R. Binda, G. Borghi, G. Calegari, M. Cassanelli, G. Grisoni, J. Kools, F. Marioni, S. Moretti, M. Pedrali, A. Ritucci, M. Rossi, G. Salmaso, G. Valsecchi, F. Zocchi for the support and the collaboration.

I am grateful to UNIVERSITÀ DELL' INSUBRIA for this Ph.D. course in Astronomy and Astrophysics an especially to Prof. A. Treves for continuous support and coordination of the Ph.D course. Many thanks also to all my Ph.D. colleagues for the friendly collaboration.

ASI (Italian Space Agency) is acknowledged for financing the contracts for the Simbol-X Pre-Phase A, the New Hard X-ray Mission Phase A and the Technological Development Program (ASI-TDP). I thank particularly B. Negri, M. Piermaria, Q. Rioli for the collaboration. I would like to thank also P. Attinà of THALES-ALENIA SPACE and R. Buzzi, M. Ottolini, G. Parodi of BCV Progetti.

Part of the Ph.D work has been supported by MPE (Max-Planck-Institute fur extraterrestrische Physik) and DLR (German Space Agency) in the context of the eROSITA mission. I thank particularly H. Brauninger, V. Burwitz, J. Eder, M. Freyberg, P. Friedrich and P. Predehl of MPE for the support and the valuable collaboration. In the contest of the eROSITA project I would like to thank also M. Erhard, R. Graue, S. Gutruf, D. Kampf of KAYSER-THREDE company and M. Zimmermann of ZEISS company.

I thank HESS and MAGIC collaborations for supporting the qualification activities of the cold-slumping technique and in particular M. Doro, A. Foester, E. Giro and M. Mariotti. MPI Munich is acknowledged for the optical measurements performed on the prototype mirrors.

I thank R. Freeman (CEO) and R. Morton of ZEEKO Ltd company, J. Arnold of LT ULTRA company for the useful discussions and the collaboration.

I would like to thank M. Lavagna (POLITECNICO MILANO), A. Saggion (UNIVERSITÀ DI PADOVA) e M. Uslenghi (IASF MILANO) for reviewing my Ph.D thesis.